HAL
open science

Application of a high-resolution weather model in the area of the western Gulf of Corinth for the tropospheric correction of interferometric synthetic aperture radar (InSAR) observations

Nikolaos Roukounakis

To cite this version:

Nikolaos Roukounakis. Application of a high-resolution weather model in the area of the western Gulf of Corinth for the tropospheric correction of interferometric synthetic aperture radar (InSAR) observations. Ocean, Atmosphere. Université Paris sciences et lettres; Panepistīmio Patrōn, 2019. English. NNT : 2019PSLEE042 . tel-02967065

HAL Id: tel-02967065

https://theses.hal.science/tel-02967065v1

Submitted on 14 Oct 2020

HAL is a multi-disciplinary open access archive for the deposit and dissemination of scientific research documents, whether they are published or not. The documents may come from teaching and research institutions in France or abroad, or from public or private research centers.

L'archive ouverte pluridisciplinaire **HAL**, est destinée au dépôt et à la diffusion de documents scientifiques de niveau recherche, publiés ou non, émanant des établissements d'enseignement et de recherche français ou étrangers, des laboratoires publics ou privés.

PSL UNIVERSITÉ PARIS

THÈSE DE DOCTORAT
DE L'UNIVERSITÉ PSL

Préparée à l'Ecole Normale Supérieure
Dans le cadre d'une cotutelle avec Université de Patras, Grèce

Application d'un modèle météorologique à haute résolution à la correction troposphérique d'observations interférométriques de radar à synthèse d'ouverture (InSAR) dans la région de l'ouest du golfe de Corinthe, Grèce

Application of a high-resolution weather model in the area of the western Gulf of Corinth for the tropospheric correction of interferometric synthetic aperture radar (InSAR) observations

Soutenue par
Nikolaos ROUKOUNAKIS
Le 23 Octobre 2019

Ecole doctorale n° 560
Sciences de la terre et de l'environnement et physique de l'univers, Paris

Composition du jury :

Stéphane, JACQUEMOUD Université Denis Diderot – Paris VII	*Président*
Konstantinos, KATSAMPALOS Université Aristotle de Thessaloniki	*Rapporteur*
Laurent, MOREL CNAM, Le Mans	*Rapporteur*
Cécile, DOUBRE Ecole et Observatoire des Sciences de la Terre, Strasbourg	*Examinateur*
François, LOTT CNRS, Paris	*Examinateur*
Athanassios, ARGIRIOU Université de Patras	*Directeur de thèse*
Pierre, BRIOLE CNRS, ENS, Paris	*Directeur de thèse*

ENS | PSL

Abstract

Space geodesy techniques (SAR interferometry and GNSS) have recently emerged as an important tool for mapping regional surface deformations due to tectonic movements. A limiting factor to this technique is the effect of the troposphere, as horizontal and vertical surface velocities are of the order of a few mm yr^{-1}, and high accuracy (to mm level) is essential. The troposphere introduces a path delay in the microwave signal, which, in the case of GNSS Precise Point Positioning (PPP), can nowadays be successfully removed with the use of specialized mapping functions. Moreover, tropospheric stratification and short wavelength spatial turbulences produce an additive noise to the low amplitude ground deformations calculated by the (multitemporal) InSAR methodology. InSAR atmospheric phase delay corrections are much more challenging, as opposed to GNSS PPP, due to the single pass geometry and the gridded nature of the acquired data. Several methods have been proposed, including Global Navigation Satellite System (GNSS) zenithal delay estimations, satellite multispectral imagery analysis, and empirical phase/topography estimations. These methods have their limitations, as they rely either on local data assimilation, which is rarely available, or on empirical estimations which are difficult in situations where deformation and topography are correlated. Thus, the precise knowledge of the tropospheric parameters along the propagation medium is extremely useful for the estimation and minimization of atmospheric phase delay, so that the remaining signal represents the deformation mostly due to tectonic or other geophysical processes.

In this context, the current PhD Thesis aims to investigate the extent to which a high-resolution weather model, such as WRF, can produce detailed tropospheric delay maps of the required accuracy, by coupling its output (in terms of Zenith Total Delay or ZTD) with the vertical delay component in GNSS measurements. The model initially is operated with varying parameterization in order to demonstrate the best possible configuration for our study, with GNSS measurements providing a benchmark of real atmospheric conditions. In the next phase, the two datasets (predicted and observed) are compared and statistically evaluated for a period of one year, in order to investigate the extent to which meteorological parameters that affect ZTD, can be simulated accurately by the model under different weather conditions. Finally, a novel methodology is tested, in which ZTD maps produced from WRF and validated with GNSS measurements in the first phase of the experiment are used as a correction method to eliminate the tropospheric effect from selected InSAR interferograms. Results show that a high-resolution weather model which is fine-tuned at the local scale can provide a valuable tool for the tropospheric correction of InSAR remote sensing data.

Résumé

La Géodésie spatiale, par interférométrie radar à synthèse d'ouverture (InSAR) et Global Navigation Satellite System (GNSS), permet de cartographier les déformations tectoniques de la Terre. Les vitesses inter-sismiques, sont petites, de l'ordre de quelques mm an^{-1}. Pour atteindre une précision de positionnement relatif millimétrique, surtout dans la composante verticale, les délais troposphériques affectant les signaux GNSS et InSAR doivent être parfaitement corrigés.

Pour le GNSS, les délais troposphériques peuvent être évalués précisément grâce à la géométrie d'observation et à la redondance des données. La précision est telle que ces délais sont désormais assimilés en routine dans les modèles météorologiques.

La correction des interférogrammes est plus complexe parce que les données InSAR ne contiennent pas d'information permettant de remonter explicitement aux délais troposphériques. Au premier ordre, il est possible de calculer la part de l'interférogramme corrélée avec la topographie et de la corriger. Mais cette correction n'éliminer pas les hétérogénéités de courte longueurs d'onde ni les gradients régionaux. Pour cela il faut utiliser d'autres méthodes qui peuvent être basées sur l'utilisation des délais zénithaux GNSS disponibles dans la région ou sur des modèles météorologiques à haute résolution, ou sur une combinaison des deux.

Les délais zénithaux GNSS présentent l'intérêt de leur exactitude et de leur précision maîtrisée, mais dans la plupart des régions, ils ne sont disponibles, au mieux, qu'à quelques dizaines de points dans une image typique de 100 x 100 km. A l'opposé les modèles troposphériques à haute résolution apportent une vision matricielle globale, cependant leur précision est difficile à évaluer, surtout en zone de montagne.

Dans ma thèse, je calcule, sur la partie ouest du golfe de Corinthe, et pour l'année 2016, des modèles météorologiques à la résolution de 1 km, à l'aide du modèle américain WRF (Weather Research and Forecasting). Je compare les délais zénithaux prédits par le modèle avec ceux observés à dix-neuf stations GNSS permanentes. Ces données GNSS me permettent de choisir, parmi cinque jeux différents de paramètres de calcul WRF, celui qui aboutit au meilleur accord entre les délais GNSS et ceux issus de mes modèles. Je compare ensuite les séries temporelles GNSS de l'année 2016 aux sorties de modèles aux dix-neuf pixels correspondants. J'utilise enfin les sorties de mes modèles pour corriger les interférogrammes Sentinel-1 produits dans la zone d'étude avec des intervalles d'acquisition de 6, 12, 18 et 24 jours pour lesquels la cohérence des interférogramme demeure généralement élevée. Je montre qu'un modèle météorologique à haute résolution, ajusté à l'échelle locale à l'aide de données GNSS disponibles, permet une correction troposphérique des interférogrammes qui élimine une partie significative des effets de courte longueur d'onde, jusqu'à 5 km environ, donc plus courte que la longueur d'onde typique du relief.

Acknowledgements

I would like to express my gratitude to my supervisors, Research Director Pierre Briole (ENS), Professor Athanassios Argiriou (UPAT), Professor Ioannis Kioutsioukis (UPAT), and Research Director Adrianos Retalis (NOA) for their guidance, support and valuable contribution during my study. I would also like to thank my Thesis reporters, Professor Laurent Morel (CNAM) and Professor Konstantinos Katsampalos (AUTH), for their very useful input and comments. I gratefully acknowledge my employer, National Observatory of Athens, and especially the Director of my hosting Institute (IERSD) Professor Nikolaos Michalopoulos for facilitating me in every aspect during the realization of this Thesis. Moreover, I would like to thank my two colleagues at NOA, Panagiotis Elias and Dimitrios Katsanos for their valuable contribution and input at difficult times! I would like to thank the entire staff of the Laboratory of Geology of the Ecole Normale Supérieure, Paris, France, Helene Lyon-Caen, Dimitri Dimitrov, Maurin Vidal, Alex Nercessian, Alex Rigo and the whole CRL team who sustain the CRL Project. Finally, I would like to thank Rosa Pacione at EUREF for providing ZTD data, ESA for providing Sentinel-1 SAR data, the NOA METEO team (Vasiliki Kotroni and Konstantinos Lagouvardos) for providing meteorological data, and GRNET for allowing access to their HPC facilities (ARIS research platform).

Table of Contents

1. Introduction **1**

1.1 Background 1

1.2 Space Geodesy 2

1.3 The Corinth Rift Laboratory (CRL) 5

1.4 Rationale – Objectives 8

2. Tropospheric effects in GNSS and InSAR and current correction techniques **9**

2.1 Neutral atmospheric delay in space geodesy techniques 9

2.2 Tropospheric effects in GNSS measurements 9

2.2.1 Theory of refractivity and calculation of Zenith Hydrostatic Delay and Zenith Wet Delay 9

2.2.2 Current correction methods/ state of the art 13

2.2.3 GNSS Meteorology 16

2.3 Tropospheric effects in InSAR measurements 18

2.3.1 Interferometric Synthetic Aperture Radar (InSAR) fundamentals and main limitations 18

2.3.2 Tropospheric artefacts in InSAR and current correction methods 20

3. Numerical Weather Prediction (NWP) Models and their applications **25**

3.1 Numerical modelling of the troposphere 25

3.2 Applications of high-resolution local-area models (LAMs) 27

3.2.1 Operational forecasting 27

3.2.2 Atmospheric research and climate re-analysis 28

3.2.3 Estimation of water vapour profiles – tropospheric correction 30

4. The PaTrop experiment **32**

4.1 Experimental setup and description of the study area 32

4.2 Data processing 35

4.2.1 Calculation of Zenith Total Delay (ZTD) from GNSS data 36

4.2.2 Calculation of Zenith Total Delay (ZTD) from WRF data 36

5. Configuration and parameterization of WRF 1x1 km re-analysis **38**

5.1 Model description 38

5.2 Model configuration and parameterization of physical components 38

5.3 Sensitivity analysis and evaluation of WRF schemes with GNSS data 42

5.3.1 Results of WRF vs. GNSS ZTDs for five different model schemes 42

5.3.2 Results of improved model topography with the use of high-resolution DEM 47
5.4 Concluding Remarks 52
6. Validation of WRF derived tropospheric delay maps with GNSS ZTD measurements for the PaTrop period (January-December 2016) 53
6.1 Annual variability of WRF vs. GNSS ZTD and evaluation of model performance 54
6.2 Seasonal characteristics of WRF vs. GNSS ZTD and evaluation of model performance 57
6.2.1 Results for S1 (January-March 2016) 61
6.2.2 Results for S2 (April-June 2016) 63
6.2.3 Results for S3 (July-September 2016) 65
6.2.4 Results for S4 (October-December 2016) 67
6.3 Comparison of different tropospheric GNSS processing protocols at PAT0 station 69
6.4 Uncertainty and sources of error in high-resolution WRF vs. GNSS derived ZTD 71
6.4.1 A case of WRF vs. GNSS de-correlation and comparison with meteorological surface data 72
6.5 Concluding Remarks 76
7. InSAR Tropospheric Correction with the use of WRF Derived Delay Maps 80
7.1 Introduction 80
7.2 Methodology 81
7.3 Results and Discussion 84
7.4 Concluding Remarks 129
8. Conclusions – Perspectives 130

Appendix

A. Timeseries and bias plots of WRF MOD1-MOD5 vs. GNSS ZTDs for the test period (17-29 June 2016) 134
B. Timeseries, bias plots and correlation plots of WRF MOD5 vs. GNSS ZTDs for the whole PaTrop period (Jan-Dec 2016). 146

Bibliography 159

List of Tables

2.1 Typical high values of Zenith Total Delay (ZTD) at sea level 13

2.2 PPP vs. network GNSS processing strategy 15

2.3 Overview of satellite SAR systems 18

3.1 Typical high values of Zenith Total Delay (ZTD) at sea level 26

4.1 Locations and characteristics of permanent GNSS stations used in PaTrop 34

4.2 CRL tropospheric solution settings 35

5.1 WRF parameterization options used for the PaTrop sensitivity analysis 42

5.2 Pearson Correlation Co-efficient results for all schemes (17/6-29/6/2016) 44

5.3 Mean Bias results for all schemes (17/6-29/6/2016) 44

5.4 Mean Average Bias results for all schemes (17/6-29/6/2016) 45

5.5 RMSE results for all schemes (17/6-29/6/2016)..... 45

5.6 Absolute elevation differences and MAE at 16 GNNS nearest WRF grid points for 5 topographical datasets (d04). ASTER 1s global GDEM v2 is used as the reference map. 48

5.7 Pearson Correlation Co-efficient results for MOD5 with 5 topograpical sets (17/6-29/6/2016)..... 50

5.8 Mean Absolute Bias results for MOD5 with 5 topograpical sets (17/6-29/6/2016)..... 50

5.9 Locations and characteristics of WRF grid point nearest to GNSS station (ASTER 1s DEM) ... 51

6.1 Statistical indices of complete WRF ZTS vs. GNSS ZTD time series – Jan-Dec 2016 55

6.2 Seasonal statistical indices of WRF ZTS vs. GNSS ZTD time series – 2016..... 58

6.3 σ values within error range – S1 61

6.4 σ values within error range – S2 63

6.5 σ values within error range – S3 65

6.6 σ values within error range – S4 67

6.7 σ values within error range – WRF vs. PAT0 EUREF solution..... 70

6.8 Comparison of seasonal statistical indices of WRF vs. EUREF and WRF vs. CRL ZTD time series –2016..... 70

7.1 Dates of Sentinel-1 interferograms examined, corresponding WRF vs. GNSS ZTD average bias differences (Δbias), and RMS and SD differences between original and corrected interferograms 126

List of Figures

1.1 Geophysical processes that affect geodetic observations as a function of spatial and temporal scale 4

1.2 Simplified geology and the fault network in the Corinth Rift 6

1.3 Gulf of Corinth: Velocities for the period 2017-2018 and focal mechanisms 2003-2018 7

2.1 Schematic presentation of individual slant path delays (SPDs) from three GNSS satellites and their mapping to zenith total delay (ZTD) 12

2.2 Main GNSS positioning techniques used 14

2.3 Crustal deformation monitoring with InSAR..... 20

2.4 Tropospheric delay estimates for different correction methods 23

3.1 Physical processes mathematically modelled in NWP forecasting models..... 25

3.2 Effects of topography on local wind patterns 29

4.1 Map of the PaTrop study area, Western GoC. 32

4.2 Photos of newly installed PaTrop GNSS permanent stations in Kalavrita and Mesologgi 33

4.3 Example of GNSS-WRF geometry for ANOC Station 37

5.1 Map showing the four nested domains (d01-d04) used for WRF weather re-analysis over the Western GoC 39

5.2 RMSE distribution for each model configuration at the 16 stations 46

5.3 Distribution of model validation metrics (MAB, RMSE and PPC) per station elevation h – MOD5 47

5.4 Map of domain 4 showing elevation differences: a) GTOPO 30s minus ASTER 1s DEM opt3; b) ASTER 1s DEM opt1 minus ASTER 1s DEM opt3 49

6.1 Underlying topography of domain 4, ASTER 1s DEM opt4 54

6.2 Plots of: (a) RMSE vs. horizontal distance s between WRF grid point and GNSS station; (b) MB vs. GNSS station elevation h. 56

6.3 Distribution of validation metrics (MAB, RMSE and PPC) per station elevation h 57

6.4 Monthly variability of MAB at the 19 PaTrop stations, classified per terrain type 59

6.5 Distribution of validation metrics (MAB, RMSE and PPC) per station elevation h, and season (S1-S4)..... 60

6.6 Absolute bias plot for all stations, season S1 62

6.7 Absolute bias plot for all stations, season S2 64

6.8 Absolute bias plot for all stations, season S3 66

6.9 Absolute bias plot for all stations, season S4 68

6.10 Correlation plots of WRF vs. EUREF and EUREF vs. CRL ZTDs at PAT0 station 69

6.11 Bias plots of WRF vs. EUREF and WRF vs. CRL ZTDs at PAT0 station 69

6.12 Graph of WRF vs. GNSS ZTD time series (top); graph of WRF vs. METEO surface temperature Ts and surface relative humidity RH (middle); graph of WRF vs. METEO surface pressure at sea level Ps plus wind distribution (bottom). KALA station 73

6.13 Graph of WRF vs. GNSS ZTD time series (top); graph of WRF vs. METEO surface temperature Ts and surface relative humidity RH (middle); graph of WRF vs. METEO surface pressure at sea level Ps plus wind distribution (bottom). ANOC station 74

6.14 Graph of WRF vs. GNSS ZTD time series (top); graph of WRF vs. METEO surface temperature Ts and surface relative humidity RH (middle); graph of WRF vs. METEO surface pressure at sea level Ps plus wind distribution (bottom). PAT0 station 75

6.15 Maps of water vapour mixing ratio at eta level 6 as calculated by the WRF re-analysis in 3h intervals 77

6.16 Maps of water vapour mixing ratio at eta level 6 as calculated by the WRF re-analysis in 3h intervals 78

7.1 Example of producing a differential ZTD map from the subtraction of two single ZTD maps, produced with WRF at the times of InSAR acquisitions 82

7.2 Example of atmospheric correction of an interferogram (18/9-30/9, track 80) 82

7.3 Coherence maps for Sentinel-1 ascending track 175 (left) and descending track 80 (right), over the extended western GoC area 85

7.4 Wrapped interferogram from SAR acquisitions on 30/09/2016 and 06/10/2016, track 175 in radar geometry (left). Corresponding WRF-derived wrapped differential LOS delay map (right) 86

7.5 Wrapped interferogram from SAR acquisitions on 30/09/2016 and 06/10/2016, track 175 in radar geometry (left). Corresponding residual map after subtraction of WRF-derived wrapped differential LOS delay map from the interferogram (right) 87

7.6 Wrapped interferogram from SAR acquisitions on 30/09/2016 and 24/10/2016, track 175 in radar geometry (left). Corresponding WRF-derived wrapped differential LOS delay map (right) 88

7.7 Wrapped interferogram from SAR acquisitions on 30/09/2016 and 24/10/2016, track 175 in radar geometry (left). Corresponding residual map after subtraction of WRF-derived wrapped differential LOS delay map from the interferogram (right) 89

7.8 Wrapped interferogram from SAR acquisitions on 30/09/2016 and 05/11/2016, track 175 in radar geometry (left). Corresponding WRF-derived wrapped differential LOS delay map (right) 90

7.9 Wrapped interferogram from SAR acquisitions on 30/09/2016 and 05/11/2016, track 175 in radar geometry (left). Corresponding residual map after subtraction of WRF-derived wrapped differential LOS delay map from the interferogram (right) 91

7.10 Wrapped interferogram from SAR acquisitions on 06/10/2016 and 24/10/2016, track 175 in radar geometry (left). Corresponding WRF-derived wrapped differential LOS delay map (right) 92

7.11 Wrapped interferogram from SAR acquisitions on 06/10/2016 and 24/10/2016, track 175 in radar geometry (left). Corresponding residual map after subtraction of WRF-derived wrapped differential LOS delay map from the interferogram (right).. 93

7.12 Wrapped interferogram from SAR acquisitions on 06/10/2016 and 11/12/2016, track 175 in radar geometry (left). Corresponding WRF-derived wrapped differential LOS delay map (right) 94

7.13 Wrapped interferogram from SAR acquisitions on 06/10/2016 and 11/12/2016, track 175 in radar geometry (left). Corresponding residual map after subtraction of WRF-derived wrapped differential LOS delay map from the interferogram (right).. 95

7.14 Wrapped interferogram from SAR acquisitions on 24/10/2016 and 05/11/2016, track 175 in radar geometry (left). Corresponding WRF-derived wrapped differential LOS delay map (right) 96

7.15 Wrapped interferogram from SAR acquisitions on 24/10/2016 and 05/11/2016, track 175 in radar geometry (left). Corresponding residual map after subtraction of WRF-derived wrapped differential LOS delay map from the interferogram (right).. 97

7.16 Wrapped interferogram from SAR acquisitions on 24/10/2016 and 17/11/2016, track 175 in radar geometry (left). Corresponding WRF-derived wrapped differential LOS delay map (right) 98

7.17 Wrapped interferogram from SAR acquisitions on 24/10/2016 and 17/11/2016, track 175 in radar geometry (left). Corresponding residual map after subtraction of WRF-derived wrapped differential LOS delay map from the interferogram (right).. 99

7.18 Wrapped interferogram from SAR acquisitions on 24/10/2016 and 23/11/2016, track 175 in radar geometry (left). Corresponding WRF-derived wrapped differential LOS delay map (right) 100

7.19 Wrapped interferogram from SAR acquisitions on 24/10/2016 and 23/11/2016, track 175 in radar geometry (left). Corresponding residual map after subtraction of WRF-derived wrapped differential LOS delay map from the interferogram (right).. 101

7.20 Wrapped interferogram from SAR acquisitions on 24/10/2016 and 05/12/2016, track 175 in radar geometry (left). Corresponding WRF-derived wrapped differential LOS delay map (right) 102

7.21 Wrapped interferogram from SAR acquisitions on 24/10/2016 and 05/12/2016, track 175 in radar geometry (left). Corresponding residual map after subtraction of WRF-derived wrapped differential LOS delay map from the interferogram (right).. 103

7.22 Wrapped interferogram from SAR acquisitions on 25/08/2016 and 18/09/2016, track 80 in radar geometry (left). Corresponding WRF-derived wrapped differential LOS delay map (right) 104

7.23 Wrapped interferogram from SAR acquisitions on 25/08/2016 and 18/09/2016, track 80 in radar geometry (left). Corresponding residual map after subtraction of WRF-derived wrapped differential LOS delay map from the interferogram (right).. 105

7.24 Wrapped interferogram from SAR acquisitions on 25/08/2016 and 30/09/2016, track 80 in radar geometry (left). Corresponding WRF-derived wrapped differential LOS delay map (right) 106

7.25 Wrapped interferogram from SAR acquisitions on 25/08/2016 and 30/09/2016, track 80 in radar geometry (left). Corresponding residual map after subtraction of WRF-derived wrapped differential LOS delay map from the interferogram (right).. 107

7.26 Wrapped interferogram from SAR acquisitions on 25/08/2016 and 18/10/2016, track 80 in radar geometry (left). Corresponding WRF-derived wrapped differential LOS delay map (right) 108

7.27 Wrapped interferogram from SAR acquisitions on 25/08/2016 and 18/10/2016, track 80 in radar geometry (left). Corresponding residual map after subtraction of WRF-derived wrapped differential LOS delay map from the interferogram (right).. 109

7.28 Wrapped interferogram from SAR acquisitions on 18/09/2016 and 30/09/2016, track 80 in radar geometry (left). Corresponding WRF-derived wrapped differential LOS delay map (right) 110

7.29 Wrapped interferogram from SAR acquisitions on 18/09/2016 and 30/09/2016, track 80 in radar geometry (left). Corresponding residual map after subtraction of WRF-derived wrapped differential LOS delay map from the interferogram (right).. 111

7.30 Wrapped interferogram from SAR acquisitions on 18/09/2016 and 06/10/2016, track 80 in radar geometry (left). Corresponding WRF-derived wrapped differential LOS delay map (right) 112

7.31 Wrapped interferogram from SAR acquisitions on 18/09/2016 and 06/10/2016, track 80 in radar geometry (left). Corresponding residual map after subtraction of WRF-derived wrapped differential LOS delay map from the interferogram (right).. 113

7.32 Wrapped interferogram from SAR acquisitions on 18/09/2016 and 18/10/2016, track 80 in radar geometry (left). Corresponding WRF-derived wrapped differential LOS delay map (right) 114

7.33 Wrapped interferogram from SAR acquisitions on 18/09/2016 and 18/10/2016, track 80 in radar geometry (left). Corresponding residual map after subtraction of WRF-derived wrapped differential LOS delay map from the interferogram (right).. 115

7.34 Wrapped interferogram from SAR acquisitions on 06/10/2016 and 24/10/2016, track 80 in radar geometry (left). Corresponding WRF-derived wrapped differential LOS delay map (right) 116

7.35 Wrapped interferogram from SAR acquisitions on 06/10/2016 and 24/10/2016, track 80 in radar geometry (left). Corresponding residual map after subtraction of WRF-derived wrapped differential LOS delay map from the interferogram (right).. 117

7.36 Wrapped interferogram from SAR acquisitions on 18/10/2016 and 24/10/2016, track 80 in radar geometry (left). Corresponding WRF-derived wrapped differential LOS delay map (right) 118

7.37 Wrapped interferogram from SAR acquisitions on 18/10/2016 and 24/10/2016, track 80 in radar geometry (left). Corresponding residual map after subtraction of WRF-derived wrapped differential LOS delay map from the interferogram (right).. 119

7.38 Wrapped interferogram from SAR acquisitions on 17/11/2016 and 23/11/2016, track 80 in radar geometry (left). Corresponding WRF-derived wrapped differential LOS delay map (right) 120

7.39 Wrapped interferogram from SAR acquisitions on 17/11/2016 and 23/11/2016, track 80 in radar geometry (left). Corresponding residual map after subtraction of WRF-derived wrapped differential LOS delay map from the interferogram (right).. 121

7.40 Wrapped interferogram from SAR acquisitions on 29/11/2016 and 11/12/2016, track 80 in radar geometry (left). Corresponding WRF-derived wrapped differential LOS delay map (right) 122

7.41 Wrapped interferogram from SAR acquisitions on 29/11/2016 and 11/12/2016, track 80 in radar geometry (left). Corresponding residual map after subtraction of WRF-derived wrapped differential LOS delay map from the interferogram (right).. 123

7.42 Wrapped interferogram from SAR acquisitions on 05/12/2016 and 11/12/2016, track 80 in radar geometry (left). Corresponding WRF-derived wrapped differential LOS delay map (right) 124

7.43 Wrapped interferogram from SAR acquisitions on 05/12/2016 and 11/12/2016, track 80 in radar geometry (left). Corresponding residual map after subtraction of WRF-derived wrapped differential LOS delay map from the interferogram (right).. 125

7.44 Correlation of RMS reduction between original and corrected interferograms and Δbias 127

7.45 Correlation of SD reduction between original and corrected interferograms and Δbias 128

7.46 Correlation of % SD reduction vs. % RMS reduction for the 20 cases studied 128

Abbreviations and Acronyms

APS Atmospheric Phase Screen

ASTER Advanced Spaceborne Thermal Emission and Reflection Radiometer

CDDIS Crustal Dynamics Data Information System

CPU Central Processing Unit

CRL Corinth Rift Laboratory

DEM Digital Elevation Model

DLR Deutsche Lebensmittel Rundschau

DEM Digital Elevation Model

DORIS Doppler Orbitography and Radio-positioning by Integrated Satellite

DWD Deutscher Wetterdienst

ECMWF European Centre for Medium-Range Weather Forecasts

EPN European Processing Network

ESA European Space Agency

GAM Global Atmospheric Model

GoC Gulf of Corinth

GGOS Global Geodetic Observing System

GMF Global Mapping Function

GNSS Global Navigation Satellite System

GPS Global Positioning System

GPT Global Pressure and Temperature model

GRNET Greek Research and Technology Network

HPC High Performance Computer

IGS International GNSS Service

IWV Integrated Water Vapour

JPL Jet Propulsion Laboratory

LAGEOS Laser GEOdynamics Satellite

LAM Limited-Area Model

LEO Low Earth Orbit

LOS Line-of-Sight

MERIS MEdium Resolution Imaging Spectrometer

MODIS Moderate Resolution Imaging Spectroradiometer

NCEP National Centers for Environmental Prediction

NGSLR Next Generation Satellite Laser Ranging

NWP Numerical Weather Prediction

PPP Precise Point Positioning

PWV Precipitable Water Vapour

SAR Synthetic Aperture Radar

SGP Space Geodesy Project

SINEX Solution Independent Exchange format

SRTM Shuttle Radar Topography Mission

SLR Satellite Laser Ranging

TRF Terrestrial Reference Frame

USGS United States Geological Survey

VLBI Very Long Baseline Interferometry

VMF Vienna Mapping Function

WRF Weather Research and Forecasting Model

ZHD Zenith Hydrostatic Delay

ZTD Zenith Total Delay

ZWD Zenith Wet Delay

.....

1. Introduction

1.1 Background

Space geodesy techniques (SAR interferometry and GNSS) have recently emerged as an important tool for mapping regional surface deformations due to tectonic movements. A limiting factor to this technique is the effect of the troposphere, as horizontal and vertical surface velocities are of the order of a few mm yr^{-1}, and high accuracy (to mm level) is essential. The troposphere introduces a path delay in the microwave signal, which, in the case of GNSS Precise Point Positioning (PPP), can nowadays be successfully removed with the use of specialized mapping functions [Bevis et al., 1992; Boehm et al., 2006a; Tesmer et al., 2007; Bock et al., 2016]. Moreover, tropospheric stratification and short-wavelength spatial turbulences produce an additive noise to the low amplitude ground deformations calculated by the (multitemporal) InSAR methodology. InSAR atmospheric phase delay corrections are much more challenging, as opposed to GNSS PPP, due to the single pass geometry and the gridded nature of the acquired data. Several methods have been proposed, including local atmospheric data collection [Delacourt et al., 1998], Global Navigation Satellite System (GNSS) zenithal delay estimations [Williams et al., 1998; Webley et al., 2002; Li et al., 2006a; Onn and Zebker, 2006], satellite multispectral imagery analysis [Li et al., 2006b], assimilation of meteorological data in atmospheric models [Wadge et al., 2002; Puysségur et al., 2007] and empirical phase/topography estimations [e.g., Wicks et al., 2002; Biggs et al., 2007; Cavalié et al., 2008; Lin et al., 2010; Bekaert et al., 2015b]. These methods have their limitations, as they rely either on local data assimilation, which is rarely available, or on empirical estimations which are difficult in situations where deformation and topography are correlated. Thus, the precise knowledge of the tropospheric parameters along the propagation medium is extremely useful for the estimation and minimization of atmospheric phase delay, so that the remaining signal represents the deformation mostly due to tectonic or other geophysical processes. In fact, recent studies [Doin et al., 2009; Jolivet at al., 2011, 2014; Kinoshita et al., 2012; Bekaert et al., 2015a] have investigated this trend by calculating tropospheric delays from the output of local or global weather models. However, the low resolution and the generic configuration of the models used have, so far, inhibited the full exploitation of this method.

On the other hand, the same remote sensing techniques used by geophysicists for measuring crustal deformations and other geological phenomena, can provide very useful information of meteorological and climatological interest. In fact, if the same path delay due to the water vapour content in the troposphere can be accurately estimated, it can be used (as Integrated Water Vapour or IWV) in numerous meteorological applications, from assimilation into weather forecasting models [e.g., Poli et al., 2007; Moll et al., 2008; Schwitalla et al., 2011; Szintai and Mile, 2015] to mapping of the 3D distribution of water vapour in the atmosphere [e.g., Wang et al., 2007; Flores et al., 2008; Shangguan et al., 2013]. For example, GNSS is now an established atmospheric observing system, which can accurately sense water vapour, the most abundant greenhouse gas, accounting for 60–70% of atmospheric warming. In Europe, the application of GNSS in meteorology started roughly two decades ago, and today it is a well-established field in both research and operation [Guerova et al., 2016]. With respect to InSAR, there is still no established methodology which can make use of the

interferometric data for meteorological applications. However, with the onset of new satellite missions (such as the European Space Agency's Sentinel 1 and 2), it is highly probable that this will happen in the near future, and meteorologists will be able to use data from InSAR imagery to enhance the weather forecasting capabilities of existing Numerical Weather Prediction models.

The primary objective of this PhD Thesis is to couple the vertical delay component in GNSS measurements (Zenith Total Delay or ZTD) with the output from a high-resolution meteorological model (WRF), in order to produce a 3D tomography of the troposphere over the study area of the western Gulf of Corinth, Greece. High resolution re-analysis enables a more precise description of local topographic forcings due to orography or land-sea contrasts, and therefore processes strongly forced by topography, such as wind profiles, orographic precipitation and relative humidity, can be represented much more accurately. The model is operated with varying parameterization in order to demonstrate the best possible configuration for our study, with GNSS measurements providing a benchmark of real atmospheric conditions. In the second phase of the study, a novel methodology is developed, in which ZTD maps produced from WRF and validated with GNSS measurements in the first phase of the experiment will be used as a correction method to eliminate the tropospheric effect from selected InSAR interferograms.

1.2 Space Geodesy

Geodesy is the science of the Earth's shape, rotation, and gravitational field including their evolution in time. In the past, geodesists were using terrestrial measurements, for example land surveying methods or gravity observations, in order to measure the earth's topographical features or determine the geoid. In recent decades, it has been possible to study the evolution of these "three pillars of geodesy" in time in greater detail, due to the development of space-based geodetic technologies and the realization of a truly global reference system of co-ordinates [Altamimi et al., 1993, 2002]. Space-geodetic techniques which are used to observe the geodetic properties of the Earth include Very Long Baseline Interferometry (VLBI), Satellite Laser Ranging (SLR), Global Navigation Satellite Systems (GNSS) (such as the US Global Positioning System (GPS) or Russian GLONASS), and the French Doppler Orbitography and Radio-Positioning by Integrated Satellite (DORIS) system. These space-geodetic methods provided the basis for the global reference system that is needed in order to assign precise coordinates to terrestrial features and thereby determine how these vary over time. The Terrestrial Reference Frame (TRF) is nowadays the foundation for virtually all airborne, space-based and ground-based Earth observations [Herring, 2007].

Geodetic measurements can be influenced by a variety of Earth processes over a range of spatial and temporal scales, including geophysical processes (crustal deformation associated with plate tectonics, earthquakes, and volcanoes), atmospheric processes (weather and climate dynamics, atmospheric chemistry), oceanic and hydrological processes (tides, ocean circulation, motions and mass fluctuations of glaciers and ice shelves, hydrology and continental water storage). Space geodesy methods have been proven as an invaluable tool for monitoring these diverse processes, as they have provided integrated and geo-referenced sets of observations on global to regional spatial scales with high spatial and temporal resolution. For example, since the end of the last century, VLBI and GNSS have been playing an important role to accurately measure crustal deformation due to

tectonic plate movements with a precision of centimetres to sub-millimetres [e.g. Tralli et al., 1988; Larson and Agnew, 1991; Segall and Davis, 1997; Argus et al., 1999; Larson et al., 2003]. Other geophysical applications of space geodesy include [Blewitt, 2007]:

- GNSS seismology, e.g. interseismic strain accumulation by tracking the relative positions between networks of GNSS stations in and around plate boundaries [Kreemer at al., 2003, 2006b], postseismic processes and rheology of the Earth's topmost layers, by inverting the decay signature of GNSS station positions in the days to decades following an earthquake [Pollitz, 1997; Kreemer et al., 2006a], seismic waves observations with GNSS [Nikolaidis et al., 2001;] etc.
- Magmatic processes, by measuring time variation in the position of stations located on volcanoes or other regions of magmatic activity, such as hot spots. [Beauducel et al., 2000; Hooper et al., 2004; Lundgren et al., 2004].
- Rheology of the Earth's mantle and ice-sheet history, by measuring the vertical and horizontal velocities of GNSS stations in the area of postglacial rebound (glacial isostatic adjustment) [Lidberg et al., 2007; Sella et al., 2007], or time-variable gravity [Cox and Chao, 2002; Cheng and Tapley, 2004; Paulson et al., 2007; Tamisiea et al., 2007].
- Mass redistribution in the Earth's fluid envelope (allowing for the study of atmosphere–hydrosphere–cryosphere–solid-Earth interactions), mostly by means of SLR, such as measuring the time variation in Earth's shape, the velocity of the solid-Earth centre of mass [Watkins and Eanes, 1997; Ray, 1998; Chen et al., 1999], Earth's gravity field [Nerem et al., 1993; Gegout and Cazenave, 1993; Cheng and Tapley, 1999, 2004], and Earth's rotation in space by SLR determination of the exchange of angular momentum between the solid Earth and fluid components of the Earth system [Chao et al., 1987].
- Global change in sea level, by measuring vertical movement of the solid Earth at tide gauges, by measuring the position of space-borne altimeters in a global reference frame, and by inferring exchange of water between the oceans and continents from mass redistribution monitoring.
- Hydrology of aquifers by monitoring aquifer deformation inferred from time variation in 3-D coordinates of a network of GNSS stations on the surface above the aquifer.
- Providing a global reference frame for consistent georeferencing and precision time tagging of nongeodetic measurements and sampling of the Earth, with applications in seismology, airborne and space-borne sensors and general fieldwork. [Altamimi et al., 2002; Altamimi, 2005].

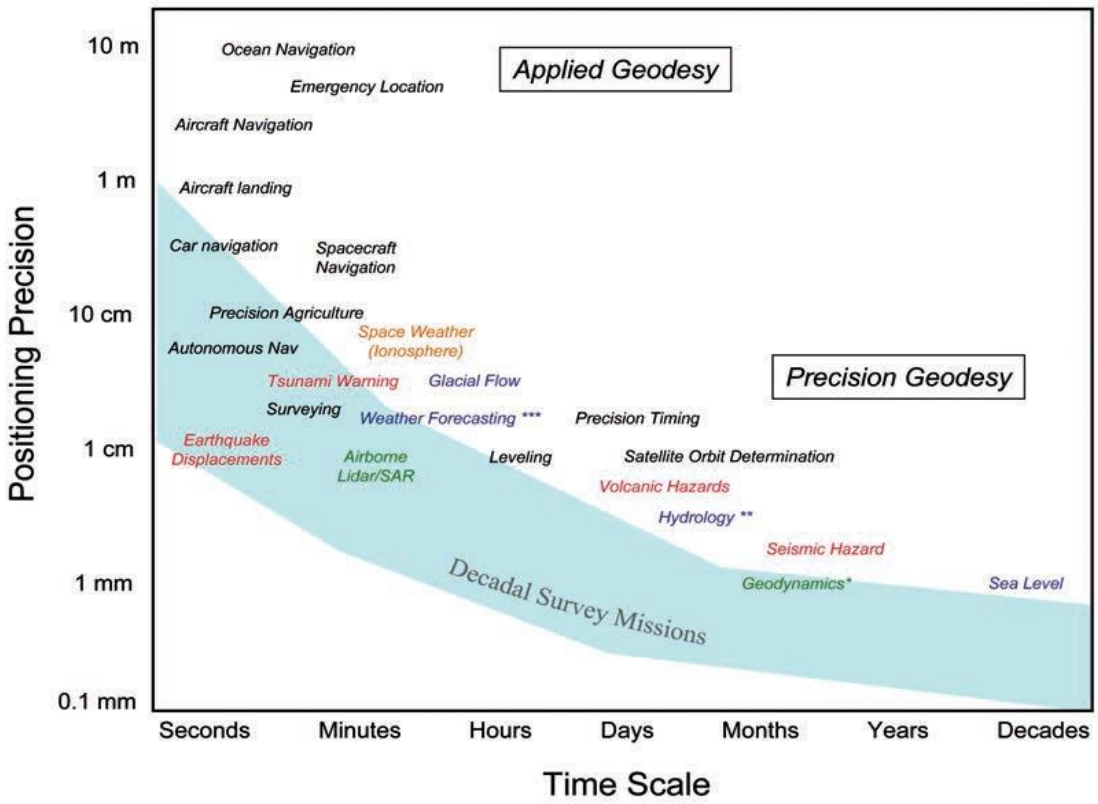

** Plate motion, plate deformation, mountain building, mass transport, ice-sheet changes*
*** Vertical surface motion from GNSS/GPS and InSAR for ground water management*
**** Water vapour and other meteorological information from GNSS/GPS ground stations and radio occultations in space*

Figure 1-1. Geophysical processes that affect geodetic observations as a function of spatial and temporal scale (Source: National Research Council. Precise Geodetic Infrastructure: National Requirements for a Shared Resource. Washington, DC: The National Academies Press, 2010).

The required precision for each of the current geodetic applications as a function of the time interval to which they refer is illustrated in Figure 1-1. It is seen that the most demanding applications at the shortest time intervals include GNSS seismology and tsunami warning systems, whereas at the longest time intervals, the most demanding applications include sea level change and geodynamics. Consistency in connecting the longest to the shortest time scales requires an accurate and stable global terrestrial reference frame, which supports the demanding requirements of the geodetic infrastructure. As a general rule, estimation of GNSS station velocity can be achieved with precision < 1 mm yr^{-1} using > 2.5 years of continuous data [Blewitt, 2007].

An equally important remote sensing technology for studying geophysical phenomena is Synthetic Aperture Radar (SAR), an active radar system mounted on satellites, which transmits microwaves and receives the scattered signals back from the Earth's surface. Although not a space geodesy method in the narrow sense, SAR observation has been used to monitor many of the

aforementioned processes with great success. During the past two decades, SAR Interferometry (InSAR) has evolved into an established method for measuring:

- Surface deformations associated with earthquakes [e.g. Massonnet and Feigl, 1995; Delacourt et al., 1997; Delouis et al., 2002; Feigl et al., 2002], volcanic activities [e.g. Pritchard and Simons, 2002; Sykioti et al., 2003; Pedersen and Sigmundsson, 2006], land subsidence and uplift [e.g. Massonnet et al., 1997; Carnec et al., 1999; Bawden et al., 2001; Carbognina et al., 2004] and landslides [e.g. Colesanti et al., 2003; Catani et al., 2005].
- Land topography at high spatial and vertical resolution, producing precise topographic maps of both the Earth and Venus [Meyer and Sandwell, 2012].
- Glacier and ice sheet dynamics [e.g. Goldstein et al., 1993; Joughin et al., 1996a; Mohr et al., 1998; Gray et al., 2001].
- Hydrological parameters, such as soil moisture content [e.g. Gabriel et al., 1989; Nolan et al., 2003; Makkearson et al., 2006] and inland water level variations [Alsdorf et al., 2000; Romeiser et al., 2007].

In fact, the combination of high spatial resolution InSAR methodology with high temporal resolution GNSS point measurements produces even better results, with respect to most of these geophysical parameters, and in recent years many studies are exploiting this method to potentially map highly accurate deformations (i.e. at sub-centimetre levels) [Wang and Wright, 2012; Walters et al., 2014; Ozawa et al., 2016].

Space geodesy is revolutionizing the way that environmental parameters are being monitored and is increasing our understanding of the complex Earth system. At the same time, it contributes to mitigating the impact of major geohazards, such as earthquakes, volcanic eruptions, landslides, tsunamis, hurricanes, floods and extreme weather.

1.3 The Corinth Rift Laboratory (CRL)

The Gulf of Corinth (GoC) is known as one of the most active intra-continental rifts in the world. Separating continental Greece to the North from the Peloponnese to the South, the 120 km long structure has been long identified as a site of intense geophysical activity. Geodetic studies conducted during the past 20 years based on GNSS and InSAR observations have revealed North-South extension rates up to 1.5 cm yr^{-1} [Briole et al., 2000; Avallone et al., 2004], one of the highest worldwide. The Gulf of Corinth also shows one of the highest seismicity rates in the Euro-Mediterranean region, having produced a number of strong earthquakes in recent years: Alkyonides (1981, M=6.7), Galaxidi (1992, M=5.8), Aigio (1995, M=6.2), and Efpalio (2010, M=5.3) (Figure 1-3). The Gulf of Corinth belongs to the general tectonic region of the Eastern Mediterranean, where dynamics are complex. The dominant characteristic of the region is the subduction of the African and Anatolian plates along the Hellenic Arc, which controls the rifting as a result of the extension in the back-arc region of the Aegean subduction zone, enhanced by the interaction with the Western tip of the North Anatolian Fault [Armijo et al., 1996, 2004; Jolivet, 2001; Hubert-Ferrari et al., 2003; Kokkalas et al., 2006; Reilinger et al., 2010; Pérouse et al., 2012].

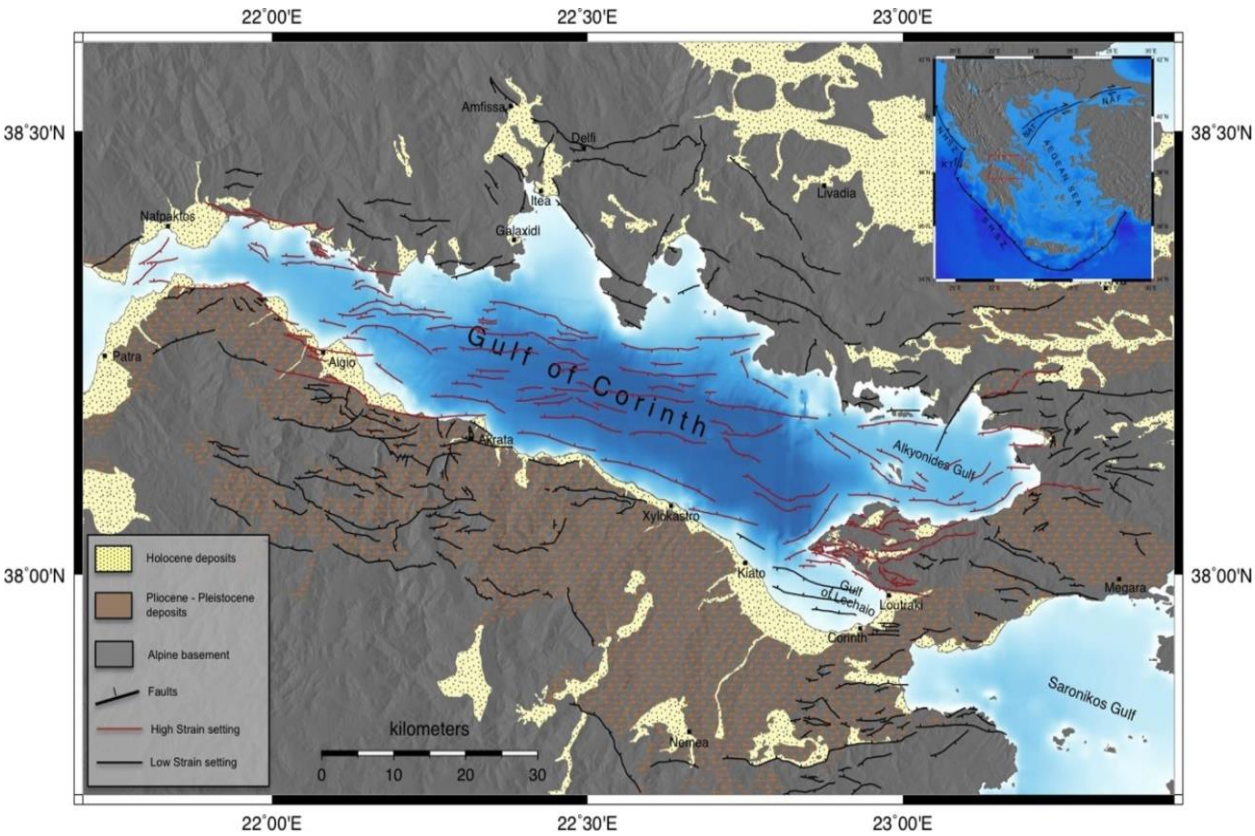

Figure 1-2. Simplified geology and the fault network in the Corinth Rift. Faults in red (high strain setting) indicate the currently active Rift zone and faults in black (low strain setting) the currently inactive Rift zone. (Source: Michas et al., 2015).

With regards to the fault structure, The Gulf of Corinth appears as an asymmetrical rift [Bernard et al., 2016], with the most active normal faults dipping north, resulting in the long term subsidence of the northern coast and a general uplift of the southern coast (northern Peloponnese) [Armijo et al., 1996; Palyvos et al., 2007; Elias et al., 2009]. The fault system consists of a large number of offshore and on-shore (well visible at the surface) long faults, most of them striking E-W (e.g. Eliki, Kamari, Psathopyrgos, Aigio, Trizonia, Eratini), along which large earthquakes occur. The stratigraphy reflects the present and quaternary tectonics of the rift [Bernard et al., 2016]: to the north of the gulf, the mountainous, subsiding Hellenides limestone nappes are outcropping almost everywhere along the rift; to the south, these nappes are mostly covered by a thick (several hundreds of meters) conglomerate layer, and only outcrop on the footwall of the southern active faults [e.g., Armijo et al., 1996; Ghisetti and Vezzani, 2004]. Along the coastline, and offshore, on the walls of the normal faults, the conglomerates are covered by finer, recent deposits (sands and clay), up to 150 m thick in the Aigion harbour [Pitilakis et al., 2004; Cornet et al., 2004b]. The fault structure and the geology of the Gulf of Corinth are illustrated in Figure 1-2.

In this context, the Corinth Rift Laboratory (CRL) has been established in recent years, as a large international research effort bringing together scientists from a number of European countries and institutions [Cornet et al., 2001, 2004a; Web: http://www.crlab.eu].

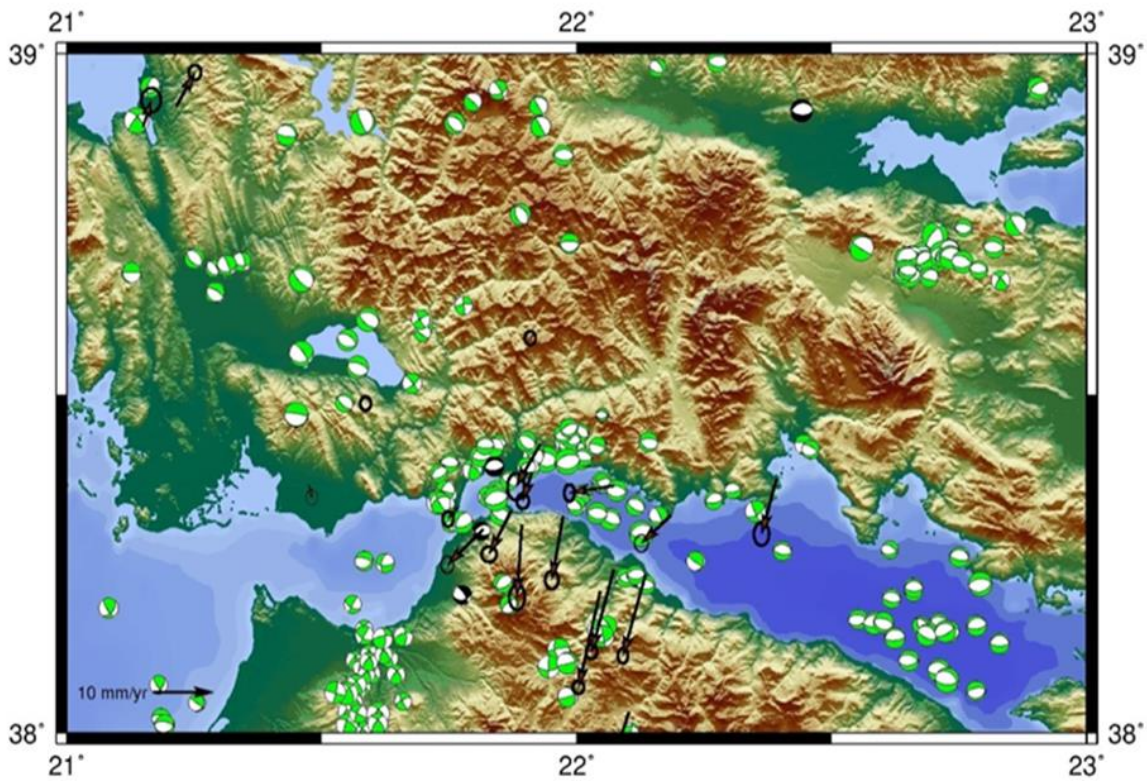

Figure 1-3. Gulf of Corinth: Velocities for the period 2017-2018 and focal mechanisms 2003-2018 (Source: crlab.eu).

The CRL project has been studying the short and long term mechanics of the normal fault system, with ongoing research mostly focused on the western part of the rift, as recent tectonic activity is shown to be migrating westwards based on a number of indicators [Bernard et al., 2016]: (1) local strain rates are higher (reaching a maximum of 16 mm yr^{-1} at the western tip); (2) microseismic activity is more prominent; (3) this area has not experienced destructive (M>5.5) earthquakes in the last century; (4) in the past 40 years, seismic activity has been migrating westwards, with the last major earthquake occurring in 1995 at Aigio (M=6.2) [Tselentis et al., 1996; Bernard et al., 1997]. Tectonic studies in the area of the Western Gulf of Corinth have produced detailed maps of the main presently active faults, both onshore [e.g. Flotté et al., 2005; Palyvos et al., 2005, 2008; Ford et al., 2009, 2013; Papanikolaou et al., 2009; Michas et al., 2015], and offshore [Stefatos et al., 2002; Sakellariou et al., 2003, 2007; Bell et al.,2009; Taylor et al., 2011; Charalampakis et al., 2014; Beckers et al., 2015]. At the same time, the monitoring network of CRL is steadily expanding, and currently includes seismometer arrays (both onshore and submarine), strain gauges, tidal gauges, inclinometers, as well as a dense array of 25 permanent GNSS stations, providing continuous geodetic measurements in the area (Figure 1-3). In fact, the combination of long-term permanent and campaign GNSS observations with active satellite observations (InSAR), processed with advanced differential interferometry methodologies (i.e. PSI and SBAS) is capable of providing precise geodetic measurements at high resolution, thus greatly enhancing the knowledge of local crustal deformations with multiple benefits for monitoring co-seismic, post-seismic, as well as aseismic discontinuities.

1.4 Rationale – Objectives

In the context of CRL, the need for high-quality satellite data is emphasized, as it can provide valuable information about crustal deformations and fault dynamics. Meteorology is therefore an integral part of the monitoring effort, as the precise knowledge of the tropospheric state can remove a main source of error from the data which is the delay due to the atmospheric refraction of the signal. On the other hand, the synergy of remote sensing techniques such as GNSS and InSAR used for geodetic measurements with meteorological applications can provide very useful information of meteorological and climatological interest. It is, for example, highly possible that in the near future, InSAR near real-time data will be assimilated in weather forecasting models for improving their predictions, in the same way that GNSS data are currently being used.

With this in view, the current PhD Thesis aims to investigate the extent to which a high-resolution weather model, such as WRF, can produce detailed tropospheric delay maps of the required accuracy, by coupling its output (in terms of Zenith Total Delay or ZTD) with the vertical delay component in GNSS measurements. The model initially is operated with varying parameterization in order to demonstrate the best possible configuration for our study, with GNSS measurements providing a benchmark of real atmospheric conditions. In the next phase, the two datasets (predicted and observed) are compared and statistically evaluated for a period of one year, in order to investigate the extent to which meteorological parameters that affect ZTD can be simulated accurately by the model, under different weather conditions. Finally, a novel methodology is tested, in which ZTD maps produced from WRF and validated with GNSS measurements in the first phase of the experiment will be used as a correction method to eliminate the tropospheric effect from selected InSAR interferograms.

2. Tropospheric Effects in GNSS and InSAR and Current Correction Methods

2.1 Neutral Atmospheric Delay in Space Geodesy Techniques

The Earth's neutral atmosphere introduces a propagation delay, due to refraction, in all space geodetic techniques which use microwave signals at frequencies ranging from 300 MHz to 300 GHz. Atmospheric refraction is mainly caused by the spatial and temporal variations of vapour content in the lower atmosphere (troposphere), and it is the principal error source in space geodesy applications such as GNSS [Solheim et al., 1999], VLBI [Treuhaft and Lanyi, 1987], Satellite Altimetry [Desportes et al., 2007], and Interferometric Synthetic Aperture Radar (InSAR) [Hanssen, 2001; Li et al., 2005; Onn and Zebker, 2006]. In this chapter, the tropospheric effect in GNSS and InSAR measurements detecting crustal deformations is discussed and current correction techniques are presented. On the other hand, the "noise" effect of the atmospheric water vapour in geodetic measurements can also be regarded as a "signal" in meteorological terms [Bevis et al., 1992], and therefore its precise determination can be useful in a number of associated applications which are also discussed.

2.2 Tropospheric Effects in GNSS Measurements

2.2.1 Theory of Refractivity and Calculation of Zenith Hydrostatic Delay and Zenith Wet Delay

Global Navigation Satellite Systems (GNSS) is a well-established and highly accurate geodetic technique which allows us to monitor crustal deformations at the millimetre level. The first system of its kind, known as GPS (Global Positioning System), was initially operated by the U.S. Air Force and became available for civilian use in the 1980s, currently consisting of 32 satellites in medium Earth orbit. In recent years, additional constellations have become operational, such as the Russian GLONASS, the European GALILEO, and the Chinese Beidou, all with global coverage.

GNSS signals emitted from satellites to ground receivers are delayed and bent when propagating through the atmosphere (Figure 2-1). The upper part of the atmosphere (ionosphere) is a dispersive medium, and therefore its first order delay effect (phase advance), which is on the order of 1-50 m, can be eliminated by combining observations from two GNSS L-band frequencies in the range from 1.16 to 1.61 GHz [Spilker, 1978; Ware et al., 1996]. The remaining ionospheric effect due to higher-order terms is estimated to be on the order of sub-millimeter to several centimeters and is usually ignored. However, with recent advancements in GNSS positioning and sub-centimeter accuracies currently achievable, the correction of this term is becoming increasingly important [e.g. Bassiri and Hajj, 1993; Kedar et al, 2003; Liu et al, 2016].

The delay associated with the lower part of the neutral atmosphere (troposphere) is non-dispersive at GNSS frequencies and cannot be eliminated in a similar way. Within this layer, waves travel slower than in a vacuum (where the refraction index n =1) and also travel in a curved path instead of a straight line [Bevis et al., 1992]. The signal delay is expressed as an equivalent increase in travel path length (ΔL), given by:

$$\Delta L = \int_L n(s)ds - G \tag{2.1}$$

where *n(s)* is the refractive index as a function of position s along the curved ray path *L*, and *G* is the straight-line geometrical path length through the atmosphere (the path that would occur if the atmosphere was replaced by a vacuum).

Equivalently:

$$\Delta L = \int_L [n(s) - 1]\, ds + [S - G] \tag{2.2}$$

where *S* is the path length along *L*. The first term on the right is an expression of the slowing effect, and the second term is an expression of bending. The bending term [S – G] is much smaller (about 1 cm or less), for paths with elevations greater than about 15°.

Equation (2.2) can also be formulated in terms of atmospheric refractivity *N*, defined as:

$$N = 10^6(n - 1) \tag{2.3}$$

The total delay along the zenith path, also known as Zenith Total Delay (ZTD) is expressed as:

$$ZTD\ (mm) = \int_0^\infty N dz \tag{2.4}$$

Now *N* is a function of temperature, pressure, and water vapour pressure, according to the following relationship [Smith and Weintraub, 1953]:

$$N = 77.6\left(\frac{P}{T}\right) + 3.73 \times 10^5\left(\frac{P_v}{T^2}\right) \tag{2.5}$$

where *P* is the total atmospheric pressure (mbar), *T* is the atmospheric temperature (°K), and P_v is the partial pressure of water vapour (mbar). This expression is considered accurate to about 0.5% under normal atmospheric conditions [Resch, 1984]. A more accurate formula for refractivity in non-ideal gases is provided by Thayer [1974]:

$$N = k_1\left(\frac{P_d}{T}\right)Z_d^{-1} + k_2\left(\frac{P_v}{T}\right)Z_v^{-1} + k_3\left(\frac{P_v}{T^2}\right)Z_v^{-1} \tag{2.6}$$

where k_1 = (77.604 ± 0.014) K mbar^{-1}, k_2 = (64.79 ± 0.08) K mbar^{-1}, k_3 = (3.776 ± 0 .004)x10^5 K^2 mbar^{-1}, P_d is the partial pressure of dry air (mbar) and Z_d^{-1}, Z_v^{-1} are the inverse compressibility factors of dry

air and water vapour respectively. Both of these factors, which are corrections for non-ideal gas behaviour, have nearly constant values that differ from unity by a few parts per thousand [Owens, 1967]. The errors in the constants of equation (2.6) limit the accuracy with which the refractivity can be calculated to about 0.02% [Davis et al., 1985].

The first term on the right in equation (2.5) represents the "hydrostatic" delay i.e. the delay which is mainly due to the "hydrostatic" constituents (gases excluding water vapour). It is sometimes referred as "dry" delay, but the term is misleading, as it also includes a significant contribution from water vapour (due to the non-dipole component of water vapour refractivity). The hydrostatic delay forms the largest part of total delay, and can be accurately modelled as it is directly proportional to atmospheric pressure [Saastamoinen, 1972; Davis et al., 1985]. Using the hydrostatic equation and integrating vertically through the atmosphere we obtain for the total hydrostatic zenith delay (ZHD):

$$ZHD\ (cm) = k_1 \int_0^{\infty} \frac{P_d}{T} dh = 77.6\, R_d \int_0^{\infty} \rho(h)\, dh = 77.6\, \frac{R_d\, P_s}{g} \qquad (2.7)$$

where g is the location dependent gravitational constant, P_s is surface pressure (mbar), ρ is air density (g/cm^3), and R_d = 2.87 x 10^6 cm^{2}sec^{-2}K^{-1} is the gas constant for dry air. Elgered et al. (1991) adopted a model in which the zenith hydrostatic delay (ZHD) is given by:

$$ZHD\ (mm) = (2.2779 \pm 0.0024)\, P_s / f\ (\lambda, H) \qquad (2.8)$$

where P_s is surface pressure (mbar), and

$$f\ (\lambda, H) = (1 - 0.00266\, cos2\lambda - 0.00028H) \qquad (2.9)$$

accounts for the variation in gravitational acceleration with latitude λ and the height H of the surface above the ellipsoid (in km). Therefore, equations (2.7) and (2.8) demonstrate that a barometric measurement can be used to estimate the zenith hydrostatic delay with high accuracy. If the barometric pressure is known to 1 mbar, zenith hydrostatic delay can be estimated with an accuracy of 2.5 mm [Solheim et al., 1999].

The second and third terms on the right in equation (2.6) represent the "wet" delay i.e. the delay which is due to the water vapour content of the troposphere, and in particular due to the dipole component of its refractivity, which is about 20 times larger than the non-dipole component [Bevis et al., 1992]. Since Zenith Wet Delay (ZWD) is mainly a function of partial water vapour pressure (P_v) and air temperature (T), it can be calculated with a numerical integration through a full atmospheric profile, using these two meteorological parameters together with the two refractivity constants k_2' (K mbar^{-1}) and k_3 (K^2 mbar^{-1}):

$$ZWD = 10^{-6} \int_H^{\infty} \left(k_2' \frac{P_v}{T} + k_3 \frac{P_v}{T^2} \right) dh \qquad (2.10)$$

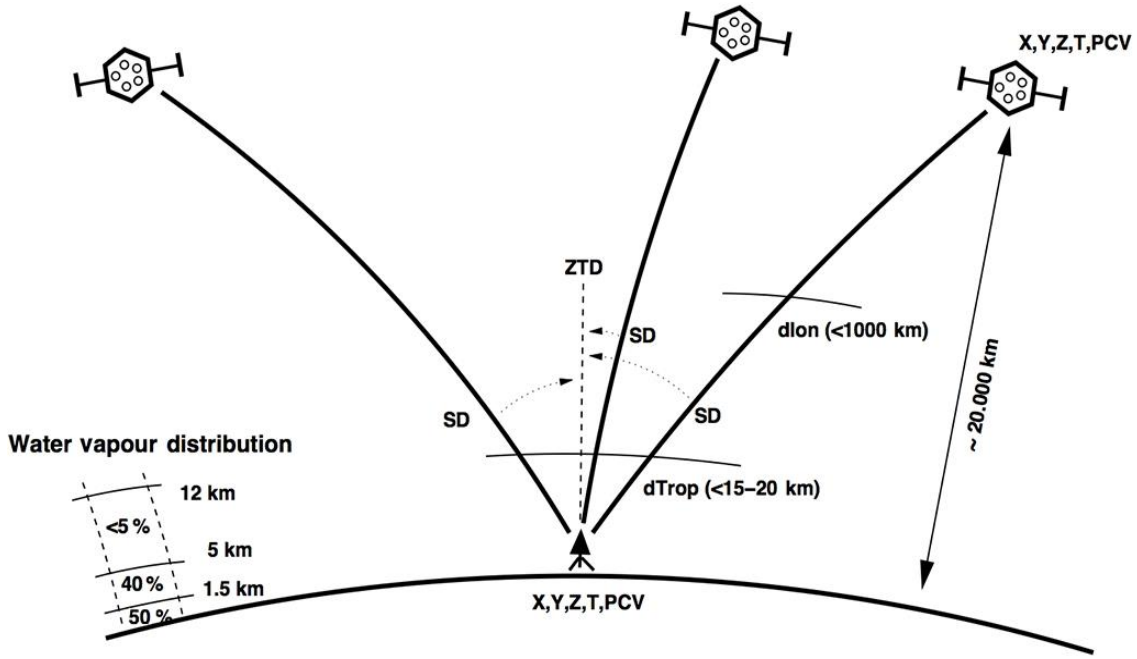

Figure 2-1. Schematic presentation of individual slant path delays (SPDs) from three GNSS satellites and their mapping to zenith total delay (ZTD) (Source: Guerova et al., 2016).

The delay is given in the units of *h* [Davis et al., 1985]. It is usually adequate to approximate this expression by:

$$ZWD = (0.382 \pm 0.004)K^2\ mbar^{-1} \int_H^{\infty} \frac{P_v}{T^2}\ dh \qquad (2.11)$$

Equations (2.10) and (2.11) can be evaluated from profiles of P_v and T provided by meteorological instruments such as radiometers, LIDARs, Fourier transform infrared spectrometers, or radiosondes. However, as these data are rarely available at the GNSS receiver location, and the water vapour profile can fluctuate significantly both in spatial and temporal terms, ZWD is much more difficult to model than ZHD.

Dry air and water vapour are not the only atmospheric constituents which affect the propagation of the GNSS signal. It has been demonstrated that non-gaseous constituents such as hydrometeors (i.e. cloud droplets, rain, hail, snow and graupel), and solid particulates (dust, sand, volcanic ash) can cause phase delays which, depending on the weather conditions, can contribute significantly to the ZTD [Solheim et al., 1999]. Table 2.1 lists typical high values of zenith GNSS propagation delays of different atmospheric constituents, based on the respective refractivities.

Table 2.1: Typical high values of Zenith Total Delay (ZTD) at sea level [Solheim et al., 1999].

Source	Magnitude (mm)	Scale height (km)
Dry air	2500	~8
Water vapour	450	~2
Hydrometeors	15	variable
Sand/dust	40	~2
Volcanic ash	0.4	variable

2.2.2 Current Correction Methods – State of the Art

In current GNSS processing software, the tropospheric delay is estimated geometrically, from combining and analysing the signal paths between each satellite and the receiver (Figure 2-1). There are several methods of tropospheric "residual" estimation, e.g. Kalman filter or least square approximation. The tropospheric processing cannot distinguish between the "hydrostatic" and "wet" components, therefore calculates ZTDs not as a sum of ZHD and ZWD, but rather as a sum of an a priori and an estimated tropospheric delay correction. The "a priori" troposphere usually contains the "hydrostatic" component which, under the assumption of hydrostatic equilibrium, is more easily determined from observations or models, plus a default value for the "wet" component. The "residual" term (correction) is estimated from the GNSS solution and represents the remaining ZWD which cannot be modelled a priori and possibly also a small "dry" fraction.

In accurate GNSS applications, a common model for the total slant path delay from the GNSS satellite to the receiver on the surface of the Earth [e.g. Teke et al., 2013] is as follows:

$$SPD(e,A) = \mathrm{m}f_h\,(e)\,ZHD + \mathrm{m}f_w\,(e)\,ZWD + mf_g\,(e)\,[G_N\cos(A) + G_E\,sin(A)] \tag{2.12}$$

where *e* and *A* are the elevation and the azimuth angle towards a specific satellite, *ZHD* and *ZWD* are the zenith hydrostatic and zenith wet delays expressed in units of metres, mf_h, mf_w, mf_g are the hydrostatic, wet, and gradient mapping functions, and G_N and G_E are the components of linear horizontal gradients. The first two terms on the right hand side represent models assuming tropospheric symmetry while the last term may be added in order to estimate a first-order asymmetry in terms of a linear horizontal gradient.

Mapping functions are models which calculate the delay of radio waves from zenith direction down to the observed elevation angle. The Niell Mapping Function (NMF) [Niell, 1996], is a development of the original form by Marini (1972), which incorporates global radiosonde data for the determination of standard profiles. It depends only on the day of year and the site location, but suffers from low

temporal and spatial resolution (1 day/15° in latitude). Subsequent mapping functions, such as the Isobaric Mapping Function (IMF) [Niell, 2000] and the Vienna Mapping Function (VMF1) [Boehm et al., 2006b] make use of Numerical Weather Model (NWM) data and have an improved temporal resolution of 6h. The VMF1 mapping function retrieves data from the European Centre for Medium-Range Weather Forecasts (ECMWF) using a ray-tracing technique, and is found to improve GNSS accuracy, as compared to NMF, by 3mm to 10mm with respect to station height [Boehm et al., 2006b]. Other models such as the Adaptive Mapping Functions (AMF) [Gegout et al., 2011] or the Potsdam Mapping Factors (PMF) [Zus et al., 2014] are also based on the concept of ray-tracing through NWMs. The Global Mapping Function (GMF) is a further development, which results from applying ninth degree spherical harmonics to the VMF1 data. When used in conjunction with the Global Pressure and Temperature model (GPT) [Boehm et al., 2007] it provides an accurate and easy to implement mapping function for most GNSS high precision applications. Weaknesses in GPT/GMF, particularly their limited spatial and temporal variability, have been eliminated by a new, combined model GPT2 [Lagler et al., 2013], and its successor Global Pressure and Temperature 2 wet (GPT2w) [Boehm et al., 2015], having improved capability to determine zenith wet delays empirically. Recently, Landskron and Boehm (2018) have proposed further improvements both to the discrete (VMF1) and empirical (GPT2w) models, called VMF3 and GPT3 respectively, which claim even higher accuracies, especially at low elevation angles.

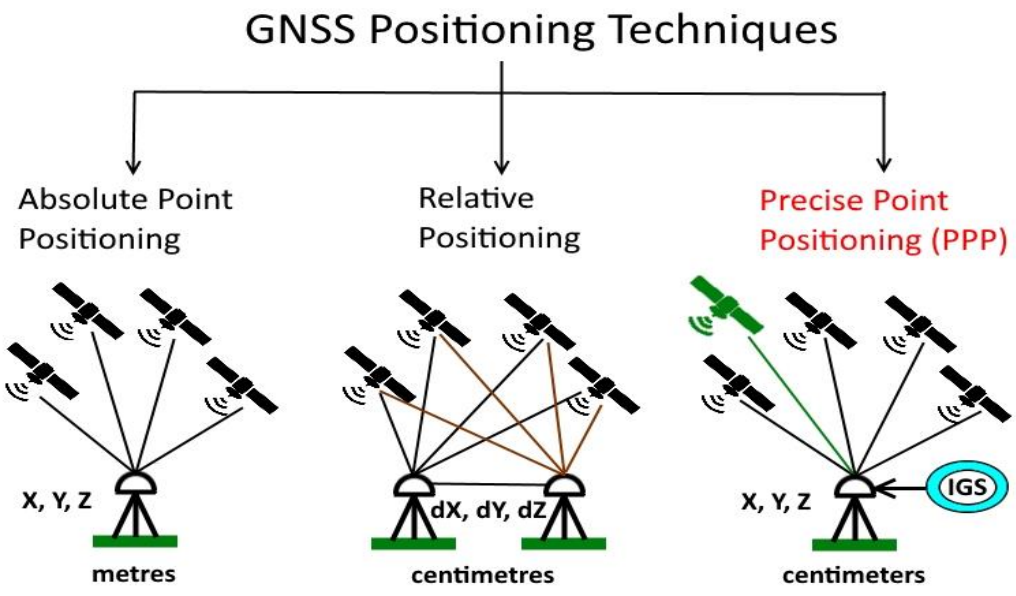

Figure 2-2. Main GNSS positioning techniques used. PPP uses State Space Representation (SSR) products, such as precise clock, orbits, and ionospheric models from tracking networks (e.g. IGS) that are delivered to the rover via satellite or internet.

Current state of the art in GNSS tropospheric data processing is based on solutions provided by the two predominant GNSS positioning techniques, Precise Point Positioning (PPP) and Relative Positioning (double-differencing). The Precise Point Positioning technique [Zumberge et al., 1997] relies on the trilateration principle to measure distances between a GNSS receiver and a minimum of four satellites, and therefore calculates the receiver's position in a three-dimensional space, provided that the receiver clock synchronization error is precisely known. Accurate satellite orbit and clock products are provided by the International GNSS Service (IGS), and ionospheric effects are eliminated with the use of a linear LC3 combination (dual-frequency pseudo-range and carrier-phase measurements). Other limiting factors (e.g. tropospheric delay) are either estimated simultaneously as additional unknown parameters, or modelled with the use of specialized functions. Relatively long observation periods are required in PPP applications, and recent studies [e.g. Hesselbarth, 2008] demonstrate that hourly position estimates can reach sub-decimetre accuracy, while observation periods of 4h provide a positioning accuracy at the cm level. On the other hand, Relative Positioning uses double-difference observations from a network of GNSS stations in order to eliminate receiver and satellite clock errors without the use of external products. This makes it possible to segregate the errors attributable to the receiver clock biases from those from other sources, therefore improving the efficiency of the estimation of the integer cycle ambiguity in a carrier phase observation.

Table 2.2: PPP vs. network GNSS processing strategy [Guerova et al., 2016].

	Precise point positioning (PPP) (using raw observations)	Network solution (using double-differences)
Advantages	Small NEQ (clocks & ambiguities pre-eliminated)	Independence of external precise satellite clock products
	Station by station individual approach (keeping CPU with increasing number of sites/parameters (higher sampling rate, improved modelling, etc.)	Sensitive to relative models; needs large network
	Site-dependent effects do not contaminate other solutions	Correlations between parameters of all stations taken into account
	Sensitive to absolute troposphere	
Disadvantages	Requires external precise satellite clock corrections consistent with orbits	Large normal equations
	Requires precise models for undifferenced observations	Increasing CPU with increase in number of sites/parameters
		Sensitive to relative model

Figure 2-2 illustrates the two techniques, as compared to absolute point GNSS positioning. Both are capable of producing precise estimates of ZTDs and ZWDs, with short-term RMS errors around 3-4

mm in the ZTD [Guerova et al., 2016]. The choice of technique depends on a number of factors, including the availability of external satellite clock products, the time scale required for the solution (utilisation of real-time, near real-time or final products), CPU availability etc. Table 2.2 lists the strong and weak points of the two GNSS tropospheric processing strategies.

2.2.3 GNSS Meteorology

As already discussed, continuous GNSS observations provide accurate estimations of the tropospheric error which limits geodetic and geophysical applications. At the same time, they are an excellent tool for studying the Earth's atmosphere, as the observed Integrated Water Vapour (IWV) can be routinely used in a variety of related applications, including numerical weather forecasting, atmospheric research, and space weather applications. The potential of GNSS observations for tropospheric monitoring was initially suggested in the early 90's [Tralli and Lichten, 1990; Bevis et al., 1992, 1994], when a relationship between the vertically integrated water vapour (IWV) and an observed zenith wet delay was established:

$$ZWD = \frac{PW}{\Pi} \tag{2.13}$$

where precipitable water *PW* is defined as vertically integrated water vapour (IWV) expressed as the height of an equivalent column of liquid water, and the dimensionless quantity Π is given by:

$$\Pi = \frac{10^6}{\rho\, R_v\, [(k_3/T_m) + k_2']} \tag{2.14}$$

[Bevis et al., 1994], where ρ is the density of liquid water, R_v is the specific gas constant for water vapour, and T_m is a weighted mean temperature of the atmosphere defined as:

$$T_m = \frac{\int \frac{P_v}{T}\, dz}{\int \frac{P_v}{T^2}\, dz} \tag{2.15}$$

In fact the relative error in Π closely approximates the relative error in T_m and it has been demonstrated that it is possible to predict T_m from surface temperature observations with a relative RMS error of about 2% [Bevis et al., 1992].

Nowadays, the Zenith Total Delay (ZTD) can be obtained with sub-centimetre accuracy from GNSS data analysis [Byun and Bar-Sever, 2009; Chen et al., 2011; Guerova et al., 2016], and the Zenith Hydrostatic Delay (ZHD) is precisely calculated by means of tropospheric models [e.g. Saastamoinen, 1973], provided that representative meteorological data, either observed near GNSS sites or derived from numerical weather models (NWMs), are available. Therefore the Zenith Wet Delay (ZWD) can be also derived as the difference between ZTD and ZHD [Jin and Luo, 2009], which can then be

converted into precipitable water (PW) in metric units using equation (2.13). Previous studies have demonstrated that the PW derived from GNSS can reach an accuracy of about 2 mm [Boccolari et al., 2001].

A synergy between GNSS measurements and meteorological observations, can therefore offer a broad range of applications. Firstly, high-quality tropospheric delay and PW estimates provide valuable information for weather forecasting. The assimilation of GNSS-derived ZTDs into numerical weather prediction (NWP) models produces improved forecasts of temperature, wind, and precipitation [Poli et al., 2007; Schwitalla et al., 2011; Arriola et al., 2016]. Météo France and the UK Met Office were the first National Meteorological and Hydrological Services (NMHSs) to incorporate the large-scale operational use of GNSS data in Europe, following the establishment of the E-GVAP network in 2005 [Guerova et al., 2016]. Today both institutions report a positive impact from the use of GNSS data in both regional and global NWP models. Several other institutions now use GNSS delay data operationally, and it is expected that many more will follow in the near future. The use of GNSS tropospheric data in NWP models may also prove beneficial for monitoring severe weather events, such as intense precipitation, often associated with strong convection [van Baelen et al., 2011; Brenot et al., 2013]. The life cycle/intensity of precipitation systems, as well as the development of frontal systems can be linked to the variations of the GNSS IWV, and therefore valuable information can be collected from Real-Time (RT) data streams providing water vapour distribution profiles. This technique, also known as 3-D tomography, has been a research topic in the past two decades [Troller et al., 2006a; Bender et al., 2009], and is based on the exploitation of a large number of slant path delays (SPDs) from a dense network of GNSS stations, which cover most parts of the atmosphere from different directions in order to obtain a spatially resolved field of water vapour or humidity. There are several constraints regarding this technique, and quality and stability of the 3-D field is affected by a number of factors such as the spatiotemporal distribution of the observations, the reconstruction method, the initial field, etc. [Shangguan et al., 2013]. Additional observations are therefore often required to validate the results, such as radiosonde profiles, synoptic observations, radio occultation data etc. As the density of GNSS stations worldwide is steadily increasing and processing quality and speed are improving, it is expected that real-time humidity fields at high spatial and temporal resolution, on a national level for instance, might be available in the near future. Finally, a relatively new field where GNSS tropospheric products can have a significant contribution is climate monitoring. Climate models and observations predict IWV increases of approximately 7% per every ^{o}C of temperature increase due to global warming [Trenberth et al., 2005], with changes in water vapour content affecting the hydrological cycle, causing larger differences between dry and wet areas. Ongoing GNSS studies, although so far limited, have been able to confirm such indications. For example, linear long-term trends in IWV, of the order of -0.5 to 1 kg m^{-2} per decade, have been found in Sweden [Gradinarsky and Jarlemark, 2004; Ning and Elgered, 2012], and more recently, a global analysis of GNSS and DORIS data also revealed IWV trends in the range ± 2 kg m^{-2} per decade, in good agreement with ERA-Interim re-analysis and microwave satellite data [Bock et al., 2014].

2.3 Tropospheric Effects in InSAR Measurements

2.3.1 Interferometric Synthetic Aperture Radar (InSAR) Fundamentals and Main Limitations

Before discussing the concept of tropospheric effect in InSAR measurements, it is important to understand the fundamental principles of this remote sensing technique, which is becoming increasingly popular among geodesists, geophysicists and environmental scientists alike, as a tool for monitoring a number of terrestrial processes, as we have seen in Paragraph 1.2. Specifically with regards to measuring deformations of the Earth's crust, InSAR in combination with ground-based geodetic monitoring, such as GNSS, can identify surface movements of millimetre to centimetre scale with high spatial resolution [Wang and Wright, 2012; Walters et al., 2013; Ozawa et al., 2016].

Synthetic Aperture Radar (SAR) satellites acquire images of the Earth's surface by emitting radar pulses and analysing the reflected signal, therefore it is an active remote sensing system. As with all radar sensors, it operates in the microwave domain (like GNSS), at different frequencies for each satellite constellation (Table 2.3), with longer wavelengths being more effective at penetrating through dielectric materials, such as clouds, fog and dust. Satellites mounted with SAR sensors follow a near-polar orbit at an altitude ranging from 500 to 800 km above the Earth's surface and collect images of the same area over time, as they are continuously circumnavigating the globe. The time taken for a satellite to re-pass over the same area is called the 'revisiting time'. Since the launch of the first ERS satellites in 1992, numerous systems have been orbiting the Earth, providing higher resolution images, faster repeat times and data redundancy for many parts of the world. Table 2.3 presents an overview of different SAR satellite generations and their basic characteristics.

Table 2.3: Overview of satellite SAR systems

SAR System	Launch year	Country - Organisation	Band	Wavelength (cm)	Revisiting time (days)
ERS-1	1992	ESA	C	5.7	35
JERS-1	1992	Japan	L	23.5	44
ERS-2	1995	ESA	C	5.7	35
RADARSAT-1	1995	Canada	C	5.7	24
ENVISAT	2002	ESA	C	5.7	35
ALOS-1	2006	Japan	L	23.5	46
RADARSAT-2	2007	Canada	C	5.7	24
TerraSAR-X	2007	DLR	X	3.1	11
COSMO SkyMed	2007	Italy	X	3.1	15
Sentinel-1	2014	ESA	C	5.7	12
ALOS-2	2014	Japan	L	23.5	14
Sentinel-2	2016	ESA	C	5.7	12

An important signal property of radar is that it can record both amplitude and phase information for each ground target. Amplitude is related to the energy of the backscattered signal and it is proportional to the reflective properties of the ground target (metal and hard objects are more reflective thus the amplitude of the backscattered signal is higher). Phase, on the other hand, is related to the distance between antenna and target, and it is the property of the radar signal that is used in estimating displacement in interferometric applications. The phase of a pixel (ϕ) includes information on the phase shift caused by the scattering effect (ϕ_s) and the propagation phase delay from the SAR antenna to the ground target and back (ϕ_p):

$$\varphi = \varphi_s + \varphi_p \tag{2.16}$$

where the backscatter phase shift ϕ_s is the net phase of the coherent sum of the contributions from all elemental scatterers inside a pixel, and the signal propagation delay ϕ_p is related to the distance R between the SAR antenna and the ground target:

$$\varphi_p = \frac{4\pi}{\lambda} R \tag{2.17}$$

The sensor-to-target distance R is equal to an integer number of wavelengths λ, plus a term equal to a fraction of λ. The phase of the signal represents this fraction of a cycle, with values from 0 to 2π, it is therefore said to be measured in modulo-2π. Two radar images acquired over the same area but at different times will have almost the same backscatter phases ϕ_s (provided that the scattering property did not change), and therefore the phase difference $\Delta\varphi$ can be expressed as follows:

$$\Delta\varphi = \varphi_2 - \varphi_1 = \varphi_{p2} - \varphi_{p1} = \frac{4\pi}{\lambda} \Delta R + t + e + \alpha \tag{2.18}$$

where λ is the wavelength, ΔR is the displacement in the Line Of Sight (LOS), t is a topographic distortion term arising from slightly different viewing angles of the two satellite passes, e is noise due to decorrelation effects, and α is a phase shift due to different atmospheric conditions at the time of the two radar acquisitions.

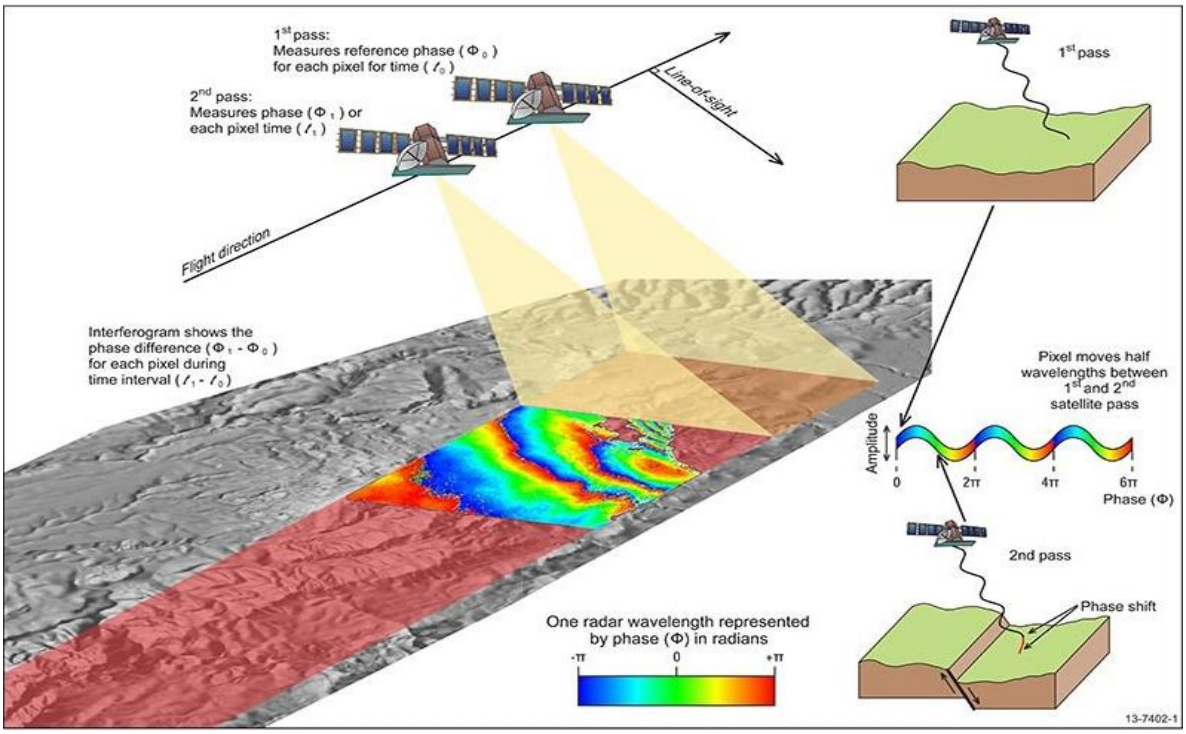

Figure 2-3. Crustal deformation monitoring with InSAR. Two SAR images of the same area are acquired at different times. The phase shift recorded between the two acquisitions represents the surface movement at each pixel, which is mapped as an interferogram (Source: Geoscience Australia website: http://www.ga.gov.au).

Equation (2.18) demonstrates that the signal phase change is equal only to the difference of distances between two observations plus a "noise" term and it is the fundamental equation of Interferometric Synthetic Aperture Radar (InSAR), or SAR Interferometry (Figure 2-3). The measured signal phase change can be visually represented as an interferogram, i.e. a digital matrix of numerical values ranging from $-\pi$ to $+\pi$ (modulo-2π phase variations) converted into a map. If adequately corrected for all the noise terms of equation (2.18), an interferogram represents the changes in surface displacement between the times of the two acquisitions.

2.3.2 Tropospheric Artefacts in InSAR and Current Correction Methods

As discussed in the previous paragraph, Interferometric Synthetic Aperture Radar (InSAR) can potentially produce accurate (at the millimetre level) fields of ground deformation over large areas (hundreds of kilometres) [Massonnet and Feigl, 1998; Rosen et al., 2000; Hanssen, 2001]. The accuracy of this technique is affected by a number of factors, including orbital errors, phase decorrelation [Zebker and Villasenor, 1992], topographic residuals, phase-unwrapping errors, and extra path delay due to the propagation of the microwave signal through the atmosphere [Tarayre and Massonnet, 1996; Hanssen, 2001]. The majority of these error sources have been adequately accounted for in recent years, with advances in InSAR technology or the employment of innovative techniques that remove them in a consistent manner. For example, orbital errors for modern

satellites with precise orbits are small, and velocity uncertainties are of the order of 0.5 mm yr^{-1} over 100 km distance [Fattahi and Amelung, 2015]. Also, topographic residuals in repeat-pass interferometry can be corrected by means of simultaneous analysis of a time series of SAR acquisitions or the use of external topographic datasets (Digital Elevation Models) [Fattahi and Amelung, 2013]. However, the detection of low-amplitude, long-wavelength deformation fields such as those resulting from interseismic strain accumulation or postseismic motion remains challenging, mainly because of interferometric decorrelation and atmospheric propagation delays [Wright et al., 2001; Jolivet et al., 2011; Béjar-Pizarro et al., 2013].

Although SAR Interferometry is a technique which uses microwave signals, similarly to GNSS, it is more challenging in terms of atmospheric phase delay corrections, due to several reasons, including the small number of satellites, the single pass geometry and the gridded nature of the acquired data. Several methods have so far been pursued to mitigate the tropospheric delay in InSAR data, which can be divided into two general groups, the empirical and the predictive methods. Empirical methods examine the correlation between interferometric phase and elevation within individual interferograms. Tropospheric delays are estimated by assuming a linear relation between elevation h and the interferometric phase $\Delta\varphi$ in a non-deforming region [Wicks et al., 2002] or in a spatial band insensitive to deformation [Lin et al., 2010]. A modification of this method uses additional a priori information from a deformation model to remove a preliminary displacement factor prior to estimating the linear correlation gradient [Elliot et al., 2008]. Although these phase-based methods are capable of reducing the tropospheric delay, they have limited application as they assume a spatially uniform troposphere. There have been attempts to overcome this limitation by means of a piece-wise slope correction over multiple windows [Lin et al., 2010; Béjar-Pizarro et al., 2013] which however could not remove the bias from other phase contributions. Finally, an alternative empirical method to the linear approximation was proposed by Bekaert et al (2015b), where a power-law model provides a better estimate of the spatially-varying tropospheric signal in the presence of deformation. As a general rule, empirical methods are not effective when the expected deformation signal correlates with topography, such as over volcanoes [e.g. Delacourt et al., 1998] or across major topographic steps [e.g. Elliott et al., 2008]. Such approaches are successful in selected cases but their use cannot be generalized and evaluation of the results is necessary.

Predictive methods, on the other hand, use input data from external sources in order to calculate the tropospheric delay of an interferogram. These methods can be categorised as follows:

- Use of GNSS delay measurements [Williams et al., 1998; Onn and Zebker, 2006; Löfgren et al., 2010].
- Use of multi-spectral observations from the Medium Resolution Imaging Spectrometer (MERIS) onboard the Envisat satellite or the Moderate Resolution Imaging Spectroradiometer (MODIS) onboard the Terra and Aqua satellites [Li et al., 2009, 2012; Puysségur et al., 2007; Walters et al., 2013].
- Use of output information from Numerical Weather Prediction (NWP) models [Wadge et al., 2002; Foster et al., 2006, 2013; Doin et al., 2009; Jolivet et al., 2011, 2014; Kinoshita et al., 2013; Walters et al., 2014].

In general, these methods have also been partially successful as they rely on high-precision local data collocated in space and time, which are not always available for the times of SAR acquisitions. However, they are better suited for estimating the turbulent and coherent short-scale component of the tropospheric term than phase-based methods, and as such produce better results. Each method has its strengths and weaknesses, for example GNSS ground stations in most areas are sparsely distributed and tropospheric delay data can only be used at the exact location of each station, especially where there is significant topographical and/or meteorological variability. It is usually not adequate to use GNSS data as a standalone correction technique, but rather in combination with additional datasets, e.g. spectrometer measurements [Puysségur et al., 2007]. Also, spectrometers can only provide precise data under cloud-free and daylight conditions. However, their ability to measure Precipitable Water Vapour (PWV) accurately at high spatial resolution (250-1000 meters) makes them a highly efficient technique, under suitable conditions. The MERIS PWV accuracy has been estimated close to 1 mm, equivalent to 6 mm of Zenith Wet Delay (ZWD) for each epoch, or 9 mm between two epochs [Li et al., 2006b]. This is equivalent to approximately 1 cm in radar line-of-sight for ENVISAT data with an incidence angle of 23°. With respect to MODIS, PWV accuracy has been estimated at best equal to that of MERIS, and at worst twice that of MERIS [Bekaert et al., 2015b].

With regards to NWP models, recent studies have focused both on the use of Global Atmospheric Models (hereafter GAMs) and Limited-Area Models (LAMs) to predict delays at the time of SAR acquisitions and correct for the stratified tropospheric delays. In a study where data from three GAMs (ERA40, OPERA and NARR) were used [Doin et al., 2009], it was shown that tropospheric artefacts were better removed compared with InSAR derived delay/elevation ratios, in cases where the correlation between elevation and displacement is large, as expected in volcanoes (e.g., Etna, Beauducel et al., 2000), on some fault segments (e.g., Haiyuan, Cavalie et al., 2008), or in subsident basins (e.g., Mexico City, Lopez et al., 2009). When coherence of the interferogram is poor, it is proposed to correct wrapped interferograms from the stratified tropospheric delay before unwrapping, in order to reduce unwrapping errors [Pinel et al., 2011]. Further attempts to exploit output from GAM products, such as ERA-Interim, NARR or MERRA [Jolivet et al., 2011, 2014], for corrections in different geographical and tectonic environments, demonstrated a better estimation of stratified tropospheric delay and rather poor results for estimating turbulent patterns on single interferograms. Higher prediction rates were demonstrated in continental locations with more predictable atmospheric conditions. By removing the stratified component, unwrapping was enhanced over rough terrains where the interferometric phase may be aliased, and the accuracy of deformation measurements in case of earthquakes was improved.

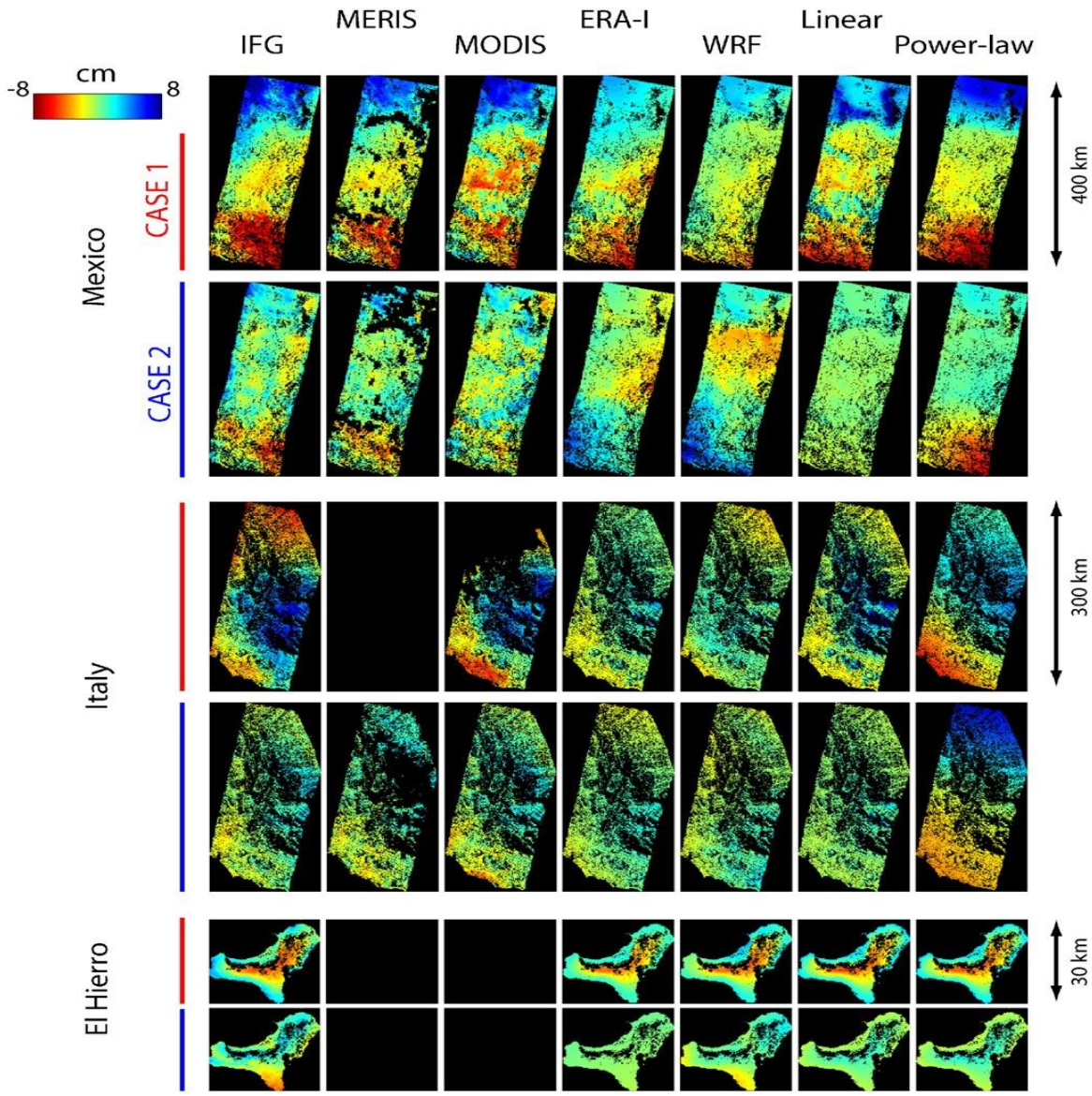

Figure 2-4. Tropospheric delay estimates for different correction methods over Mexico, Italy, and El Hierro. Two examples are shown for each region. Case 1 (red) corresponds to an example where the tropospheric delay is mainly correlated with the topography. Case 2 (blue) represents an example with a more turbulent and spatially-varying tropospheric signal. Columns give from left to right, the unwrapped interferogram, and the estimated tropospheric corrections using MERIS, MODIS, ERA-I, WRF, the linear method, and the power-law method. MERIS and MODIS spectrometers have a hydrostatic component of ERA-I included, to allow for comparison with phase-based correction methods. All observations are converted to displacements in the radar line-of-sight (Source: Bekaert et al., 2015b).

Global Atmospheric Models suffer from low temporal and spatial resolution, and output data need to be interpolated in space and time in order to match the resolution of an interferogram and the exact acquisition times. Therefore the technique of using high-resolution regional weather models (LAMs) nested within coarser, global, weather models to estimate the atmospheric delay [Foster et al., 2006, 2013; Puysségur et al., 2007; Wadge et al., 2010; Eff-Darwich et al., 2011; Kinoshita et al.,

2013; Bekaert et al., 2015b] is gaining ground. Foster et al. (2006, 2013) exploited the MM5 regional model at high horizontal resolution (3 km) to obtain tropospheric delay fields over the Island of Hawaii and Mount St Helens in the U.S. with mixed success, as the model configuration fails to accurately predict tropospheric delays at shorter wavelengths (under 8 km) in most cases. More recently, Bekaert et al. (2015b) produce tropospheric delay fields with the WRF regional model over three test-regions with complex topography, including Southern Mexico, Italy, and El Hierro. The model is nested at 7 km horizontal resolution and is initiated with data from the Global Forecast System (GFS). Results are compared with tropospheric delays obtained with other state-of-the-art methods, including MERIS and MODIS spectroscopy, ERA-Interim, and both the conventional linear and power-law empirical methods. The statistical analysis demonstrated that spectrometers provided the largest RMSE reduction, but only under daylight and cloud-free conditions. Phase-based methods (linear and power-law) outperformed the weather models in regions where tropospheric delays were correlated with topography, but in regions where this was less apparent, due to atmospheric turbulence and dynamic local weather, weather models offered a better performance. Figure 2-4 illustrates the effect of each correction method on a series of selected interferograms.

3. Numerical Weather Prediction (NWP) Models and their Applications

3.1 Numerical Modelling of the Troposphere

Numerical modelling is the most common method used by meteorologists in order to predict or reconstruct the atmospheric conditions. Several different types of weather models exist nowadays, collectively called Numerical Weather Prediction (NWP) Models, which use systems of differential equations that describe atmospheric dynamics based on the laws of physics, fluid flow, and chemistry. These equations are usually discretized into 3-dimensional grid-cells based on a coordinate system, and are supplemented with physical parameterizations of the atmosphere for processes which are either too small or too complex to be directly predicted, such as turbulent diffusion, radiation, cloud formation and precipitation, heat exchange, sub-grid scale orographic drag and non-orographic gravity wave drag, and convection, as illustrated in Figure 3-1.

Apart from modelling the dynamics of the atmosphere and the physical processes that occur, modern NWP models can also accurately simulate other processes in the Earth system that influence the weather such as atmospheric composition (O_3 and NO_X chemistry, CH_4 oxidation, formation of organic aerosols), the marine environment (coupled ocean-atmosphere models) and land processes (soil, vegetation, surface hydrology, the kinematic effects of terrain). With the development of high-performance computing (HPC) technology, NWP models have become increasingly complex, with the ability to predict even microscale phenomena such as tornadoes and boundary layer eddies, sub-microscale turbulent flows over buildings, as well as synoptic and global flows.

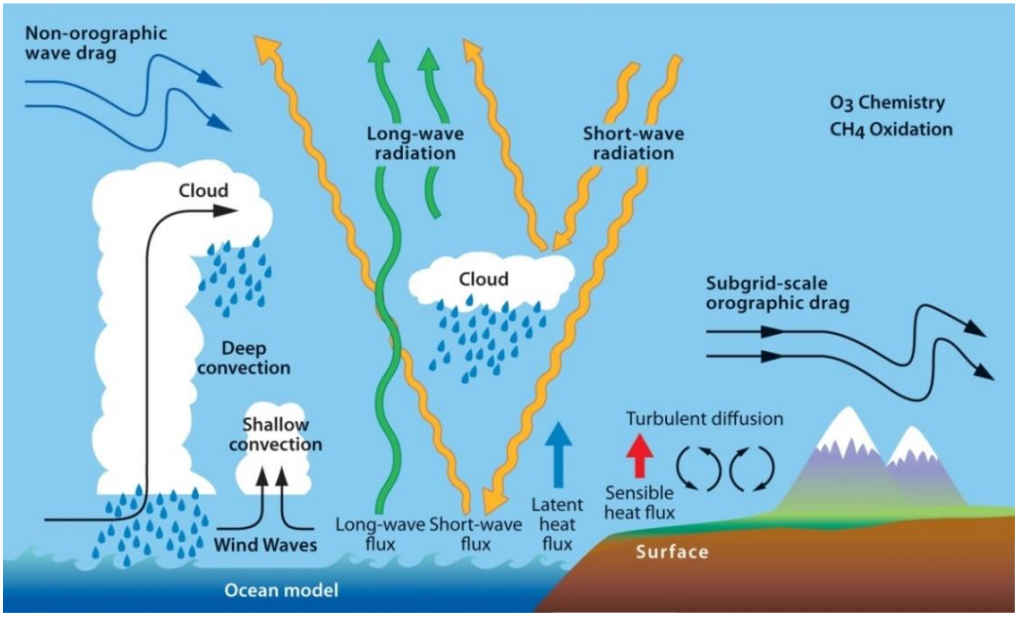

Figure 3-1. All physical processes associated with radiative transfer, convection, clouds, surface exchange, turbulent mixing, subgrid-scale orographic drag and non-orographic gravity wave drag are mathematically modelled in NWP forecasting models (Source: ECMWF).

Atmospheric models can be classified according to their horizontal domain, in global, covering the entire Earth, or regional, covering a part of the Earth. Global Atmospheric Models (GAMs) have a coarse spatial and temporal resolution and therefore are less demanding in terms of computing power. They use spectral methods for providing numerical solutions at the horizontal dimension level (ranging from 20 to 300 km) and finite-difference methods for the vertical dimension. On the other hand, regional models (also called limited-area models or LAMs) have denser grid spacing than GAMs, utilizing the available computer resources to simulate weather parameters in a smaller area. Horizontal resolution of LAMs can be as low as 100 m in modern applications, which means that they can explicitly resolve smaller-scale meteorological phenomena that cannot be represented by global models. Conditions at the edge of a regional model's domain are introduced from global models (boundary conditions), and initial conditions are provided by entering observation data into the model. These include radiosonde, satellite and ground observation data from a number of weather services worldwide, which are unevenly distributed in space and time, and therefore are processed by data assimilation and objective analysis methods, which perform spatial and temporal interpolation of the values, in order to be used by the model's algorithms [Krishnamurti, 1995].

Table 3.1: Common Numerical Weather Prediction Models in use

Global Atmospheric Models	Developer
GFS (Global Forecast System)	NOAA
IFS (Integrated Forecast System)	ECMWF
ARPEGE	Météo-France
ICON	DWD/MPI (Germany)
UM (Unified Model)	UK Met Office
GEM (Global Environmental Multiscale Model)	MSC (Canada)
NOGAPS	US Navy
IGCM	University of Reading (UK)
Regional Models	**Developer**
WRF (Weather Research Forecast)	NCEP/NCAR
RAMS (Regional Atmospheric Modelling System)	Colorado State University
MM5	Penn State/NCAR
HIRLAM/HARMONIE	European NWP research consortium
UKV	UK Met Office
ARPS (Advanced Region Prediction System)	University of Oklahoma
GEM LAM	MSC (Canada)
ALADIN/AROME	Météo-France
COSMO	Consortium of 7 European Weather Services

As opposed to GAMs, regional models use finite-difference methods in all three dimensions (horizontal and vertical), and as such require high-performance computing systems (HPCs) to process high-resolution simulations in relatively short time-scales. This means that the hydrostatic

approximation which is made in GAMs is omitted, and that the vertical momentum equation is explicitly solved instead, which allows for resolving small-scale mesoscale phenomena such as cumulus convection and sea-breeze circulations. Regional high-resolution models are therefore non-hydrostatic, as opposed to GAMs, in which the hydrostatic approximation is used for modelling flows at the synoptic and sub-synoptic scales, and horizontal resolutions larger than 10 km. Table 3.1 lists the most common NWP models used for global and regional forecasting today.

3.2 Applications of High-Resolution Limited-Area Models (LAMs)

3.2.1 Operational Forecasting

Operational weather forecasting was traditionally performed with coarse-scale GAMs by weather services around the world. In recent years, and with the advent of high-performance computer systems, high-resolution operational forecasting (with a mesh of 10 km or less) has become increasingly popular, and many weather services have developed their own versions of convection-permitting regional models, configured at local conditions. The advantage of high-resolution modelling is that it provides more detailed short-range forecasts, as certain atmospheric processes, as well as surface features such as coastlines and orography, are represented more accurately. For example, convective clouds are typically less than 10 km in horizontal extent, and therefore are represented as sub-grid processes at global model resolutions. In contrast, a 1.5 km model can produce the convection explicitly on the model grid. Boundary conditions are commonly provided by global models, and additional data (such as moisture profiles from satellites or ground-based radars) are assimilated based on their availability. Therefore, high-resolution NWP models are designed to improve short-range (up to 48 hours) forecasts of near-surface weather conditions (cloud formation, frontal precipitation, fog, orographically and thermally induced wind profiles), as well as severe weather events triggered by deep moist convection, such as supercell thunderstorms, intense mesoscale convective complexes, prefrontal squall-line storms and heavy snowfall from wintertime mesocyclones.

Typical modern-day examples of high-resolution NWP models used by weather services in Europe for operational weather forecasting are AROME, UKV, HIRLAM/HARMONIE and COSMO. AROME [Seity et al., 2011; Brousseau et al., 2011] was developed by Météo-France and became operational in 2008. Nowadays, it runs at a horizontal resolution of 1.3 km over the area of metropolitan France, and produces five daily forecasts with a window of 48 hours ahead. The model is initialised with boundary conditions from the ARPEGE-IFS GCM, and is also supplied with data from a radar network (Doppler wind and precipitation) and a GNSS network (PWVs), which are assimilated every hour. Since its first operation, AROME has provided improved short-range forecasts of intense precipitation events which occur during the autumn season over the Western Mediterranean region, winter snowstorms, as well as extreme urban heat events during summer heat waves. Similarly, the UKV model [Tang et al., 2013] is the convection-permitting version of the Unified Model (UM) operated by the UK Met Office. Nested within the global configuration of UM, with a 1.5 km grid resolution over the British Isles, it provides better forecasts of convective rainfall or storms which can result in flooding events or disruptive snow in winter. Input data are assimilated every three

hours, providing additional information, mainly about water vapour distribution, which improves the forecasts of specific weather parameters such as precipitation, cloud cover, visibility and 10-metre wind out to 12 hours ahead. The HIRLAM/HARMONIE and COSMO forecast systems are also high-resolution mesoscale models developed by consortia of European weather services, for operational use by their participating members. The HIRLAM programme, started in 2006, has resulted in the development of the HARMONIE-AROME model (through a collaboration with the ALADIN consortium led by Météo-France and ECMWF), which is currently the main operational weather forecast system in Denmark, Estonia, Finland, Iceland, Ireland, Lithuania, the Netherlands, Norway, Spain, and Sweden, with a typical grid resolution of 2.5 km. The Consortium for Small-scale Modelling (COSMO) is another collaborative project between 8 European weather services, led by Deutscher Wetterdienst (DWD). Since 2007, the COSMO high-resolution model has been running operationally at DWD with a resolution of 2.8 km for Germany, with other centres (including the Swiss, Italian, Greek, Romanian, Russian, Polish and Israeli weather services) implementing applications with similar resolutions in the following years.

3.2.2 Atmospheric Research – Climate Re-analysis

Apart from operational weather forecasting, high-resolution LAMs are extensively used in recent years for atmospheric research at increasingly higher spatial resolutions. Modern applications utilise dynamical downscaling at the scale of hundreds of meters [Soltanzadeh et al., 2016]), making it possible to study near-surface phenomena and other microscale processes with unprecedented detail. There are generally two downscaling methods, statistical and dynamical downscaling [Benestad et al., 2007]. Statistical downscaling empirically links large-scale atmospheric parameters (predictors) with local-scale climate variables, and is therefore heavily dependent on the availability of observational data [Wilby and Dawson, 2013]. On the other hand, dynamical downscaling uses data from a coarse global model to feed a high-resolution regional model. This method benefits from the assimilation of detailed surface forcing information (topography, land use etc.), as well as global historical re-analysis datasets available from international weather services (such as the European ECMWF or the American NCEP) and is therefore being extensively used by the research community.

Atmospheric studies involving dynamical downscaling with high-resolution LAMs focus either on the estimation of local meteorological parameters and climatic patterns (detailed wind fields, precipitation characteristics, local humidity etc.), or on the actual validation of the model used, depending on its parameterization and intercomparison with observational data. Common non-operational LAMs which have been employed for research and climate re-analysis include MM5, RAMS and WRF. In recent years, WRF [Michalakes et al., 2004; Skarmarock et al., 2008] has become the most widely used model, due to its versatility as an open-source package supported by a large user community and the fact that it can be operated efficiently on parallel computing platforms, making it suitable for use in a wide range of applications at high horizontal resolutions (down to 1 km or less). In the domain of detailed wind field characterisation, WRF has been employed by numerous studies to identify the wind variability, especially over complex terrain, with applications in wind energy planning and performance, transport and dispersion of air pollution, forest fire prediction etc. High-resolution modelling is particularly useful in the case of mountainous regions, as well as large sea surfaces, due to the absence of data from ground weather stations. The effects of

topography on wind patterns, such as upslope/downslope wind, gap flow and channelling (Figure 3-2) are well demonstrated in diverse regions such as the Iberian Peninsula [Jimenez et al., 2012], the Eastern Mediterranean [Miglietta et al., 2013], the Andes [Puliafito et al., 2015], and Northern Greece [Koletsis et al., 2016], with inner domain configurations ranging from 1-4 km. With respect to wind regime identification over sea surfaces, the WRF model has also been employed for the study of small-scale and terrain-driven features such as sea-breeze circulation systems near coastal areas [Papanastasiou et al., 2010], as well as for the purpose of offshore wind energy assessment in the North Sea [Lorenz et al., 2016] at a 3 km horizontal resolution. Another domain where high-resolution modelling provides important information is the study of regional precipitation patterns. Complex topography is again an important factor, as orographic lift greatly influences local precipitation variability and extreme precipitation events [Lagouvardos et al., 1996; Pytharoulis et al., 2016]. Downscaling simulations with WRF have shown significant improvements in representing mean precipitation fields and extreme rainfall events in Spain with a 9 km inner domain configuration [Cardoso et al., 2013], and a more accurate spatial distribution compared to the ERA-Interim precipitation analysis over most locations in Germany [Warrach-Sagi et al., 2013]. More recently, attempts to simulate intense precipitation events [Pytharoulis et al., 2016; Madala et al., 2016] at high-resolution (1.5 and 3 km respectively) also suggest that although the strong synoptic forcing plays a primary role in the formation of storms, the spatiotemporal variability is strongly affected by topography. Finally, a third domain where high-resolution LAMs can produce better estimates through dynamical downscaling is water vapour profiles, which will be covered in the next paragraph due to its importance for the mitigation of tropospheric noise in GNSS and InSAR techniques.

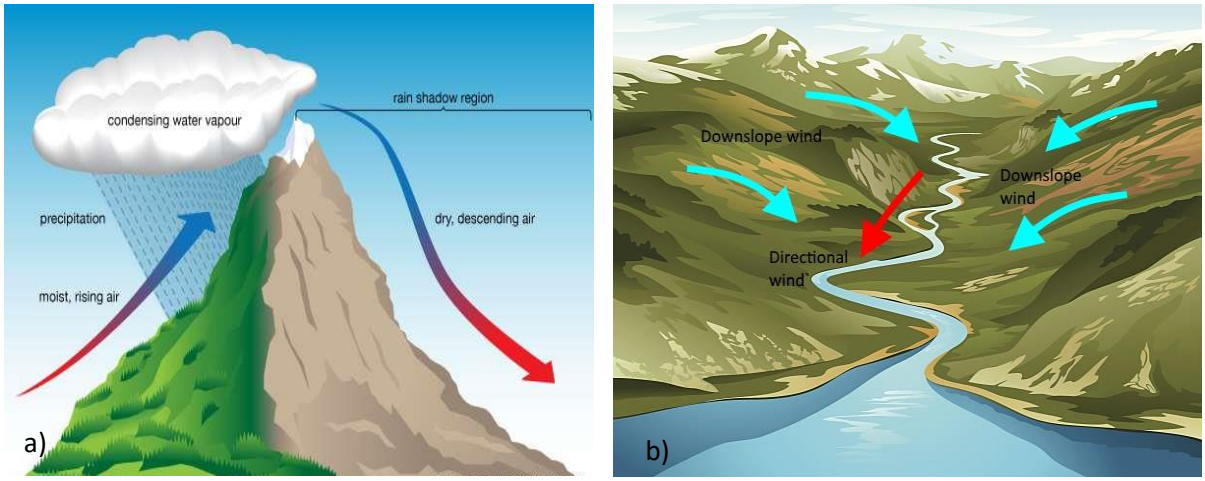

Figure 3-2. Effects of topography on local wind patterns: orographic lift (a) and directional wind channeling (b).

3.2.3 Estimation of Water Vapour Profiles

The ability of LAMs to capture a range of small-scale near-surface atmospheric processes is also important for the estimation of water vapour profiles in the lower troposphere. Water vapour is a highly variable parameter, both spatially and temporally, and as such it is not successfully estimated by coarser GAM models. Initially, NWP models were used for validating precipitable water vapour (PWV) estimates derived from GNSS measurements [Walpersdorf et al., 2001; Tomassini et al., 2002; Schwitalla et al., 2008]. However, with the development of GNSS technology (PPP and double-differencing), the focus has shifted towards data intercomparison, and several recent studies have employed WRF in order to compare the output of high-resolution LAM simulations of PWV with GNSS point measurements [Bender et al., 2008; Mateus et al., 2010] as well as water vapour maps from MERIS [Alshawaf et al., 2012; Cimini et al., 2012]. In fact, as we have discussed in previous sections, PWV products from remote sensing methods are nowadays so accurate, that can be used not only for validating the output of NWP models, but also as initial conditions assimilated within the model itself. These studies generally report the following findings:

a) Medium to long-scale water vapour signals (greater than 20 km) can be well predicted by LAMs; however the short wavelength distribution is not always represented accurately.
b) There is a seasonal variation in the water vapour distribution predictability of LAMs, with largest errors between model and observations (bias and standard deviation) occurring during summer and smallest during winter. Systematic diurnal errors have also been observed.
c) Biases show significant differences between different LAMs employed and observation data, but also differ with region and with time, similarly to changes in NWP model skills. Model configuration and parameterization are also important parameters that can affect the NWP ability to “catch” the shortwave vapour signals.

The estimation of water vapour profiles by LAMs is particularly important for the calculation of ZWD fields, as in the current study. Observational datasets, such as GNSS measurements, provide a benchmark for comparison and validation of the model results. Systematic biases between the two datasets are “artificial” or “real”, depending on whether they are due to technical discrepancies or caused by differences in the temperature, pressure and humidity fields produced by the model [Guerova et al., 2016]. For example, the change to absolute antenna phase centre calibration in GNSS data processing, which has reduced the PWV (or equivalently the ZTD) GNSS bias relative to all NWP models, is an artificial bias of on/off nature. Similarly, the calculation of PWV or ZTD values from model variables (such as water vapour pressure or temperature) can vary between different model configurations, depending on the observation operators used and corrections for height offsets between GNSS antenna and the model topography. On the other hand, “real” biases are associated with the parameterization of physical processes in LAMs and uncertainties introduced from the driving GAM model [Prein et al., 2015]. In particular, it has been shown that the model setup and physical parameterization can affect the intrinsic water balance [Awan et al., 2011; Fersch et al., 2012, 2014], with sensitivity studies suggesting that parameters such as microphysics scheme

(MP), land surface model (LSM), planetary boundary layer scheme (PBL) and cumulus convection scheme (CC) can have a stronger effect on the precipitation and relative humidity (RH) fields [Schwitalla et al., 2008; Madala et al., 2016; Kioutsioukis et al., 2016]. Therefore, the setup of the high-resolution model is an important step when simulating water vapour profiles at the 1-km scale, and physical and other parameterizations have to be carefully fine-tuned for the specific study region and climatic conditions. In Chapter 5, the parameterization of the high-resolution WRF model used in this study will be further discussed, and a sensitivity analysis is performed for identifying the most suitable configuration for the area of the Corinth Gulf.

4. The PaTrop Experiment

4.1 Experimental Setup and Description of the Study Area

The experiment, with the code name PaTrop (Patras–Troposphere), was implemented for providing the data needed for this study. The PaTrop test site covers an area of approximately 150 × 90 km in the region of the Western Gulf of Corinth (GoC), as shown in Fig. 4-1. A network of nineteen permanent Topcon GB1000 and Topcon Net G3A GNSS receivers fitted with Topcon PG-A1 antennas provided the GNSS data and the subsequent in-situ tropospheric zenithal delay measurements. Ten of those receivers were newly installed during the campaign in order to expand the existing Corinth Rift Observatory GNSS network which continuously monitors surface displacements in the area. Installation of the PaTrop stations was done according to the standard procedure followed for all CRL permanent GNSS stations, with antennas being fitted on solid surfaces (usually on top of high buildings with minimum multipath effects), and receivers placed indoors with telemetry capability for real-time data transmission (Fig. 4-2). The stations' locations were carefully selected to cover the whole extent of the study area, while capturing a variety of different topographical and meteorological conditions (i.e. coastal, inland, or mountainous terrain), at elevations between 0-1020 m ASL. This was deemed necessary, in order to account mainly for water vapour variations resulting from orographic, coastal, and frontal gradients that could be present. The exact co-ordinates, elevations and characteristics of each station are listed in Table 4.1.

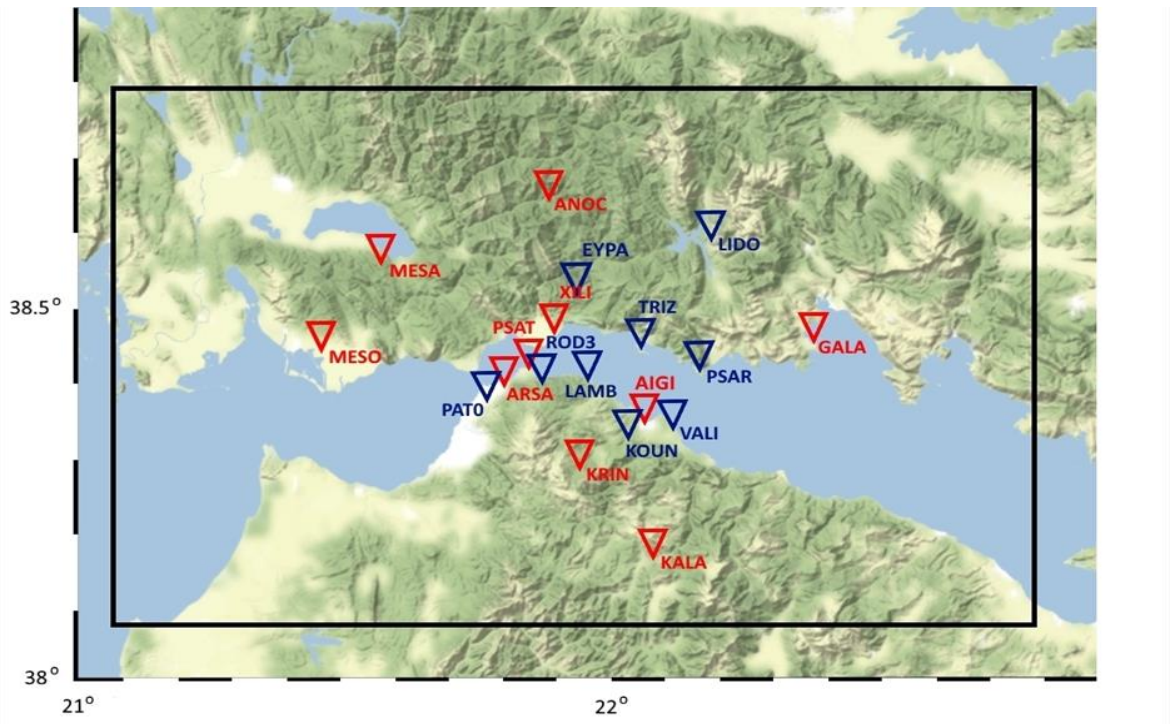

Figure 4-1. Map of the PaTrop study area, Western GoC. Previously installed permanent GNSS stations are marked in blue colour, newly installed GNSS stations marked in red colour. The black box indicates the location of the 1x1 km inner domain of the WRF re-analysis run (Domain 4).

The experiment started in September 2015 and lasted until December 2016, with the overall aim to obtain the longest possible time-series of tropospheric delay observations, to be used in conjunction with results from the WRF high-resolution tropospheric modelling.

Figure 4-2. Photos of newly installed PaTrop GNSS permanent stations in Kalavrita (left) and Mesologgi (right)

Concurrently with the field campaign, the modelling setup and configuration was also implemented. The primary objective of PaTrop was to couple the zenithal tropospheric delay (ZTD) delay derived from GNSS data with the ZTD derived from the output of a high-resolution meteorological model (WRF), in order to investigate the model's capability to reproduce the tropospheric conditions that contribute to the noise signal (in particular the highly variable water vapour distribution), and provide a benchmark of real observational data for validating the model output. Therefore, the installation, setup and operation of the WRF model for performing weather re-analysis runs over the PaTrop area on a routine basis, was an integral part of the experiment. The model was installed on the ARIS high-performance computer facilities operated by the Greek Research and Technology Network (GRNET) in Athens, following a successful application of the PaTrop project and an initial allocation of 50,000 core hours for the needs of configuring and testing the model. During the preparatory stage (January – March, 2016), version 3.7.1 of WRF was installed and configured for running the model at a 1x1 km horizontal resolution. After some initial tests, it was decided to use 10 nodes with 20 processor cores each (i.e. 200 cores) for running the desired configuration at an optimal speed, while achieving faster allocation of resources. Computational performance under the 1x1 km configuration, ignoring I/O and initialization, was approximately 80 min for a 30h run corresponding to 24h of usable output data.

During the production period (June 2016 – June 2017), 650,000 core hours were allocated to the PaTrop project, which were used for performing parameterization trials (see Chapter 5), and the final sequence of re-analysis runs. Numerical methods and algorithms incorporated in the WRF model represent complex physico-chemical processes in the atmosphere and land-ocean-atmosphere interactions. Running WRF at high-resolution is a demanding task, as the model can

easily become unstable if the correct configuration is not used (physical parameters, time step, vertical levelling etc.) and therefore numerous tests need to be performed, in order to specify the exact initial conditions and parameterization of the model. Keeping the spatial resolution at 1 km, a series of different re-analysis runs were produced to demonstrate the best possible configuration for our study, which is an approach supported theoretically and practically to tackle uncertainties in high-resolution modelling. This parametric analysis was performed for a two-week period (17-29 June 2016), during which the output of five different model configurations was tested against GNSS tropospheric measurements from the network of permanent stations in the study area. Furthermore, the initial tests included efforts to improve the model topography by introducing a high-resolution Digital Elevation Model (ASTER 1s) and fine-tuning its interpolation parameters in the WRF pre-processing step. The model setup and results of the parametric analysis are presented in detail in Chapter 5.

Table 4.1: Locations and characteristics of permanent GNSS stations used in PaTrop

Code	Name	Co-ordinates		Elevation AEL (m)	Elevation ASL (m)	Newly installed
		LAT	LON			
ANOC	Ano Chora	38.5945	21.9251	1058	1020	X
ARSA	Platani (Arsakeio)	38.3011	21.8167	147	115	X
AIGI	Aigion	38.2420	22.0727	175	142	X
GALA	Galaxidi	38.3754	22.3916	67	33	X
EYPA	Efpalio	38.4268	21.9284	197	166	
KALA	Kalavrita	38.0305	22.1021	746	716	X
KOUN	Kounina	38.2094	22.0457	595	564	
KRIN	Krini	38.1894	21.9598	788	758	X
LAMB	Lambiri	38.3203	21.9731	43	10	
LIDO	Lidoriki	38.5289	22.2010	595	550	
MESA	Mesarista	38.4845	21.5866	503	477	X
MESO	Mesologgi	38.3663	21.4749	30	2	X
PAT0	Patra EUREF	38.2836	21.7867	121	91	
PSAR	Psaromita	38.3217	22.1843	89	55	
PSAT	Psathopirgos	38.3286	21.8714	50	19	X
ROD3	Rodini	38.3080	21.8922	483	452	
TRIZ	Trizonia	38.3653	22.0727	57	25	
VALI	Valimitika	38.2337	22.1348	42	9	
XILI	Hiliadou	38.3855	21.9120	34	4	X

In the next step, the final sequence of daily re-analysis runs, based on the optimum configuration, was initiated, covering a 12-month period (January 2016 – December 2016). As consecutive runs of the model needed to be performed to cover a long time period, automation was important, something that was achieved with the development of specific codes (in Linux shell script) that enabled us to run consecutive daily runs on the ARIS system, store the output files in specified folders and retrieve desired meteorological data from the output files in TXT format. These codes were developed during the preparatory 2-month period, and further improved and complemented with additional coding (in Linux and Fortran) for processing of the results and incorporating GNSS

derived solutions, during the production period. Ultimately, the aim of the PaTrop project was to automate all the procedures (WRF runs for any time period and location desired, data retrieval, data processing and validation with GNSS solutions) so that the correction of InSAR acquisitions would be performed with the "touch of a button" on a routine basis, through the use of the ARIS platform.

4.2 Data Processing

Processing of the GNSS data started after the end of the experimental campaign and included calculations of zenith tropospheric delays (ZTDs) every 30 min using the JPL NASA Precise Point Positioning (PPP) GIPSY-OASIS 6.4 software. High-precision International GNSS Service (IGS) final orbit data were used, while the quality of the sites ensured that multipath effects would not bias the estimated ZTDs. Static tropospheric processing with no mapping function was used, and a priori ZHD was estimated from an elevation-dependent function. It was intended to use a simple set of parameters in order to compare the WRF model output with a geometrical GNSS calculation which does not assimilate data from external sources. The exact settings of the processing protocol used are listed in Table 4.2:

Table 4.2: CRL tropospheric solution settings – all stations

Software	Gipsy 6.4
GNSS	GPS and GLONASS
Troposphere estimated parameters	ZTD (5 min)
Mapping function	None
Ionosphere	HOI included
Ocean tides	FES2004
ZTD timestamp	hh:00 and hh:30
Elevation cut-off	5

At PAT0 station (which is also part of the EUREF network), in addition to the CRL tropospheric processing protocol, a combined solution was provided by the European Processing Network (EPN), of five different tropospheric solutions by partner institutions, using different software and a combination of mapping functions (GMF, VMF and VMF1). The availability of two different GNSS tropospheric solutions at PAT0 allowed us to investigate the effect that different processing settings have on the consistency and accuracy of GNSS derived ZTD values, and estimate bias with respect to WRF derived ZTDs (see Chapter 6).

With regards to the processing of WRF tropospheric data, values of surface pressure (P_s), as well as air temperature and water vapour pressure (T, p_v) in the vertical column (for each of the 45 vertical pressure levels) were derived every 30 min, at hh:00 and hh:30 hours, at the nearest 1 km grid point from each GNSS station, to coincide with the observational time-series. An automatic routine calculates the "dry" and "wet" delay terms separately, from the three parameters (P_s, T, p_v),

together with the point elevation and layer heights, finally adding up the two to calculate the ZTD value. WRF derived ZTDs are calculated at the exact elevation of the GNSS receiver, by vertically interpolating these parameters, thus minimising errors due to vertical height differences between the two datasets. A detailed description of the calculation methods follows.

4.2.1 Calculation of Zenith Total Delay (ZTD) from GNSS Data

GNNS ZTDs are calculated every 30 min, as described in the previous paragraph. Values at hh:00 and hh:30 are taken in order to match WRF output:

ZTD (mm) = Tropospheric Residual + A priori Zenith Hydrostatic Delay (ZHD)

A priori ZHD is calculated from:

$$\textbf{ZHD = 1013 * 2.27 * exp (-0.000116 * h)} \qquad (4.1)$$

where h is the station elevation in metres above ellipsoid (AEL). This is the elevation used by GIPSY and is different from the elevation above geoid (AGL), which is approximated by elevation above sea level (ASL).

For example, if the tropospheric residual value at KRIN station (elev: 788m AEL) at 16:30 is 112 mm, then:

ZTD = 112 + (1013 * 2.27 * exp (-0.000116 * 788)) = 2211 mm

4.2.2 Calculation of Zenith Total Delay (ZTD) from WRF Data

WRF ZTDs are calculated every 30 min at the nearest 1 km grid point from the GNSS station, from the following output parameters:

a) Atmospheric surface pressure (P_s), in mbar
b) Air temperature (T) at 45 vertical pressure layers, in K
c) Water vapour pressure (p_v) at 45 vertical pressure layers, in hPa

ZTD (mm) = ZHD + ZWD

With: $$\textbf{ZHD} = (\mathbf{2.2779 \pm 0.0024})\, \boldsymbol{P_s} / \boldsymbol{f}(\boldsymbol{\lambda}, \mathbf{H}) \qquad (4.2)$$

where P_s is the total pressure (mbar) at the Earth's surface, and:

$$f\ (\lambda, H)\ =\ (1 - 0.00266\ cos2\lambda - 0.00028H) \qquad (4.3)$$

accounts for the variation in gravitational acceleration with latitude λ and the height H of the surface above the ellipsoid (in km).

and:

$$\mathbf{ZWD} = (\mathbf{0.382} \pm \mathbf{0.004})\boldsymbol{K^2 mbar^{-1}} \int \left(\frac{p_v}{T^2}\right) \boldsymbol{dz} \qquad (4.4)$$

where p_v is the water vapour pressure (mbar), and T the air temperature (K), integrated along the zenith path z. In practice, we calculate one ZWD per vertical layer, and we add the 45 values to obtain the total ZWD.

Figure 4-3 illustrates graphically the GNSS-WRF geometry used in the calculation of the respective ZTD values.

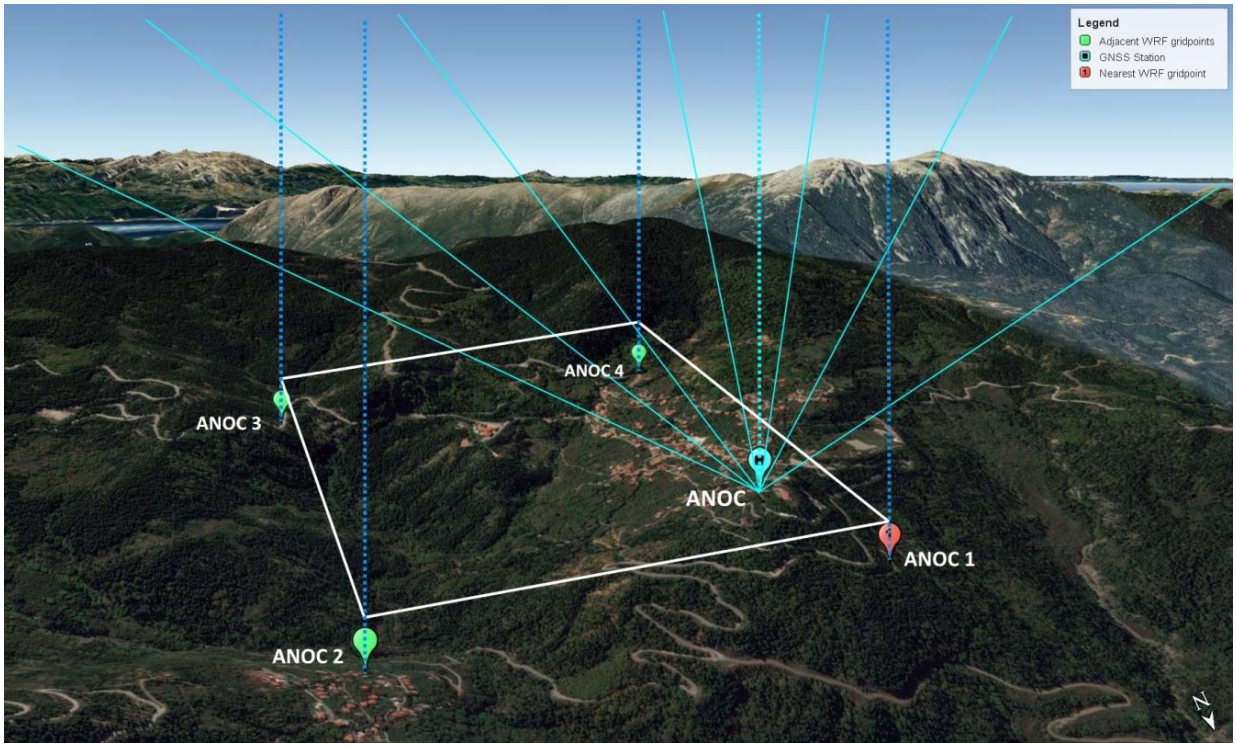

Figure 4-3. Example of GNSS-WRF geometry for ANOC Station (h=1020m). Dark blue dotted lines depict the ZTD path calculated by WRF at the four nearest grid points, light blue lines depict the GNSS slant paths measured by the receiver at the time of acquisition and light blue dotted line depicts the ZTD path calculated by the GIPSY tropospheric processing.

5. Configuration and Parameterization of WRF 1x1 km Re-analysis

5.1 Model Description

The Weather Research and Forecasting (WRF) model [Michalakes et al., 2004; Skarmarock et al., 2008] is a widely used open-source weather forecasting and re-analysis model that can be configured by the user according to the specific needs of each study. It has been developed by the U.S. National Center for Atmospheric Research (NCAR) and the National Center for Environmental Prediction (NCEP) in the late 1990's as a mesoscale Numerical Weather Prediction system designed for both atmospheric research and operational forecasting applications (NWP models and their applications are discussed in detail in Chapter 3). It is a non-hydrostatic model (with a hydrostatic option) using terrain-following vertical (sigma) coordinates based on hydrostatic pressure, and Runge-Kutta 2nd and 3rd order time integration schemes, and 2nd to 6th order advection schemes in both the horizontal and vertical planes. The Arakawa C-grid method is employed for grid staggering, while a time-split small step integration scheme is used for acoustic and gravity wave propagation.

As discussed previously, WRF has a proven record of producing high-resolution meteorological simulations down to a scale of hundreds of meters. It can be installed and operated in parallel mode using multi-processor computing resources, and therefore computational time can be greatly reduced for high-resolution simulations covering large geographical areas, such as PaTrop. The WRF system contains two modules: The WPS pre-processing module and the main ARW (Advanced Research WRF) dynamical core. The pre-processing system consists of three programs which prepare input data for use by the main ARW core. The *geogrid* program defines model domains and interpolates static geographical data to the grids; *ungrib* extracts meteorological fields from GRIB-formatted initial condition files; and *metgrid* horizontally interpolates the meteorological fields to the model grids. The ARW dynamical core contains an initialization program which vertically interpolates meteorological fields to WRF sigma levels, and the numerical solving module which calculates output parameters based on the physical and dynamical parameterization set by the user.

5.2 Model Configuration and Parameterization of Physical Components

For the high-resolution dynamical downscaling simulation performed with WRF v 3.7.1 over the PaTrop area of the western Gulf of Corinth, four nested domains were used (d01-d04), with a horizontal resolution of 27, 9, 3 and 1 km respectively, as shown in Figure 5-1; two-way nested i.e. feedback from nest to its parent domain. The vertical layer distribution consists of 45 sigma levels up to a height of about 20 km (0.1 hPa), with bottom layers being more densely populated. Boundary conditions for the model initialization were taken from the ERA-Interim global climate re-analysis database [ECMWF; https://www.ecmwf.int/en/forecasts/datasets], with a 75 km horizontal resolution, 35 vertical layers and 6 h temporal resolution. The model was initiated every day from the ERA-Interim input data at 18:00 local time, producing 30 h simulations with the first 6 h being

spin-up time. Model output was recorded every 30 minutes, from which Zenith Hydrostatic Delays (ZHD) and Zenith Wet Delays (ZWD) were calculated as described in Section 4.2.

Terrestrial input information consisted of global data sets for soil categories, land-use, terrain height, annual mean deep soil temperature, monthly vegetation fraction, monthly albedo, maximum snow albedo and slopes. The initial land topography dataset used was the Global 30 Arc-Second Elevation Model (GTOPO30) provided by United States Geological Survey (USGS), with a 30'' resolution for the smaller domain (d04), and coarser resolutions (10', 5', 2') for domains d01-d03 respectively. Similarly, land-use categories were taken from USGS 24-category data, which are available for different horizontal resolutions (10', 5', 2', 30''). The horizontal resolution of terrestrial datasets is set by the user during the WPS pre-processing step. The highest horizontal resolution available in the USGS terrestrial data is 30", which roughly corresponds to 1 km.

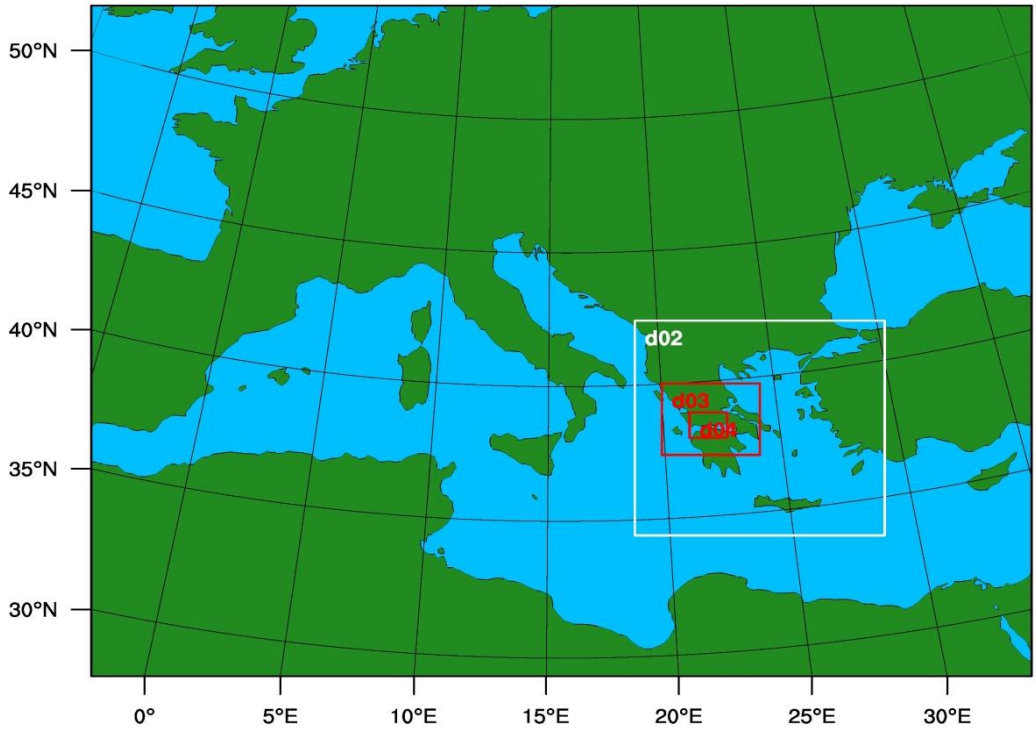

Figure 5-1: Map showing the four nested domains (d01-d04) used for WRF weather re-analysis over the Western GoC.

For the model physical and dynamical parameterization, five different schemes were tested, in order to evaluate each scheme for its forecasting skill. There have been numerous studies validating the output of different model configurations with observations under specific conditions [e.g., Mooney et al., 2013; Kotlarski et al., 2014; Garcia-Diez et al., 2015; Kioutsioukis et al., 2016], showing that globally there is no optimal scheme, but rather different schemes produce better results with respect to application, domain, season, variable, etc. Therefore, a model parameterization test was performed for a two-week period (17-29 June 2016), during which the output of the five different

model configurations was tested against GNSS tropospheric measurements from 16 permanent stations in the study area (d04).

The schemes were selected based on existing studies where similar high-resolution WRF simulations were used. All five schemes use the same parameterization for radiation physics (shortwave and longwave) and cumulus convection. In the first three schemes (MOD1, MOD2 and MOD3), cumulus convection is modelled in the 27 km domain according to the Kain–Fritsch scheme [Kain and Fritsch, 1990; Kain et al., 1993]. The cumulus scheme is not activated for the 9, 3 and 1-km domains, because at higher resolution the model can theoretically resolve convection explicitly [Kain et al., 2004]. In schemes MOD4 and MOD5, cumulus convection was turned on for d02 (9km) in order to test the effect of cumulus parameterization in a smaller domain. Convection plays an important role for cloud formation and is controlled by micro-scale processes such as mixtures of updrafts and downdrafts. These simulated convective features are less distinguishable as model resolution become coarser, therefore parameterization becomes necessary, although computationally demanding. Furthermore, in locations such as the Gulf of Corinth, where cloud formation is strongly influenced by the intense topography (land-sea contrasts and mountainous features), it is expected that cumulus parameterization in the 9km domain will better represent the effects of subgrid scale processes on the grid variables, particularly in the case of squall line formation, thunderstorms and other strong convection events.

The long wave radiation is simulated by the RRTM scheme [Mlawer et al., 1997] with the default diffusion scheme selected. The shortwave radiation is simulated by the Dudhia scheme [Dudhia et al, 1989]. Both are typical schemes for high-resolution WRF simulations, as found in Koletsis et al. (2016) in the area of N. Greece, Kioutsioukis et al. (2016) using 2-km domains over parts of Europe, and Katsanos et al. (2014) in Spain.

With respect to microphysics, land surface and planetary boundary layer options, the model was originally configured with the basic options for a less computationally demanding ERA-Interim dynamical downscaling at 1-km horizontal resolution. This first parameterization scheme (MOD1) uses:

- Noah land surface model scheme [Chen and Dudhia, 2001] with soil temperature and moisture in four layers, fractional snow cover and frozen soil physics, as used by Jiang et al. (2012), Zhang et al. (2014), Katsanos et al. (2014), and Nunalee et al. (2015).
- Revised MM5 Monin-Obukhov surface layer physics scheme, with Carlson-Boland viscous sub-layer [Jimenez et al., 2012], as used by Silverman et al. (2013) and Zhang et al. (2014) for similar 1-km downscaling simulations.
- WRF Single-Moment 3-class (WSM3) microphysics scheme [Hong et al, 2004], which is a simple, efficient scheme with ice and snow processes suitable for mesoscale grid sizes [Garcia-Diez et al., 2015].
- Mellor-Yamada-Janjic (Eta) TKE scheme [Janjic et al, 1994] for the calculation of planetary boundary layer (PBL), which is a one-dimensional prognostic turbulent kinetic energy scheme with local vertical mixing, as used by Katsanos et al. (2014) and Kioutsioukis et al. (2016).

MOD1 was further configured with damping turned on (damp_opt 1 was used which adds a layer of increased diffusion near the model top to control reflection from the upper boundary) and a time-off centering (epssm) value of 0.5. (i.e. control of vertically-propagating sound waves). These settings stabilised the model behaviour under certain conditions where fast-propagating sound waves can cause the simulation to crash.

In the second scheme (MOD2), the microphysics (mp) scheme was changed to Morrison double-moment [Morrison et al., 2009], in order to investigate the effect of a more complex model which uses double-moment ice, snow, rain and graupel for cloud-resolving simulations [Warrach-Sagi et al., 2013; Kioutsioukis et al., 2016].

In the third scheme (MOD3), the same configuration as MOD2 is used, with a change in land surface parameters, in which the Pleim-Xiu land surface model and Pleim-Xiu surface layer physics is used [PX LSM; Pleim and Xiu 1995; Xiu and Pleim 2001]. The model was developed to provide realistic ground temperature, soil moisture, and surface sensible and latent heat fluxes in mesoscale meteorological models. It includes a 2-layer force-restore soil temperature and moisture model. Grid aggregate vegetation and soil parameters are derived from fractional coverage of land use categories and soil texture types. There are two indirect nudging schemes that correct biases in 2-m air temperature and moisture by dynamic adjustment of soil moisture [Pleim and Xiu, 2003] and deep soil temperature [Pleim and Gilliam, 2009].

In the fourth scheme (MOD4), the same configuration as MOD3 is used, this time with the cumulus scheme activated for the second domain (9 km), as explained above.

Finally, the fifth scheme (MOD5) uses the parameterization of Jiang et al. (2012) and Zhang et al. (2014), as it refers to a study with similar dynamical downscaling characteristics (input dataset and horizontal resolution), performed over a complex terrain with land-sea contrasts (Hong Kong island). The parameters changed compared with the previous schemes are microphysics (SBU-YLin model is used, sophisticated scheme that has ice, snow and graupel processes, suitable for real-data high-resolution simulations), PBL scheme (YSU used in conjunction with SBU-YLin; Hong et al., 2006], and surface layer scheme (MM5 similarity). The NOAH model is used for land surface. Again, cumulus convection is activated for the second domain (9 km). Table 5.1 lists the parameterization used in each scheme.

Furthermore, in order to test the impact of a more detailed topography on the re-analysis output, a high-resolution terrestrial dataset of d04 was introduced (ASTER 1” global GDEM v2), with a horizontal grid of 30m. The geogrid module of WPS was run with four different interpolation methods when horizontally interpolating the terrain field, thus producing four different output maps to be used as the underline topography of d04. The sensitivity analysis that follows also includes the comparison of WRF output with the four different ASTER configurations against the original GTOPO30 configuration.

Table 5.1: WRF parameterization options used for the PaTrop sensitivity analysis

	MOD1	MOD2	MOD3	MOD4	MOD5
Microphysics scheme (mp)	WSM3	Morrison	Morrison	Morrison	SBU-YLin
Land surface scheme (sf)	NOAH	NOAH	Pleim-Xiu	Pleim-Xiu	NOAH
Surface layer physics scheme (sfclay)	Monin-Obukhov	Monin-Obukhov	Pleim-Xiu	Pleim-Xiu	MM5 similarity
Radiation physics scheme (sw)	Dudhia	Dudhia	Dudhia	Dudhia	Dudhia
Radiation physics scheme (lw)	RRTM	RRTM	RRTM	RRTM	RRTM
Planetary boundary layer physics scheme (pbl)	Mellor-Yamada-Janjic (Eta) TKE	Mellor-Yamada-Janjic (Eta) TKE	ACM2	ACM2	YSU
Cloud physics scheme (cu)	Kain-Fritsch at 27 km	Kain-Fritsch at 27 km	Kain-Fritsch at 27 km	Kain-Fritsch at 27 and 9 km	Kain-Fritsch at 27 and 9 km

5.3 Sensitivity Analysis and Evaluation of WRF Schemes with GNSS Data

The sensitivity analysis was performed for a two-week period (17-29 June 2016), with the aim to test different WRF parameterization schemes and the effect of topography on the model output. Tropospheric data (i.e. ZTD values) from the CRL GNSS network provided the benchmark for the analysis, for comparison with ZTDs derived from WRF at the nearest grid point. The experimental setup and data processing methodology is described in Chapter 4. The selection of the test period for the sensitivity analysis was based on grounds of weather conditions (i.e. high temperatures and the occurrence of a convective storm event during the last days of June), which theoretically would produce high levels of ZTD variation. Out of the 19 GNSS stations of the PaTrop network, 16 were fully operational during this period; therefore three stations (GALA, PSAT and AIGI) were not included in the analysis.

5.3.1 Results of WRF vs. GNSS ZTDs for Five Different Model Schemes

Time series of WRF MOD1-MOD5 vs. GNSS ZTDs at 16 PaTrop points for the test period (17-29 June 2016) are presented in Annex A, Figures A-1 to A-16. Temporal resolution is 30 min and all times are in UTC. Locations are presented in order of increasing elevation ASL.

In order to establish the correlation between the observed and predicted time series, the following metrics are used, which give us a quantitative indication of the prediction skill of different model schemes with respect to the GNSS network dataset:

Mean Bias (MB): $$\bar{\sigma} = \frac{\sum(f_i - o_i)}{N} \quad (5.1)$$

Mean Absolute Bias (MAB): $$|\bar{\sigma}| = \frac{\sum(|f_i - o_i|)}{N} \quad (5.2)$$

Root Mean Square Error (RMSE): $$RMSE = \sqrt{\frac{\sum(f_i - o_i)^2}{N}} \quad (5.3)$$

Pearson Correlation Coefficient (PCC): $$r = \frac{\frac{1}{N}\sum_i(f_i - \bar{f})(o_i - \bar{o})}{\sigma_f \sigma_o} \quad (5.4)$$

where f_i denotes the model value, o_i the observational value, N is the number of pairs in the examined time series, σ_f is the standard deviation of the model values and σ_o the standard deviation of the observations.

A summary of the regression statistics for schemes MOD1-MOD5 is presented in Tables 5.2 – 5.5, where highlighted cells indicate the best performance at each location.

- Results at most stations exhibit a strong correlation between WRF derived ZTDs and GNSS values, with the exception of the last two days of the experiment (28-29/6) where the model shows significant deviation from the observed data. All schemes seem to follow the overall trend (including the storm event of 25-26/6). The PCC at the 16 locations, for the test period, ranges from 0.57 at LIDO to 0.85 at PAT0, both with the MOD5 scheme (Table 5.2). Overall, MOD3, MOD4 and MOD5 exhibit the strongest correlation, with MOD5 having the highest R score (0.74). The model in general seems to slightly underpredict the observed data, especially for high ZTD values. Mean bias (MB) values (Table 5.3) indicate that, on average, this offset ranges from -14.9 mm (MOD1) to -11.6 mm (MOD5). Bias plots of predicted (WRF) minus observed (GNSS) ZTDs of MOD5 are presented in Annex A, Figures A-17 to A-20.
- Mean absolute bias (MAB) is a measure of the average absolute error between the two time series. Mean absolute bias values at the 16 locations range from about 15 mm at KALA to 26 mm at ANOC (Table 5.4). Schemes with more sophisticated physical parameterization, better suited for high-resolution re-analysis (MOD4 and MOD5) exhibit the lowest overall MAB values (19.5 mm). Similarly, root mean square error (RMSE) values range from 21 mm at KALA to 31 mm at ANOC (Table 5.5). Figure 5.2 illustrates the RMSE spread between the 16 points, for each model configuration. It is shown that schemes with a more complex physical parameterization (MOD4 and MOD5) exhibit lower RMSE values, as well as narrowest spread than initial WRF configurations. Results also indicate that the RMSE distribution is more homogeneous among coastal and inland stations (blue and green colours), than stations in mountainous locations (orange and red).

Table 5.2: Pearson Correlation Co-efficient results for all schemes (17/6-29/6/2016)

R	Elevation (m)	MOD1	MOD2	MOD3	MOD4	MOD5
MESO	2	0.73	0.74	0.78	0.77	0.81
XILI	4	0.70	0.71	0.76	0.78	0.77
VALI	9	0.70	0.68	0.70	0.71	0.73
LAMB	10	0.70	0.71	0.74	0.75	0.76
TRIZ	25	0.63	0.61	0.70	0.70	0.70
PSAR	55	0.69	0.68	0.75	0.73	0.73
PAT0*	91	0.77	0.78	0.81	0.84	0.85
ARSA	115	0.74	0.75	0.79	0.82	0.83
EYPA	166	0.67	0.68	0.74	0.75	0.75
ROD3	452	0.71	0.71	0.74	0.76	0.77
MESA	477	0.67	0.69	0.74	0.74	0.74
LIDO	550	0.60	0.60	0.67	0.60	0.57
KOUN	564	0.71	0.69	0.71	0.73	0.75
KALA	716	0.66	0.66	0.69	0.70	0.73
KRIN	758	0.68	0.66	0.67	0.70	0.72
ANOC	1020	0.66	0.67	0.72	0.72	0.70
AVG16		**0.69**	**0.69**	**0.73**	**0.73**	**0.74**

* Metrics for PAT0 station correspond to the CRL tropospheric solution

Table 5.3: Mean Bias results for all schemes (17/6-29/6/2016)

MB	Elevation (m)	MOD1	MOD2	MOD3	MOD4	MOD5
MESO	2	-18.5	-19.0	-17.3	-16.2	-15.0
XILI	4	-23.4	-23.9	-22.8	-17.4	-17.0
VALI	9	-7.9	-9.7	-10.0	-3.8	-3.4
LAMB	10	-5.5	-6.9	-6.6	-1.1	-1.2
TRIZ	25	-17.5	-17.8	-16.9	-17.6	-16.2
PSAR	55	-10.7	-12.1	-12.0	-7.2	-6.1
PAT0*	91	-21.1	-20.7	-16.5	-17.8	-19.7
ARSA	115	-12.2	-13.5	-11.0	-7.5	-7.8
EYPA	166	-13.3	-14.2	-12.7	-8.1	-7.3
ROD3	452	-19.0	-19.7	-18.5	-16.0	-21.5
MESA	477	-19.3	-20.2	-19.0	-18.1	-16.1
LIDO	550	-9.7	-11.0	-12.2	-7.7	-5.5
KOUN	564	-15.1	-16.5	-15.2	-11.8	-11.8
KALA	716	-4.4	-6.1	-5.4	-3.8	-3.3
KRIN	758	-10.7	-12.5	-11.7	-7.9	-7.9
ANOC	1020	-29.4	-30.9	-29.8	-27.3	-25.2
AVG16		**-14.9**	**-15.9**	**-14.9**	**-11.8**	**-11.6**

* Metrics for PAT0 station correspond to the CRL tropospheric solution

Table 5.4: Mean Average Bias results for all schemes (17/6-29/6/2016)

MAB	Elevation (m)	MOD1	MOD2	MOD3	MOD4	MOD5
MESO	2	21.3	21.9	20.0	18.5	17.7
XILI	4	25.6	25.8	25.0	21.8	21.9
VALI	9	18.4	18.7	19.0	18.4	18.6
LAMB	10	18.3	18.4	17.5	17.2	17.6
TRIZ	25	20.7	21.7	20.0	19.6	20.3
PSAR	55	20.3	20.8	20.0	18.7	18.6
PAT0*	91	27.3	27.8	25.2	22.5	22.9
ARSA	115	20.4	20.9	18.5	17.8	18.3
EYPA	166	20.4	20.8	19.4	17.8	18.0
ROD3	452	21.5	22.5	21.2	20.8	21.8
MESA	477	22.6	22.8	21.8	19.7	19.5
LIDO	550	23.6	23.9	23.6	22.8	21.5
KOUN	564	19.4	20.4	19.6	18.2	18.1
KALA	716	15.7	15.8	14.6	14.7	15.1
KRIN	758	16.6	17.9	16.7	15.7	16.3
ANOC	1020	29.8	31.1	30.1	26.8	26.2
AVG16		**21.4**	**21.9**	**20.7**	**19.4**	**19.5**

* Metrics for PAT0 station correspond to the CRL tropospheric solution

Table 5.5: RMSE results for all schemes (17/6-29/6/2016)

RMSE	Elevation (m)	MOD1	MOD2	MOD3	MOD4	MOD5
MESO	2	30.5	30.9	28.3	26.1	25.1
XILI	4	32.4	32.6	30.3	26.6	26.7
VALI	9	25.2	26.4	25.4	24.4	24.4
LAMB	10	25.2	25.4	23.1	22.8	22.9
TRIZ	25	27.0	28.4	26.6	24.8	24.9
PSAR	55	26.7	28.0	26.4	24.1	23.1
PAT0*	91	29.9	30.5	25.0	24.6	27.6
ARSA	115	27.0	27.5	23.0	22.1	23.3
EYPA	166	27.3	27.6	24.7	22.6	22.8
ROD3	452	28.4	28.9	26.7	24.8	26.7
MESA	477	28.5	28.9	27.3	25.4	25.1
LIDO	550	29.8	30.0	29.5	28.0	26.6
KOUN	564	25.7	27.0	25.0	23.5	23.1
KALA	716	22.3	22.6	20.1	20.6	21.4
KRIN	758	22.8	24.5	23.0	21.7	22.2
ANOC	1020	35.5	36.5	35.1	32.2	31.4
AVG16		**27.8**	**28.5**	**26.2**	**24.6**	**24.8**

* Metrics for PAT0 station correspond to the CRL tropospheric solution

This finding could be related to the specific meteorological conditions which characterize regions with intense topography, as well as the fact that input data (e.g. measurements from surface stations) injected into the model as initial conditions, may be sparse in certain remote locations, leading to a poorer model prediction skill in these areas.

- Under turbulent and humid atmospheric conditions (e.g. afternoon of 25/6), different schemes behave in different manners. Two separate groups can be distinguished (MOD1, MOD2 and MOD3 vs MOD4 and MOD5), with the second group exhibiting a better prediction skill, possibly as a result of the Kain-Fritsch cumulus convection scheme being turned on at the 9-km domain. A significant deviation event can also be distinguished during the second half of 28/6, where the model produces a sudden "drop" in all stations (of the order of 60-120 mm) in relation with the observed ZTDs. This is discussed in more detail in Section 6.4 of the Thesis.
- Results of the physical parameterization analysis indicate that WRF configurations MOD4 and MOD5 overall exhibit a better prediction skill during the test period, with small differences between them. Turning on the Kain-Fritsch cumulus convection scheme on the 9 km domain improves model output, particularly during intense frontal events, as demonstrated by validation metrics of MOD4 in comparison with MOD3 (all physical parameters are same except the cumulus scheme). Moreover, the use of more complex microphysics schemes (such as Morrison and SBU-YLin), surface layer (Pleim-Xiu and MM5) and planetary boundary layer (ACM2 and YSU) models, although computationally demanding, further enhance the model prediction skill. Based on the results of the sensitivity analysis, MOD5 is selected as the optimum configuration for producing tropospheric delay maps for the entire PaTrop period (January-December 2016), having a slightly higher PCC, lower MB and better clustering of RMSE than MOD4.

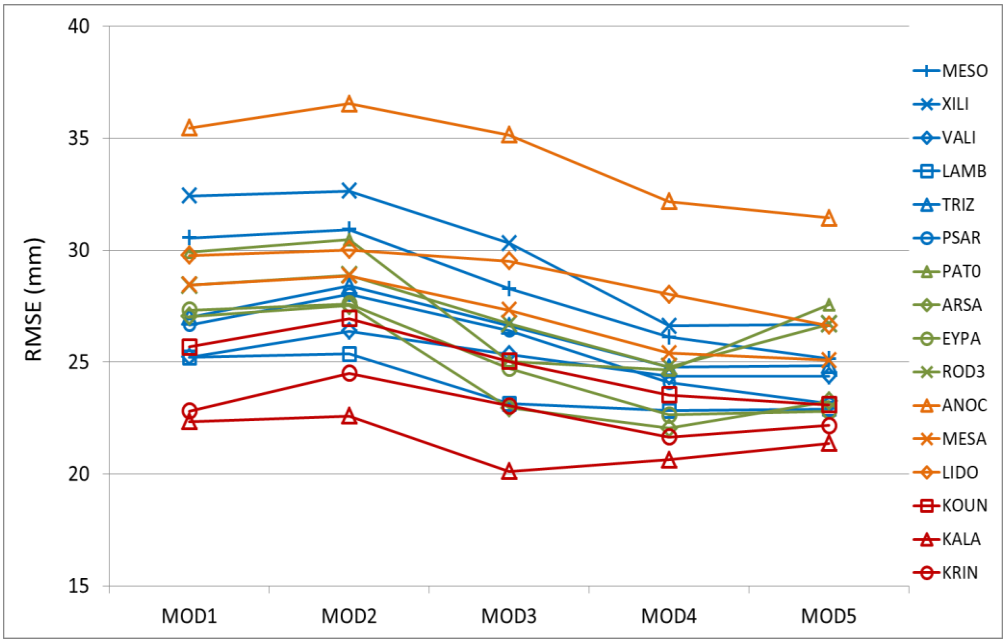

Figure 5-2: RMSE distribution for each model configuration at the 16 stations. Stations are colour-coded, according to their location: Coastal – blue; inland – green; upland north – orange; upland south – red.

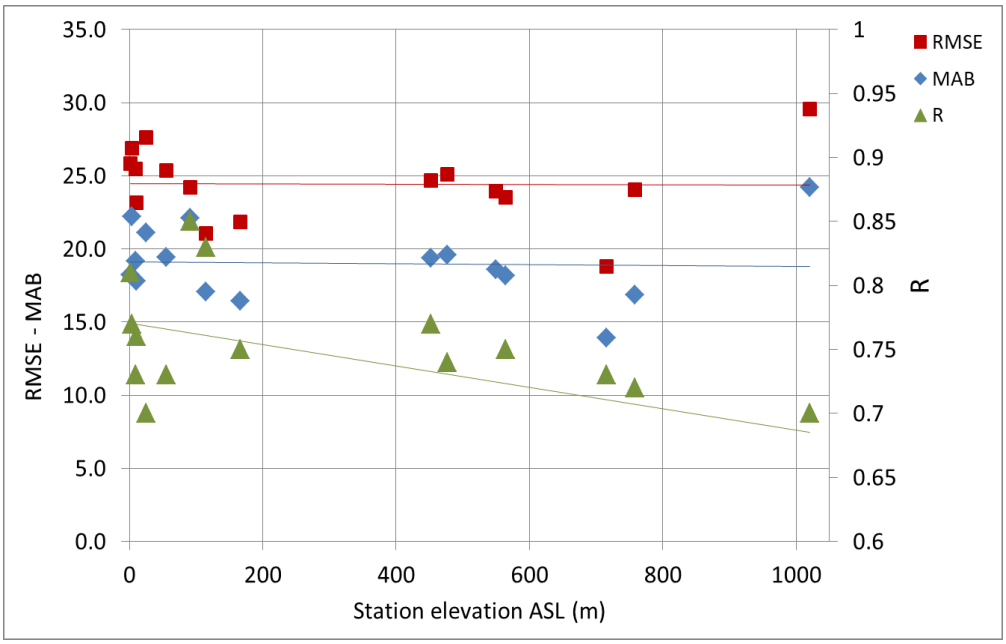

Figure 5-3: Distribution of model validation metrics (MAB, RMSE and PPC) per station elevation h – MOD5

- A graphical summary of validation metrics for MOD5 is found in Figure 5-3. We observe that although R is decreasing with increasing station elevation (as previously discussed), MAB and RMSE are not significantly increasing, which is probably a result of lower absolute ZTD values at higher altitudes where the tropospheric layer is thinner.

5.3.2 Results of Improved Model Topography with the Use of High-Resolution DEM

Weather parameters, especially temperature, wind fields and precipitation, have a close relation with topography. The presence of complex terrain causes spatial (in both the horizontal and vertical planes) and temporal variations in air flow and turbulence, which strongly influence meteorological conditions [Carvalho et al., 2002]. At high resolution (grid spacing less than 4 km), the WRF model is able to simulate subgrid processes without using certain physical parameterizations (such as convection), and fine meteorological structures driven by complex topography or land-sea contrasts (such as in the case of the Gulf of Corinth) are better represented [Papanastasiou et al., 2010; Jimenez et al., 2012]. This is particularly important for simulations of surface wind fields over complex terrain regions, where the wind spatial variability is strongly affected by orography through channelling, forced ascents, blocking, etc.

Thus, input parameters need to be adjusted for high-resolution simulations, in order to address scale effects that influence model output. An important input parameter is the spatial resolution of the topographical dataset which is used, as for high resolution models, it is desirable to have terrain data

with a resolution exceeding the model resolution (in our case 1 km) by at least a factor of 2 to 3 [Arnold et al., 2012; Zhang et al., 2014].

As described previously, land topography in the basic WRF 1x1 km model configuration was based on the default United States Geological Survey (USGS) dataset, (GTOPO30), with coarser resolutions (10′, 5′, 2′) used for domains d01, d02 and d03 respectively and a finer resolution of 30-arc seconds (30” roughly equal to 900 m), for the smaller domain (d04). In order to test the impact of a more detailed topography on the re-analysis output, a high-resolution DEM of d04 was used (ASTER 1” global GDEM v2), with a grid of 30 m. Furthermore, the GEOGRID module of WPS was run with four different interpolation methods when horizontally interpolating the terrain field, thus producing four different output maps to be used as the underlying topography of d04 during WRF re-analysis, as follows:

OPT1: Same interpolation method as for the 30s GTOPO DEM: Smoothing of topographical features ON and a sequence of average gcell, four point and average four point interpolation.

OPT2: Smoothing of topographical features OFF (no smoothing) and a sequence of average gcell, four point and average four point interpolation.

OPT3: Smoothing of topographical features OFF (no smoothing) and nearest neighbour interpolation.

OPT4: Smoothing of topographical features OFF (no smoothing) and four point interpolation.

Table 5.6: Absolute elevation differences and MAE at 16 GNNS nearest WRF grid points for 5 topographical datasets (d04). ASTER 1s global GDEM v2 is used as the reference map.

	LAT/LON		Elev. (m) REF	Elev. diff GTOPO 30s	Elev. diff ASTER 1s OPT1	Elev. diff ASTER 1s OPT2	ELEV diff ASTER 1s OPT3	ELEV diff ASTER 1s OPT4
MESO	38.364	21.474	6	3	1	0	0	0
XILI	38.384	21.914	0	8	2	1	0	0
VALI	38.231	22.134	7	2	3	0	0	1
LAMB	38.324	21.979	0	28	8	0	0	0
TRIZ	38.364	22.077	29	5	20	13	15	18
PSAR	38.321	22.179	0	0	6	5	0	0
PAT0	38.281	21.785	105	25	5	4	2	2
ARSA	38.298	21.811	94	53	14	4	0	1
EYPA	38.429	21.930	120	97	66	57	17	15
ROD3	38.311	21.895	405	36	32	29	1	2
MESA	38.488	21.581	430	66	48	14	4	6
LIDO	38.533	22.202	610	118	14	21	39	41
KOUN	38.209	22.049	530	134	56	21	14	13
KALA	38.029	22.102	741	14	11	5	12	9
KRIN	38.186	21.965	672	4	34	11	4	3
ANOC	38.597	21.924	941	7	19	23	12	13
MAE				**37.5**	**21.2**	**13**	**7.5**	**7.8**

Table 5.6 presents the mean absolute vertical errors (MAE) of the four output topographical datasets produced from the ASTER 1s DEM and the output map produced from the GTOPO 30s DEM, at the 16 GNSS nearest grid points. It is demonstrated that vertical DEM errors are greatly reduced when a high-resolution underlying topography is used, with no smoothing of topographical features and nearest neighbour or four point interpolation. Figure 5-4 illustrates elevation differences across the entire d04 of GTOPO30 minus ASTER 1s OPT3 and ASTER 1s OPT1 minus ASTER 1s OPT3.

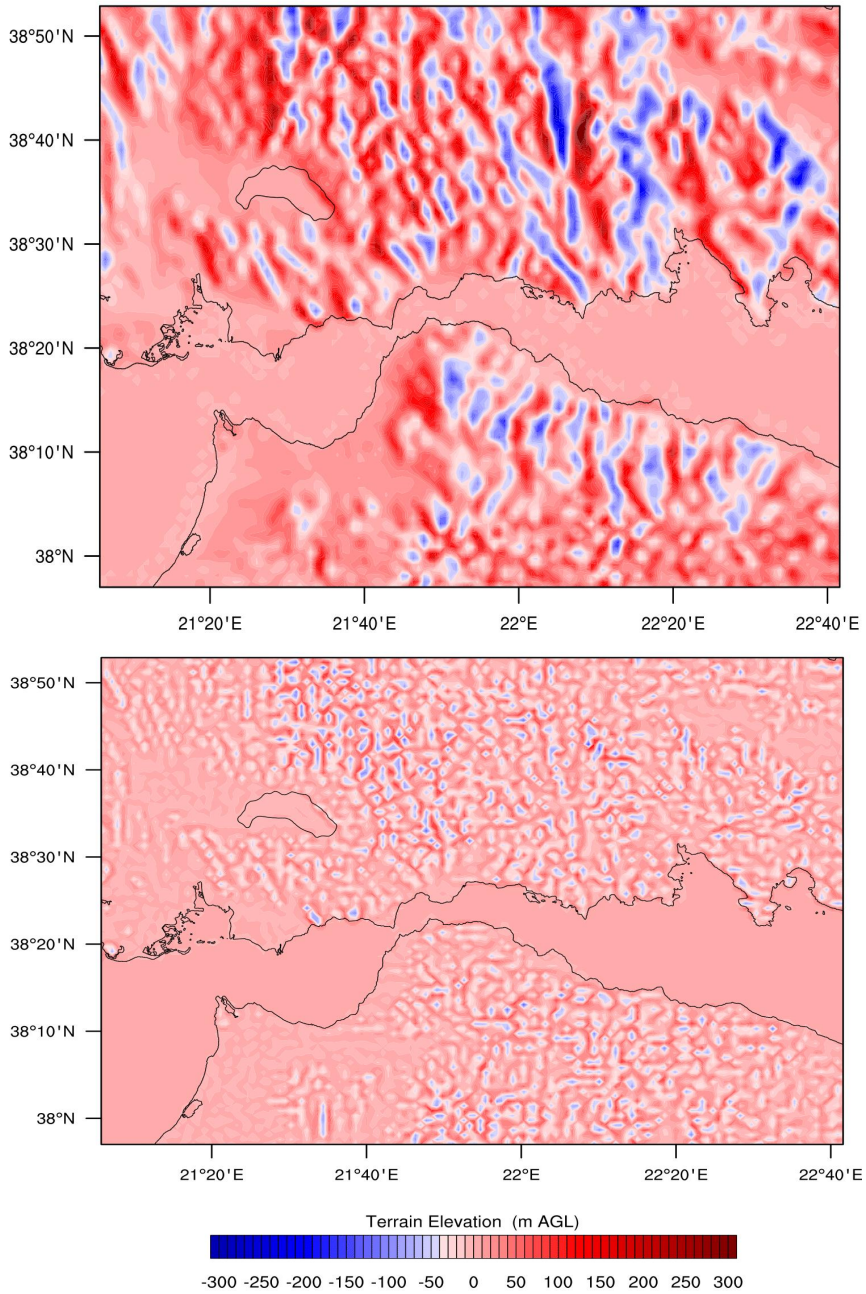

Figure 5-4: Map of domain 4 showing elevation differences: a) GTOPO 30s minus ASTER 1s DEM opt3 (no smoothing/nearest neighbour interpolation); b) ASTER 1s DEM opt1 (smoothing/3-way interpolation) minus ASTER 1s DEM opt3 (no smoothing/nearest neighbour interpolation).

Table 5.7: Pearson Correlation Co-efficient results for MOD5 with 5 topograpical sets (17/6-29/6/2016)

R	Elevation (m)	MOD5 GTOPO 30s	MOD5 ASTER 1s OPT1	MOD5 ASTER 1s OPT2	MOD5 ASTER 1s OPT3	MOD5 ASTER 1s OPT4
MESO	2	0.81	0.81	0.79	0.78	0.78
XILI	4	0.77	0.77	0.77	0.77	0.77
VALI	9	0.73	0.73	0.72	0.71	0.71
LAMB	10	0.76	0.76	0.77	0.77	0.77
TRIZ	25	0.70	0.70	0.71	0.71	0.71
PSAR	55	0.73	0.73	0.74	0.74	0.74
PAT0*	91	0.85	0.85	0.84	0.85	0.84
ARSA	115	0.83	0.83	0.83	0.83	0.83
EYPA	166	0.75	0.74	0.74	0.75	0.74
ROD3	452	0.77	0.77	0.77	0.77	0.77
MESA	477	0.74	0.74	0.73	0.74	0.74
LIDO	550	0.57	0.62	0.65	0.66	0.66
KOUN	564	0.75	0.74	0.74	0.74	0.74
KALA	716	0.73	0.76	0.76	0.76	0.76
KRIN	758	0.72	0.71	0.74	0.73	0.73
ANOC	1020	0.70	0.71	0.71	0.72	0.72
AVG16		**0.74**	**0.75**	**0.75**	**0.75**	**0.75**

* Metrics for PAT0 station correspond to the CRL tropospheric solution

Table 5.8: Mean Absolute Bias results for MOD5 with 5 topograpical sets (17/6-29/6/2016)

MAB	Elevation (m)	MOD5 GTOPO 30s	MOD5 ASTER 1s OPT1	MOD5 ASTER 1s OPT2	MOD5 ASTER 1s OPT3	MOD5 ASTER 1s OPT4
MESO	2	17.7	17.4	17.9	18.2	18.2
XILI	4	21.9	22.6	22.5	22.2	22.1
VALI	9	18.6	18.5	19.1	19.1	19.0
LAMB	10	17.6	18.7	17.8	17.8	17.7
TRIZ	25	20.3	19.6	20.4	19.9	19.7
PSAR	55	18.6	19.3	19.0	19.4	19.3
PAT0*	91	22.9	22.2	21.8	22.1	22.2
ARSA	115	18.3	18.3	17.4	17.1	17.0
EYPA	166	18.0	22.7	21.8	16.4	16.3
ROD3	452	21.8	21.7	21.4	19.4	19.5
MESA	477	19.5	24.9	21.2	19.6	19.7
LIDO	550	21.5	18.5	18.0	18.6	18.7
KOUN	564	18.1	23.2	18.7	18.2	18.1
KALA	716	15.1	14.4	14.8	13.9	14.1
KRIN	758	16.3	14.1	16.2	16.9	17.0
ANOC	1020	26.2	24.3	24.1	24.2	24.3
AVG16		**19.5**	**20.0**	**19.5**	**18.9**	**18.9**

* Metrics for PAT0 station correspond to the CRL tropospheric solution

To test the impact of high-resolution d04 topography on model output, we operate WRF MOD5 scheme with five separate topographical datasets. Results of PCC and MAB are presented in Tables 5.7 and 5.8, and location and characteristics of the 19 nearest WRF grid points are listed in Table 5.9.

- With regards to the correlation with GNSS derived ZTD time-series, it can be seen that MOD5 operated with an ASTER 1s DEM d04 topography produces marginally better results. When no smoothing and nearest neighbour/fourpt interpolation is used, the PCC is higher especially at stations located in mountainous terrain type where the relief is uneven.
- With regards to mean absolute bias (MAB), high-resolution topography reduces slightly the error margin between the predicted and the observed time-series by representing terrain features in a more detailed way. MAB is reduced to 18.9 mm from 19.5 mm when ASTER 1s OPT3 and OPT4 are used instead of the original GTOPO 30 s topography.
- The effect of introducing a high-resolution static topographical dataset on the WRF model output is less profound than other similar studies [Zhang et al., 2014; Nunalee et al., 2015], as ZTD values at the 16 nearest gridpoints are already corrected for elevation differences between the GNSS receivers and the gridpoints. Small improvements in R and MAB are attributed to a more accurate representation of topographical features which influence near surface phenomena (such as humidity), especially in upland locations. The fact that the model is more sensitive to physical parameterization than to topography is also demonstrated, with average R and MAB in all stations improving by 7.2% and 8.9% respectively (MOD1 vs MOD5), as opposed to 1.4% and 3.1% (ASTER 1s vs GTOPO 30s).

Table 5.9: Locations and characteristics of WRF grid point nearest to GNSS station (ASTER 1s DEM)

Nearest WRF grid point	Co-ordinates		Elevation ASL WRF (m)	Elevation difference (GNSS-WRF)	Horizontal distance from GNSS (m)
	LAT	LON			
ANOC_W1	38.597	21.924	953	67	287
ARSA_W1	38.298	21.811	94	21	607
AIGI_W1	38.245	22.065	128	14	612
GALA_W1	38.372	22.386	43	-10	621
EYPA_W1	38.429	21.930	137	29	293
KALA_W1	38.029	22.102	729	-13	174
KOUN_W1	38.209	22.049	517	47	288
KRIN _W1	38.186	21.965	669	89	591
LAMB_W1	38.324	21.979	0	10	436
LIDO_W1	38.533	22.202	571	-21	453
MESA_W1	38.488	21.581	434	43	625
MESO_W1	38.364	21.474	6	-4	280
PAT0_W1	38.281	21.785	103	-14	311
PSAR_W1	38.321	22.179	0	55	472
PSAT_W1	38.331	21.873	6	13	289
ROD3_W1	38.311	21.895	406	46	405
TRIZ _W1	38.364	22.077	14	11	403
VALI _W1	38.231	22.134	8	1	315
XILI_W1	38.384	21.914	0	4	241

5.4 Concluding Remarks

Five different model parameterization schemes were tested, in order to evaluate each scheme for its forecasting skill. The schemes were selected based on existing studies where similar high-resolution WRF simulations were performed, and range from schemes with relatively simple physical and dynamical parameterization to more complex schemes which require longer computational times.

In addition, in order to test the impact of a more detailed topography on the re-analysis output, a high-resolution terrestrial dataset of d04 was introduced (ASTER 1" global GDEM v2), with a horizontal grid of 30 m. Four different interpolation parameters of the terrestrial dataset were fine-tuned in the WRF pre-processing step, thus producing four different output maps to be used as the underlying topography of d04.

A model parameterization sensitivity analysis followed, for a two-week period (17-29 June 2016), during which the output of different model configurations, in terms of ZTD, was compared with GNSS tropospheric measurements from 16 permanent stations in the study area (d04). Results were tested for their statistical significance and demonstrated that the optimum WRF configuration to be used for the entire period of the PaTrop experiment was MOD5 with a high-resolution ASTER 1s DEM as the terrestrial dataset, horizontally interpolated at the nearest neighbouring pixel.

6. Validation of WRF Derived Tropospheric Delay Maps with GNSS ZTD Measurements for the PaTrop Period (January-December 2016)

Following the initial configuration of the WRF model and parameterization based on a short-scale sensitivity analysis, as described in the previous section, the main part of the PaTrop experiment extends into a whole year of validation of model re-analysis output with the use of observational tropospheric data from the CRL GNSS network in the Western Gulf of Corinth. The WRF scheme which provided the best simulation results based on the parametric test was selected (MOD5), having a more complex physical parameterization, better suited for high-resolution re-analysis simulations. This includes the SBU-YLin microphysics model [Lin et al., 2011], with a more sophisticated scheme for ice, snow, rain and graupel processes in the lower troposphere, the NOAH land surface model, the MM5 similarity scheme for surface layer physics and the YSU planetary boundary layer model [Hong et al., 2006]. In addition, MOD5 uses a cumulus convection scheme in both the 27-km and 9-km domains, thus simulating processes such as convective fluxes and the associated evaporation or condensation of water more coherently over a complex terrain with land-sea contrasts. The full description of MOD5 physical parameterization is given in Table 5.1 of the previous section.

The MOD5 output, represented as Zenith Total Delay (ZTD) values calculated from specific atmospheric parameters (surface pressure, air temperature and water vapour profiles) over the entire 1x1 km grid is validated against a dataset of GNSS derived ZTD values, providing point measurements at the 19 points where the stations are located, as illustrated in Figure 4-1.

As illustrated in Figure 5-1 of the previous section, the WRF model is setup with four nested domains, (27, 9, 3 and 1-km horizontal resolution), and a vertical discretization of 45 levels up to a height of 20 km. A high-resolution terrestrial dataset (ASTER 1s DEM) is also used for the inner domain (d04) which enables us to improve the accuracy of the model predictions with regards to the calculation of vertical ZTD profiles (Figure 6-1). The model is operated for the year 2016, and started every day with boundary conditions from the ERA-Interim database, at 18 UTC, producing 30h simulations, with the first 6h being spin-up time. Model output is recorded every 30min and the corresponding ZTD values are post calculated at hh:00 and hh:30 hours. These values are compared against GNSS derived ZTDs, at the same temporal resolution, and results are presented in the following sections as follows:

a) Annual variability of time series and model performance evaluation using simulation metrics.
b) Seasonal variability of time series and model performance evaluation using simulation metrics.
c) Comparison of different tropospheric GNSS processing protocols at PAT0 station.
d) Examples WRF vs. GNSS de-correlation and sources of error.

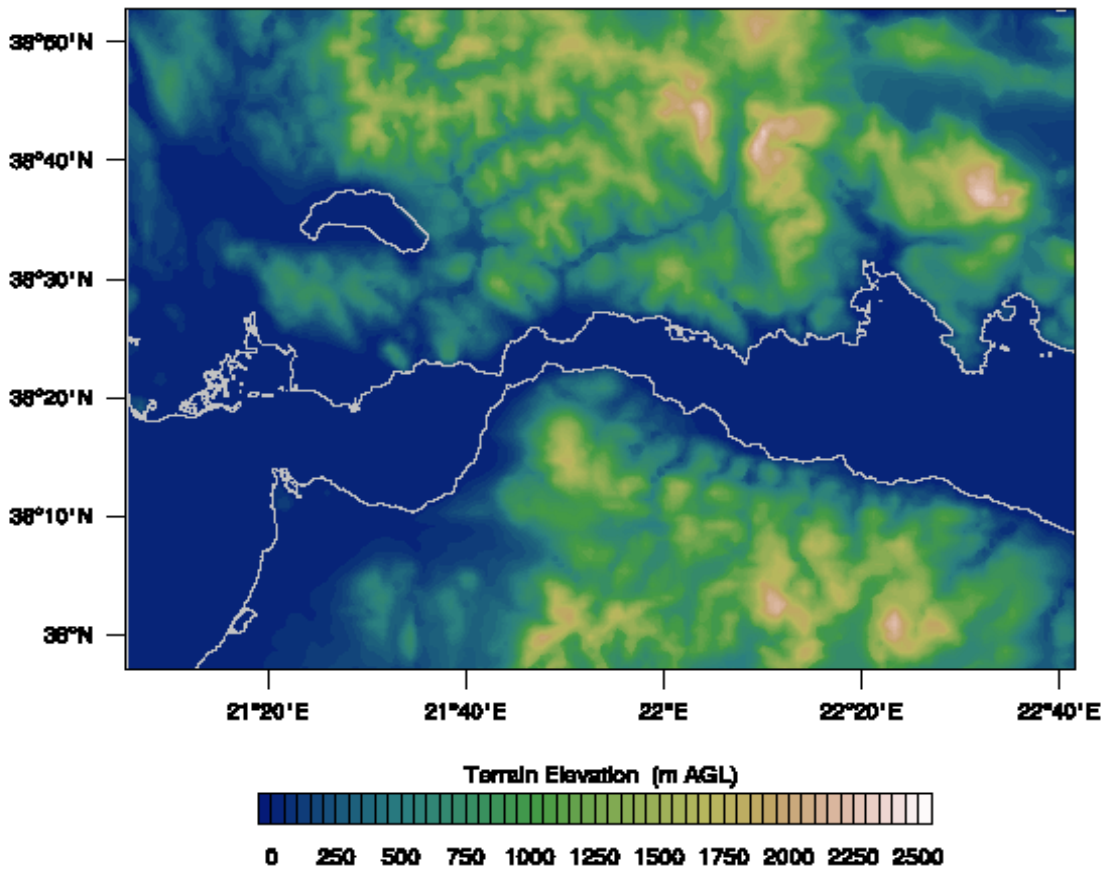

Figure 6-1. Underlying topography of domain 4, ASTER 1s DEM opt4 (no smoothing/nearest neighbour interpolation).

6.1 Annual Variability of WRF vs. GNSS ZTD and Evaluation of Model Performance

In this section the overall results of the WRF ZTD output vs. GNSS derived ZTDs are presented as follows:

Appendix B, Figures B-1 – B-5: Annual time series of WRF ZTDs vs. GNSS ZTDs at the 19 PaTrop stations.
Appendix B, Figures B-6 – B-10: Bias plots of observed ZTD (GNSS) minus predicted (WRF) at the 19 PaTrop stations.
Figures B-11 – B-13: Line-fit correlation plots of WRF ZTDs vs. GNSS ZTDs at the 19 PaTrop stations.

Macroscopically, the two ZTD datasets are closely correlated in all 19 locations, with values peaking during the warm months (July-September) and subduing during the cold period (December-March), as expected (ZTD is proportional to surface pressure and air temperature which both increase during summer). It is also evident from the oscillating pattern of the time series that in absolute terms the tropospheric delay signal shows a higher degree of variability during the second half of the year than during the first half, most probably as a result of a combination of more intense temperature and

water vapour fluctuations. As shown by the correlation plots and the bias plots, the model exhibits a small negative bias and tends to slightly underpredict ZTD values at all stations, in various degrees. Another finding is that the bias variance between the observed and predicted values follows the amplitude of the ZTD signal, having higher amplitude during the summer period.

For a more detailed analysis of the correlation between the two datasets, the same statistical indices are used as in the physical parameterization study (PCC, MB, MAB, RMSE), which give us a quantitative indication of the accuracy and variability of the model prediction with respect to the dataset of the GNSS monitoring network. A summary of the regression statistics for the whole period of study is presented in Table 6.1:

Table 6.1: Statistical indices of complete WRF ZTS vs. GNSS ZTD time series – Jan-Dec 2016

Code	Elevation ASL (m)	Mean bias MB	Mean absolute bias MAB	Root mean square error RMSE	Pearson correlation coefficient PCC
ANOC	1020	-23.8	24.5	28.3	0.92
ARSA	115	-16.4	19.2	23.9	0.92
AIGI	142	-18.1	20.7	25.3	0.92
GALA	33	-19.6	22.1	27.3	0.93
EYPA	166	-19.5	21.3	25.7	0.93
KALA	716	-11.1	14.9	19.1	0.92
KOUN	564	-16.8	19.1	23.4	0.92
KRIN	758	-19.4	21.0	26.4	0.91
LAMB	10	-14.0	19.0	22.4	0.91
LIDO	550	-12.1	16.1	20.3	0.92
MESA	477	-22.5	23.7	27.9	0.93
MESO	2	-18.3	21.4	26.7	0.91
PAT0*	91	-25.5	26.5	30.9	0.93
PSAR	55	-15.1	18.1	22.7	0.93
PSAT	19	-28.2	29.0	32.9	0.92
ROD3	452	-20.8	22.2	26.5	0.92
TRIZ	25	-21.4	22.9	27.4	0.93
VALI	9	-14.5	18.1	22.9	0.93
XILI	4	-28.0	28.6	33.1	0.93

* Metrics for PAT0 station correspond to the CRL tropospheric solution

- The Pearson correlation co-efficient *r* measures the extent to which two variables are linearly related. A PCC of 1 means that the two variables are perfectly positively linearly related and that the points in the scatter plot lie exactly on a straight line (y=x). The PCC at the 19 locations, for the entire annual time series, ranges from 0.91-0.93 i.e. it is fairly uniform, indicating that the model's variability matches the variability of the observed tropospheric delay about 90% of the time.
- Mean bias (MB) is a measure of the accuracy of the model's ZTD output with respect to the observational dataset. Mean bias values for ZTD (GNSS-WRF), range from -11.1 mm (KALA station) to -28.2 mm (PSAT station), and indicate that the model tends to slightly

underestimate the tropospheric ZTD as compared to the GNSS derived values. This finding is in-line with similar WRF evaluation studies [Garcia-Diez et al, 2013; Kioutsioukis et al, 2016] reporting consistently negative differences in relative humidity (a primary physical parameter in calculating the ZTD) with respect to ground observations in high-resolution WRF re-analysis scenarios, which are attributed to differences in vertical mixing strength and entrainment.

- Mean absolute bias (MAB) and root mean square error (RMSE) are both a measure of the absolute error between the two time series and are particularly useful, as the correction of the tropospheric component in InSAR interferograms is dependent on the model's capability to produce high-resolution differential meteograms of tropospheric delay with the minimum absolute error (of the order of magnitude of one interferometric phase cycle π). Mean absolute bias values at the 19 locations range from 14.9 mm (KALA station) to 29.0 mm (PSAT station), with RMSE values covering a similar range.

A further look into the model validation metrics for the entire PaTrop period reveals some additional trends:

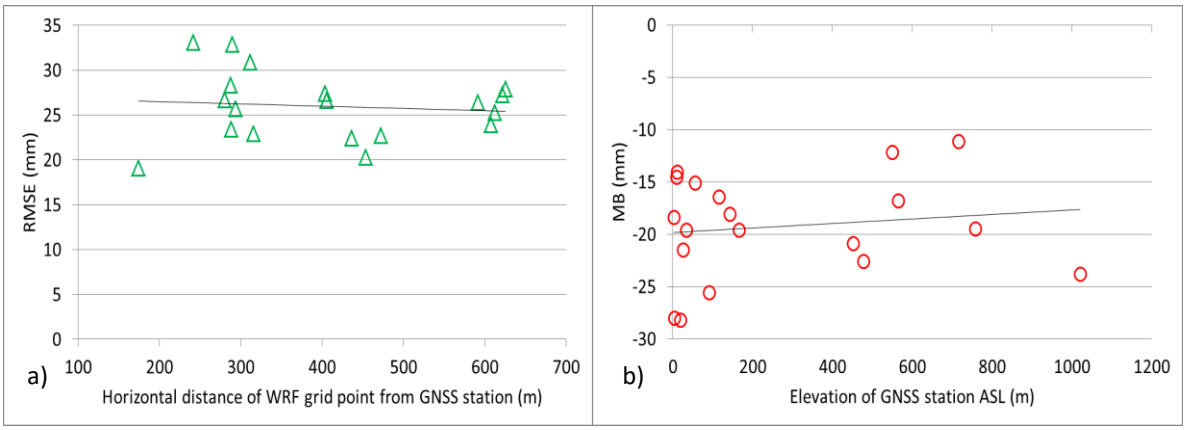

Figure 6-2: Plots of: RMSE vs. horizontal distance s between WRF grid point and GNSS station (a); MB vs. GNSS station elevation h (b).

- As shown in Figure 6-2a, the RMSE seems to be independent of the horizontal distance *s* between the GNSS station and the nearest WRF grid point where the calculation of the predicted ZTD is performed. Therefore we can conclude that the horizontal resolution of 1 km used for the WRF simulation is adequate.
- With respect to station elevation *h*, a small reduction of MB is evident with increasing h, as expected, due to smaller ZTD values (Figure 6-2b). Out of the 19 stations, the three highest mean negative biases are in XILI, PSAT and PAT0 (elevations ASL 4, 19 and 91 m), while the two lowest are in LIDO and KALA (550 and 716 m). The graphical summary of validation metrics for the entire period (Figure 6-3) also reveals that while *r* is fairly constant with increasing station elevation, MAB and RMSE exhibit a reduction.

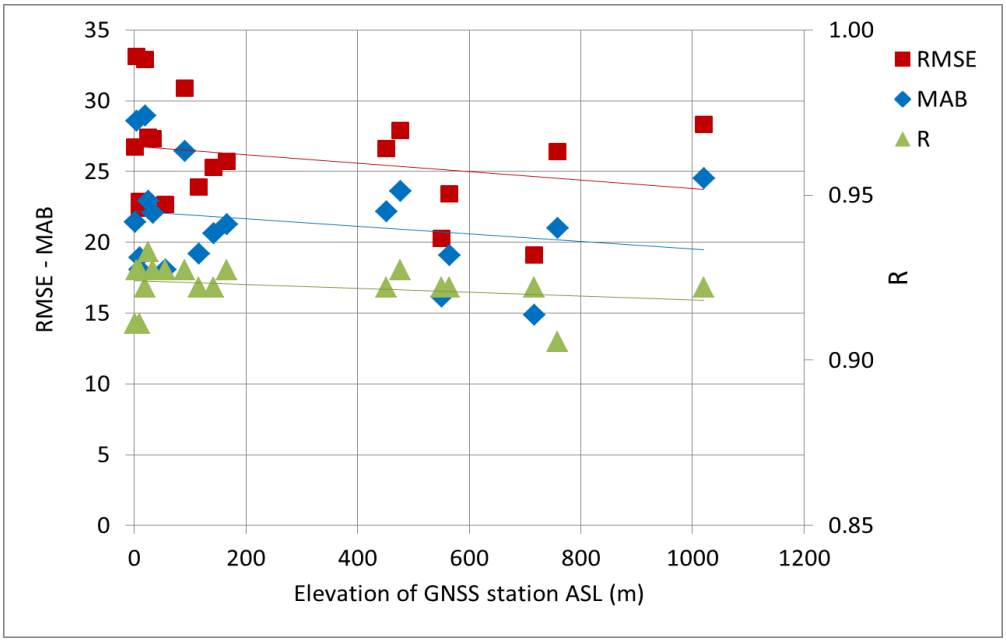

Figure 6-3: Distribution of validation metrics (MAB, RMSE and PPC) per station elevation h.

6.2 Seasonal Characteristics of WRF vs. GNSS ZTD and Evaluation of Model Performance

Further to the annual time series analysis and evaluation, it is useful to perform a more in-depth investigation of seasonal trends, which can provide an important insight into the model's forecast skill under different meteorological conditions. The year is therefore divided into four seasons (S1-S4) based on their distinct climatological characteristics as follows:

Winter S1: January – March
Spring S2: April – June
Summer S3: July – September
Autumn S4: October – December

Table 6.2 lists the corresponding model validation metrics per station and for each season. In general, model performance is better during autumn (S4), as correlation with the observed ZTD time series is high at all stations (PCC>0.9) and MAB and RMSE are lower (average MAB=20.5, RMSE=24.6). Model forecasting skill seems to deteriorate during summer (S3), where correlation is weaker (average PCC=0.83) and bias indicators are higher (MAB=22.8, RMSE=28.0). These results are in-line with seasonal climate characteristics in the region of Western Greece, as stable weather conditions and frontal precipitation patterns which prevail during autumn are well simulated by the model, whereas the combination of high temperatures and turbulent conditions during some summer days, resulting in convective storms are more difficult to be predicted.

Table 6.2: Seasonal statistical indices of WRF ZTS vs. GNSS ZTD time series – 2016

Season	S1			S2			S3			S4		
	|σ|	RMSE	PCC	|σ|	RMSE	PCC	|σ|	RMSE	PCC	|σ|	RMSE	PCC
ANOC	24.9	28.0	0.85	25.1	28.9	0.89	25.8	30.5	0.82	22.3	25.6	0.93
ARSA	19.8	24.2	0.86	18.3	22.8	0.89	20.6	25.8	0.84	18.1	22.4	0.93
AIGI	19.6	23.5	0.81	20.4	25.2	0.89	22.2	27.6	0.84	20.8	24.6	0.93
GALA	22.1	27.1	0.84	22.3	27.4	0.87	23.1	28.6	0.86	-	-	-
EYPA	20.9	24.6	0.87	20.3	24.9	0.89	22.9	27.9	0.84	21.1	25.0	0.94
KALA	14.2	18.3	0.82	15.0	19.0	0.89	16.7	21.5	0.83	13.4	17.0	0.93
KOUN	18.9	22.6	0.83	17.7	22.0	0.89	20.2	25.4	0.84	19.6	23.4	0.93
KRIN	22.7	27.9	0.75	20.7	26.6	0.87	20.4	25.7	0.82	18.3	23.3	0.91
LAMB	18.5	22.8	0.84	17.5	22.4	0.87	18.4	23.1	0.84	16.6	21.4	0.93
LIDO	16.8	20.6	0.88	16.5	20.9	0.85	16.2	21.1	0.85	15.5	19.2	0.93
MESA	22.5	26.0	0.87	22.6	26.8	0.88	26.3	31.0	0.82	23.1	27.1	0.93
MESO	20.0	23.9	0.88	20.9	25.2	0.89	25.3	32.2	0.71	20.3	24.9	0.94
PAT0*	26.0	29.4	0.88	26.1	30.4	0.88	28.6	33.1	0.82	26.4	30.4	0.93
PSAR	16.9	21.0	0.85	17.8	22.4	0.89	20.3	25.5	0.85	17.3	21.6	0.94
PSAT	30.1	33.2	0.86	28.2	32.6	0.87	28.0	33.1	0.84	29.1	32.8	0.94
ROD3	19.3	23.8	0.84	23.3	27.4	0.89	24.6	29.3	0.85	21.6	26.4	0.92
TRIZ	22.5	26.4	0.87	22.8	27.2	0.89	24.9	30.2	0.84	22.5	26.5	0.94
VALI	17.5	21.7	0.84	17.8	22.8	0.89	20.0	25.5	0.84	17.2	21.5	0.94
XILI	30.5	33.6	0.86	27.5	32.7	0.88	29.8	35.0	0.84	26.3	30.6	0.94
AVG19	**21.2**	**25.2**	**0.85**	**21.1**	**25.7**	**0.88**	**22.8**	**28.0**	**0.83**	**20.5**	**24.6**	**0.93**

* Metrics for PAT0 station correspond to the CRL tropospheric solution

When we look at the monthly variability of the mean absolute bias (Figure 6-4), a distinct "peak" in February and March is evident in most coastal and inland stations, possibly due to the winter storms which are common during this period. A second "peak" during the summer period (June-September) is explained by a combination of high temperatures and the occurrence of intense convective storm events, as discussed earlier. Stations which are located inland exhibit a more uniform monthly variability of the MAB (co-variance is high), while coastal stations exhibit a more diverse variability particularly during the "hot" season S3. In stations located upland, two separate groups are distinct: the first one including the Peloponnese stations (south) plus LIDO exhibit a smaller degree of seasonal MAB variability, while ANOC and MESA (both located in the northern Aitoloakarnania region) exhibit higher seasonal variability (distinct "peaks" during S1 and S3 and higher MAB).

Figure 6-5 illustrates the distribution of model validation metrics (MAB, RMSE and PPC) per station, for each season (S1-S4). The model correlation co-efficient (PCC) seems to be independent of the station elevation h, for all seasons (possibly with the exception of S1), whereas MAB and RMSE follow a downward trend with increasing h seasonally as annually.

In the following sections, seasonal absolute bias plots of WRF ZTD vs. GNSS ZTD are presented for all stations (Figures 6-6 – 6-9). Additionally, the seasonal error (bias) distribution and the percentage of outlying values for all stations is listed (Tables 6.3 – 6.6), which is a measure of the model's forecasting skill. The accepted "range" of model error is taken as the amplitude of one Sentinel-1 C-band cycle phase π (equal to $\lambda/2$, where λ is the SAR signal wavelength), i.e. ±23 mm of tropospheric delay, when projected to the zenithal distance.

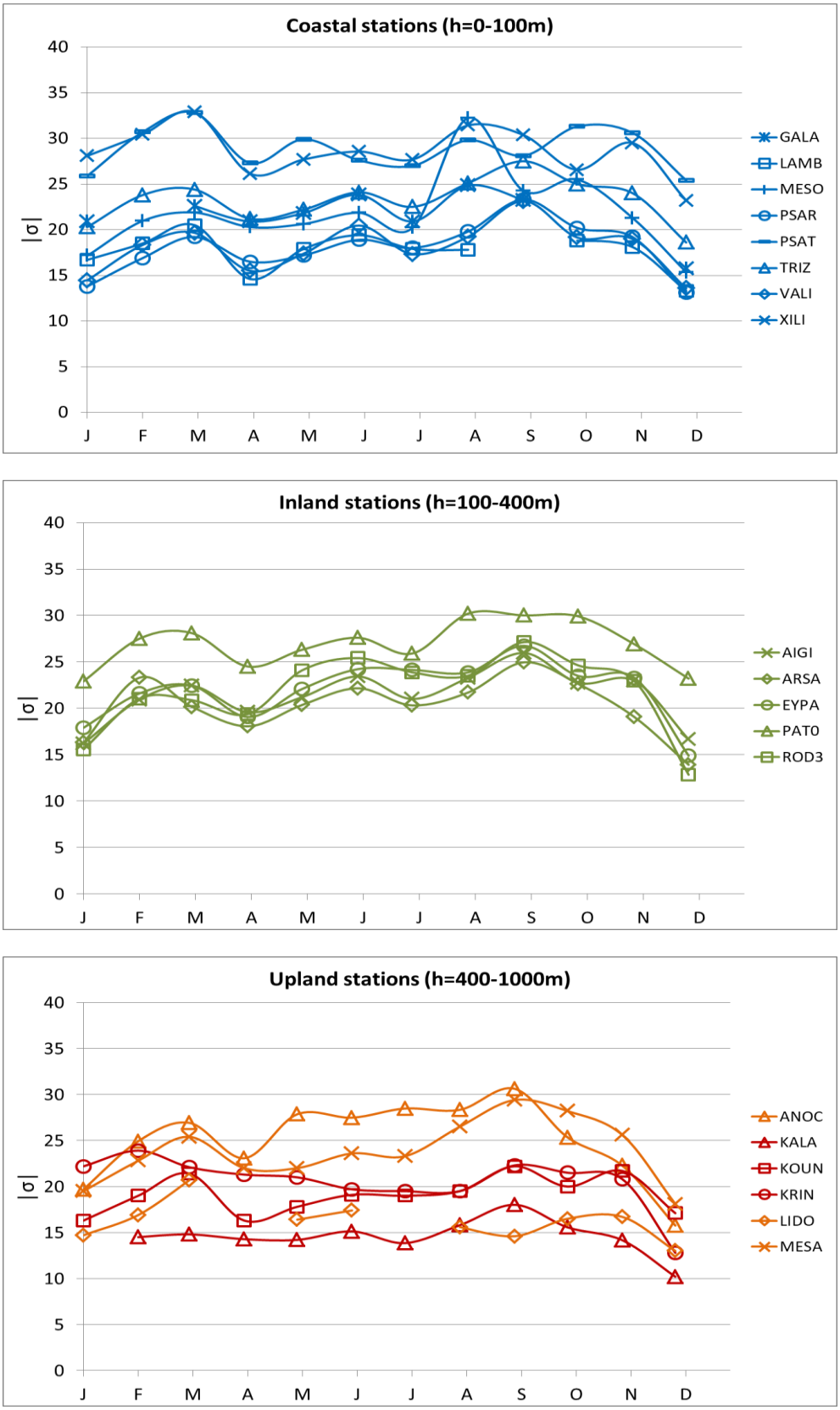

Figure 6-4: Monthly variability of MAB at the 19 PaTrop stations, classified per terrain type: coastal (a); inland (b); upland (red=north, orange=south) (c).

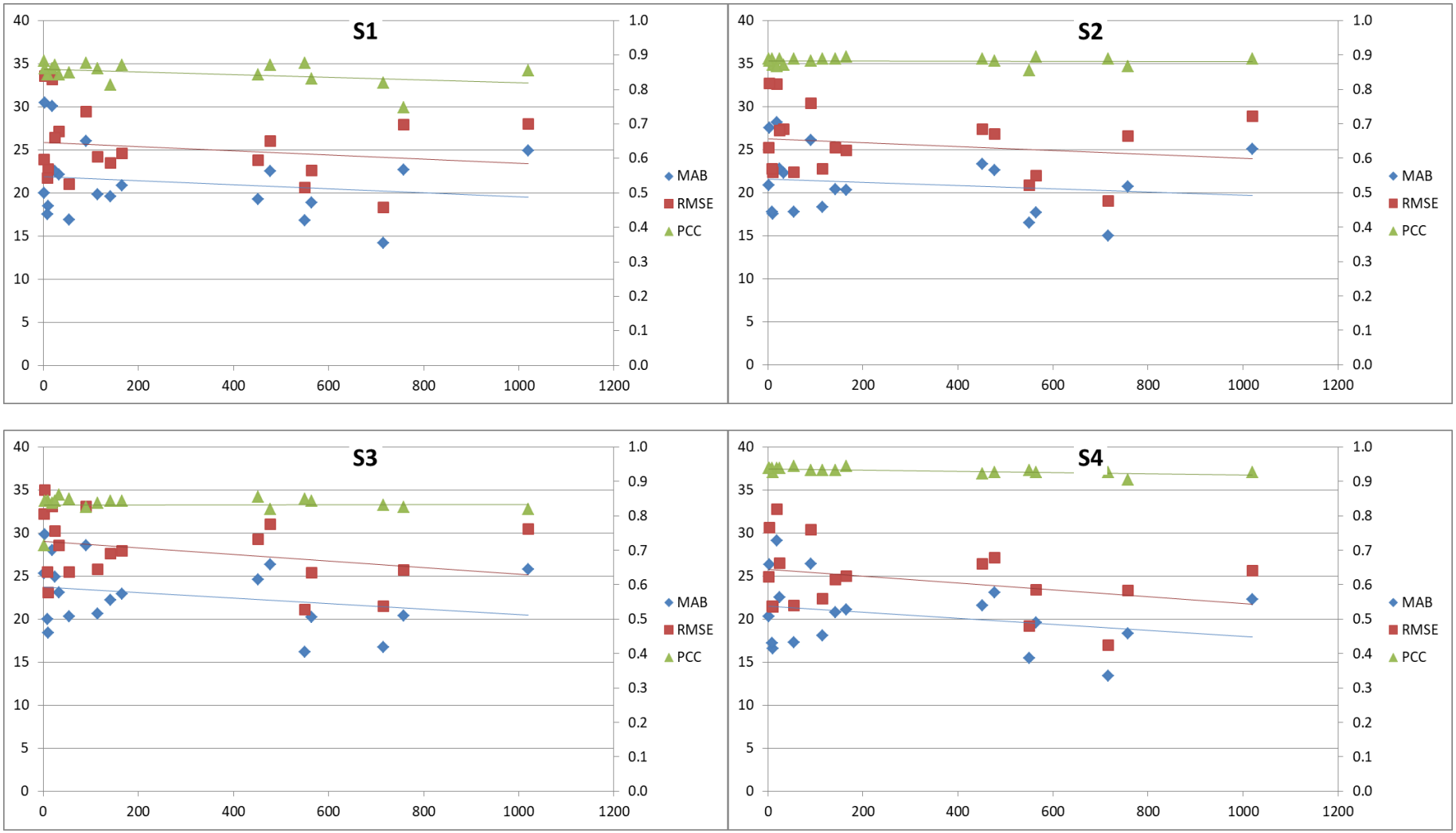

Figure 6-5: Distribution of validation metrics (MAB, RMSE and PPC) per station elevation h, and season (S1-S4).

6.2.1 Results for S1 (January-March 2016)

The winter season is characterised by a strong correlation in all stations (r=0.85), with some exceptions during possible stormy events or fast moving frontal conditions (i.e. 17/2-18/2, 29/2-1/3, 6/3-9/3, 13/3-15/3). Absolute bias is "peaking" during these dates in all stations, usually in a consistent manner across the WRF domain (Figure 6-6). However, there are instances where stations produce inconsistent results (see for example bias differences between KRIN and neighbouring KOUN and KALA stations during 12/2-14/2 and 24/3), signifying the existence of local weather events (i.e. localised precipitation on mountainous regions). Average bias during S1 is generally low with an average $|\sigma|$ of 21.2 mm.

The bias range is satisfactory during S1, with an average 60% of σ falling between π and –π (Table 6.3). Outlying values of σ are mostly distributed below the lower limit (–π), indicating that the model globally tends to underpredict ZTD during S1.

Table 6.3: σ values within error range – S1

Code	Elevation ASL (m)	Ratio of σ above π (23mm)	Ratio of σ below –π (-23mm)	Ratio of σ between π and –π
ANOC	1020	<0.01	0.53	0.47
ARSA	115	<0.01	0.33	0.67
AIGI	142	0.01	0.33	0.66
GALA	33	<0.01	0.41	0.59
EYPA	166	<0.01	0.38	0.62
KALA	716	<0.01	0.18	0.82
KOUN	564	0.01	0.31	0.68
KRIN	758	<0.01	0.42	0.58
LAMB	10	<0.01	0.32	0.68
LIDO	550	<0.01	0.26	0.74
MESA	477	<0.01	0.43	0.57
MESO	2	<0.01	0.35	0.65
PAT0*	91	<0.01	0.56	0.44
PSAR	55	<0.01	0.27	0.73
PSAT	19	<0.01	0.63	0.37
ROD3	452	<0.01	0.41	0.59
TRIZ	25	<0.01	0.45	0.55
VALI	9	<0.01	0.27	0.73
XILI	4	<0.01	0.64	0.36

* Metrics for PAT0 station correspond to the CRL tropospheric solution

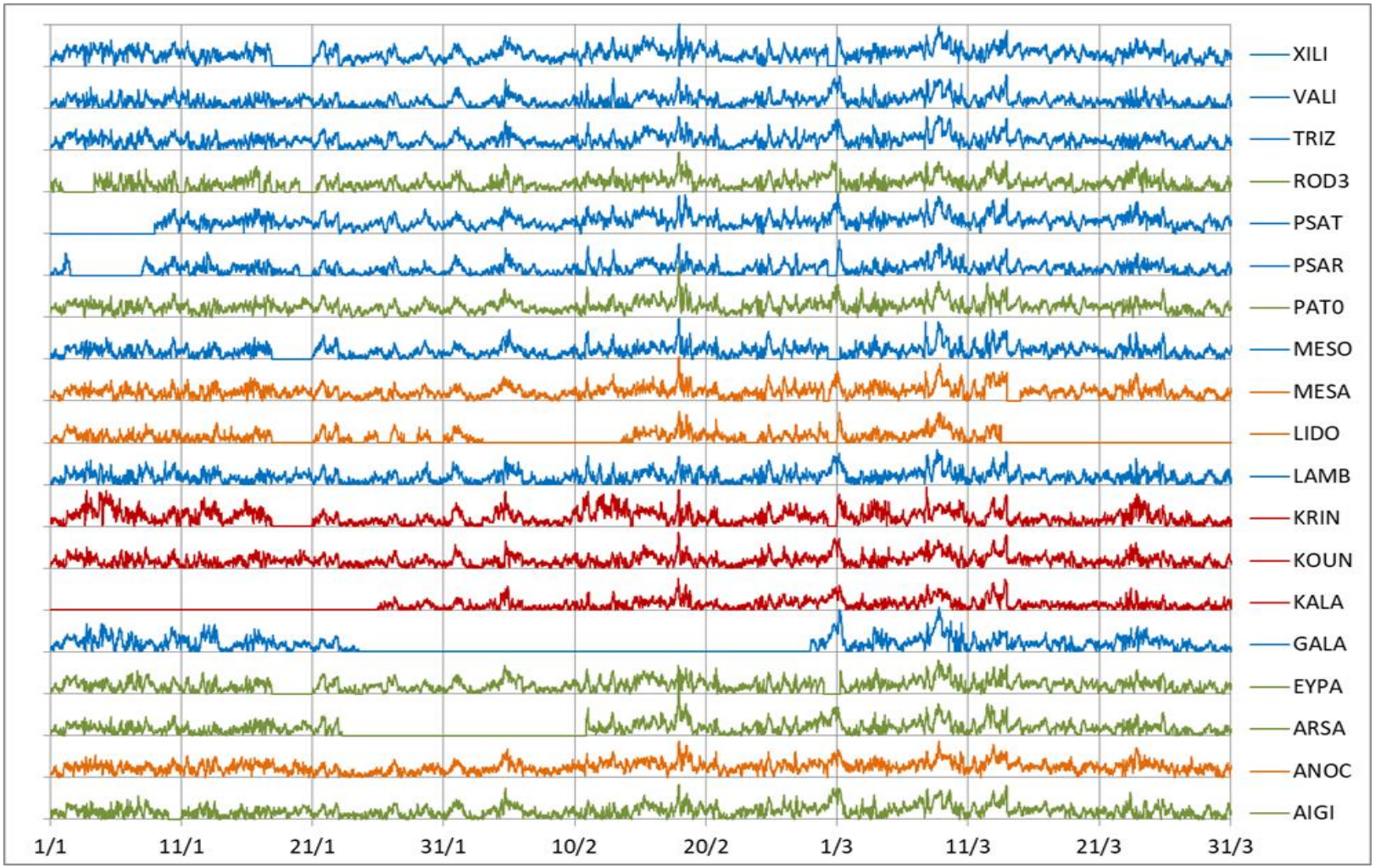

Figure 6-6: Absolute bias plot for all stations, season S1. Colours indicate terrain type: Coastal – blue; inland – green; upland north – orange; upland south – red. Values are shifted by 100mm for better readability.

6.2.2 Results for S2 (April-June 2016)

As temperatures become warmer during spring and early summer, atmospheric conditions become more stable, with MAB "peaking" less frequently than S1 but with higher amplitude, reaching 60-100 mm in some instances (Figure 6-7). Events of "noisy" model performance are identified during 24/4-26/4, middle of May and the last ten days of June (period of the parametric test). However, the model exhibits different performance characteristics from station to station during these events; for example MAB in KRIN station is showing a distinct continuous peak which is not apparent in the neighbouring KOUN or KALA stations during 24/4-26/4, indicating possible localised phenomena which are not adequately re-produced by the model.

Bias range is again satisfactory during S2 in most stations, with an average 62% of σ falling between π and –π (Table 6.4). Outlying values of σ are again mostly distributed below the lower limit (–π), but there are a few instances (2% of the total number of observations) where the model produces higher ZTDs compared to the GNSS solution.

Table 6.4: σ values within error range – S2

Code	Elevation ASL (m)	Ratio of σ above π (28mm)	Ratio of σ below –π (-28mm)	Ratio of σ between π and –π
ANOC	1020	<0.01	0.53	0.47
ARSA	115	0.02	0.30	0.68
AIGI	142	0.02	0.35	0.63
GALA	33	0.02	0.40	0.58
EYPA	166	0.01	0.36	0.63
KALA	716	0.02	0.19	0.79
KOUN	564	0.02	0.27	0.71
KRIN	758	0.01	0.34	0.65
LAMB	10	0.03	0.25	0.72
LIDO	550	0.03	0.24	0.73
MESA	477	<0.01	0.44	0.56
MESO	2	0.02	0.39	0.59
PAT0*	91	0.01	0.52	0.47
PSAR	55	0.02	0.29	0.69
PSAT	19	<0.01	0.56	0.44
ROD3	452	<0.01	0.24	0.76
TRIZ	25	0.01	0.43	0.56
VALI	9	0.03	0.26	0.71
XILI	4	<0.01	0.58	0.42

* Metrics for PAT0 station correspond to the CRL tropospheric solution

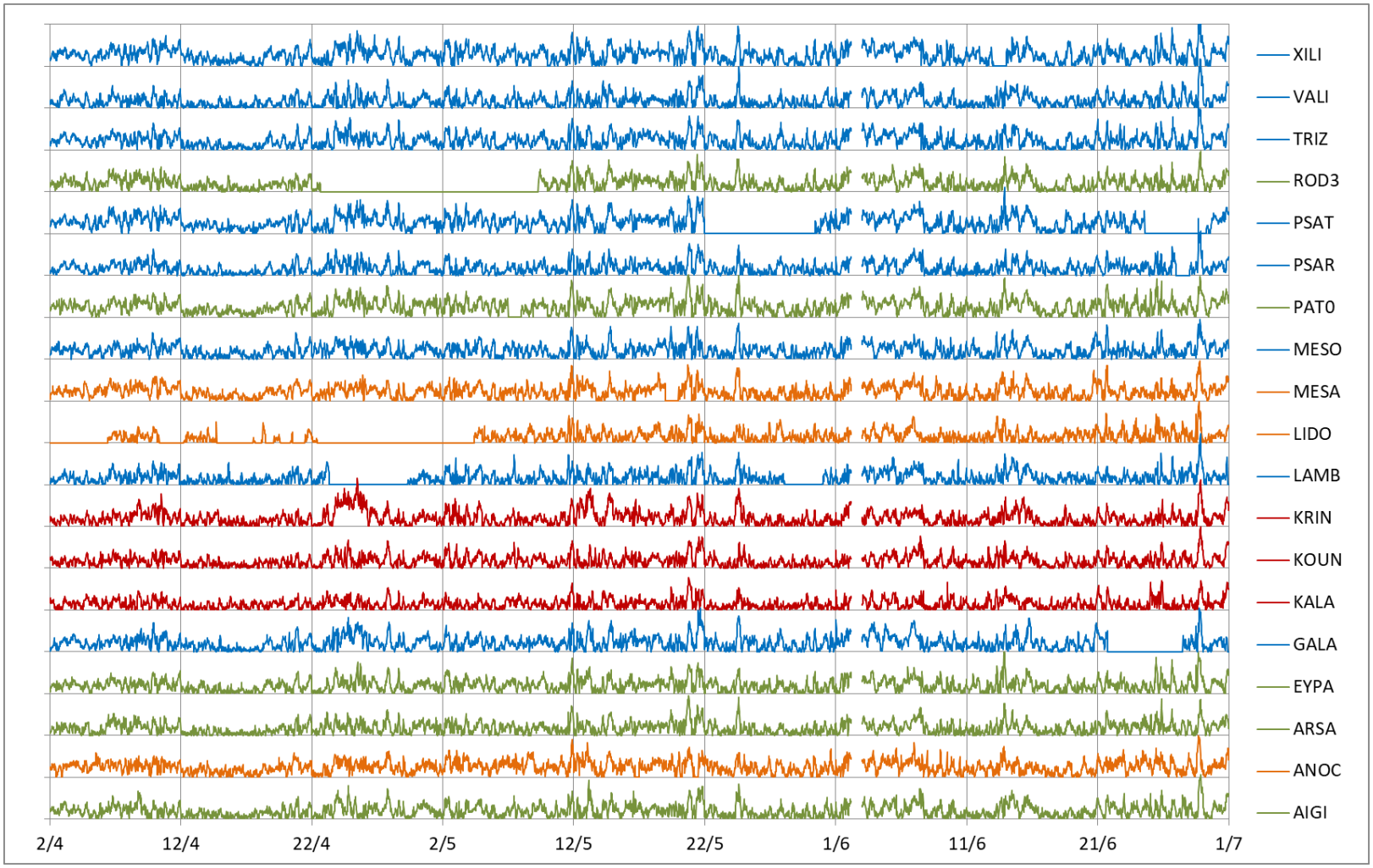

Figure 6-7: Absolute bias plot for all stations, season S2. Colours indicate terrain type: Coastal – blue; inland – green; upland north – orange; upland south – red. Values are shifted by 100mm for better readability.

6.2.3 Results for S3 (July-September 2016)

The summer season is characterised by more frequent events of model de-correlation (r=0.83) and a larger MAB. Events of increased model "noise" are identified (i.e. 2/7, 8/8-9/8, 8/9-13/9, 19/9-20/9), with WRF producing higher ZTD differences in some stations than others (e.g. MESO 3/8 and 12/8) possibly as a result of localised weather patterns. However, the model globally seems to produce a consistent output throughout the study area.

The bias distribution during S3 is less satisfactory than S1 and S2, with an average 57% of σ falling between π and –π (Table 6.5). Outlying values of σ are again mostly distributed below the lower limit (–π), but in some stations (e.g. MESO and LIDO) a higher frequency of positive WRF bias is observed.

Table 6.5: σ values within error range – S3

Code	Elevation ASL (m)	Ratio of σ above π (23mm)	Ratio of σ below –π (-23mm)	Ratio of σ between π and –π
ANOC	1020	<0.01	0.51	0.49
ARSA	115	0.02	0.36	0.62
AIGI	142	0.02	0.40	0.58
GALA	33	0.01	0.42	0.57
EYPA	166	0.01	0.43	0.56
KALA	716	0.02	0.24	0.74
KOUN	564	0.01	0.35	0.64
KRIN	758	0.01	0.35	0.64
LAMB	10	0.03	0.29	0.68
LIDO	550	0.04	0.21	0.75
MESA	477	0.01	0.51	0.48
MESO	2	0.05	0.41	0.54
PAT0*	91	0.01	0.55	0.44
PSAR	55	0.02	0.34	0.64
PSAT	19	<0.01	0.54	0.46
ROD3	452	0.01	0.52	0.47
TRIZ	25	0.01	0.47	0.52
VALI	9	0.02	0.32	0.66
XILI	4	<0.01	0.57	0.43

* Metrics for PAT0 station correspond to the CRL tropospheric solution

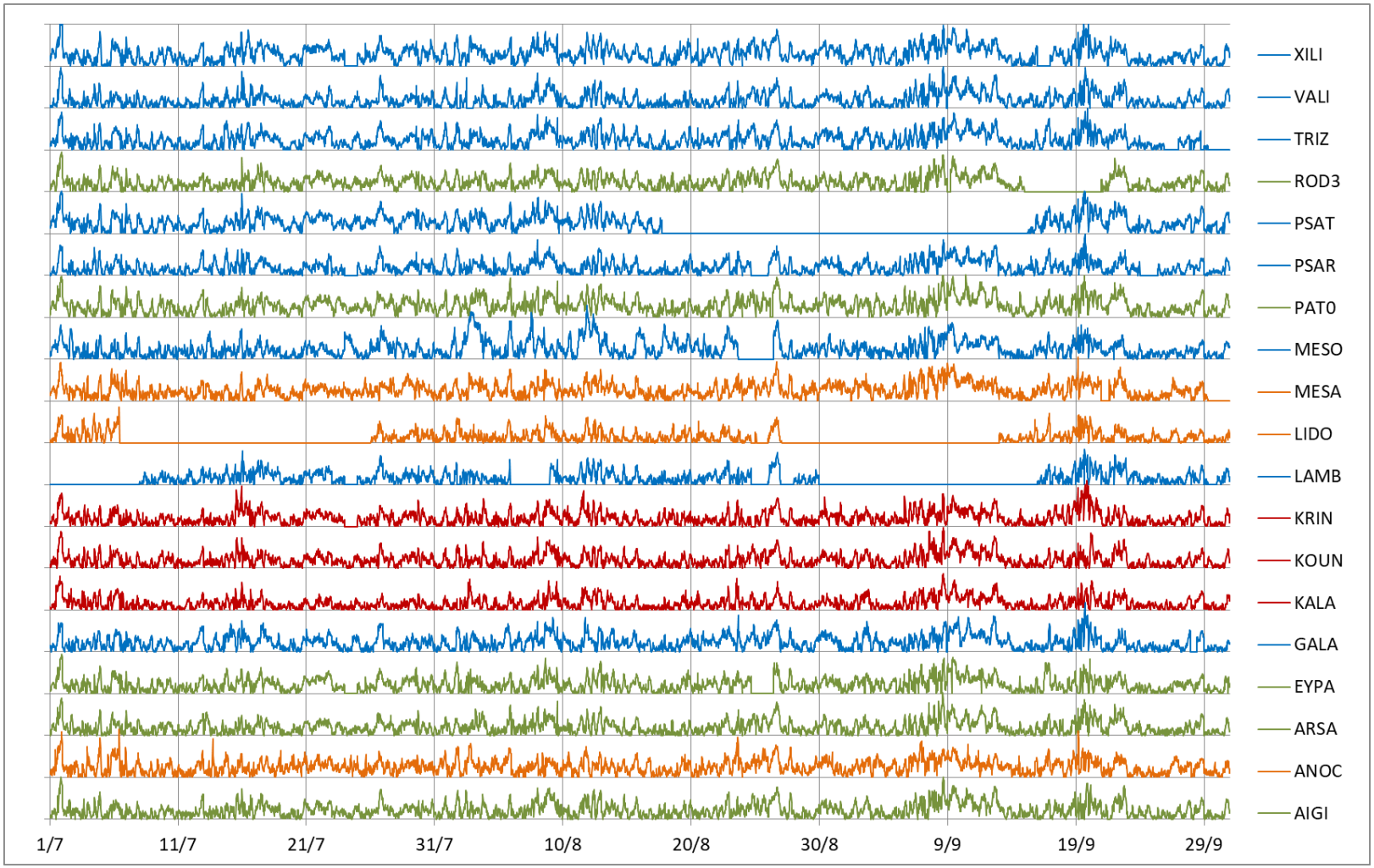

Figure 6-8: Absolute bias plot for all stations, season S3. Colours indicate terrain type: Coastal – blue; inland – green; upland north – orange; upland south – red. Values are shifted by 100mm for better readability.

6.2.4 Results for S4 (October-December 2016)

S4 is the period with the best model performance, characterised by small MAB (20.5mm) and a lower frequency of "noisy" events (13/10, 14/11-15/11). MAB is particularly low during the second half of November and December, as a result of colder weather and drier than usual conditions in western Greece. A small negative WRF bias is again present across all stations, with the model globally producing a consistent output.

Bias range is satisfactory, with an average 63% of σ falling between π and –π (Table 6.6). Similarly to S1, outlying values of σ are mostly distributed below the lower limit (–π), indicating that the model globally tends to underpredict ZTD.

Table 6.6: σ values within error range – S4

Code	Elevation ASL (m)	Ratio of σ above π (23mm)	Ratio of σ below –π (-23mm)	Ratio of σ between π and –π
ANOC	1020	<0.01	0.43	0.57
ARSA	115	0.01	0.29	0.70
AIGI	142	<0.01	0.34	0.66
GALA**	33	-	-	-
EYPA	166	<0.01	0.39	0.61
KALA	716	0.01	0.14	0.85
KOUN	564	<0.01	0.34	0.66
KRIN	758	<0.01	0.28	0.72
LAMB	10	<0.01	0.26	0.74
LIDO	550	0.01	0.21	0.79
MESA	477	<0.01	0.45	0.55
MESO	2	<0.01	0.37	0.63
PAT0*	91	<0.01	0.55	0.45
PSAR	55	<0.01	0.27	0.73
PSAT	19	<0.01	0.59	0.41
ROD3	452	<0.01	0.46	0.54
TRIZ	25	<0.01	0.42	0.58
VALI	9	<0.01	0.27	0.73
XILI	4	<0.01	0.52	0.48

* Metrics for PAT0 station correspond to the CRL tropospheric solution

** Less than 50% values

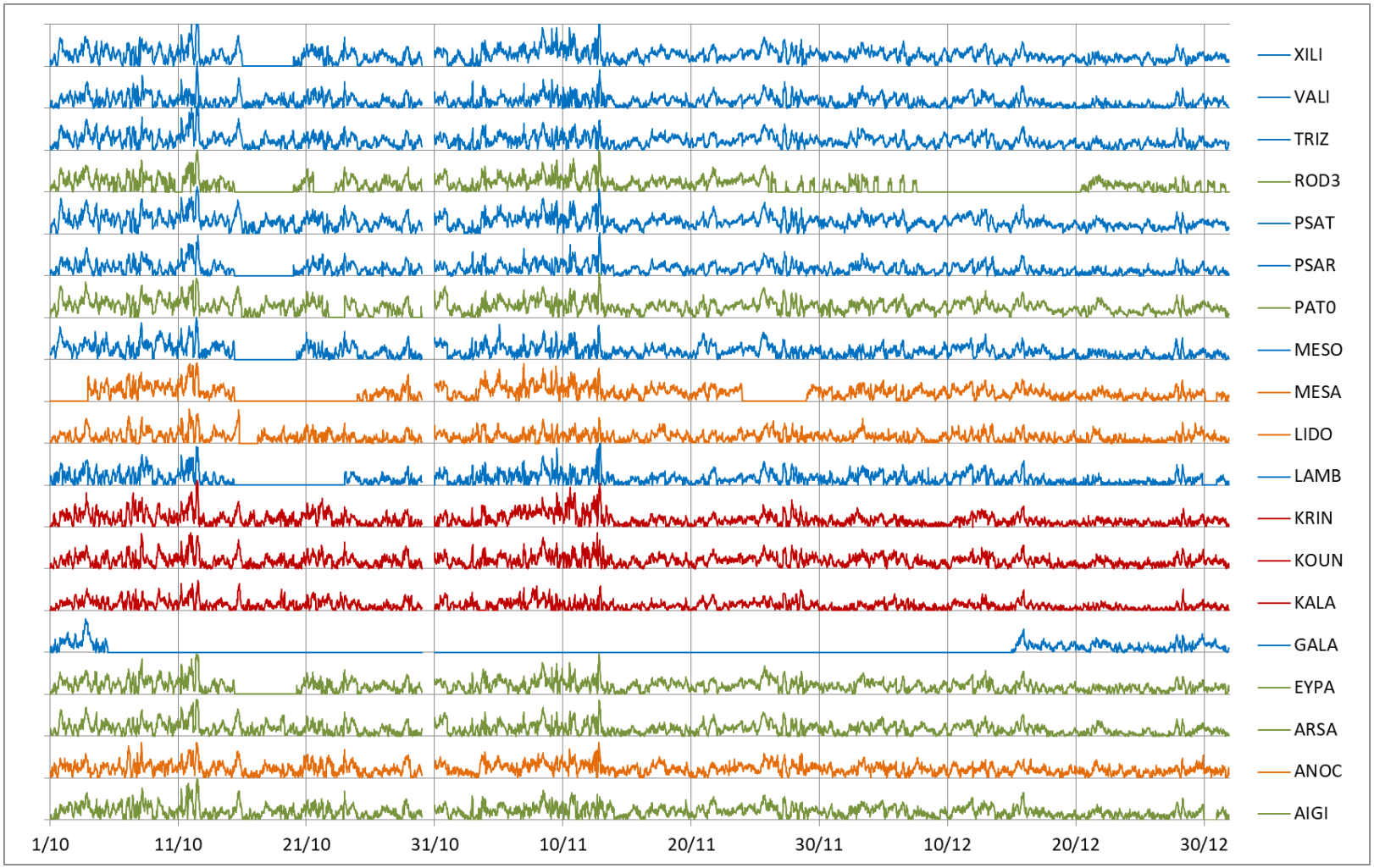

Figure 6-9: Absolute bias plot for all stations, season S4. Colours indicate terrain type: Coastal – blue; inland – green; upland north – orange; upland south – red. Values are shifted by 100mm for better readability..

6.3 Comparison of Different Tropospheric GNSS Processing Protocols at PAT0 Station

PAT0 is a reference GNSS station located at the premises of the University of Patras. The station belongs to the EUREF Permanent Network (EPN, http://www.epncb.oma.be), which follows a different tropospheric processing protocol than CRL, combining solutions from various institutions using different software and mapping functions. In this section, a combined analysis of CRL and EUREF GNSS solutions vs. WRF MOD5 is performed for the year 2016:

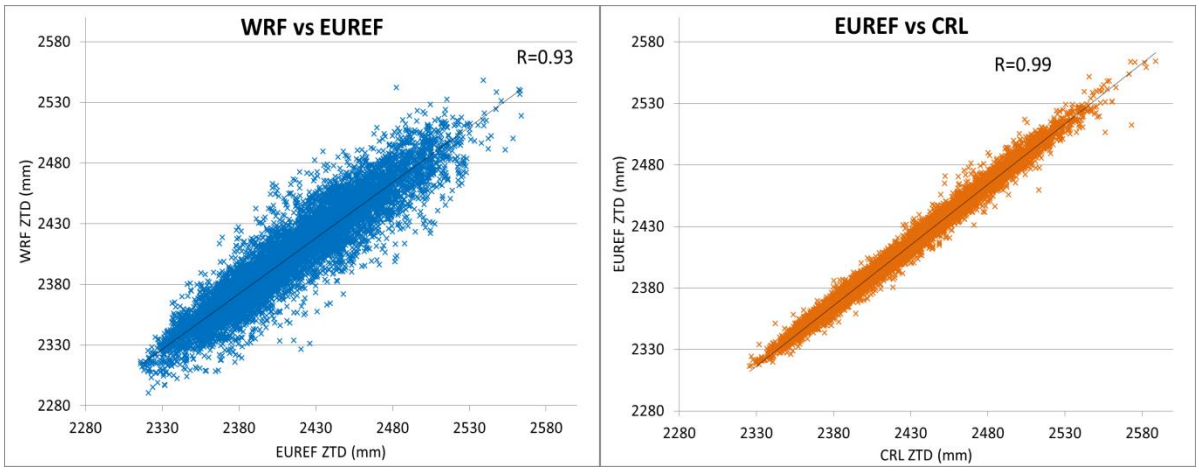

Figure 6-10: Correlation plots of WRF vs. EUREF and EUREF vs. CRL ZTDs at PAT0 station, for the entire year.

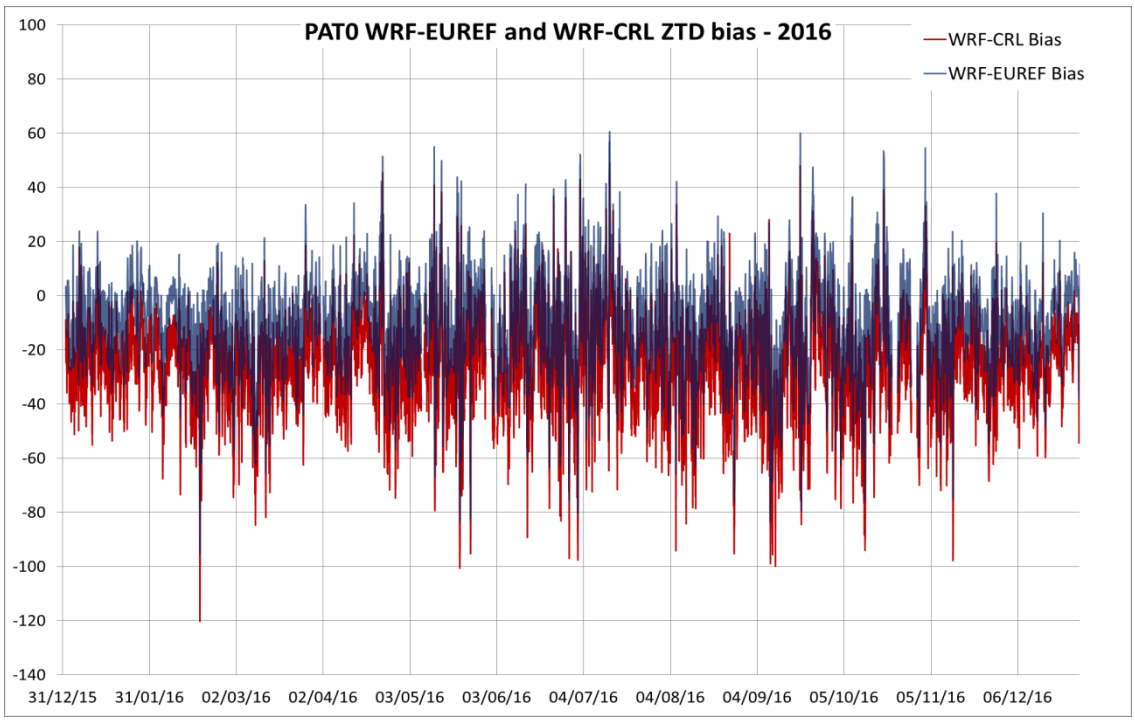

Figure 6-11: Bias plots of WRF vs. EUREF and WRF vs. CRL ZTDs at PAT0 station, for the entire year

Table 6.7: σ values within error range – WRF vs. PAT0 EUREF solution

Code PAT0	Ratio of *σ* above π (23mm)	Ratio of *σ* below –π (-23mm)	Ratio of *σ* between π and –π
S1	<0.01	0.17	0.83
S2	0.03	0.20	0.77
S3	0.03	0.24	0.73
S4	0.01	0.20	0.79

Table 6.8: Comparison of seasonal statistical indices of WRF vs. EUREF and WRF vs. CRL ZTD time series –2016

Season	S1			S2			S3			S4		
	|σ|	RMSE	PCC	|σ|	RMSE	PCC	|σ|	RMSE	PCC	|σ|	RMSE	PCC
PAT0 CRL solution	26.0	29.4	0.88	26.1	30.4	0.88	28.6	33.1	0.82	26.4	30.4	0.93
PAT0 EUREF solution	13.2	17.4	0.88	15.4	19.6	0.90	17.4	22.3	0.84	14.8	19.0	0.93
improvement	**51%**	**40%**	**-**	**40%**	**35%**	**2%**	**39%**	**33%**	**2%**	**44%**	**37%**	**-**

General remarks:

- The correlation between WRF and GNSS is marginally stronger in S2 and S3. MAB and RMSE however are significantly smaller for all periods, with the offset between the two datasets being reduced by 43% on average when the EUREF solution is used (Table 6.8).
- As a result, the ratio of predicted and observed ZTD pairs within the 2π bias range has increased to 78% as opposed to 45% with the CRL solution (Table 6.7).
- Results seem to confirm that a tropospheric solution of GNSS data without the use of a mapping function introduces a small positive offset to the ZTD time-series, possibly due to the calculation of the elevation-dependent a priori ZHD term.
- The Corinth Rift Laboratory provides two sets of ZTD tropospheric solutions from its network of GNSS stations in western Greece. The first set uses the GPT2 mapping function but includes a fewer number of stations (7 in total), whereas the second set is provided with static tropospheric processing and no mapping function, including all 19 stations of the network. In the current study, It was intended: a) to use a simple set of parameters in order to compare the WRF model output with a geometrical GNSS calculation which does not assimilate data from external sources; b) to process data from a large number of GNSS stations, so that a representative sample is used for performing the WRF parametric tests and the seasonal model validation. Therefore, it was decided to use a GNSS ZTD dataset without a mapping function, which as we have discussed here, introduces a small bias due to the a priori calculation of ZHD, but is consistent in terms of correlation with GNSS ZTD data processed with GPT2. Since this bias is differentiated in the analysis of InSAR tropospheric correction, the effect on the results (e.g. in calculating Δbias) is minimized.

6.4 Uncertainty and Sources of Error in High-Resolution WRF vs. GNSS Derived ZTDs

High-resolution modelling with WRF down to a horizontal grid spacing of 1 km provides an increased resolvability of mesoscale atmospheric processes, such as cloud convection and orographically induced flow phenomena (gap winds, lee rotors, wake vortices etc.), and therefore reduces dependency on empirical physics parameterizations which contribute to the uncertainty of the model. However, the accuracy of mesoscale NWP models is still constrained by a number of factors [Pielke et al., 2013], including:

a) Necessary physical parameterizations modelling boundary layer and land surface mechanics, radiative transfer, moisture phase change and other subgrid-scale processes which are not explicitly resolved at the 1-km scale [Nunalee et al., 2015]. As high-resolution modelling was only recently enabled with the development of high performance computing systems, many parameterization schemes used were developed for coarse resolutions, introducing significant bias to model output. In the current study, a parametric analysis was performed, using different physical parameterizations, from simple to relatively complex schemes suitable for high-resolution scenarios, in order to determine the configuration with the best forecasting skill and minimise bias.

b) Errors associated with inaccurate or unrepresentative atmospheric boundary conditions introduced from GAMs, the unphysical treatment of lateral boundary conditions and inconsistencies in the dynamics and physics between the global and regional models [Kryza et al., 2016]. Advanced data assimilation techniques which are currently available, can enhance the regional model initialization and minimise simulation bias [Ancell et al., 2011; Pu et al., 2013]. In the current high-resolution WRF re-analysis, boundary conditions for the model initialization were taken from the ERA-Interim global climate re-analysis database [ECMWF], with a 75 km horizontal resolution, 35 vertical layers and 6h temporal resolution. As new improved high-resolution datasets are becoming available worldwide every year (ERA-5 is the next to be released by ECMWF with a spatial resolution of 30 km and temporal resolution of 1h), it is anticipated that these errors will be partially eliminated.

c) The selection of the static terrain elevation dataset, which can result in under-resolved terrain features if it is not properly adjusted to the model's spatial resolution. High-resolution simulations are sensitive to orographic forcing, particularly in the lower troposphere (atmospheric boundary layer), and it has been demonstrated that terrain height discrepancies introduced by a coarse underlying DEM can introduce significant bias in modelling solutions of low-level wind or water vapour fields [Jimenez et al., 2010; Zhang et al., 2014; Nunalee et al., 2015]. In the current study, a high-resolution DEM (ASTER 1" global GDEM v2), with a grid of 30 m was introduced instead of the default GTOPO30 DEM (900 m grid), for the inner domain (d04), which resulted in some reductions of the mean bias of predicted vs. observed (GNSS derived) ZTD values.

At the same time, there are uncertainties associated with the observational GNSS dataset used for the validation of high-resolution re-analysis solutions and the calculation method used for deriving ZTD values, both from the GNSS and the WRF data. As discussed in Section 6.3, the use of different tropospheric processing protocols (depending on the settings of the software used and the

application of different mapping functions) can result in slightly different solutions with regards to the calculation of ZTD values. Moreover, the zenith tropospheric delay in PPP applications is estimated geometrically, from combining and analysing slant signal paths between each satellite and the receiver, therefore the result can differ from ZTDs derived from vertically aligned meteorological variables of WRF output (for the "wet" term). Finally, elevation differences *dh* between GNSS station and nearest WRF grid point can affect the calculation of the corresponding ZTDs, as we have already seen, especially at higher terrain heights. This discrepancy was corrected by vertically interpolating the WRF output parameters and calculating ZTDs at the same elevation as the GNSS receiver, as described in Section 4.2.

6.4.1 A Case of WRF vs. GNSS De-correlation and Comparison with Meteorological Surface Data

We investigate a case where the model output shows significant deviation with respect to the observational GNSS dataset. The time period selected corresponds to the period of the parametric analysis (i.e. second half of June 2016, and particularly the 28th of the month), where bias between WRF and GNSS ZTDs reached values of 120 mm at some stations. An attempt is made to establish possible reasons for the failure of the model, by evaluating the model output, in terms of the three meteorological variables included in the ZTD calculation, against surface data provided by the National Observatory of Athens' METEO weather station network (http://www.meteo.gr).

The analysis focuses on three locations (KALA, ANOC and PAT0) where automatic weather stations of the METEO network are installed within a very close range from corresponding GNSS stations of the PaTrop network (less than 1 km), thus minimising bias due to excessive distance between the points. In Figures 6-12 – 6-14, the variance of WRF ZTDs vs. GNSS ZTDs (top graph), WRF vs. METEO surface temperature *Ts* and surface relative humidity *RH* (middle graph), and WRF vs. METEO surface pressure at sea level *Ps* plus observed wind distribution from METEO (bottom graph), at 30 min intervals, are illustrated for the three locations. Although measurements of water vapour pressure and air temperature in the vertical tropospheric column (which would allow for a thorough examination of ZWD discrepancies) are not available, surface data still give us an indication of possible failure mechanisms:

- In all three stations (and most of other PaTrop stations see Section 5.3.1), WRF ZTD exhibits a "drop" during the afternoon and evening of June 28th which is not apparent in the GNSS ZTD, with bias reaching 120mm in stations at sea level elevation. In ANOC this drop seems to follow the WRF surface water vapour "signal" whereas in KALA and PAT0 there is no such indication. Examining surface pressure variations, a more profound differentiation between observed and predicted values is exhibited in all stations, with WRF P_s dropping when the observed P_s keeps rising. It is noted that even small errors in P_s can have a large impact on total ZTD, as ZHD constitutes about 90% of the total tropospheric delay. It is possible that a combination of "poor" P_s prediction due to an error in boundary conditions ingested by the model and a misrepresentation of the vertical water vapour profile resulted in the model failing at this instance.

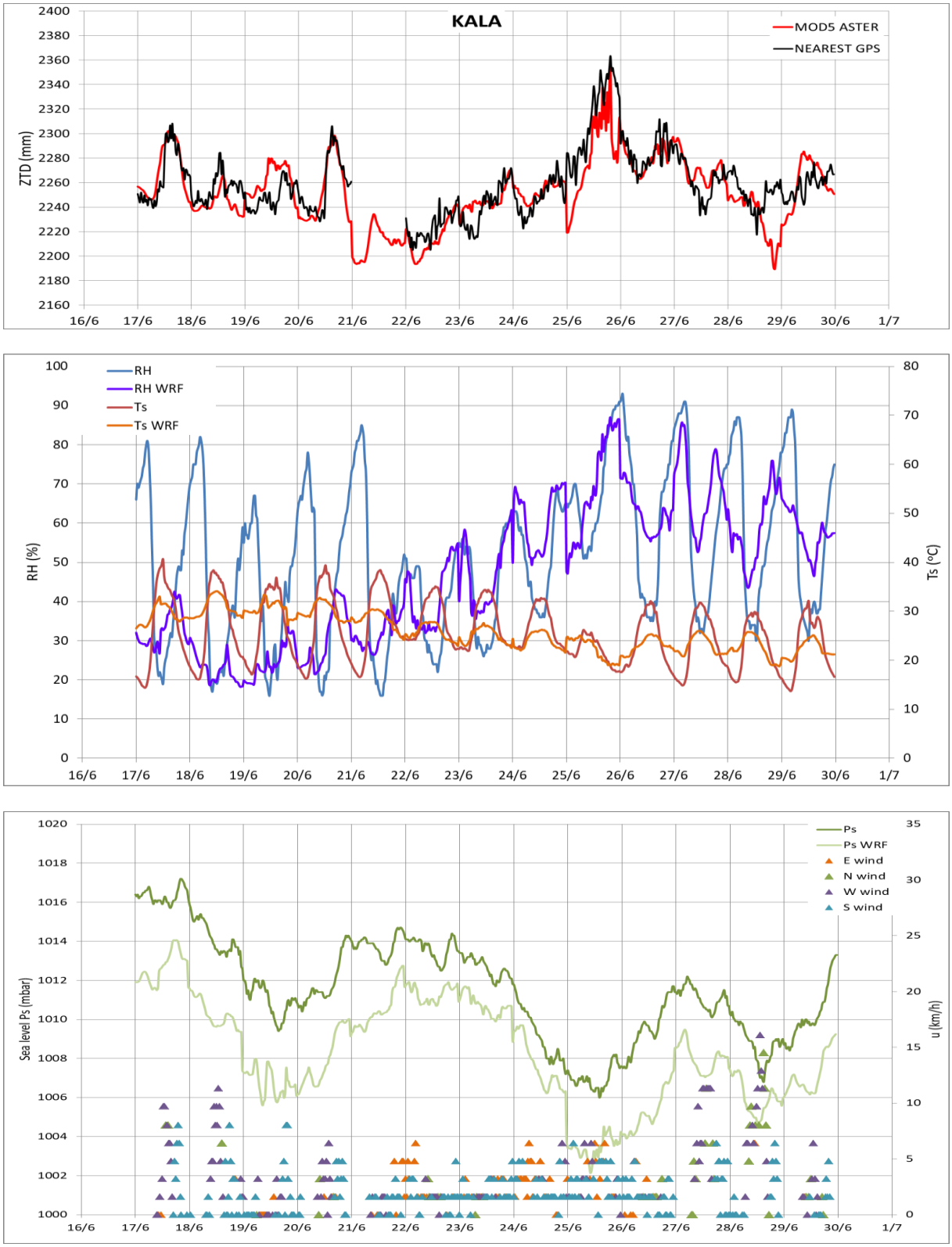

Figure 6-12: Graph of WRF vs. GNSS ZTD time series (top); graph of WRF vs. METEO surface temperature *Ts* and surface relative humidity *RH* (middle); graph of WRF vs. METEO surface pressure at sea level *Ps* plus observed wind distribution (bottom). KALA station.

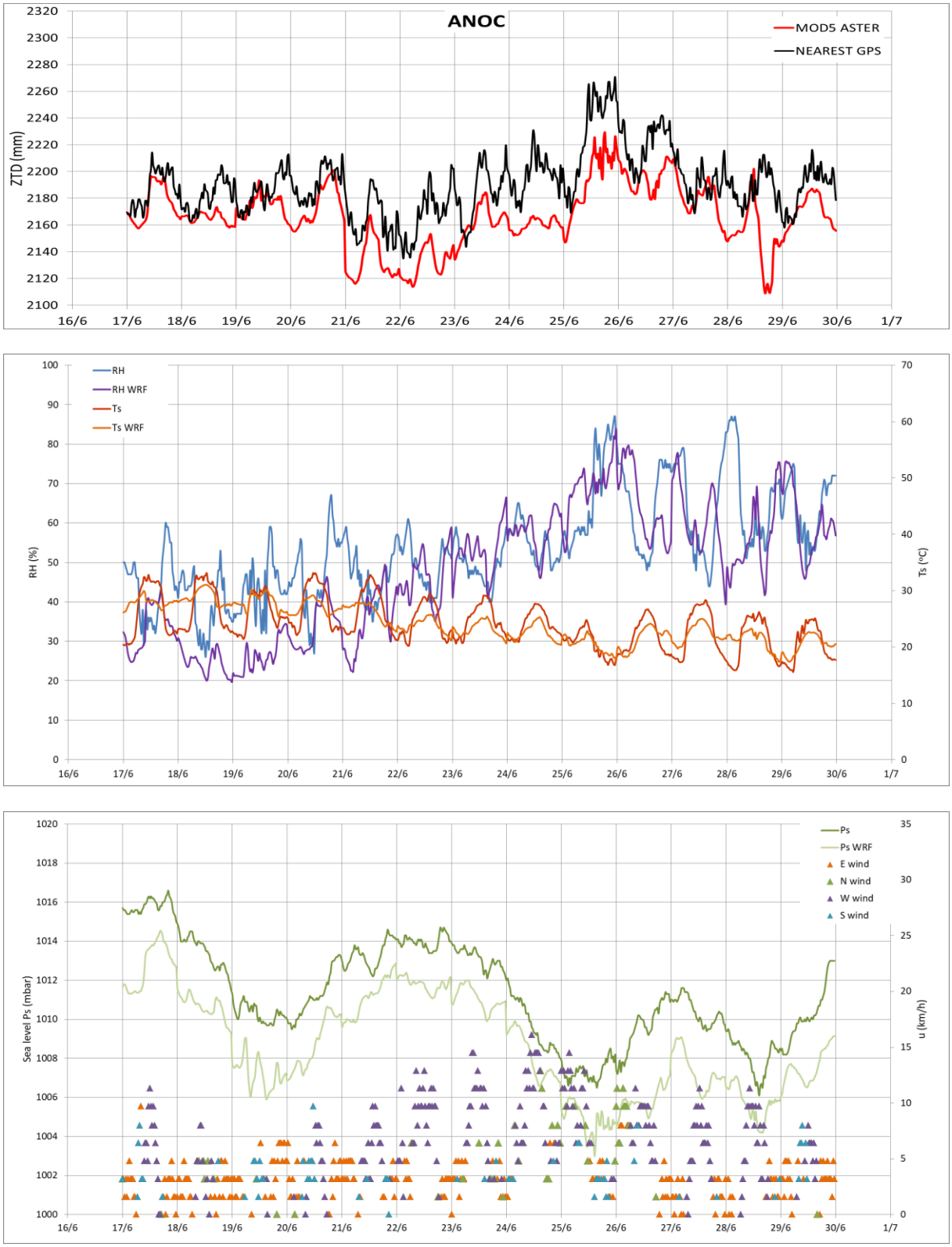

Figure 6-13: Graph of WRF vs. GNSS ZTD time series (top); graph of WRF vs. METEO surface temperature *Ts* and surface relative humidity *RH* (middle); graph of WRF vs. METEO surface pressure at sea level *Ps* plus observed wind distribution (bottom). ANOC station.

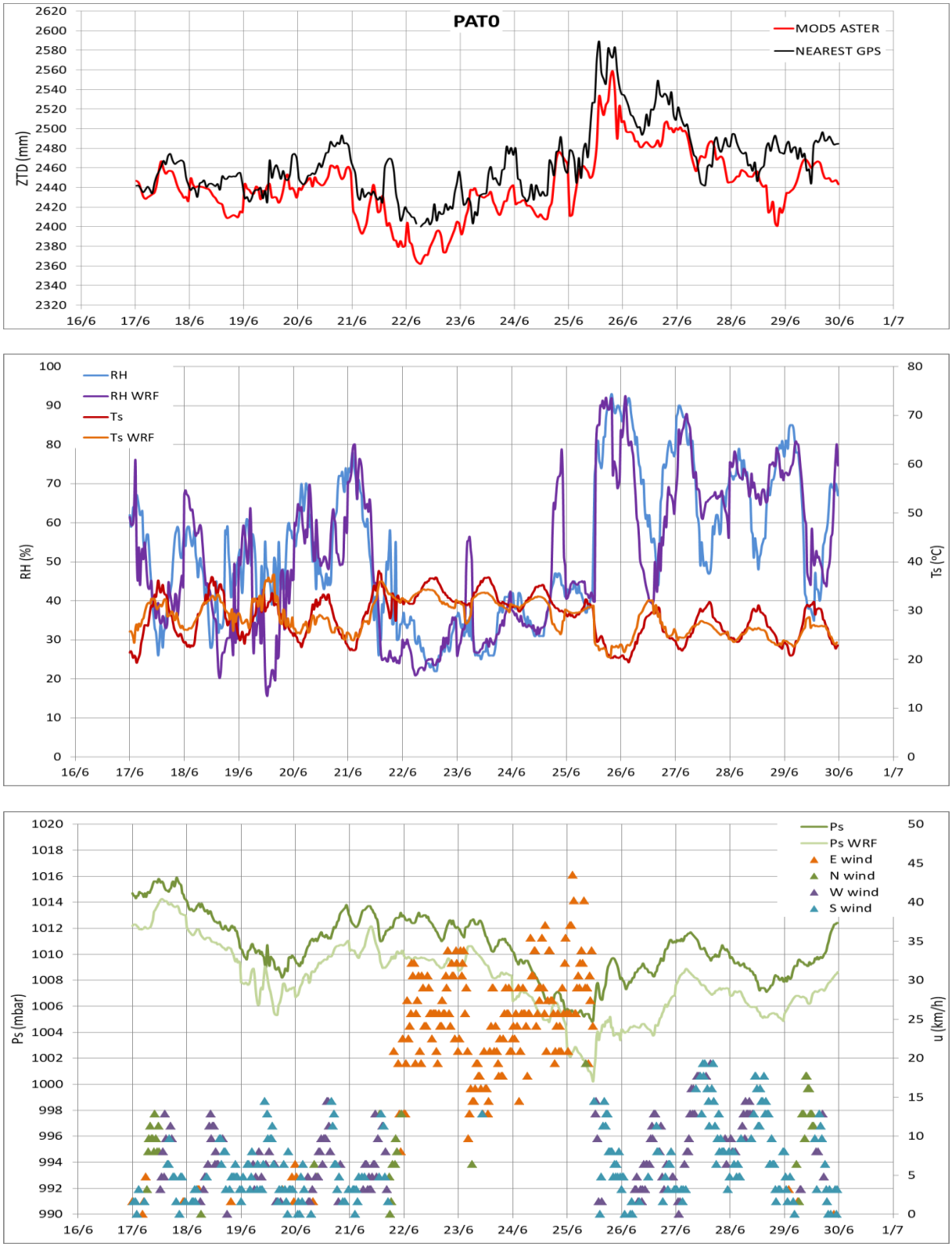

Figure 6-14: Graph of WRF vs. GNSS ZTD time series (top); graph of WRF vs. METEO surface temperature *Ts* and surface relative humidity *RH* (middle); graph of WRF vs. METEO surface pressure at sea level *Ps* plus observed wind distribution (bottom). PAT0 station.

- A second abrupt “drop” of the WRF ZTD appears during the first hours of June 25th (more prominent in KALA and PAT0). Again, this is mostly due to a corresponding drop of the predicted P_s which is a result of unrepresentative boundary conditions.
- More subtle fluctuations are caused by differences in the surface water vapour signal in the two time series. For example, in PAT0, WRF RH peaks (23/6 morning, 24/6 night, 27/6 midday) which overestimate the surface measurements are also evident in the ZTD time series. Similar differences are observed in ANOC and KALA (21/6 morning, 27/6 evening and 28/6 morning).
- Surface water vapour fluctuations which the model fails to reconstruct do not always reflect in ZTDs. A good example is KALA, where during the period 17/6-21/6, the model systematically fails to simulate the “moist” surface conditions during night time. However WRF-GNSS ZTD bias during the same period is small and this is possibly explained by a more consistent water vapour model re-analysis in the vertical column. Figures 6-15 and 6-16 illustrate the water vapour mixing ratio at eta levels 6 and 11 (approx. 0.7 and 2 km above surface), as calculated by the WRF re-analysis in 3h windows, starting on 28/6 and 00:00. The high spatial and temporal variability of water vapour distribution in the lower troposphere is demonstrated.

6.5 Concluding Remarks

Following the configuration and physical parameterization of the WRF model, based on a short-scale sensitivity analysis, the optimal scheme (MOD5 with ASTER 1s topography) is selected for the whole PaTrop period (January-December 2016), and model output is validated with the use of observational tropospheric data from the CRL GNSS network in the Western Gulf of Corinth.

The statistical analysis demonstrates that the correlation between predicted and observed ZTDs at the 19 stations is good throughout the year (correlation co-efficient ranges from 0.91-0.93), with mean bias (MB) ranging from -11.1 mm (KALA station) to -28.2 mm (PSAT station), indicating that the model tends to slightly underestimate the tropospheric ZTD as compared to the GNSS derived values. A further analysis of statistical indices reveals that this systematic negative offset (of the order of 15 mm) is caused by uncertainties in the model output, as well as uncertainties during processing of the tropospheric GNSS data.

With respect to the seasonal component, model performance is better during the autumn period (October-December), followed by the spring period (April-June). Correlation with the observed ZTD timeseries is high at all stations (correlation co-efficient is 0.93 and 0.88 respectively) and MAB and RMSE values are low. On the contrary, model forecasting skill seems to deteriorate during summer (July-September), where correlation is weaker (PCC=0.83) and MAB and RMSE values are higher (average MAB=22.8, RMSE=28.0). Setting the bias range at ±23 mm (equal to the amplitude of one Sentinel-1 C-band phase cycle when projected to the zenithal distance), it is demonstrated that the model produces satisfactory results, with a percentage of ZTD values within the bias margin ranging from 57% in summer το 63% in autumn.

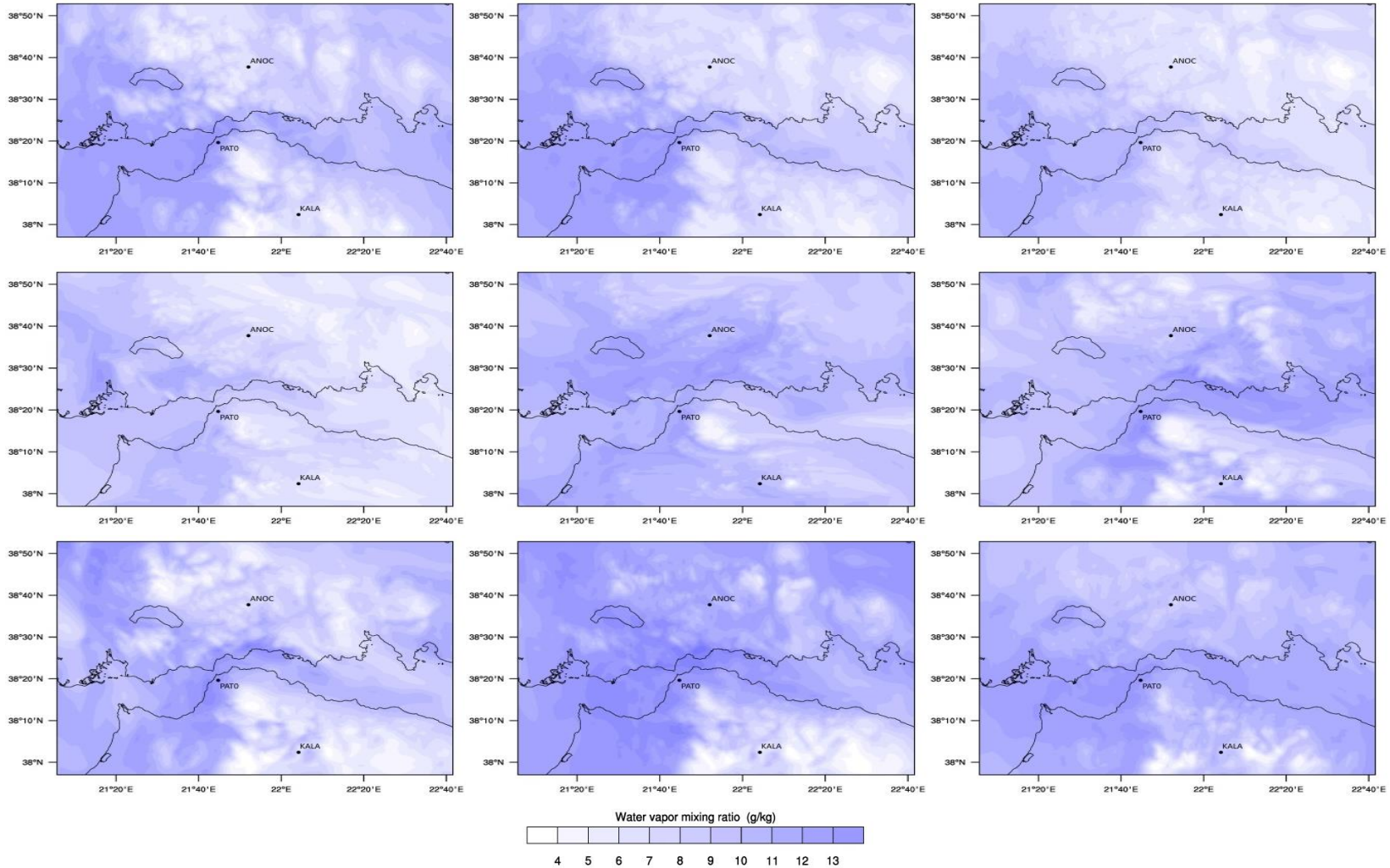

Figure 6-15: Maps of water vapour mixing ratio at eta level 6 (approx. 0.7 km above surface), as calculated by the WRF re-analysis in 3h intervals, starting on 28/6 and 00:00. Stations KALA, ANOC and PAT0 where surface data are available, are shown.

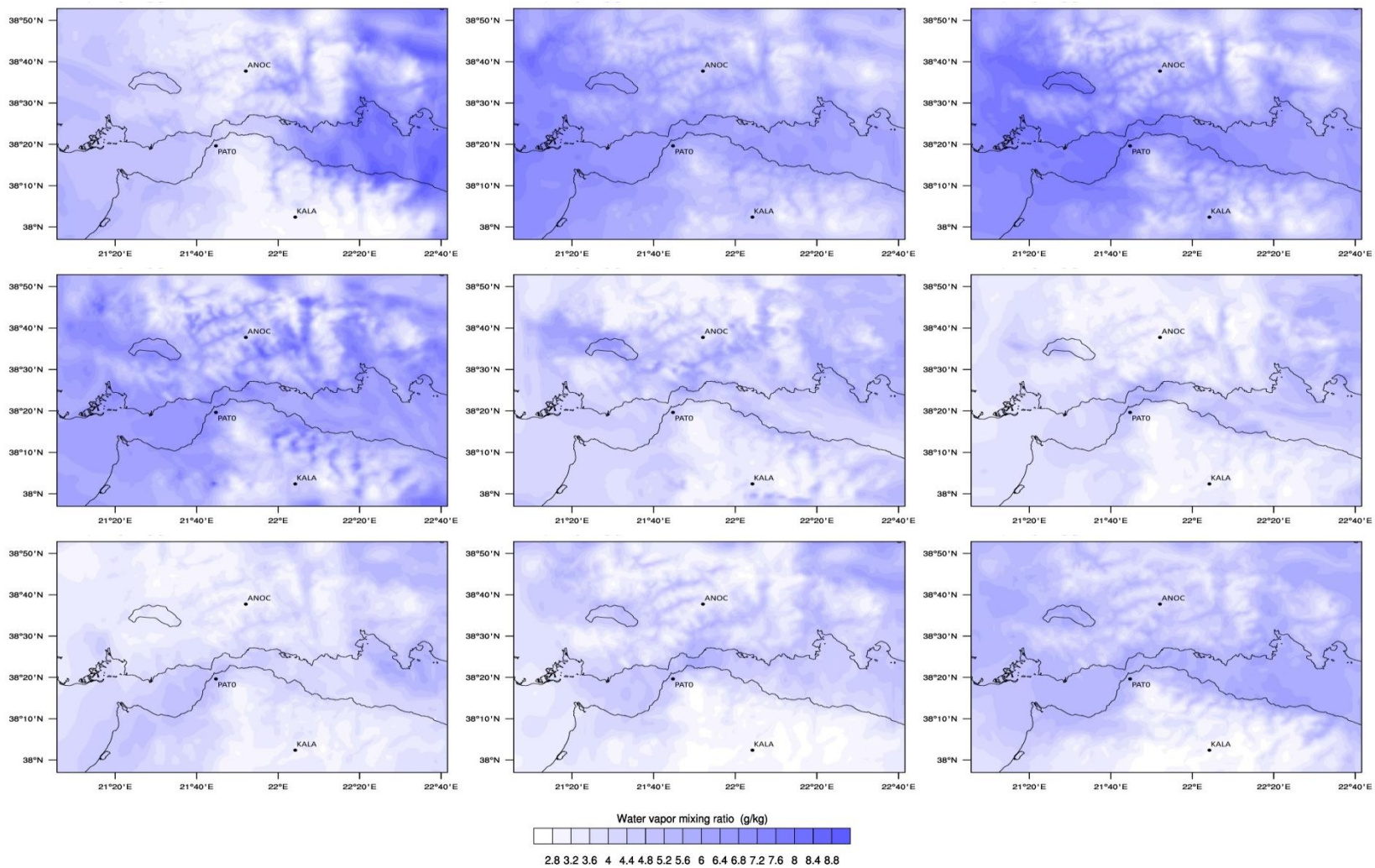

Figure 6-16: Maps of water vapour mixing ratio at eta level 11 (approx. 2 km above surface), as calculated by the WRF re-analysis in 3h intervals, starting on 28/6 and 00:00. Stations KALA, ANOC and PAT0 where surface data are available, are shown.

Examining possible model failure mechanisms, WRF output was validated with independent meteorological data from a network of ground stations in the PaTrop area. The analysis focused on three locations (KALA, ANOC and PAT0) where automatic weather stations are installed within a close range from corresponding GNSS stations. A case where model output shows significant deviation with respect to the observational GNSS dataset is investigated (i.e. second half of June 2016, and particularly the 28th of the month). Data analysis demonstrates that for the selected time period, large ZTD biases are mainly caused by "poor" surface pressure prediction due to errors in boundary conditions ingested by the model, whereas smaller (and more frequent) ZTD biases are caused by a misrepresentation of the vertical water vapour profile by the model. The analysis would further benefit from using integrated water vapour measurements in the vertical tropospheric column (IWV values) from remote sensing spectrometers (i.e. MERIS and MODIS), for studying 3-D water vapour fluctuations as estimated by the model.

7. InSAR Tropospheric Correction with the use of WRF Derived Delay Maps

7.1 Introduction

The overall aim in this chapter is to perform tropospheric corrections in interferometric synthetic aperture radar (InSAR) observations by calculating precise tropospheric delay (ZTD) fields over the PaTrop study area with the use of a high-resolution model of the troposphere (WRF). This methodology has the advantage of providing detailed simulated ZTD fields at the 1 km scale at the exact times of SAR acquisitions, and is supported by the tropospheric delay calculated at the GNSS sites, which are used as reference data for fine-tuning and validation of the model.

A number of empirical and predictive methods are currently being employed for the tropospheric correction of the atmospheric phase screen (APS) in InSAR interferograms, as already discussed in detail in Section 2.3.2, each with its strengths and limitations. The atmospheric phase screen constitutes a major noise contribution in differential interferometry (DInSAR) in particular, where the ground deformation signal is frequently "masked" by tropospheric fringes. The main component of the atmospheric phase delay is the temporal variation of the stratified troposphere (i.e. the "dry" term), which is proportional to surface pressure, a variable with a typical daily variability of 0.1 – 0.2% at the scale of an interferogram, and maximum of 0.5% [Yun et al., 2015]. Thus, it is a term which can be predicted empirically or from surface measurements, as it is correlated to the topography. However, these long wavelength stratified atmospheric signals are not easily discriminated from the ground movement signal in cases where topography and deformation are correlated [Beauducel et al., 2000], as the resulting phase patterns can coincide with the local topography. A second component is the turbulent atmospheric delay (i.e. the "wet" term), which spatially as well as temporally is much more variable than the stratified component. This short wavelength signal is correlated to the water vapour content of the lower troposphere, and can exhibit a daily variability of 50% – 100% within a few kilometres (especially in areas of steep or complex topography). Therefore, it cannot be estimated with the desired accuracy, unless a precise high-resolution 3D water vapour field can be derived from remote sensing measurements or locally applied high-resolution NWP models. Problem is more profound in single interferograms as stacking can remove this partially – considers random the turbulence is space and time.

The InSAR community has recently taken great interest in the application of NWP models as a tropospheric correction method, as it can successfully tackle many of the aforementioned challenges. High-resolution tropospheric modelling is particularly useful in the case of single interferograms, where the removal of the atmospheric phase screen (and especially the turbulent component) can reveal large-amplitude deformation signals (as in the case of an earthquake). In the western Gulf of Corinth, complex topography (i.e. land-sea contrasts, mountainous terrain) makes the removal of both the stratified and turbulent atmospheric phase screens a challenging task. By applying a high-resolution model, locally configured, and by validating the results with measurements from a dense network of permanent GNSS stations, it is envisaged that the proposed

methodology will provide a valuable tool for removing the atmospheric effect and improving overall the quality of InSAR observations in the PaTrop area.

7.2 Methodology

Output data from a high-resolution 1-km WRF re-analysis are used to calculate precise ZTD fields over the Patrop study area, at the exact times of Sentinel-1 SAR acquisitions for the ascending track 175 and descending track 80 (i.e. 1630 and 0430 UTM respectively). The setup and parameterization of the model is the one described in detail in Chapters 5 and 6 (MOD5 scheme with high-resolution ASTER 1s topography), with four nested domains, (27, 9, 3 and 1 km horizontal resolution) as illustrated in Figure 5-1, and a vertical discretization of 45 levels up to a height of 20 km. The model was initialised with boundary conditions from the ERA-Interim database, at 1800 UTC, producing 30 h simulations, with the first 6 h being spin-up time. Resulting Zenith Total Delay (ZTD) values calculated from specific model output parameters (surface pressure, air temperature and water vapour profiles) are validated against a dataset of GNSS derived ZTD values, providing point measurements at the 19 points where the stations are located.

Sentinel-1 SAR data were used in this study for the generation of InSAR interferograms, for 2016. The two ESA Sentinel-1 satellites (S1A and S1B) have a 6-day repeat time, and carry a C-band synthetic aperture radar with a 56 mm wavelength and four operating modes. Acquisitions with a 5x20 m resolution in the Interferometric Wide (IW) mode were used. In total, 19 acquisitions were combined to produce 9 interferograms for the ascending (S-N) track 175, and 11 interferograms for the descending (N-S) track 80. Temporal baselines ranged from 6 days to 42 days and perpendicular baselines were in the order of 150 m. Multilook was 6 in range and 2 in azimuth. Processing of InSAR data was done with the European Space Agency's Sentinel Application Platform (SNAP) version 5.0 software [Yague-Martinez et al., 2016; http://step.esa.int/main/toolboxes/snap], following several steps: SAR image formation, co-registration, interferogram formation, flattening (using precise orbits from ESA), and topography removing using a three arc-second (about 90 m) Shuttle Radar Topography Mission (SRTM) DEM. The final georeferenced product was resampled at 25 m using bilinear interpolation. The tropospheric correction process takes place before unwrapping the interferogram. This is done in order to minimise phase ambiguities and improve the reliability of interferogram unwrapping in a region such as the western GoC, where coherence is low due to the vegetation and rough topography which results in geometric decorrelation.

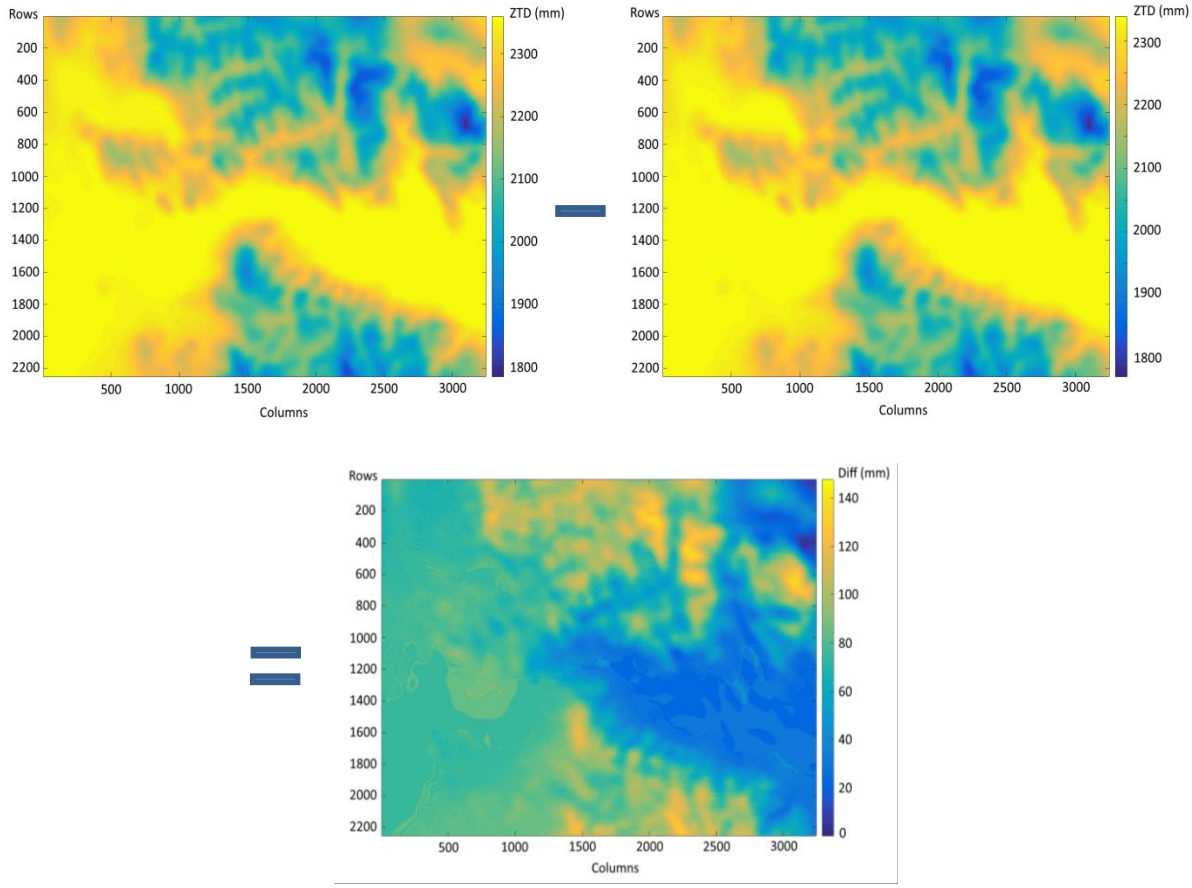

Figure 7-1. Example of producing a differential ZTD map from the subtraction of two single ZTD maps (epoch 1 – epoch 2), produced with WRF at the times of InSAR acquisitions. Pair corresponds to dates 18/9/2016 – 30/9/2016. The resulting differential ZTD map is then converted to LOS total delay map and wrapped (arithmetic values are transformed into 2π phase values), to correct the corresponding interferogram (see Figure 7-2).

The InSAR observations examined are listed in Table 7.1. Average values of WRF vs. GNSS ZTD bias are also listed in the Table. Δbias is calculated by averaging the absolute bias ($ZTD_{WRF} - ZTD_{GNSS}$) differences between epoch 1 and epoch 2, at the 19 PaTrop stations, and is an indication of the model's performance with respect to the observational data.

$$\Delta bias = \frac{\sum|(f_{i1}-o_{i1})-(f_{i2}-o_{i2})|}{N} \tag{7.1}$$

where f_{i1} and f_{i2} denote the model value at epochs 1 and 2 respectively, o_{i1} and o_{i2} the observational value at epochs 1 and 2 respectively, and N is the number of observations.

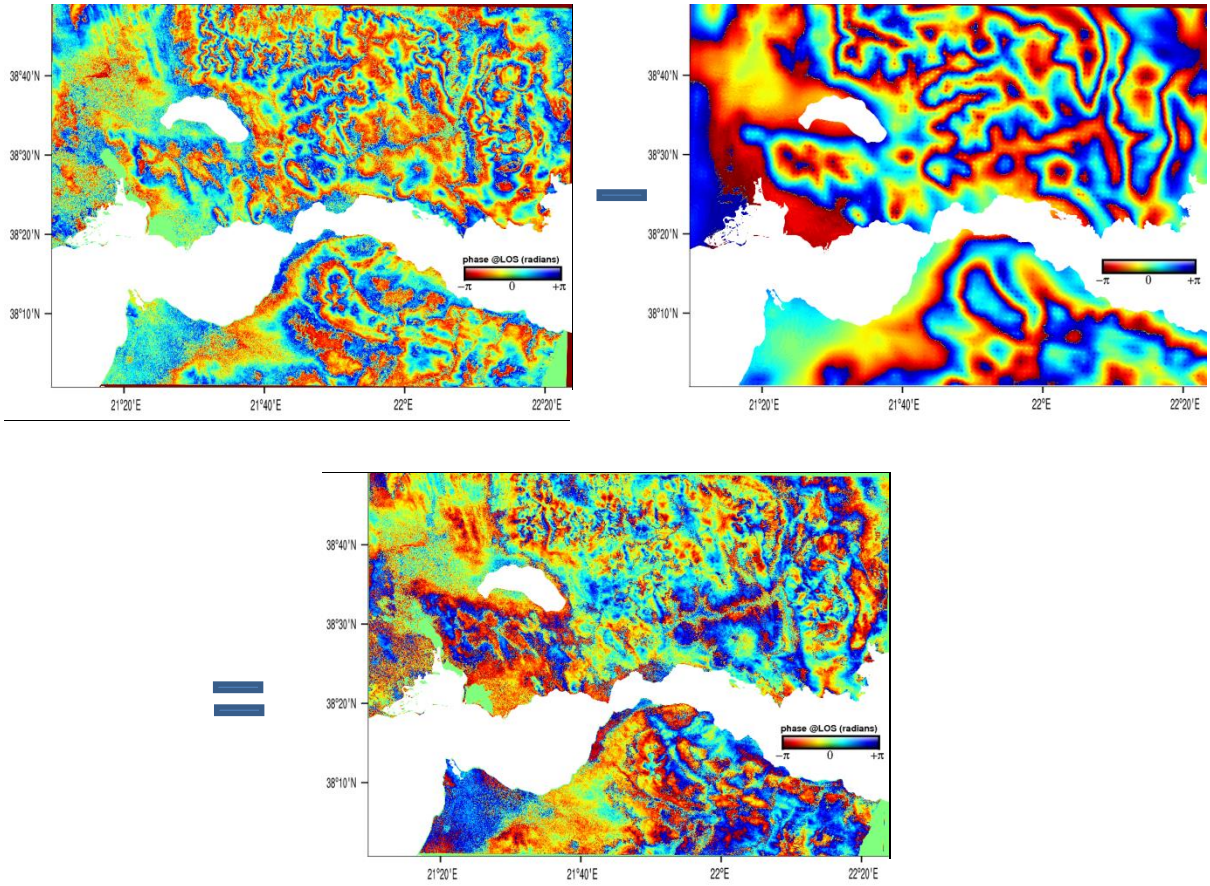

Figure 7-2. Example of atmospheric correction of an interferogram (18/9-30/9, track 80). The wrapped differential LOS delay map generated from WRF output data is subtracted from the corresponding wrapped interferogram, to produce a map of residual 2π phase cycles.

For the tropospheric correction the first step was to generate differential delay maps of the total single-path tropospheric delay at the line-of-sight (LOS), at the times of the two SAR acquisitions. This was done by subtracting the 1x1 km single ZTD map, produced by the d04 WRF output, of epoch 2 from the corresponding ZTD map of epoch 1 (Figure 7.1). In the resulting differential delay map, LOS total delay values were calculated at each 1-km grid cell by multiplying the corresponding ZTD value with cosθ, where θ is the average incidence angle of the S1 swath in IW mode (35^0). These values were then horizontally and vertically interpolated, using the weighted average inverse distance to a power gridding method, to a new 25x25 m grid corresponding to the pixel resolution of the interferogram. The resulting differential delay map is then wrapped (LOS total differences are converted into 2π interferometric phase fringes), and subtracted from the wrapped interferogram, to produce a phase map of residuals, as illustrated in Figure 7-2. Before the phase subtraction, the map of differential delay is “shifted” by minimizing the RMS between the two geotiffs, so that their average zero phases are aligned.

7.3 Results and Discussion

In this section, the results of InSAR tropospheric correction with the use of WRF derived delay maps are presented as follows:

Figure 7-3: Coherence maps for Sentinel-1 ascending track 175 and descending track 80, over the extended Western GoC area.
Figures 7-4 – 7-21: Nine examples of InSAR tropospheric correction presented in pairs (1-9), for Sentinel-1 track 175. First figure shows the wrapped interferogram and corresponding WRF-derived differential delay map. The following figure shows the same interferogram and the corresponding residual phase map after tropospheric correction.
Figures 7-22 – 7-43: Eleven examples of InSAR tropospheric correction presented in pairs (10-20), for Sentinel-1 track 80. First figure shows the wrapped interferogram and corresponding WRF-derived differential delay map. The following figure shows the same interferogram and the corresponding residual phase map after tropospheric correction.

In order to provide a quantitative assessment of the corrections applied in every case, the Root Mean Square (RMS) and Standard Deviation (SD) of the phase distribution of both the original and the corrected interferograms are calculated and their differences recorded. A reduction in the RMS or SD of the interferogram after the correction is applied is a clear indication that there is a decrease of the phase gradient and fringe continuity is smoother. Table 7.1 lists the RMS and SD results together with the corresponding Δbias value for all 20 cases examined, while Figures 7-44 and 7-45 illustrate graphically the correlation of RMS and SD with Δbias.

In most cases, corrections applied to the wrapped interferograms with the use of high-resolution WRF-derived delay fields lead to a decrease of the phase gradient, as demonstrated by the corresponding RMS and SD reductions (Table 7.1). The RMS of the corrected interferogram is improved in 16 out of 20 cases, with reductions ranging from 2.3% to 14.1% (6.2% on average), while SD is improved in all 20 cases, with reductions ranging from 8.3% to 32.7% (18.3% on average).

Furthermore, the degree of tropospheric delay correction is correlated with WRF-GNSS average bias differences (Δ_{bias}) at the times of acquisitions. This is evident in Figures 7-44 and 7-45, where the slope of the reductions in both indicators with respect to Δ_{bias} is inversely proportional. Cases with low coherence (in blue) have a wider error margin than cases with medium or high coherence, and when excluded the correlation is improved. When the correlation between the two indexes is plotted (Figure 7-46), it is confirmed that their variability is not random, and that coherence is a determining factor (two out of three cases with low coherence have outlying values).

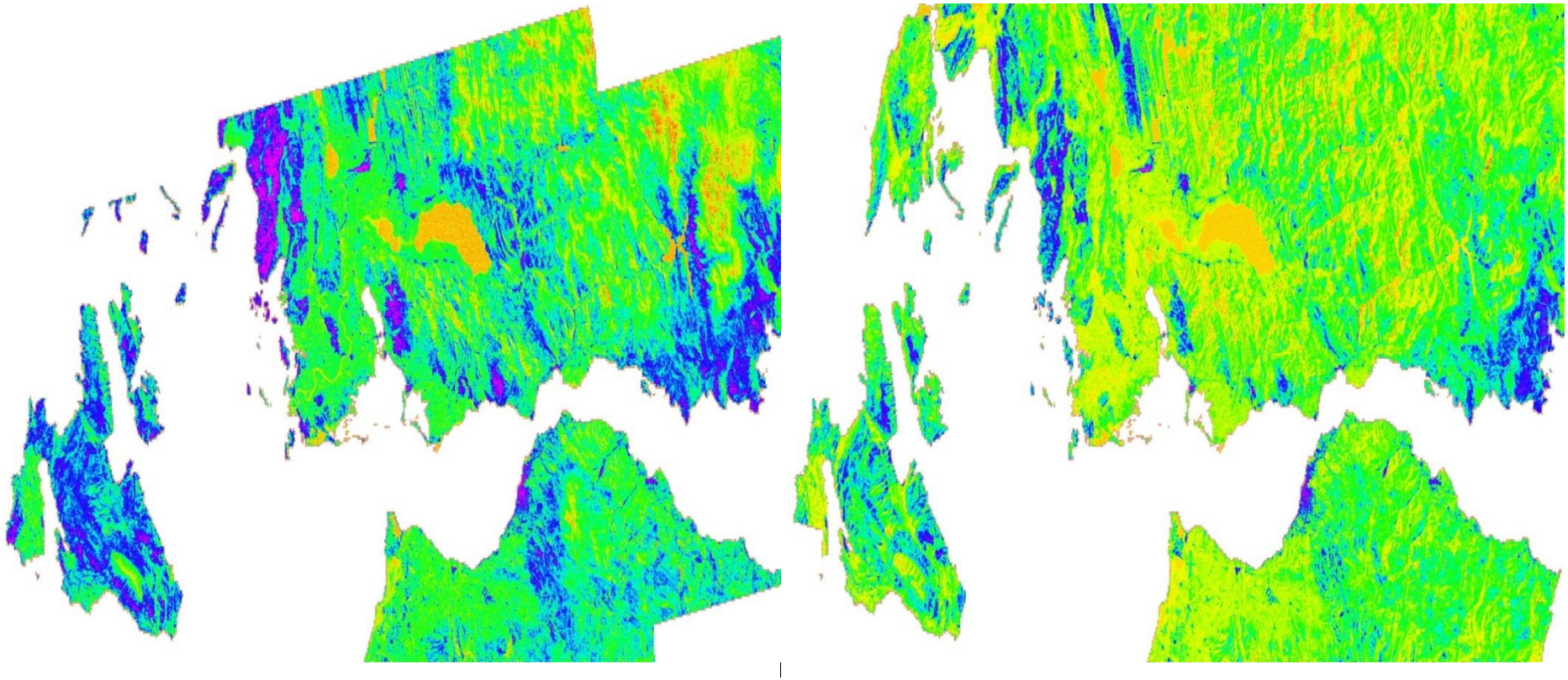

Figure 7-3. Coherence maps for Sentinel-1 ascending track 175 (left) and descending track 80 (right), over the extended western GoC area. Purple colour indicates highest and yellow indicates lowest coherence.

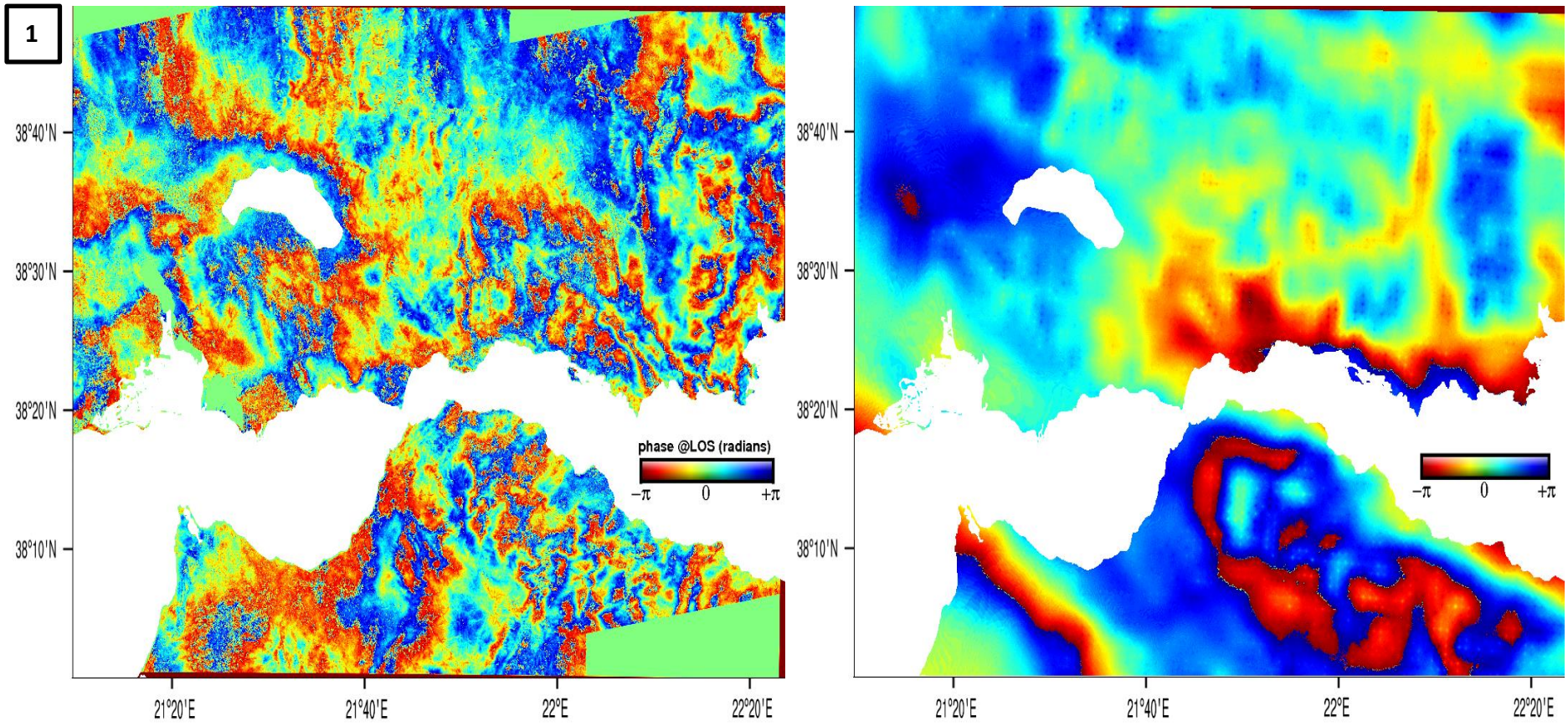

Figure 7-4. Wrapped interferogram from SAR acquisitions on 30/09/2016 and 06/10/2016, track 175 in radar geometry (left). Corresponding WRF-derived wrapped differential LOS delay map (right). The delay map in this small temporal baseline, does not recreate accurately tropospheric artifacts which are present in the interferogram.

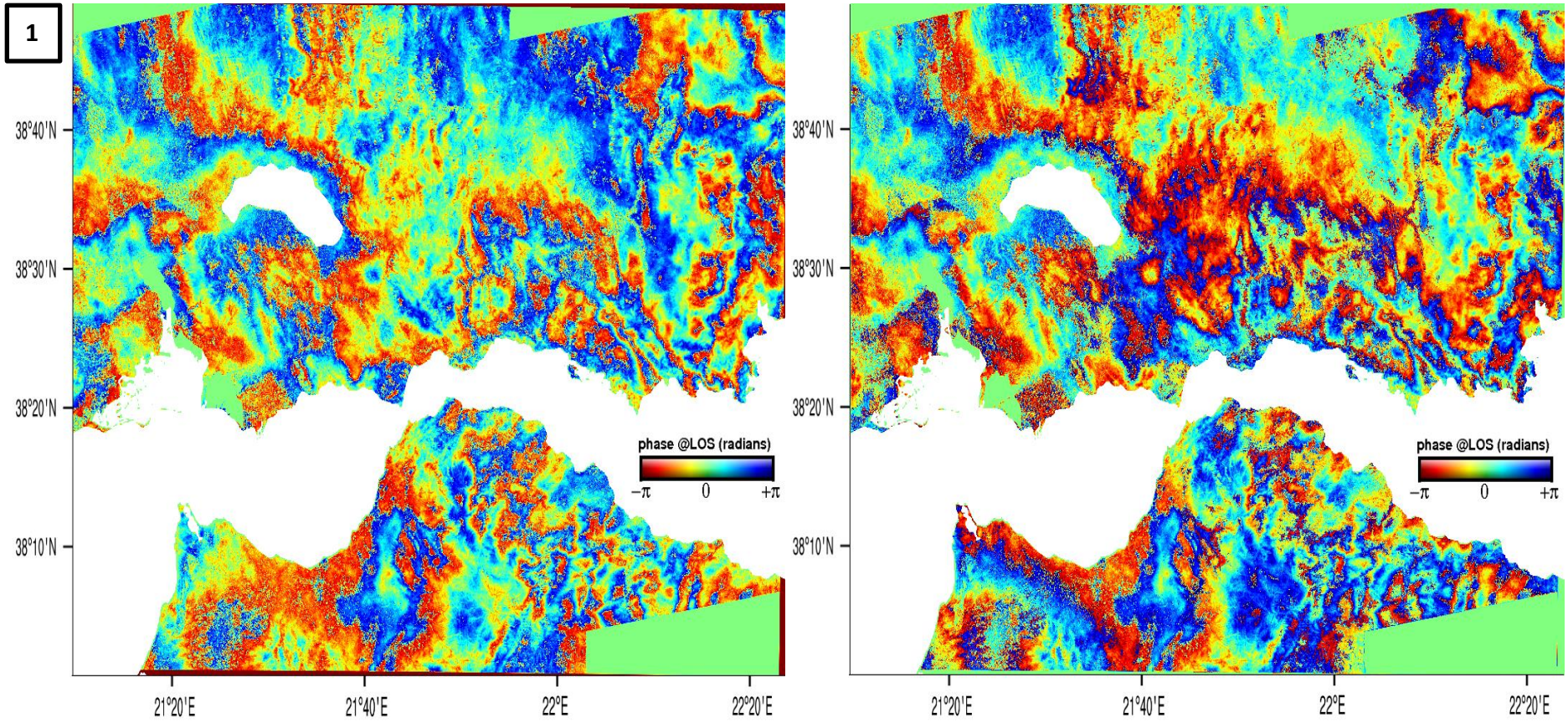

Figure 7-5. Wrapped interferogram from SAR acquisitions on 30/09/2016 and 06/10/2016, track 175 in radar geometry (left). Corresponding residual map after subtraction of WRF-derived wrapped differential LOS delay map from the interferogram (right). In this case, tropospheric fringes are not visibly reduced after the tropospheric correction.

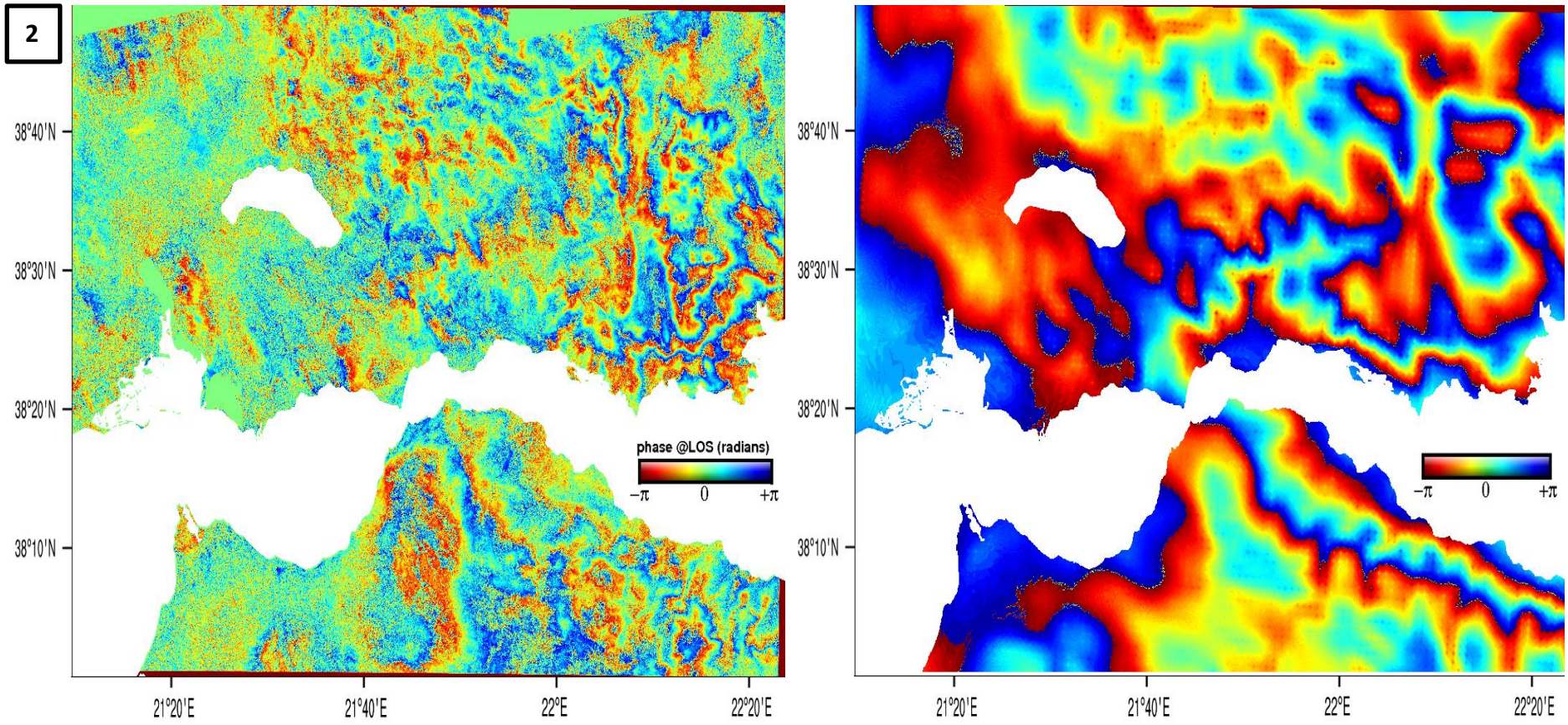

Figure 7-6. Wrapped interferogram from SAR acquisitions on 30/09/2016 and 24/10/2016, track 175 in radar geometry (left). Corresponding WRF-derived wrapped differential LOS delay map (right). The correlation between interferogram and meteogram is directly visible, for example in the Mornos valley or around the Panachaikon mountain as the model's forecasting skill is high in both acquisition epochs (Δbias low).

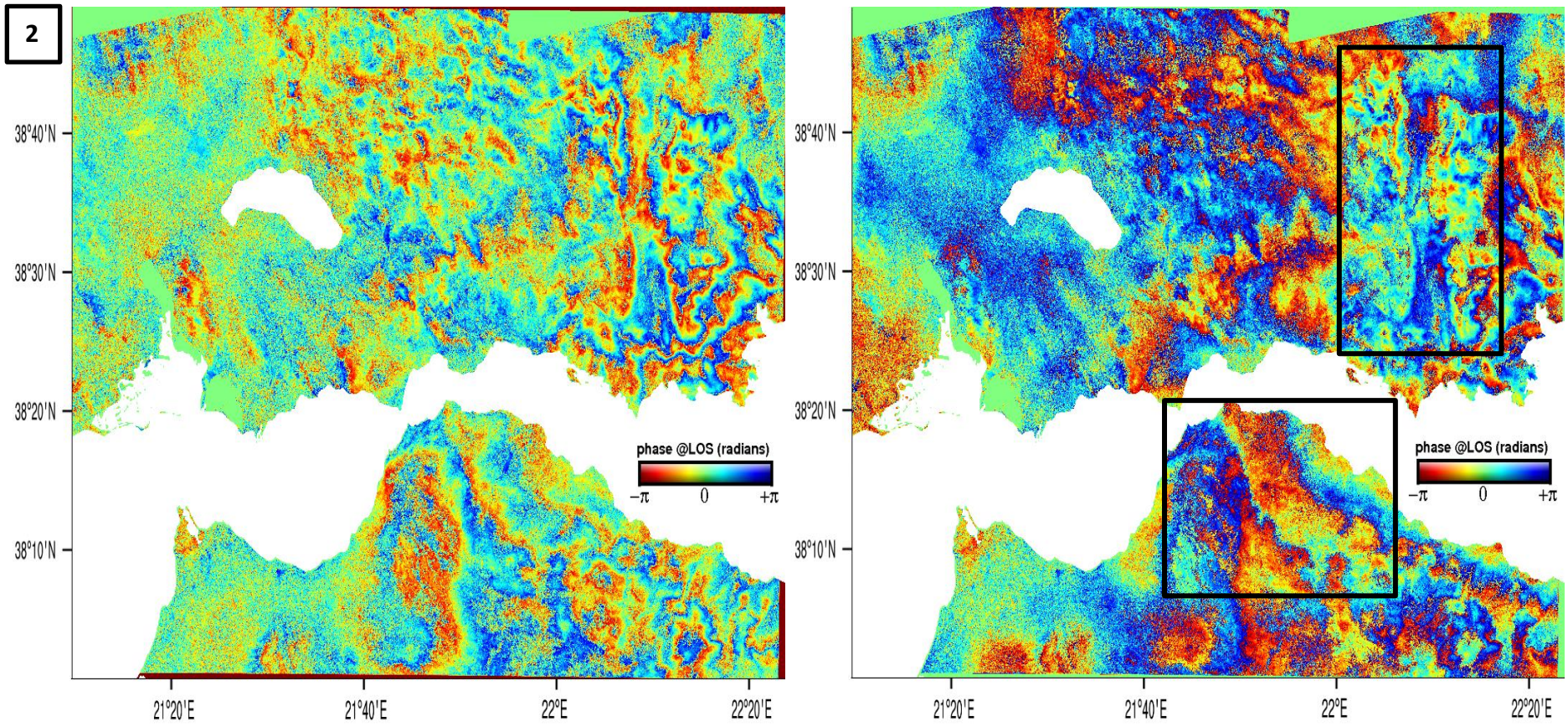

Figure 7-7. Wrapped interferogram from SAR acquisitions on 30/09/2016 and 24/10/2016, track 175 in radar geometry (left). Corresponding residual map after subtraction of WRF-derived wrapped differential LOS delay map from the interferogram (right). Δbias = -2.6. Tropospheric correction leads to some decrease of the phase gradient in several areas of the interferogram where coherence is high.

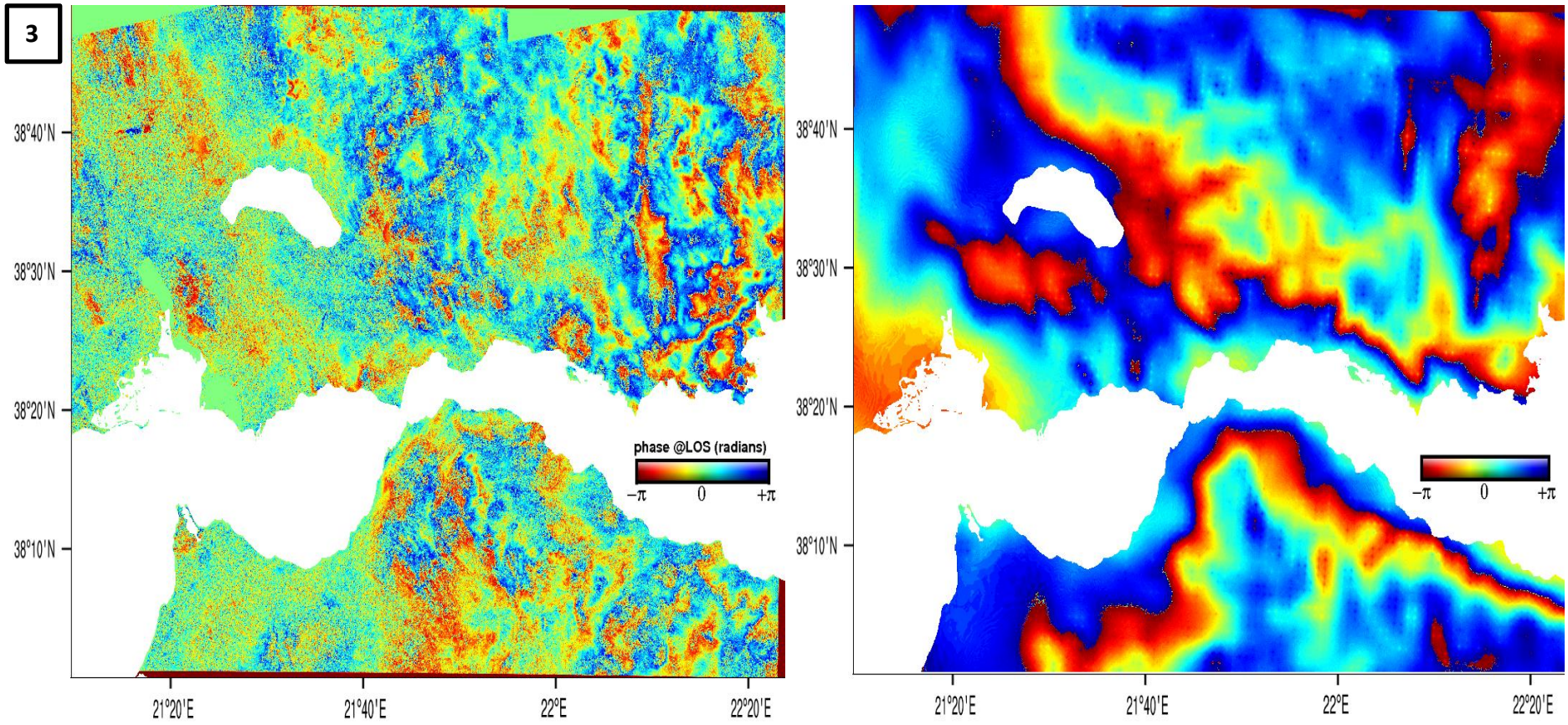

Figure 7-8. Wrapped interferogram from SAR acquisitions on 30/09/2016 and 05/11/2016, track 175 in radar geometry (left). Corresponding WRF-derived wrapped differential LOS delay map (right). Similar to example 1, Δbias is high but coherence is lower due to the longer temporal baseline (36 days), masking several tropospheric features. There is less clear visual correlation between the interferogram and the meteogram.

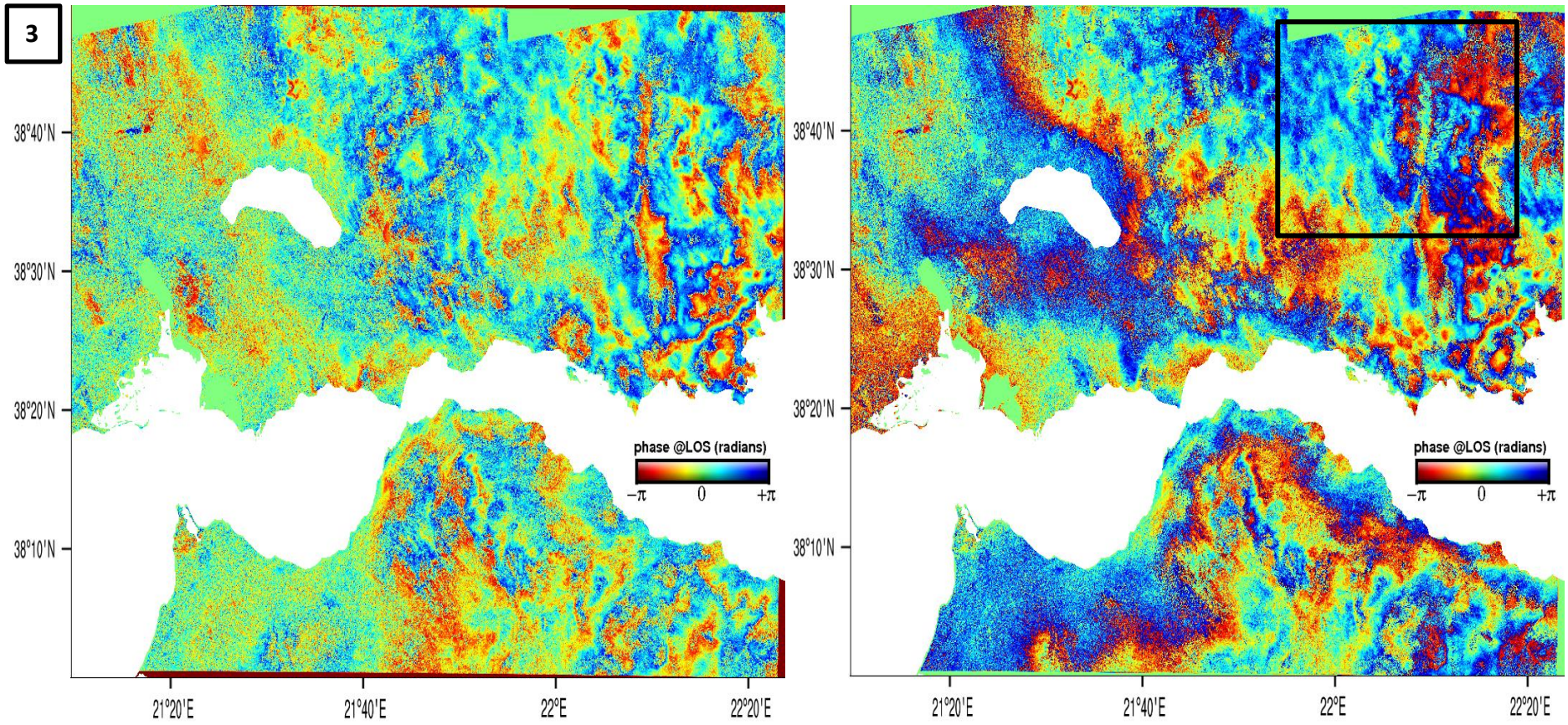

Figure 7-9. Wrapped interferogram from SAR acquisitions on 30/09/2016 and 05/11/2016, track 175 in radar geometry (left). Corresponding residual map after subtraction of WRF-derived wrapped differential LOS delay map from the interferogram (right). Tropospheric fringes are partly reduced in some areas but not in a great extent. In areas of low coherence (mostly in the western part) the differential troposphere produces an aliasing effect shown in the residual map.

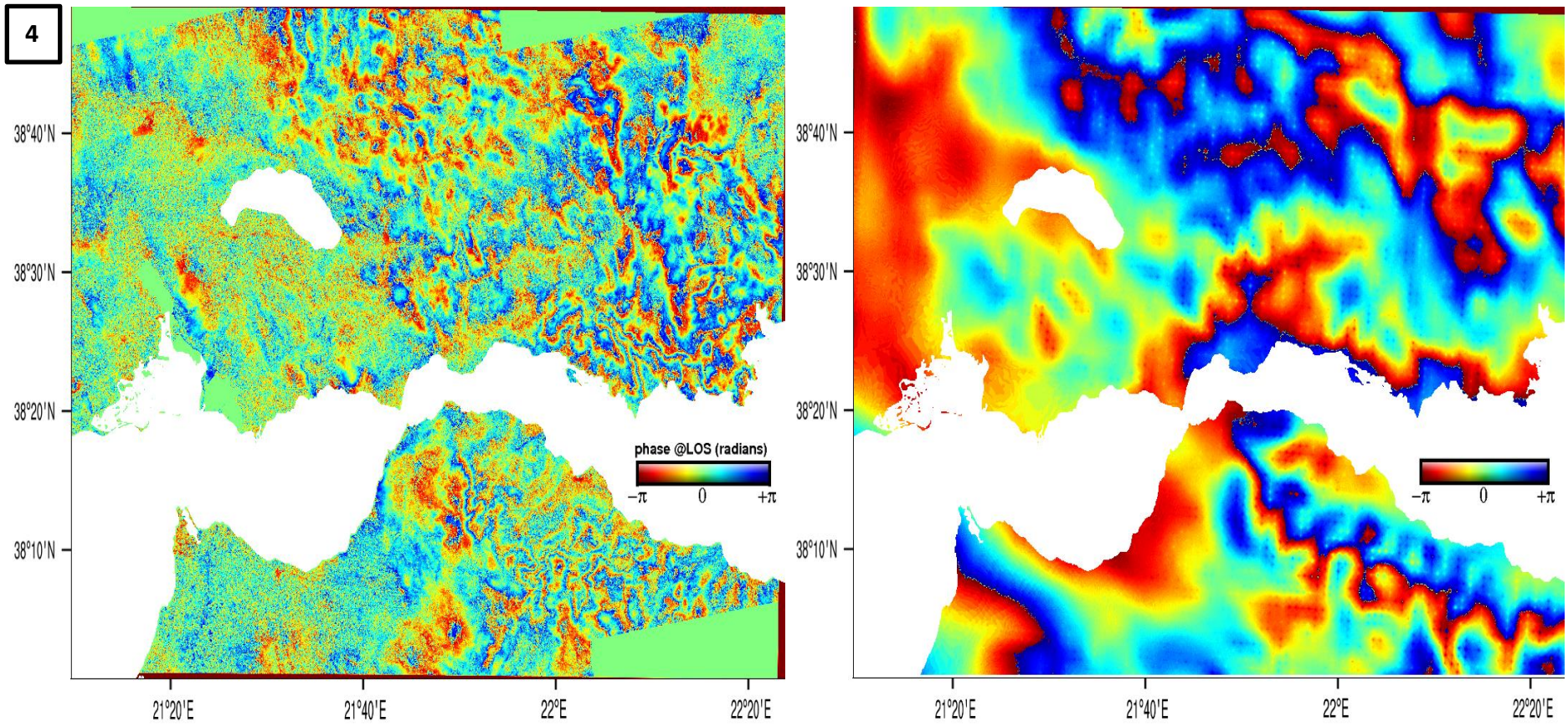

Figure 7-10. Wrapped interferogram from SAR acquisitions on 06/10/2016 and 24/10/2016, track 175 in radar geometry (left). Corresponding WRF-derived wrapped differential LOS delay map (right). An example similar to cases 1 and 3, where some (mainly long wavelength) tropospheric artifacts are captured, as indicated by the model's medium performance at the two acquisition epochs.

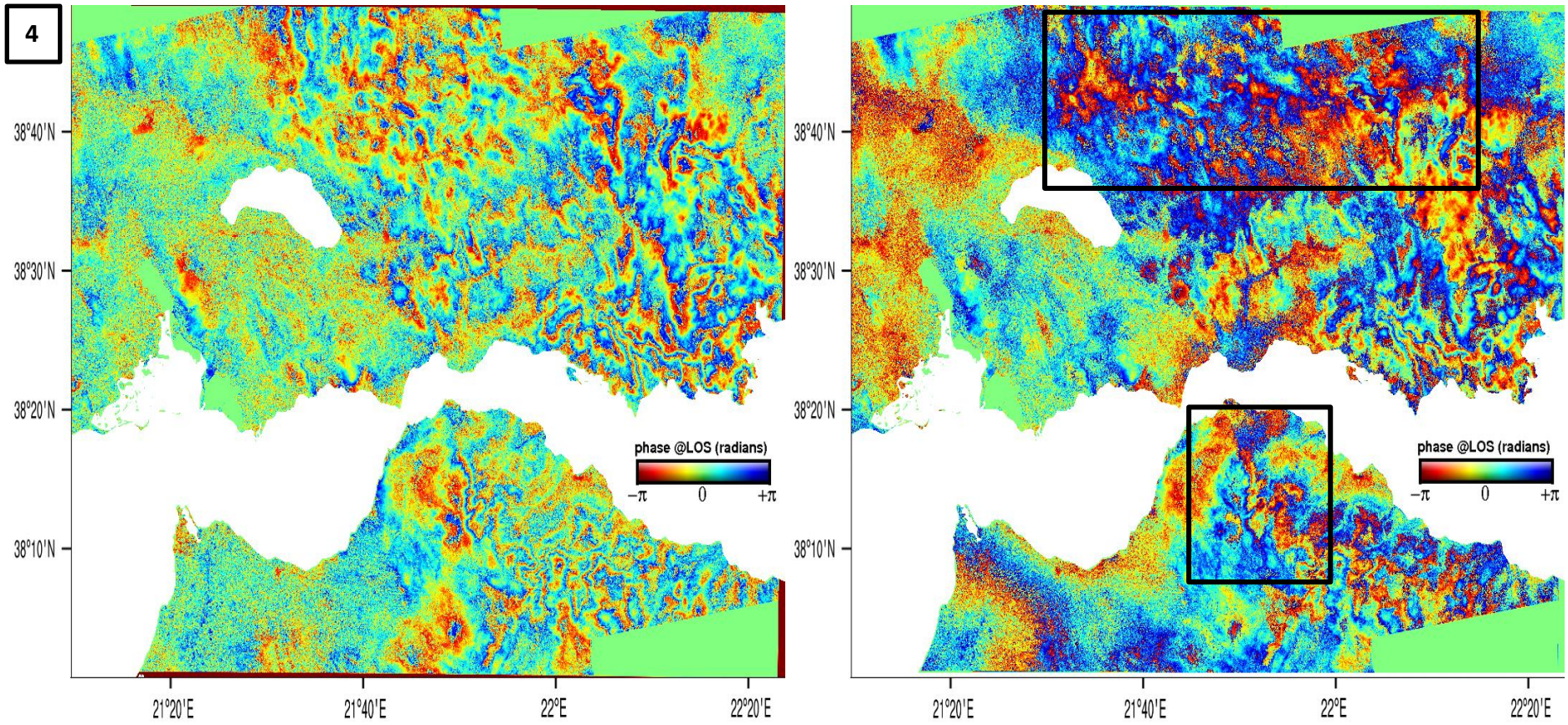

Figure 7-11. Wrapped interferogram from SAR acquisitions on 06/10/2016 and 24/10/2016, track 175 in radar geometry (left). Corresponding residual map after subtraction of WRF-derived wrapped differential LOS delay map from the interferogram (right). The density of tropospheric fringes is reduced in some locations after correction, as shown in the black boxes, accordingly with Δbias.

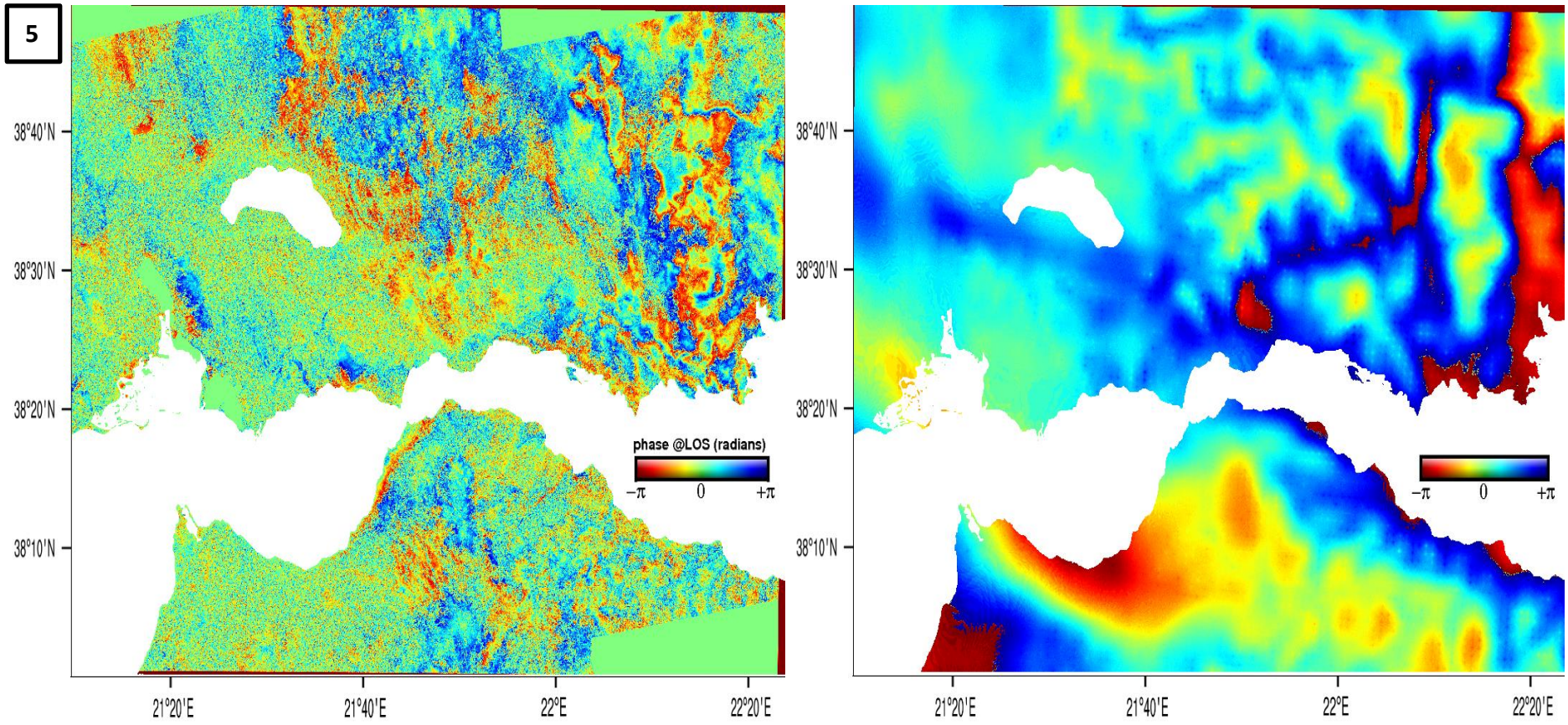

Figure 7-12. Wrapped interferogram from SAR acquisitions on 06/10/2016 and 11/12/2016, track 175 in radar geometry (left). Corresponding WRF-derived wrapped differential LOS delay map (right). The low coherence of the interferogram masks many of the tropospheric artifacts, however in areas of good coherence (northeastern part of the map and Panachaiko mountain in northern Peloponnese), broad features are represented by the model.

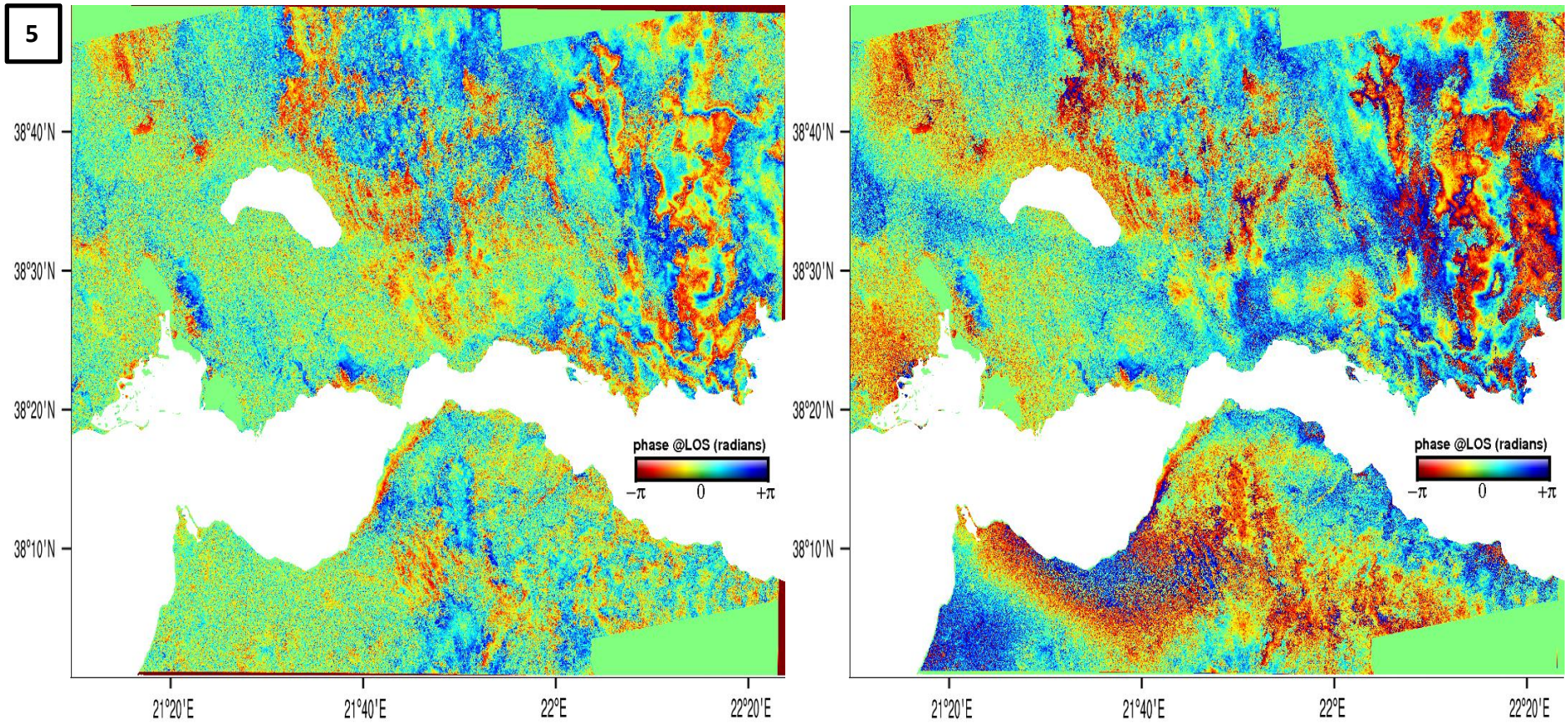

Figure 7-13. Wrapped interferogram from SAR acquisitions on 06/10/2016 and 11/12/2016, track 175 in radar geometry (left). Corresponding residual map after subtraction of WRF-derived wrapped differential LOS delay map from the interferogram (right). No significant reductions of the tropospheric phase gradients are visible in the residual map.

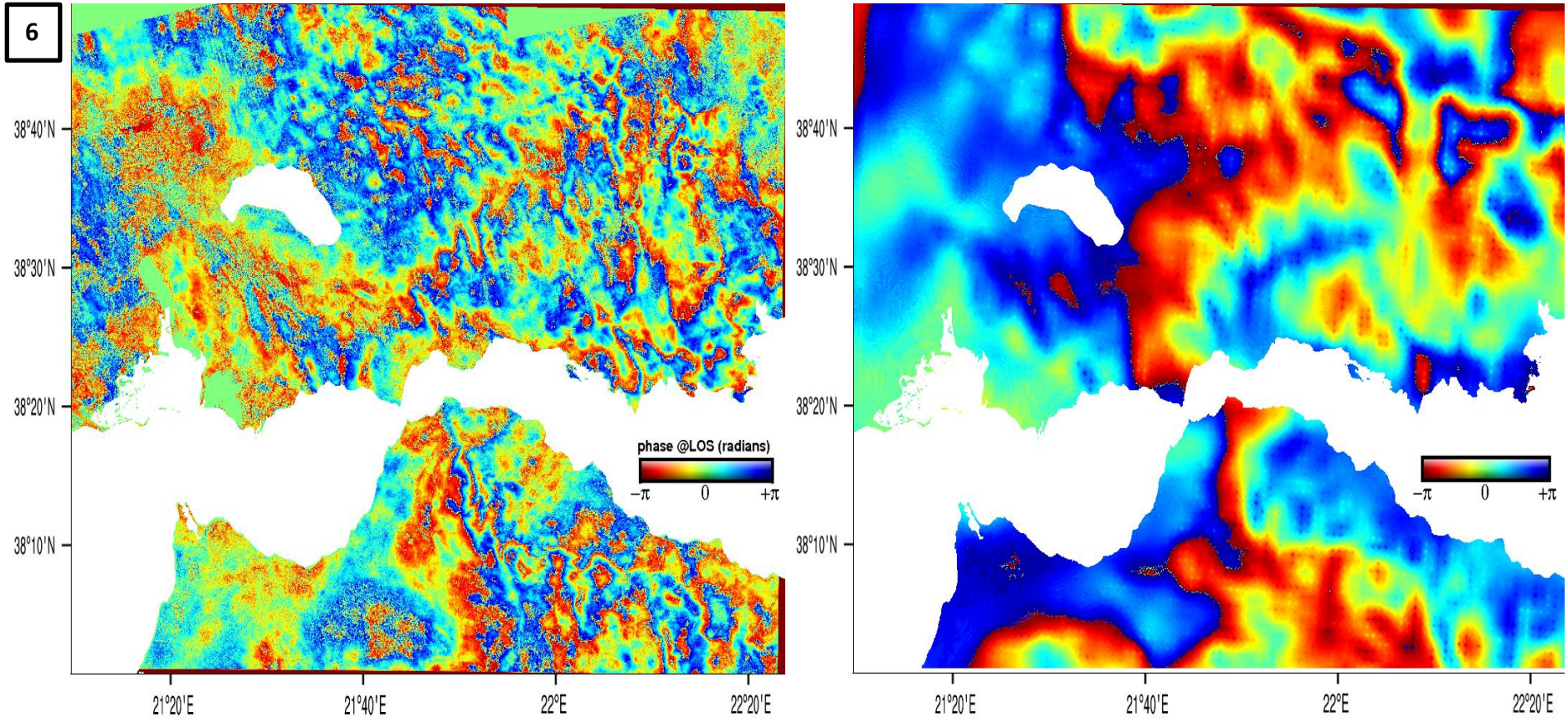

Figure 7-14. Wrapped interferogram from SAR acquisitions on 24/10/2016 and 05/11/2016, track 175 in radar geometry (left). Corresponding WRF-derived wrapped differential LOS delay map (right). Several tropospheric artifacts are respresented in the delay map (with various degrees of accuracy), mainly in the area east of lake Trichonis and the northern part of Peloponnese.

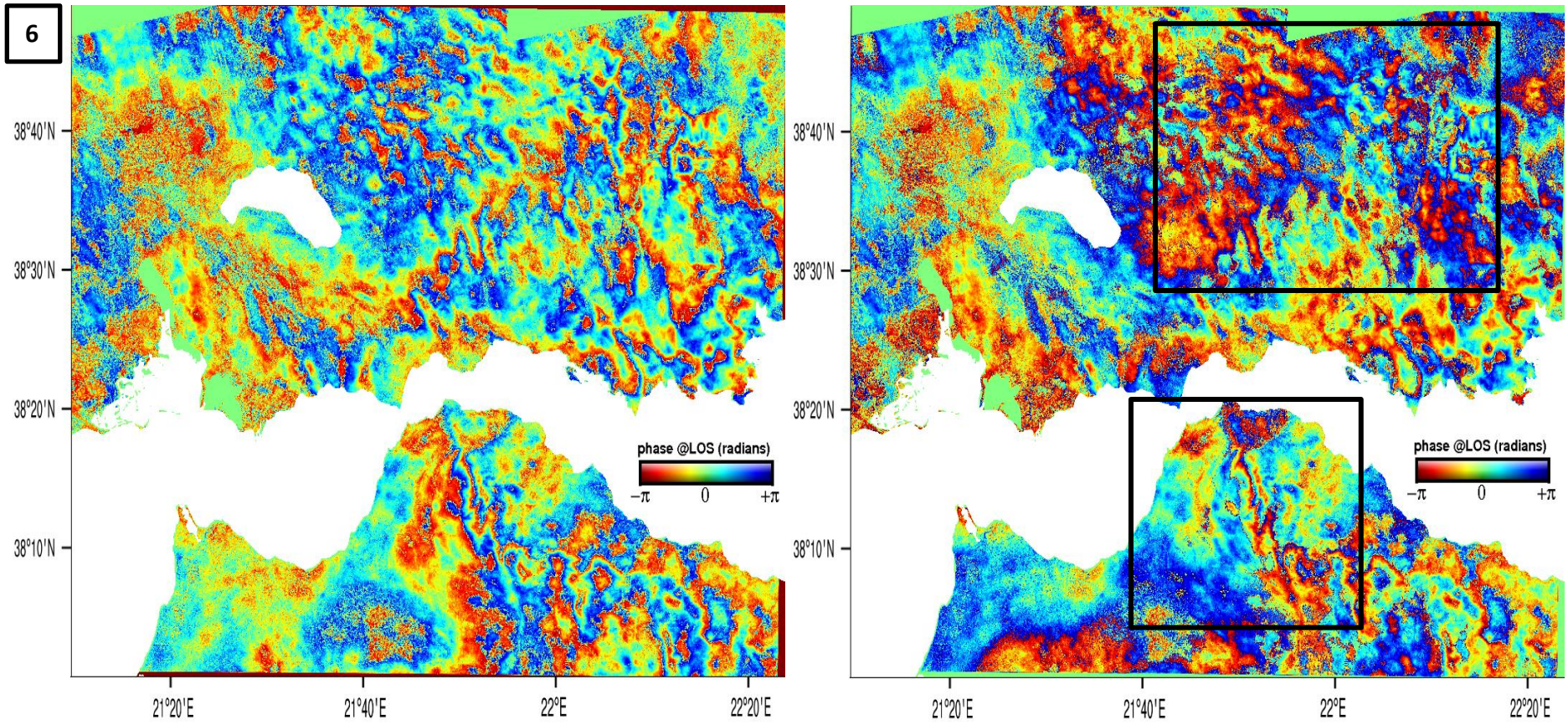

Figure 7-15. Wrapped interferogram from SAR acquisitions on 24/10/2016 and 05/11/2016, track 175 in radar geometry (left). Corresponding residual map after subtraction of WRF-derived wrapped differential LOS delay map from the interferogram (right). Coherence is relatively good in this example, a minor reduction of tropospheric fringes can be observed in areas where the model simulates well the differential troposphere.

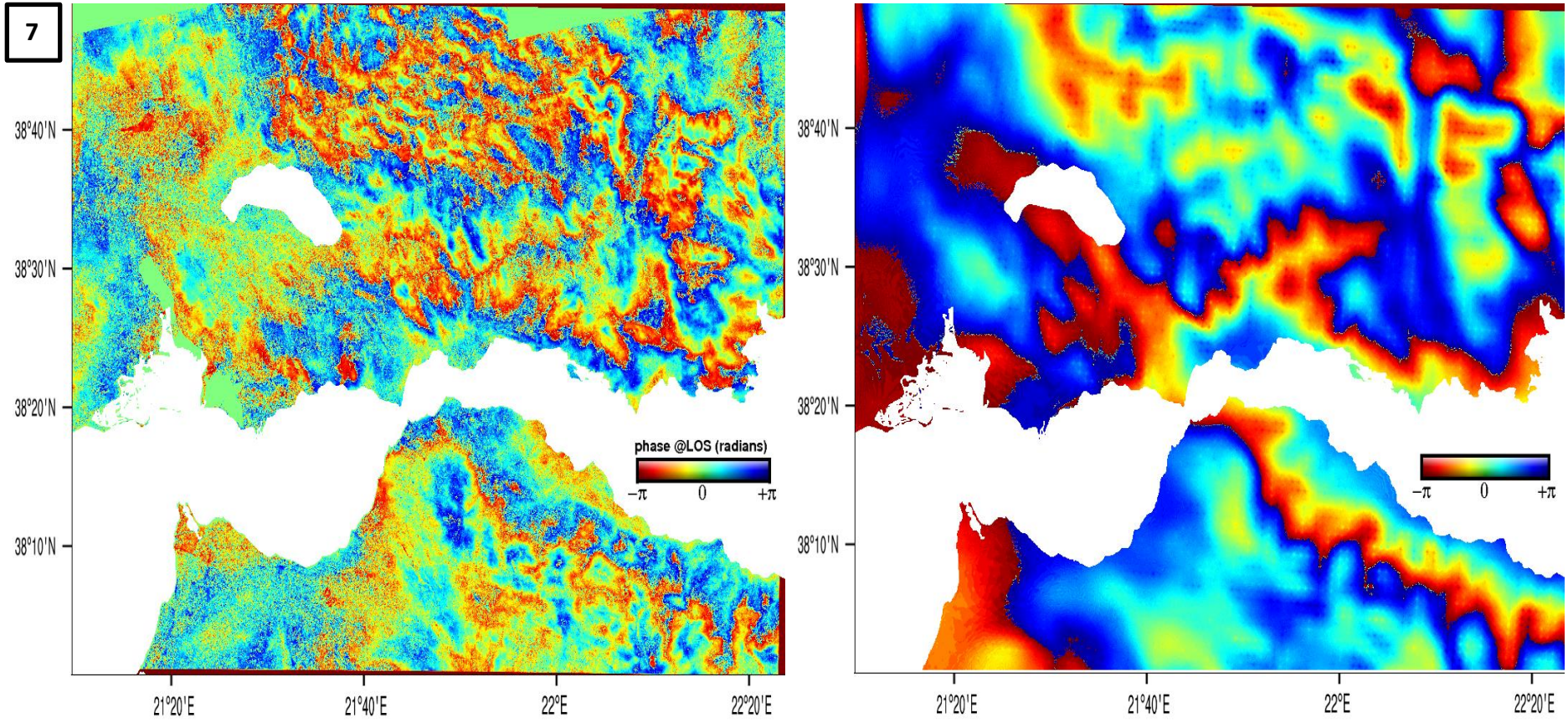

Figure 7-16. Wrapped interferogram from SAR acquisitions on 24/10/2016 and 17/11/2016, track 175 in radar geometry (left). Corresponding WRF-derived wrapped differential LOS delay map (right). The atmospheric conditions are captured well by the model, as indicated by the small Δbias, in large areas of the map.

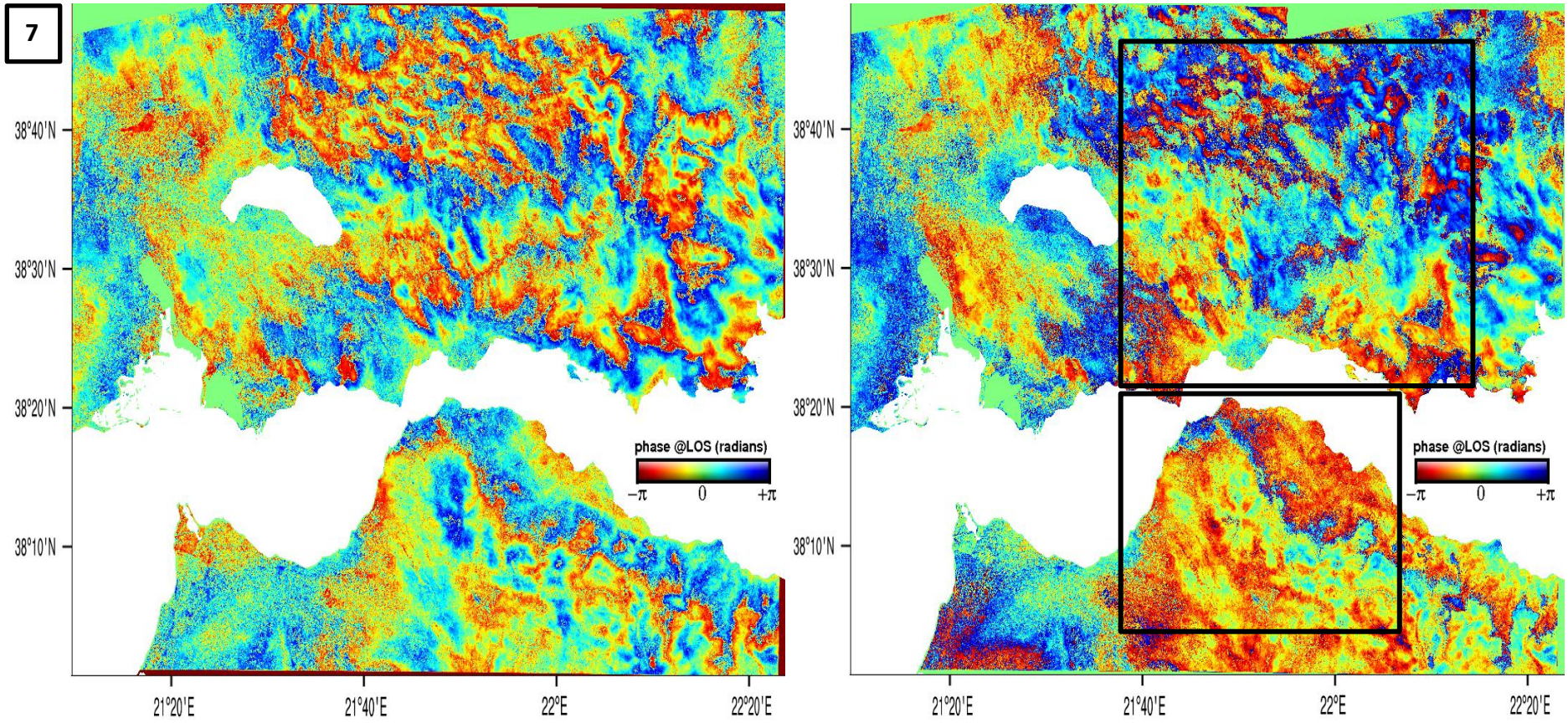

Figure 7-17. Wrapped interferogram from SAR acquisitions on 24/10/2016 and 17/11/2016, track 175 in radar geometry (left). Corresponding residual map after subtraction of WRF-derived wrapped differential LOS delay map from the interferogram (right). In this case, the density of tropospheric fringes is greatly reduced after correction, as shown in the black boxes, in northern Peloponnese as well as the area east of lake Trichonis.

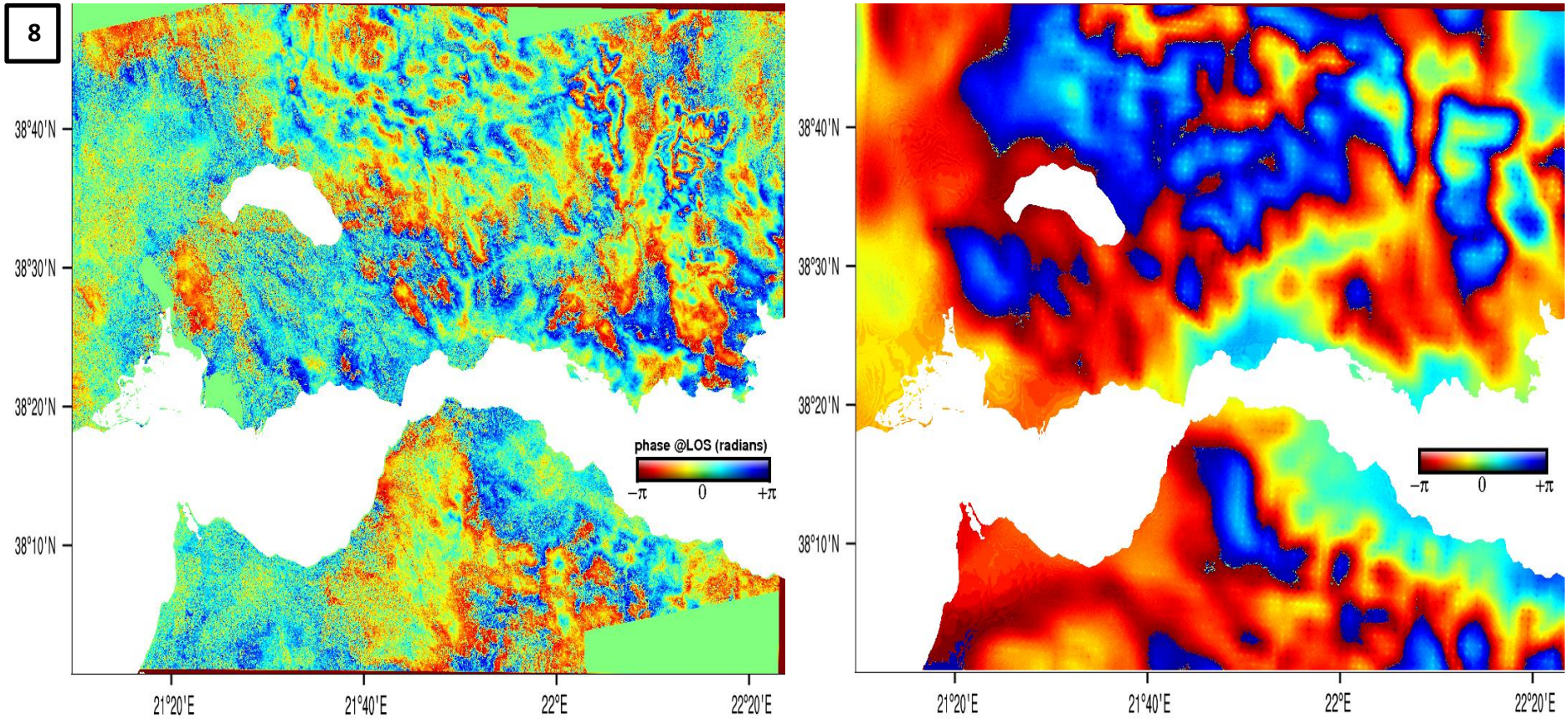

Figure 7-18. Wrapped interferogram from SAR acquisitions on 24/10/2016 and 23/11/2016, track 175 in radar geometry (left). Corresponding WRF-derived wrapped differential LOS delay map (right). Similarly to example 7, many features of the differential troposphere are captured in the delay map, which is also reflected in the consistency between GNSS and WRF at the times of acquisitions.

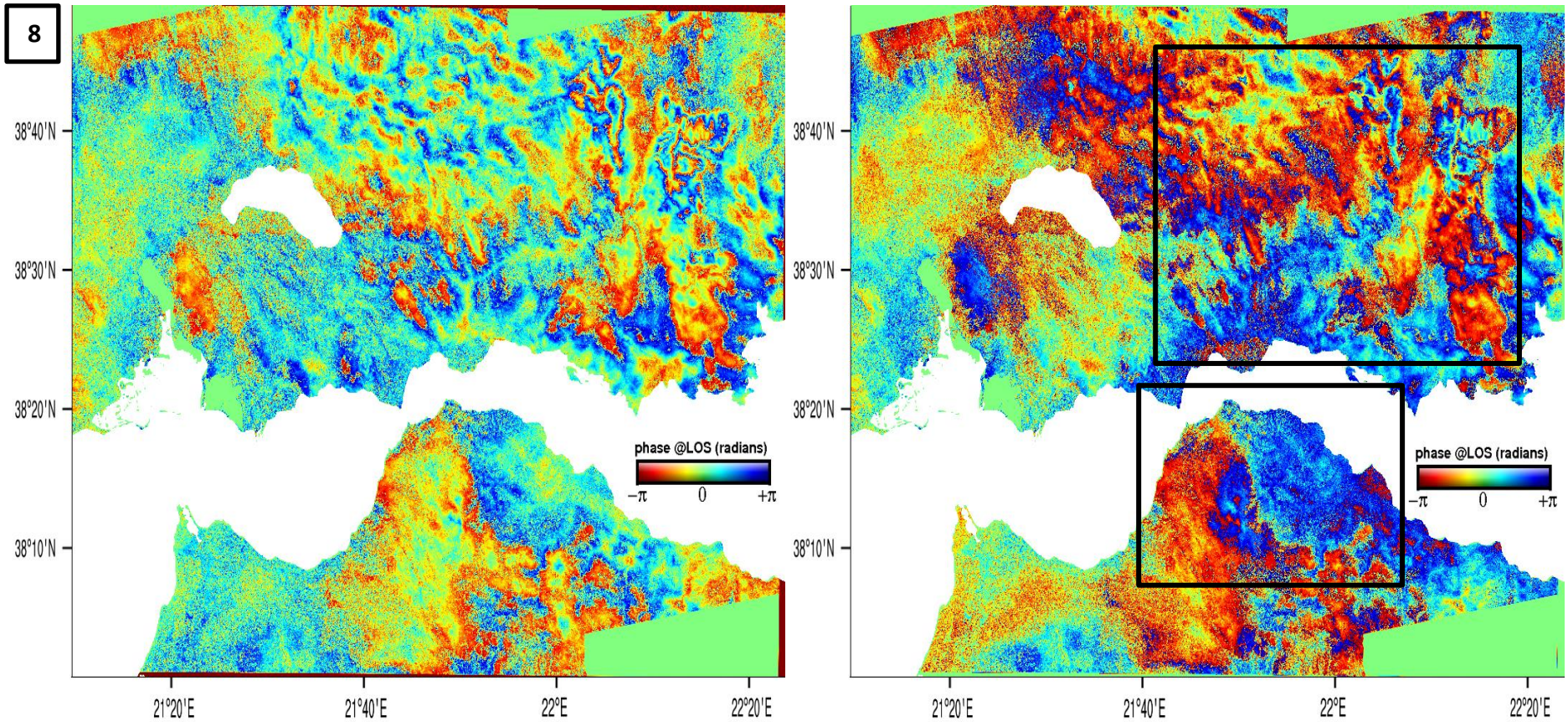

Figure 7-19. Wrapped interferogram from SAR acquisitions on 24/10/2016 and 23/11/2016, track 175 in radar geometry (left). Corresponding residual map after subtraction of WRF-derived wrapped differential LOS delay map from the interferogram (right). Again significant corrections of the phase gradient are observed, in northern Peloponnese, the Mornos valley and the area east of lake Trichonis.

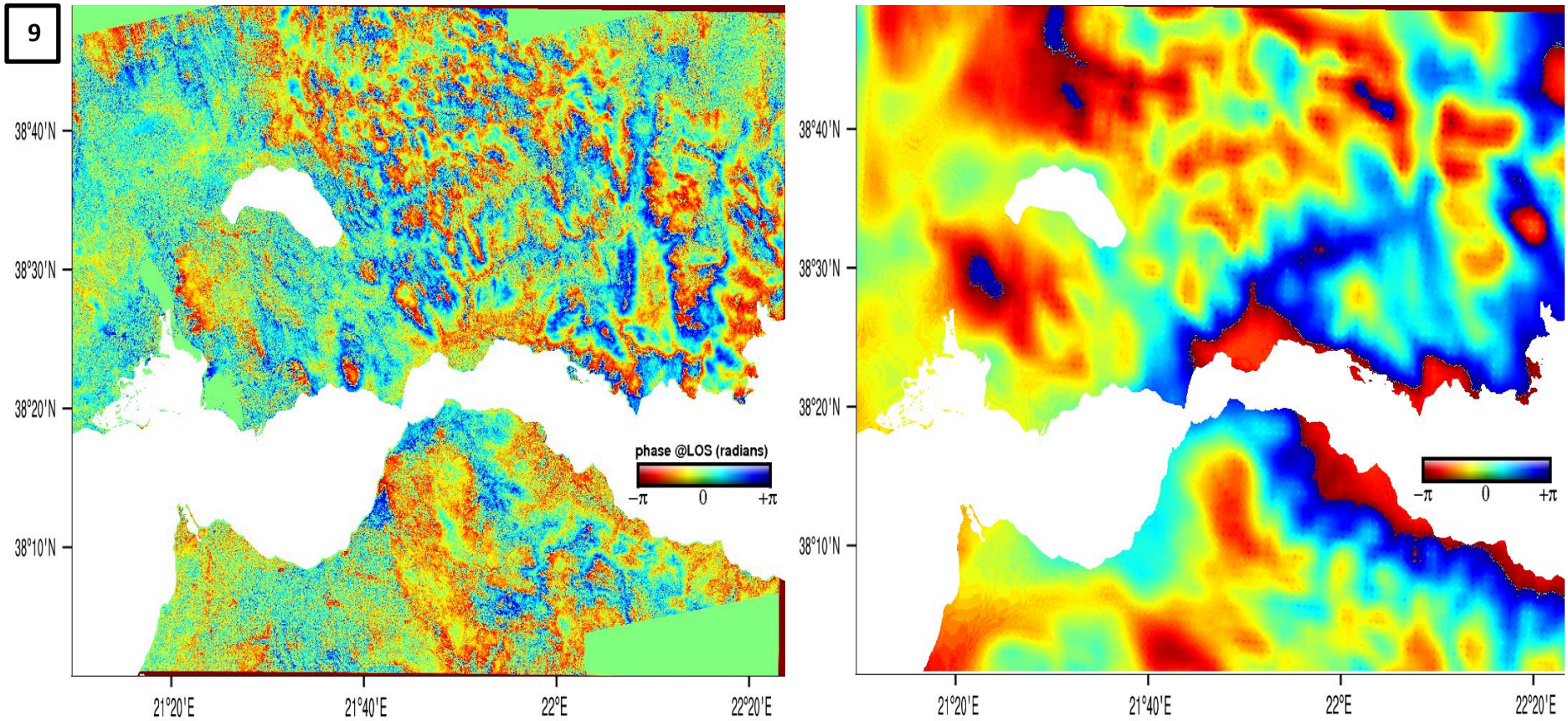

Figure 7-20. Wrapped interferogram from SAR acquisitions on 24/10/2016 and 05/12/2016, track 175 in radar geometry (left). Corresponding WRF-derived wrapped differential LOS delay map (right). Example similar to cases 7 and 8, with good correlation between the interferogram and meteogram.

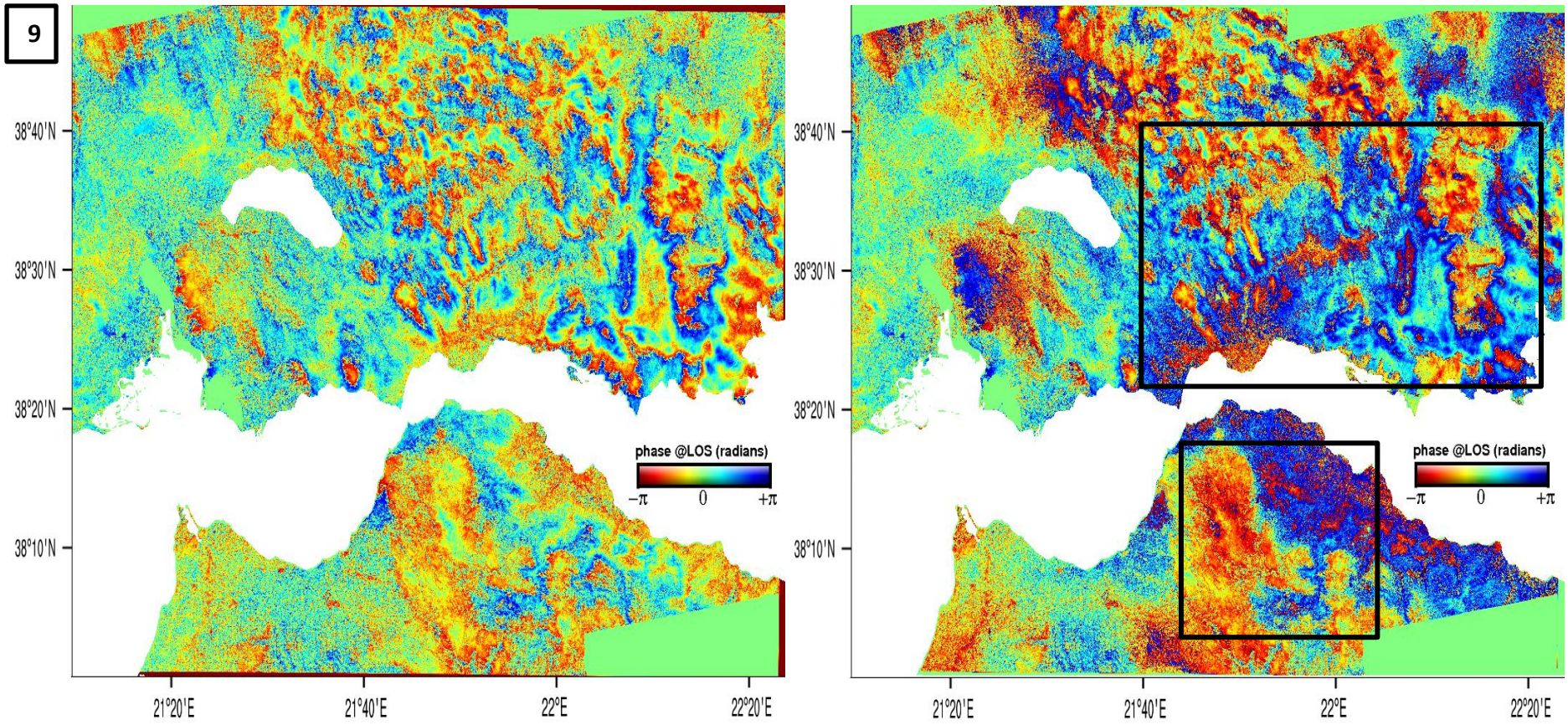

Figure 7-21. Wrapped interferogram from SAR acquisitions on 24/10/2016 and 05/12/2016, track 175 in radar geometry (left). Corresponding residual map after subtraction of WRF-derived wrapped differential LOS delay map from the interferogram (right). Good tropospheric corrections are observed particularly in northern Peloponnese and the Mornos valley, where a $-\pi$ to π phase continuity is shown in the residual map. Coherence is less good in this case.

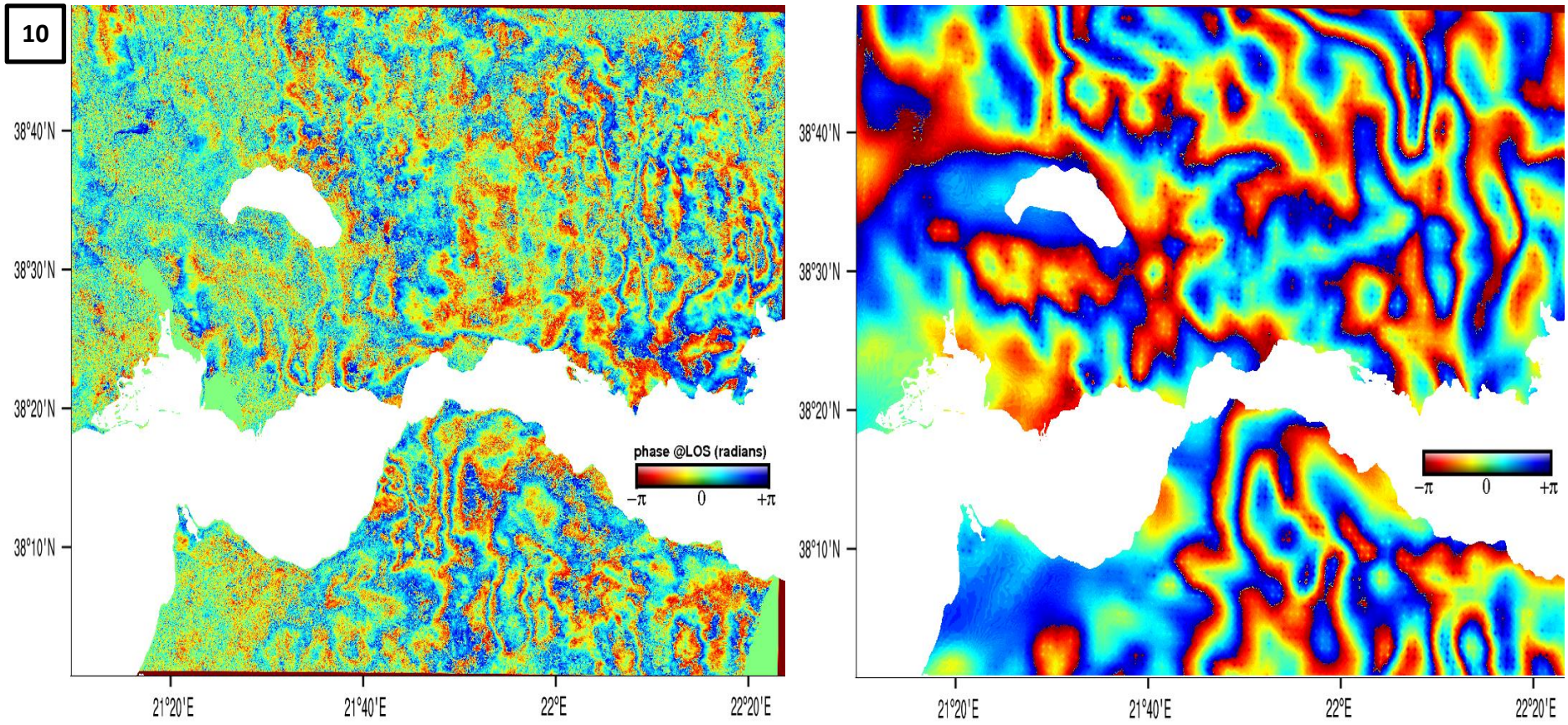

Figure 7-22. Wrapped interferogram from SAR acquisitions on 25/08/2016 and 18/09/2016, track 80 in radar geometry (left). Corresponding WRF-derived wrapped differential LOS delay map (right). The delay map captures many of the short wavelength atmospheric artifacts present in this interferogram, although with less accuracy, as indicated by high Δbias. Coherence is relatively low in this example and masks several tropospheric features.

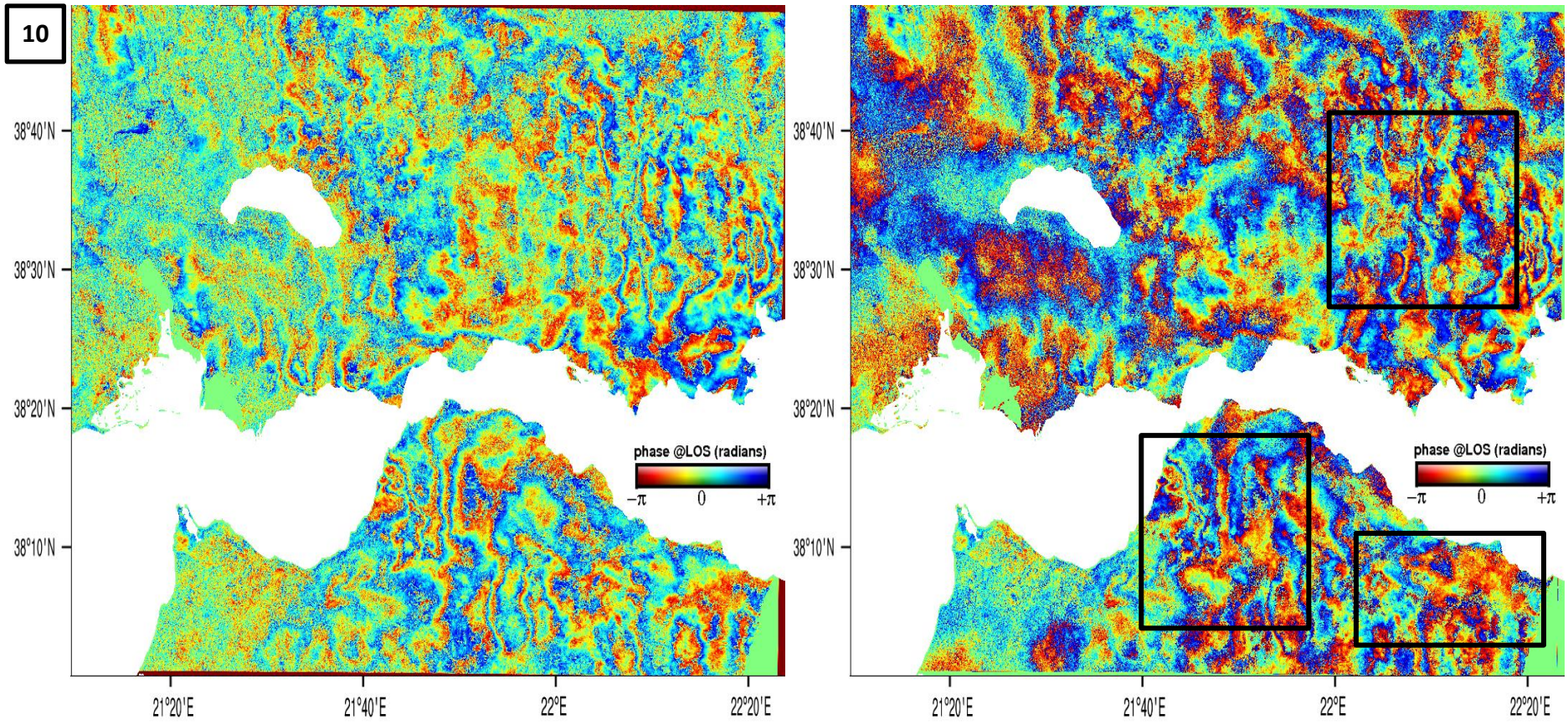

Figure 7-23. Wrapped interferogram from SAR acquisitions on 25/08/2016 and 18/09/2016, track 80 in radar geometry (left). Corresponding residual map after subtraction of WRF-derived wrapped differential LOS delay map from the interferogram (right). Minor reductions of atmospheric phase gradients can be observed in some areas of the map. Other areas however show a stronger noise-to –signal ratio after correction. Low coherence produces a strong aliasing effect in the residual map.

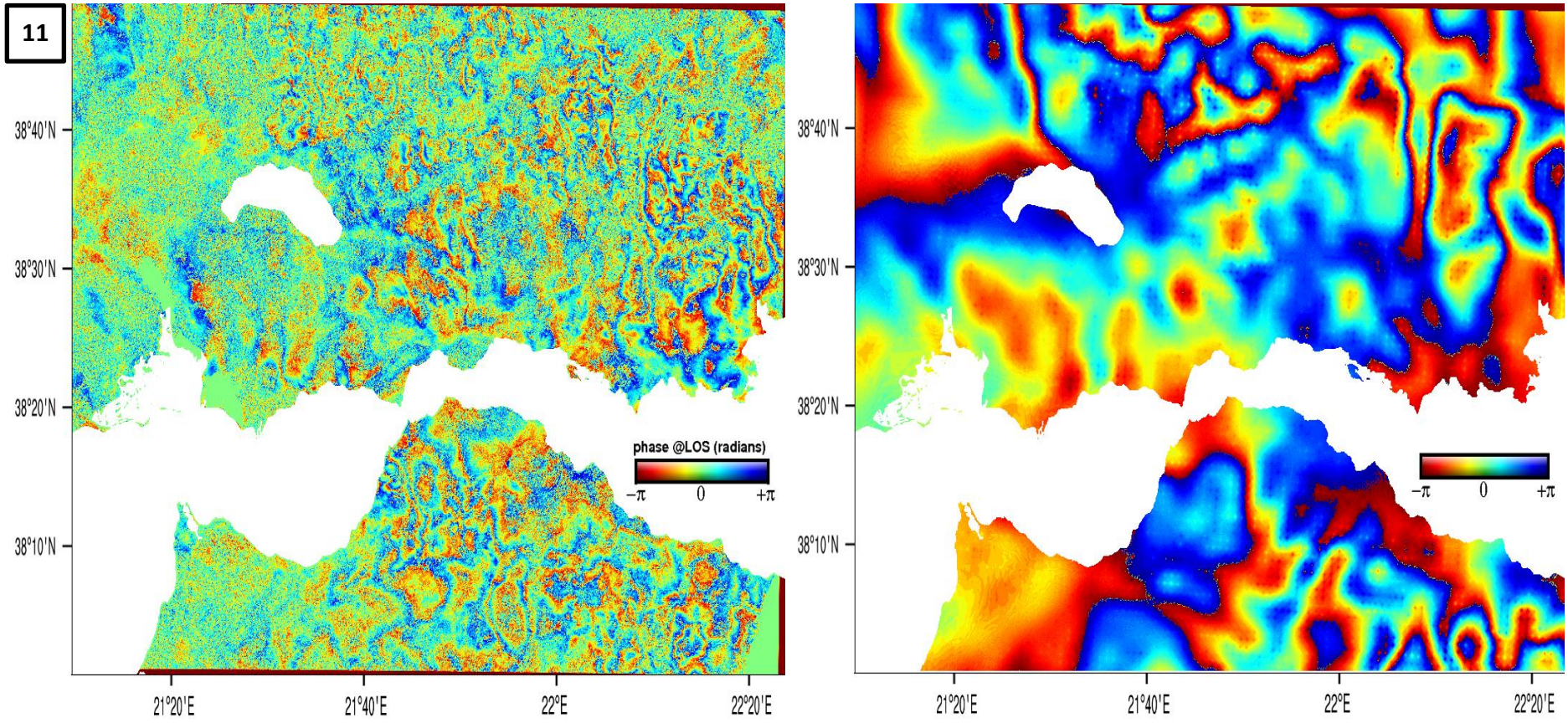

Figure 7-24. Wrapped interferogram from SAR acquisitions on 25/08/2016 and 30/09/2016, track 80 in radar geometry (left). Corresponding WRF-derived wrapped differential LOS delay map (right). Some correlation visible between the interferogram and meteogram. High Δbias gives an indication of a less accurate delay field.

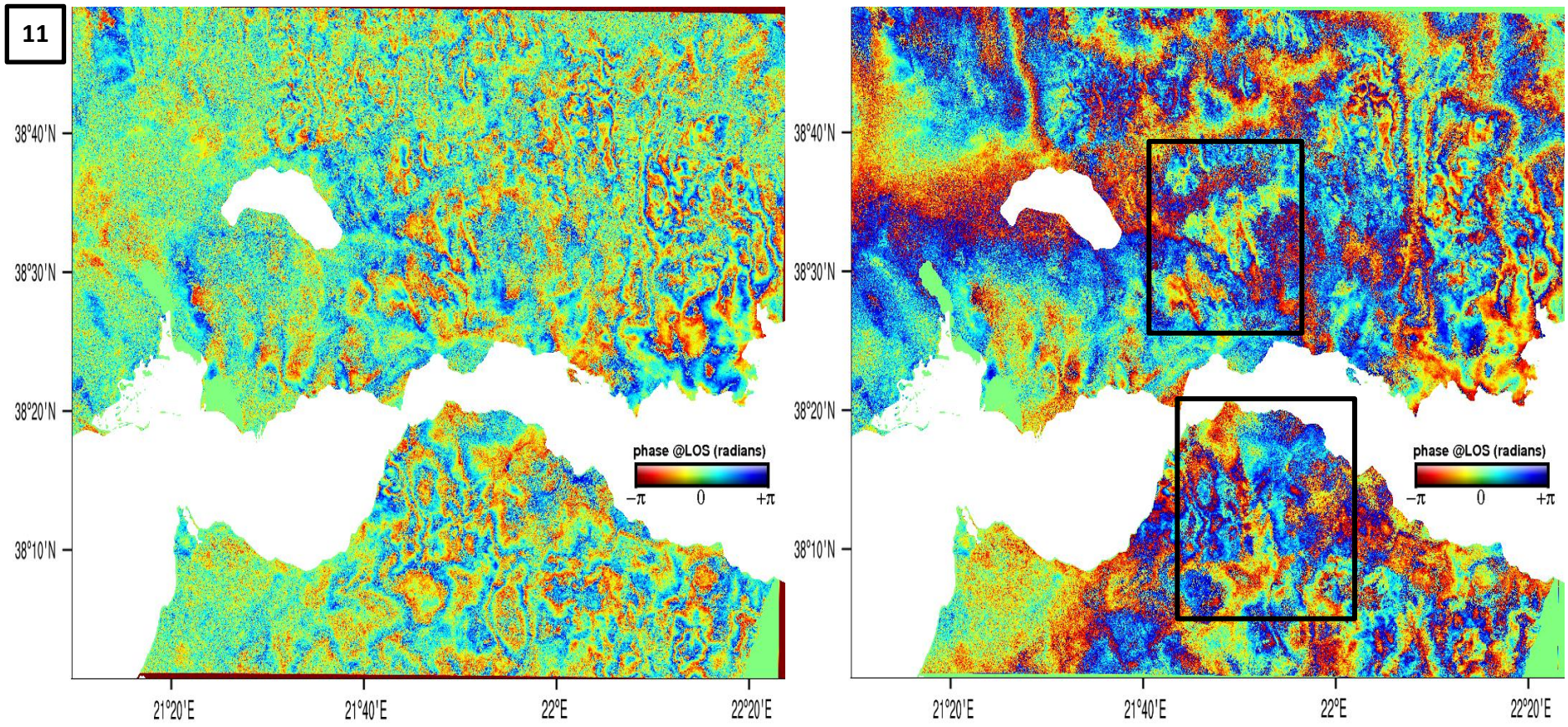

Figure 7-25. Wrapped interferogram from SAR acquisitions on 25/08/2016 and 30/09/2016, track 80 in radar geometry (left). Corresponding residual map after subtraction of WRF-derived wrapped differential LOS delay map from the interferogram (right). Troposheric corrections can be observed, in several areas of the map.

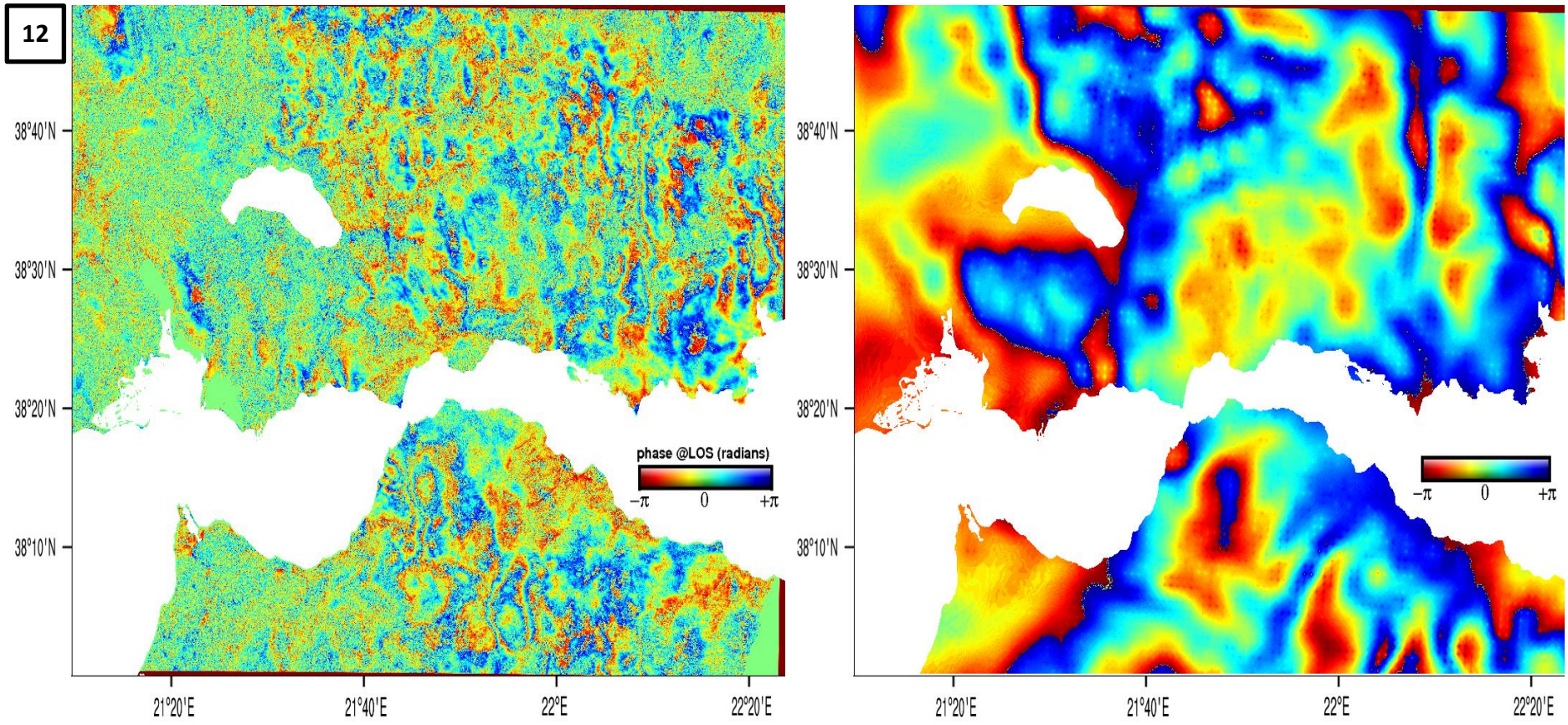

Figure 7-26. Wrapped interferogram from SAR acquisitions on 25/08/2016 and 18/10/2016, track 80 in radar geometry (left). Corresponding WRF-derived wrapped differential LOS delay map from the interferogram (right). The low coherence in the interferogram masks the tropospheric signal. However, several atmospheric artifacts are distinguished.

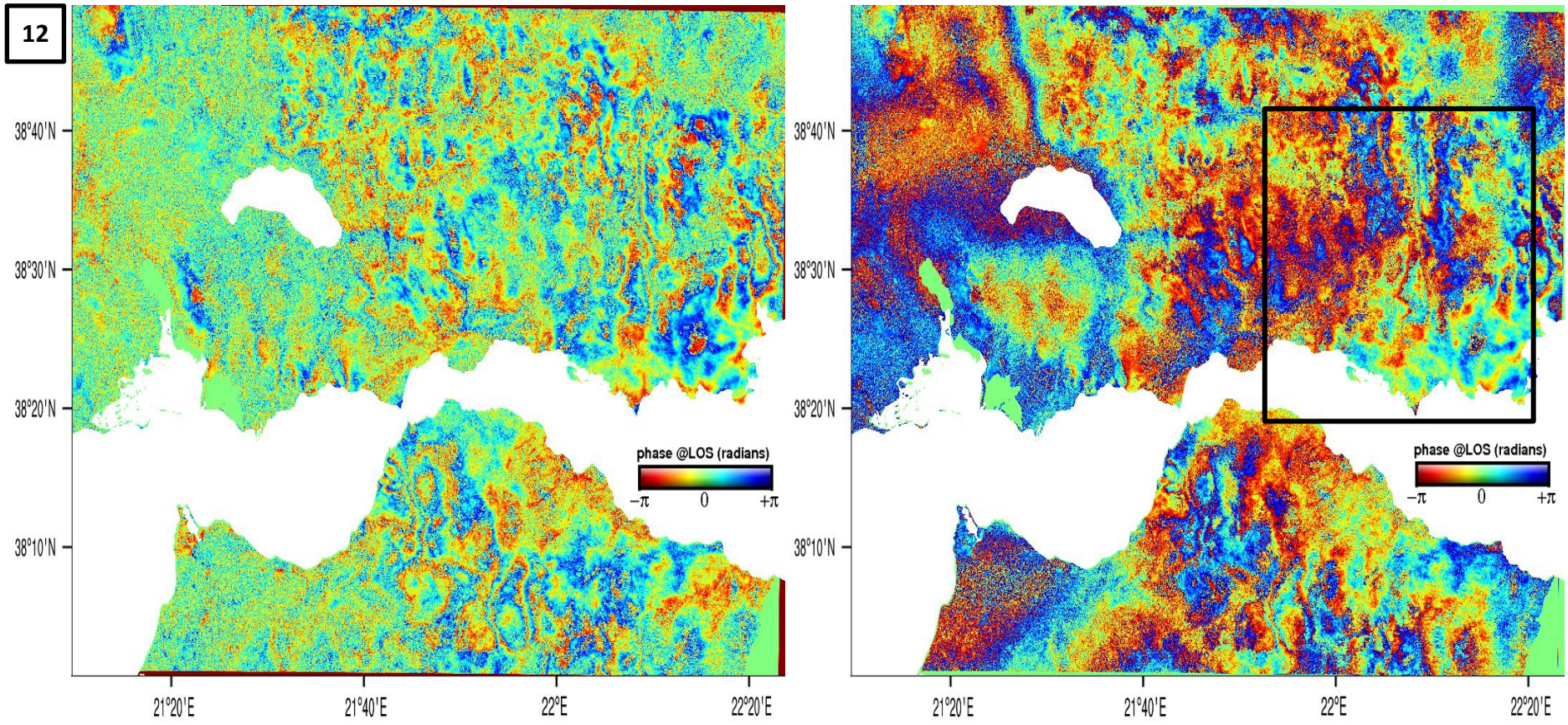

Figure 7-27. Wrapped interferogram from SAR acquisitions on 25/08/2016 and 18/10/2016, track 80 in radar geometry (left). Corresponding residual map after subtraction of WRF-derived wrapped differential LOS delay map from the interferogram (right). The fringe continuity is improved after correction, in areas of good coherence (i.e. Galaxidi – Lidoriki area).

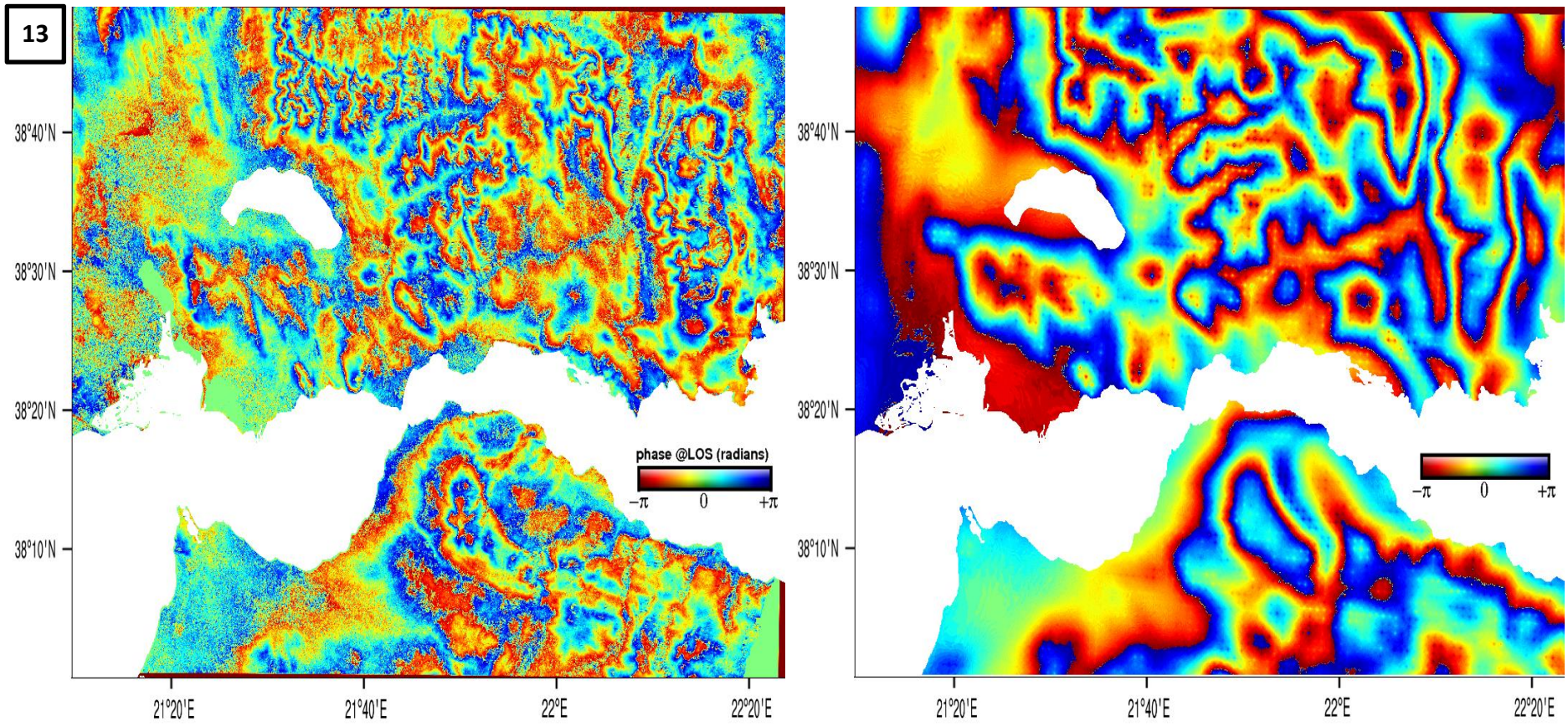

Figure 7-28. Wrapped interferogram from SAR acquisitions on 18/09/2016 and 30/09/2016, track 80 in radar geometry (left). Corresponding WRF-derived wrapped differential LOS delay map (right). An example of good consistency between WRF and GNSS, is also reflected in the good correlation between the interferogram and the delay map, with short and long wavelengths being observed.

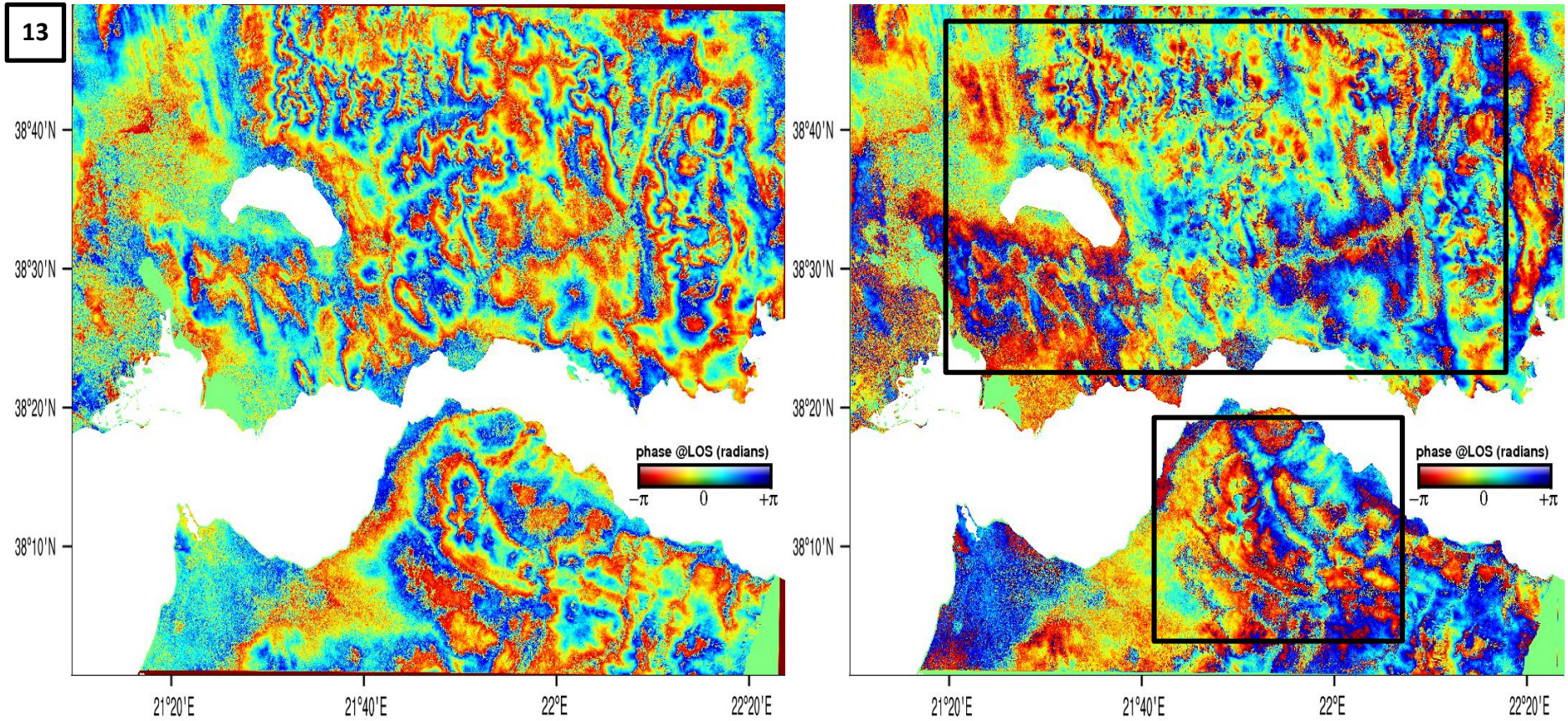

Figure 7-29. Wrapped interferogram from SAR acquisitions on 18/09/2016 and 30/09/2016, track 80 in radar geometry (left). Corresponding residual map after subtraction of WRF-derived wrapped differential LOS delay map from the interferogram (right). Good tropospheric corrections are observed across the whole extent of the interferogram in this case.

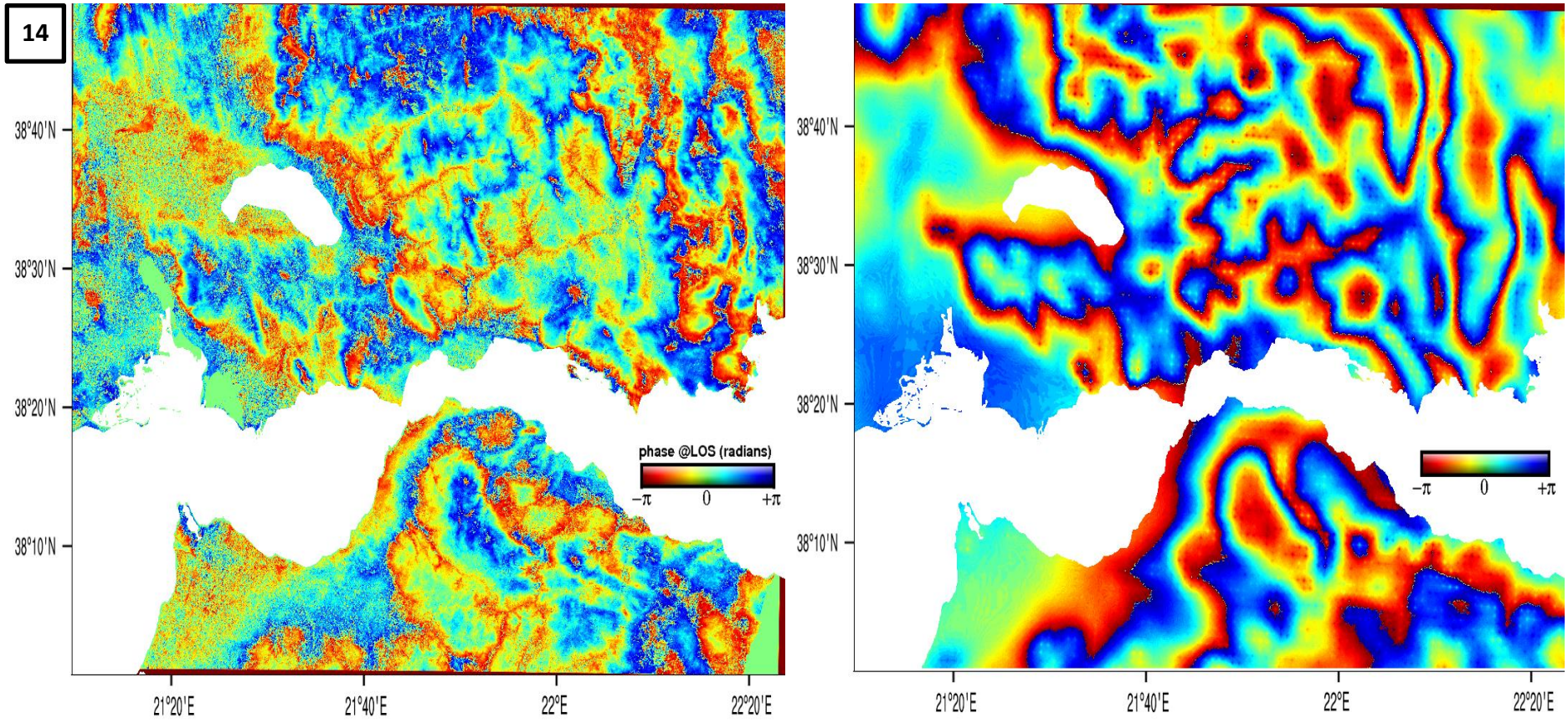

Figure 7-30. Wrapped interferogram from SAR acquisitions on 18/09/2016 and 06/10/2016, track 80 in radar geometry (left). Corresponding WRF-derived wrapped differential LOS delay map (right). Although Δbias is high, the differential troposphere is partly recreated in the corresponding delay map.

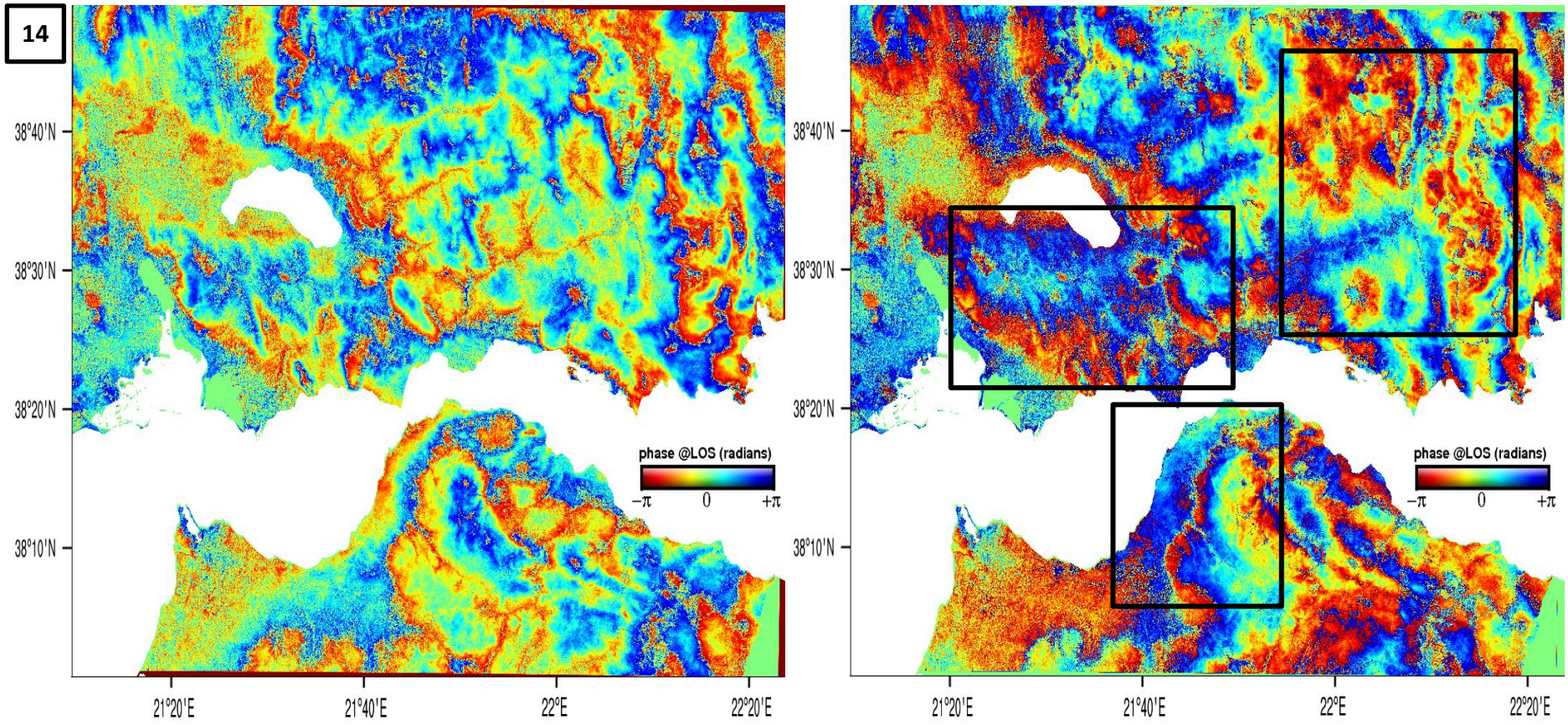

Figure 7-31. Wrapped interferogram from SAR acquisitions on 18/09/2016 and 06/10/2016, track 80 in radar geometry (left). Corresponding residual map after subtraction of WRF-derived wrapped differential LOS delay map from the interferogram (right). Fair tropospheric corrections are observed across certain areas of the interferogram in this case.

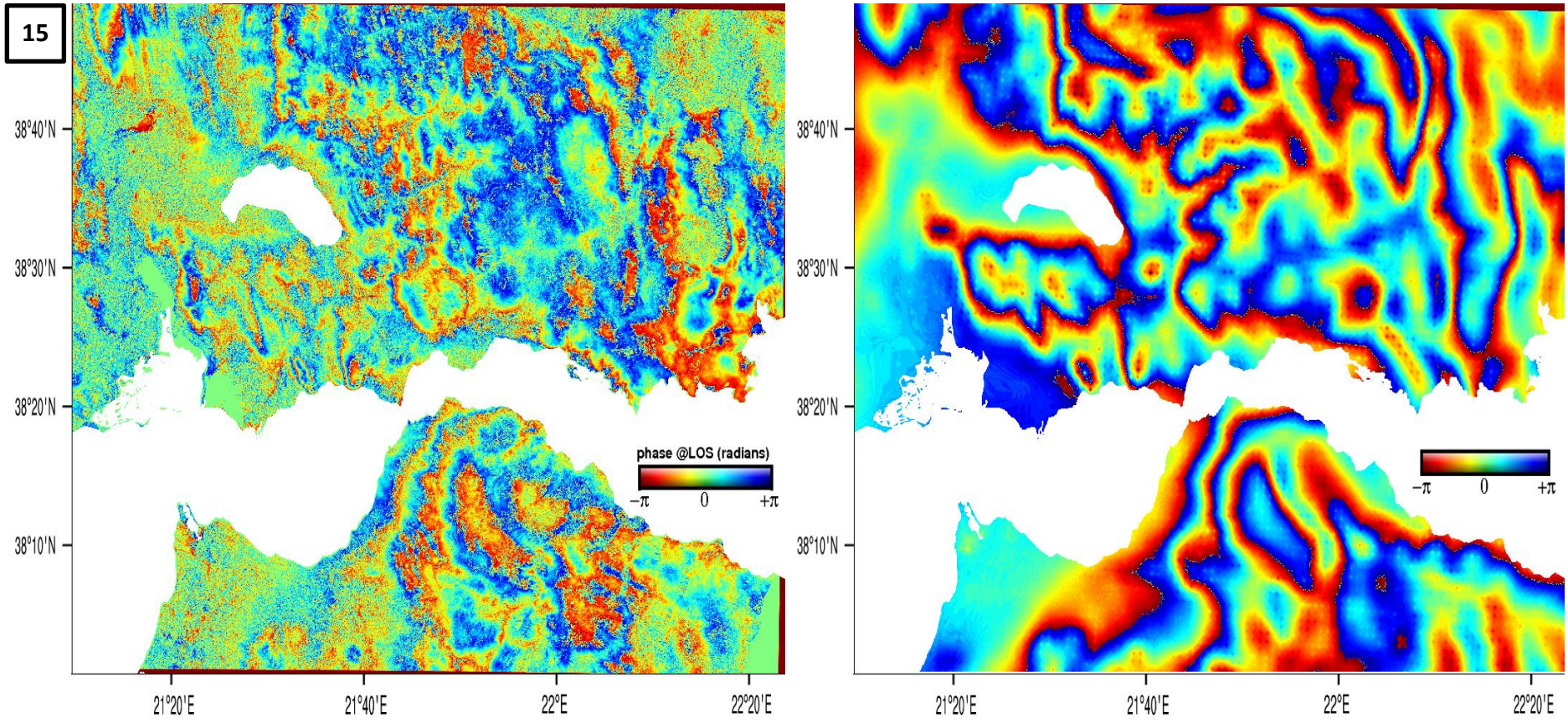

Figure 7-32. Wrapped interferogram from SAR acquisitions on 18/09/2016 and 18/10/2016, track 80 in radar geometry (left). Corresponding WRF-derived wrapped differential LOS delay map (right). Example similar to 14, but with lower coherence. Interferogram and meteogram fit relatively well here visually, particularly in the Mornos valley and northern Peloponnese.

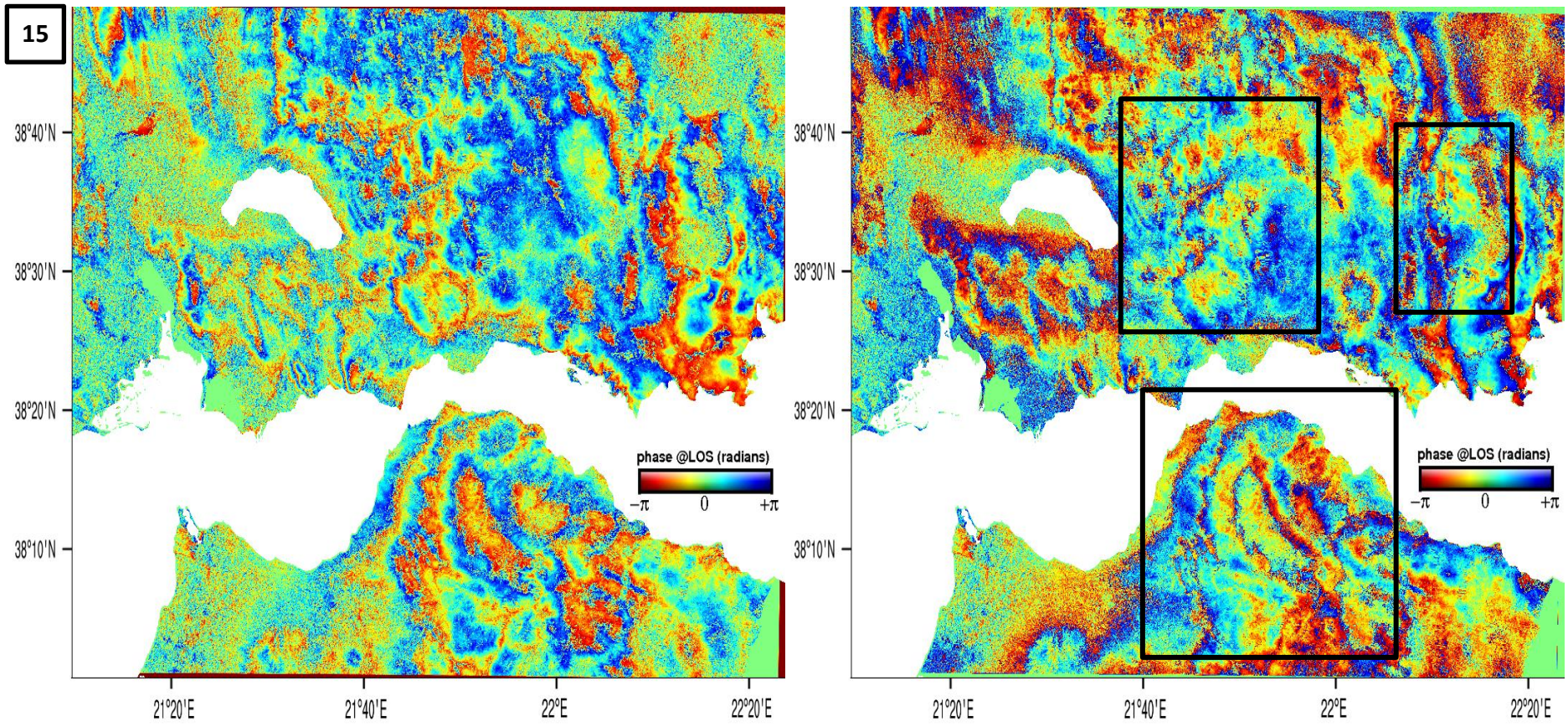

Figure 7-33. Wrapped interferogram from SAR acquisitions on 18/09/2016 and 18/10/2016, track 80 in radar geometry (left). Corresponding residual map after subtraction of WRF-derived wrapped differential LOS delay map from the interferogram (right). Fringe continuity is improved, particularly in the mountains of northern Peloponnese and Mornos valley.

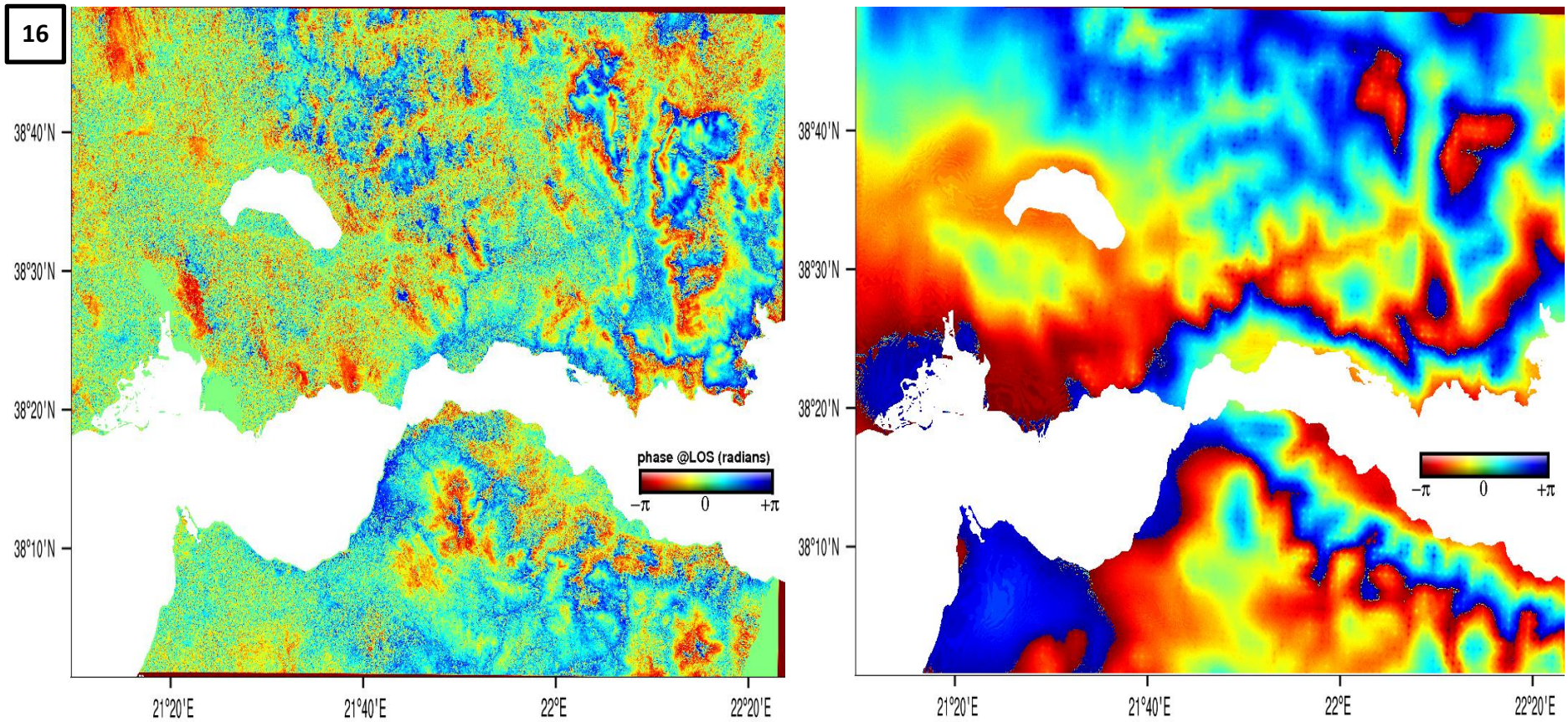

Figure 7-34. Wrapped interferogram from SAR acquisitions on 06/10/2016 and 24/10/2016, track 80 in radar geometry (left). Corresponding WRF-derived wrapped differential LOS delay map. Fair agreement between interferogram and delay map.

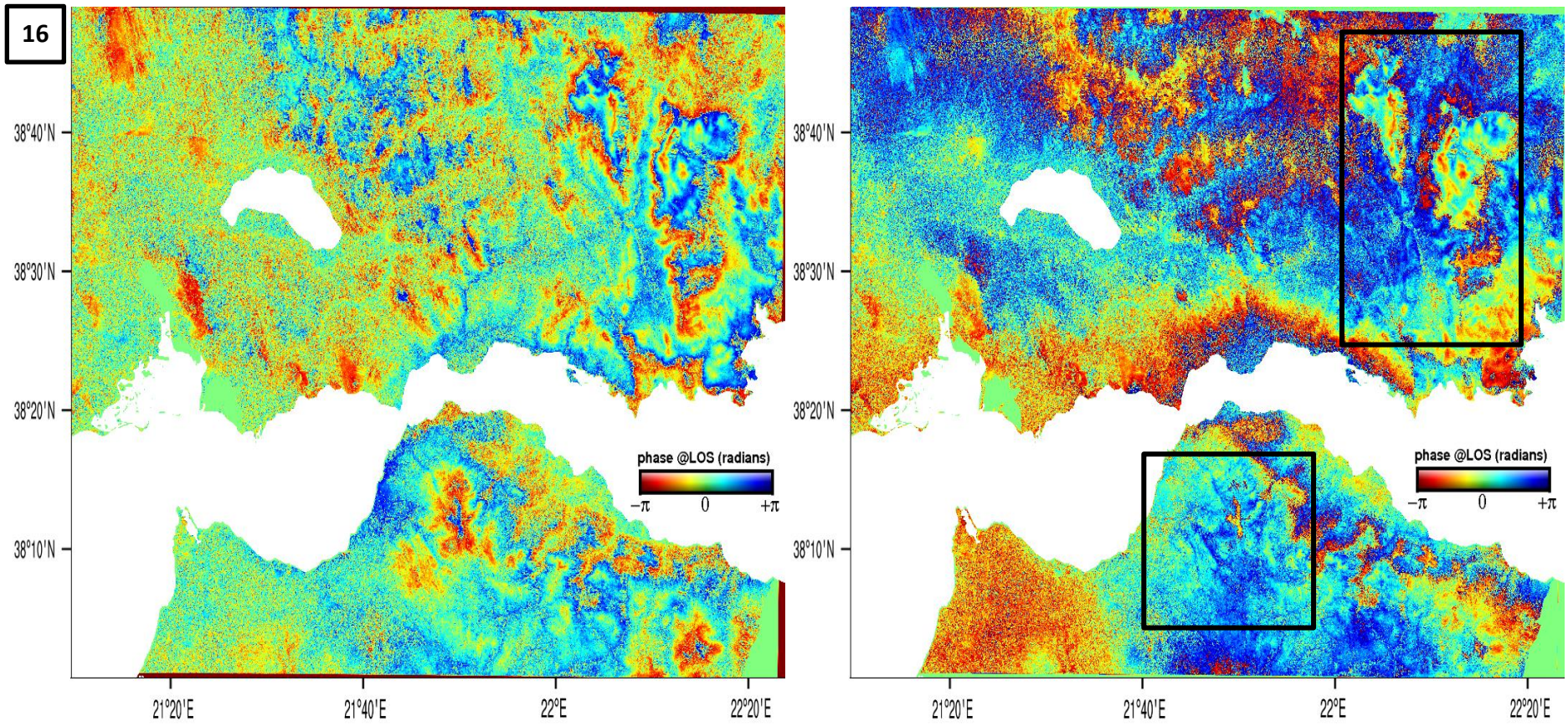

Figure 7-35. Wrapped interferogram from SAR acquisitions on 06/10/2016 and 24/10/2016, track 80 in radar geometry (left). Corresponding residual map after subtraction of WRF-derived wrapped differential LOS delay map from the interferogram (right). Tropospheric corrections can be observed but low coherence creates some aliasing in the residual map.

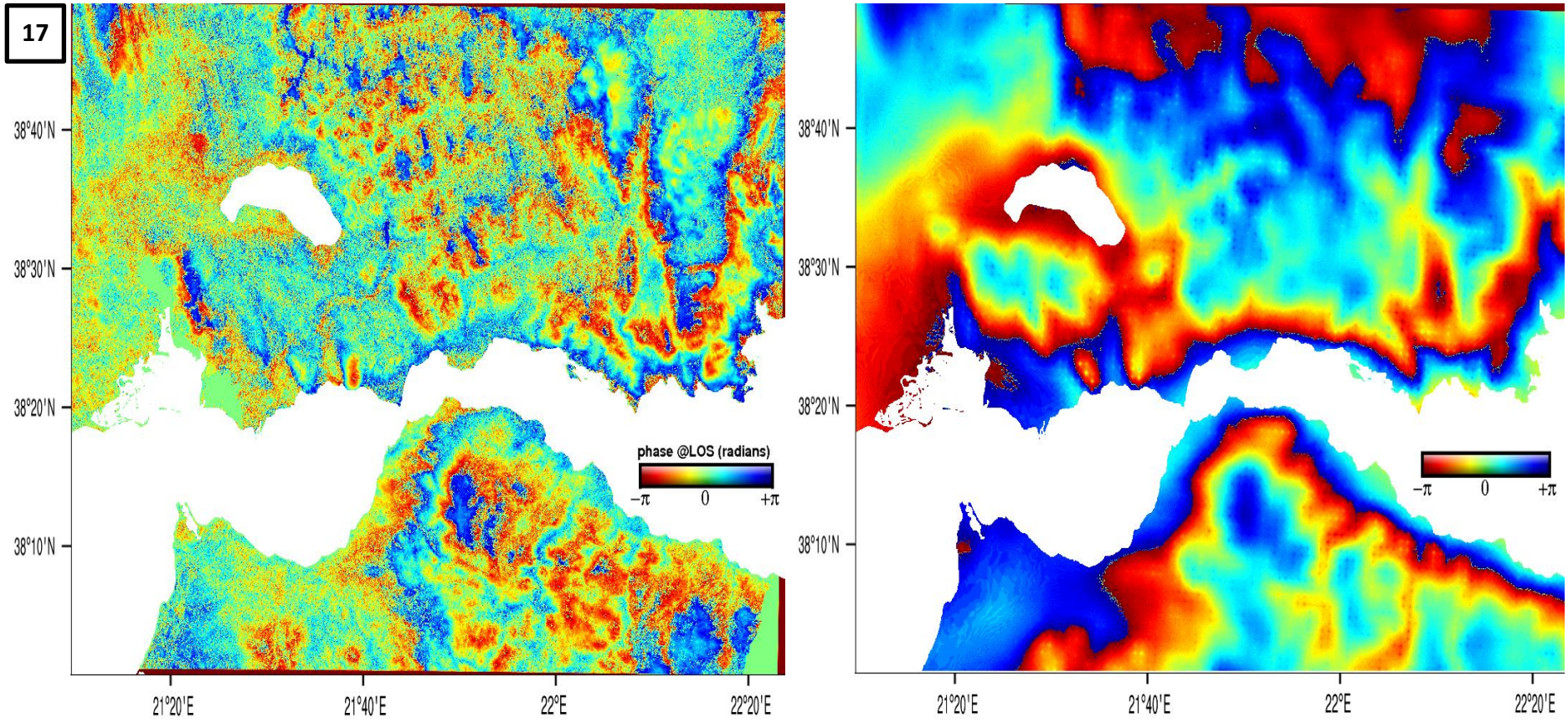

Figure 7-36. Wrapped interferogram from SAR acquisitions on 18/10/2016 and 24/10/2016, track 80 in radar geometry (left). Corresponding WRF-derived wrapped differential LOS delay map (right). Example of good consistency between WRF and GNSS, is also reflected in the comparison between the interferogram and the delay map, with short and long wavelengths being observed.

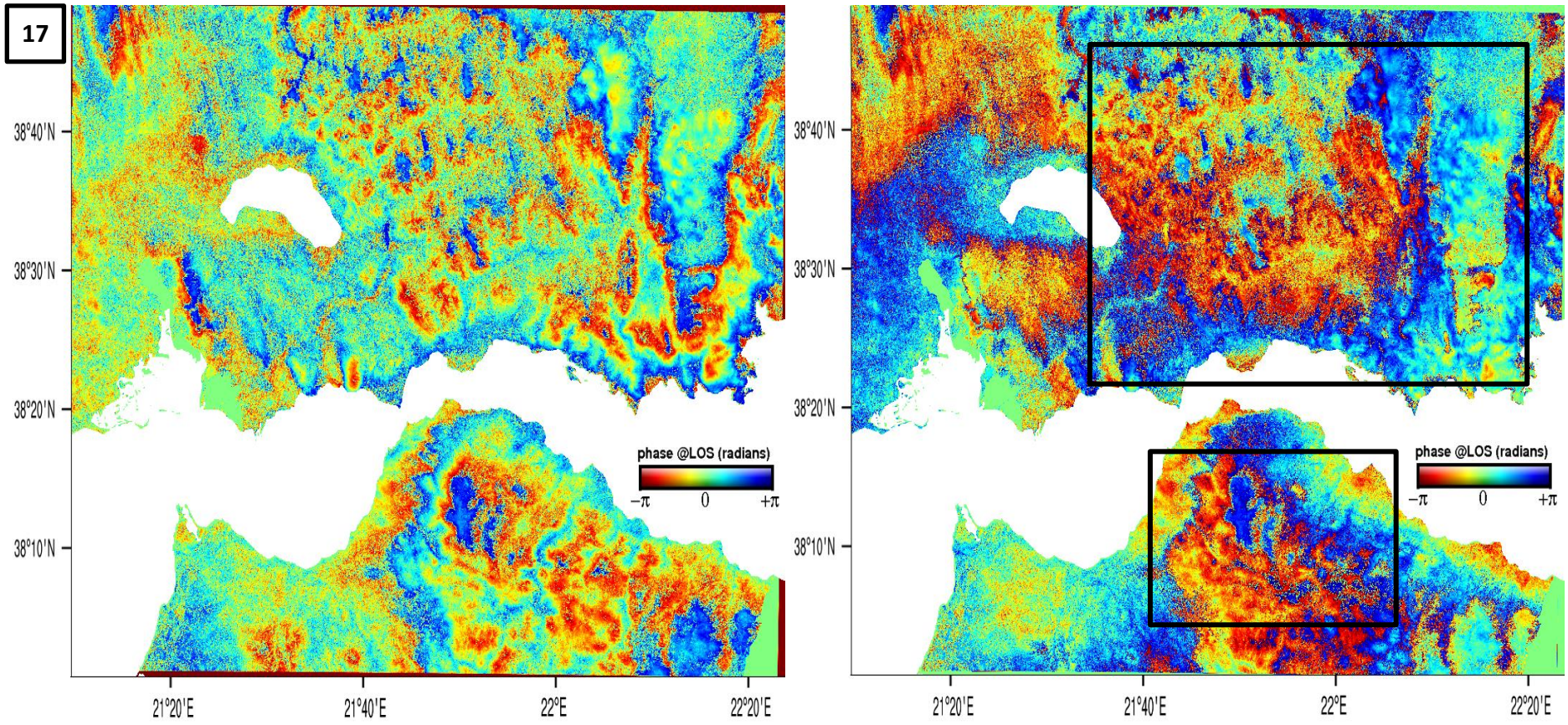

Figure 7-37. Wrapped interferogram from SAR acquisitions on 18/10/2016 and 24/10/2016, track 80 in radar geometry (left). Corresponding residual map after subtraction of WRF-derived wrapped differential LOS delay map from the interferogram (right). The resulting residual map shows a smoothing of the phase continuity in the whole extent.

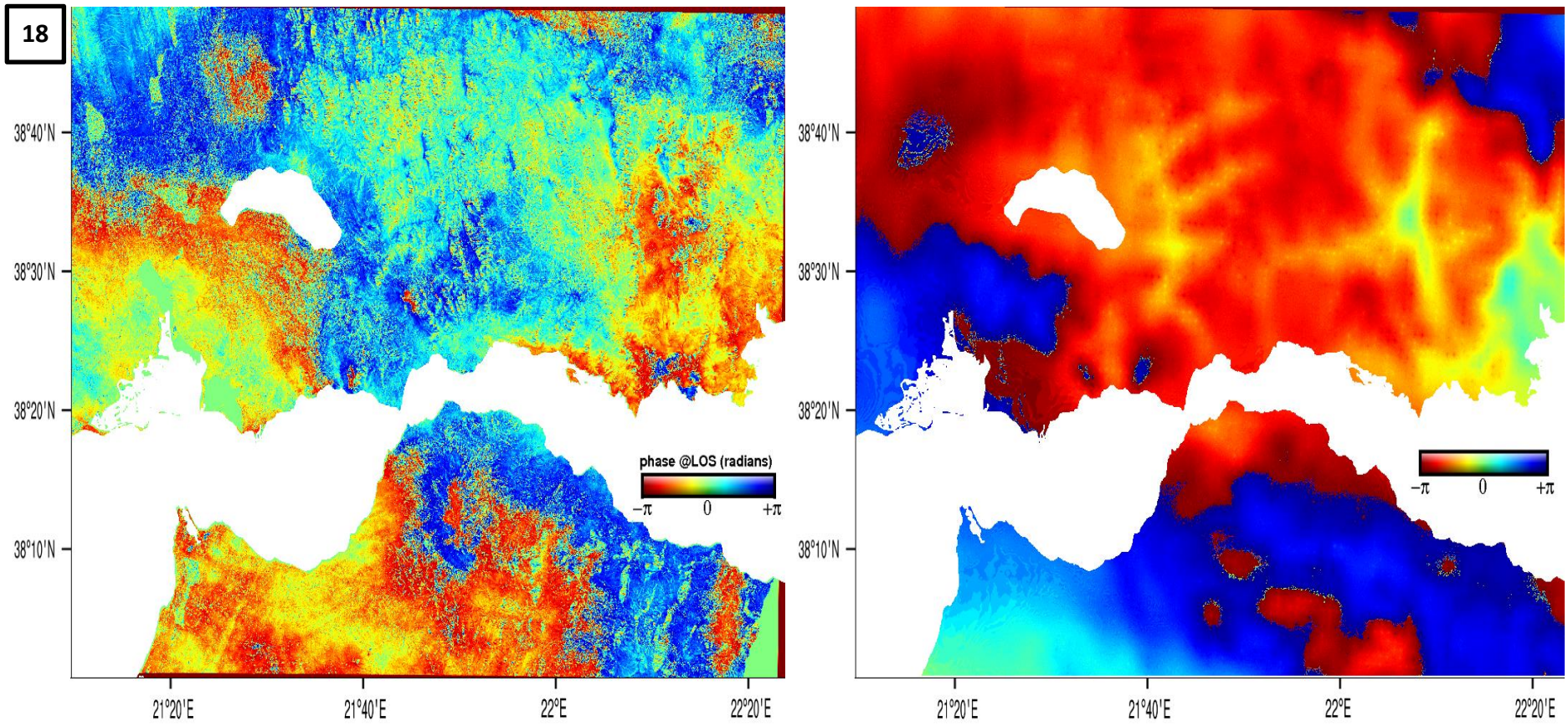

Figure 7-38. Wrapped interferogram from SAR acquisitions on 17/11/2016 and 23/11/2016, track 80 in radar geometry (left). Corresponding WRF-derived wrapped differential LOS delay map (right). In this case, tropospheric aspects are minor, as seen in both the interferogram and the WRF delay map, due to the absence of differential atmosphere between the two scenes.

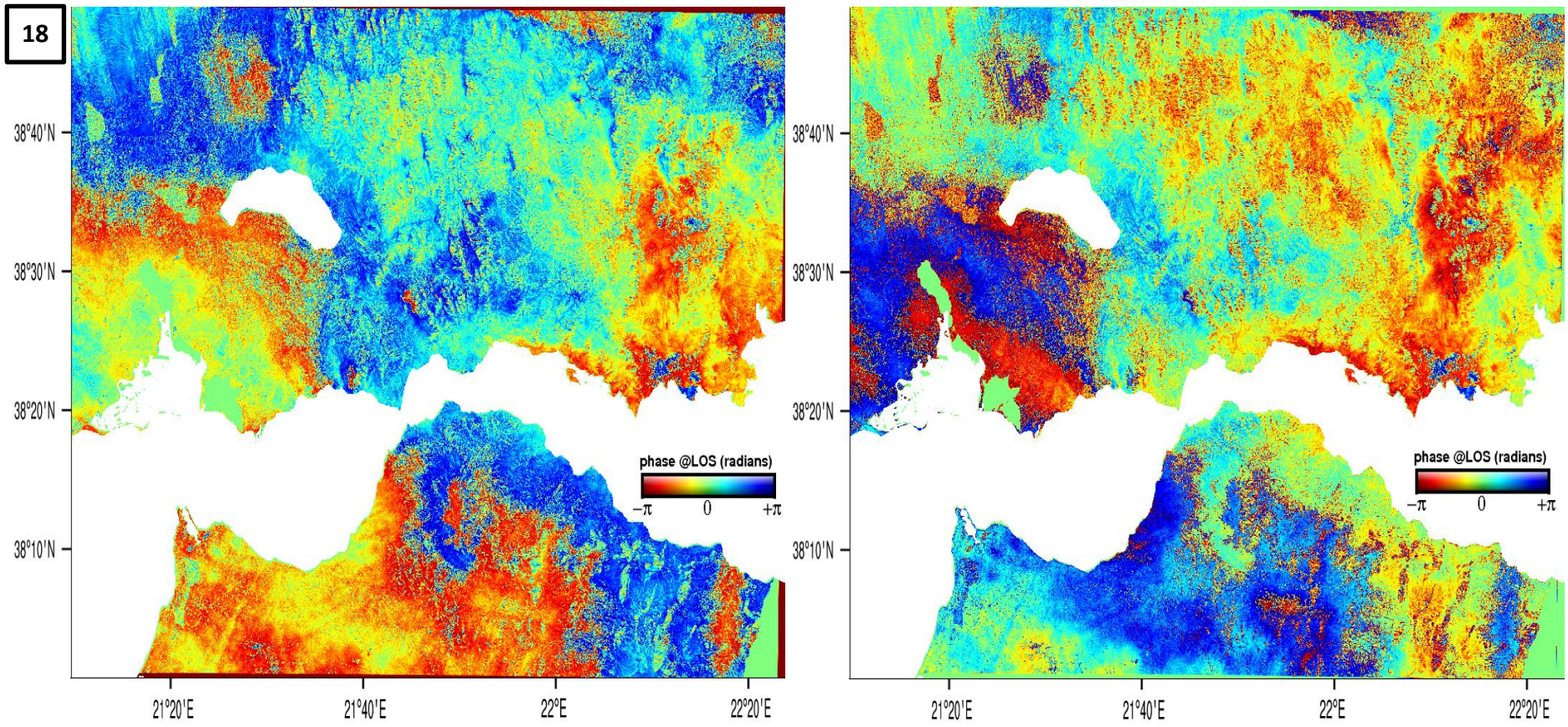

Figure 7-39. Wrapped interferogram from SAR acquisitions on 17/11/2016 and 23/11/2016, track 80 in radar geometry (left). Corresponding residual map after subtraction of WRF-derived wrapped differential LOS delay map from the interferogram (right). The tropospheric correction has a minimum impact in this case, as tropospheric fringes are absent.

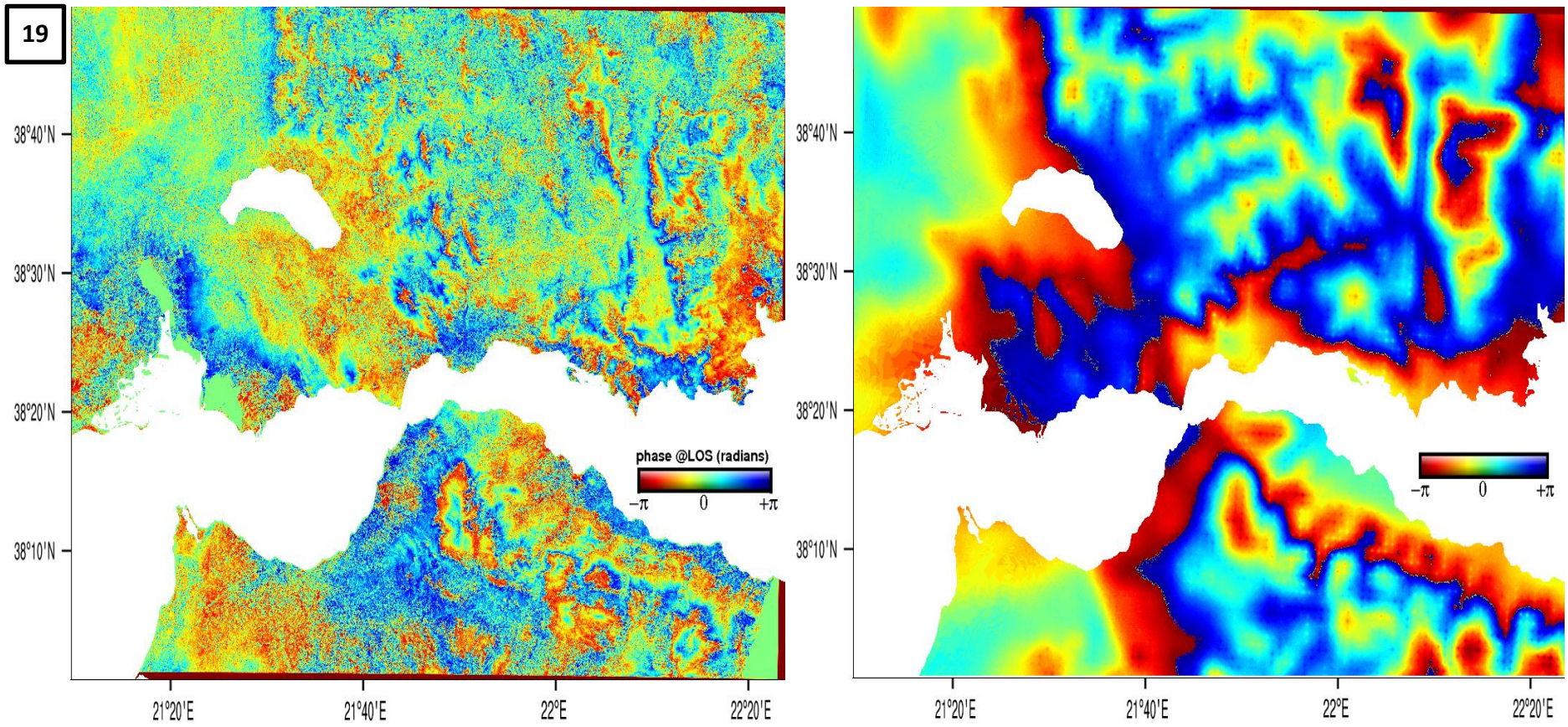

Figure 7-40. Wrapped interferogram from SAR acquisitions on 29/11/2016 and 11/12/2016, track 80 in radar geometry (left). Corresponding WRF-derived wrapped differential LOS delay map (right). Several tropospheric artifacts are respresented in the delay map, in areas of high coherence (Mornos valley and east of lake Trichonis, Panachaiko mountain).

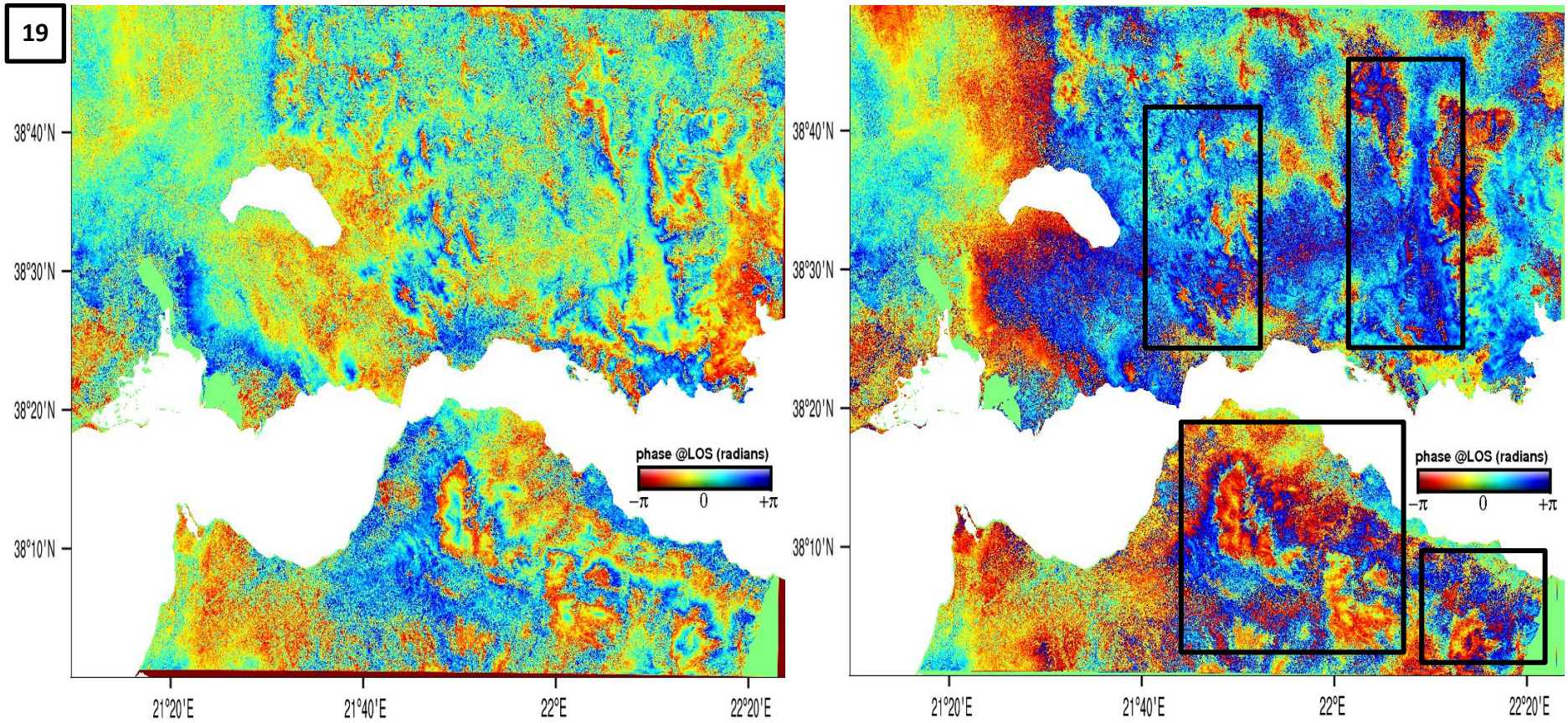

Figure 7-41. Wrapped interferogram from SAR acquisitions on 29/11/2016 and 11/12/2016, track 80 in radar geometry (left). Corresponding residual map after subtraction of WRF-derived wrapped differential LOS delay map from the interferogram (right). Tropospheric correction leads to a significant decrease of the phase gradient in areas of the interferogram where coherence is high, as shown by the black boxes in the residual image.

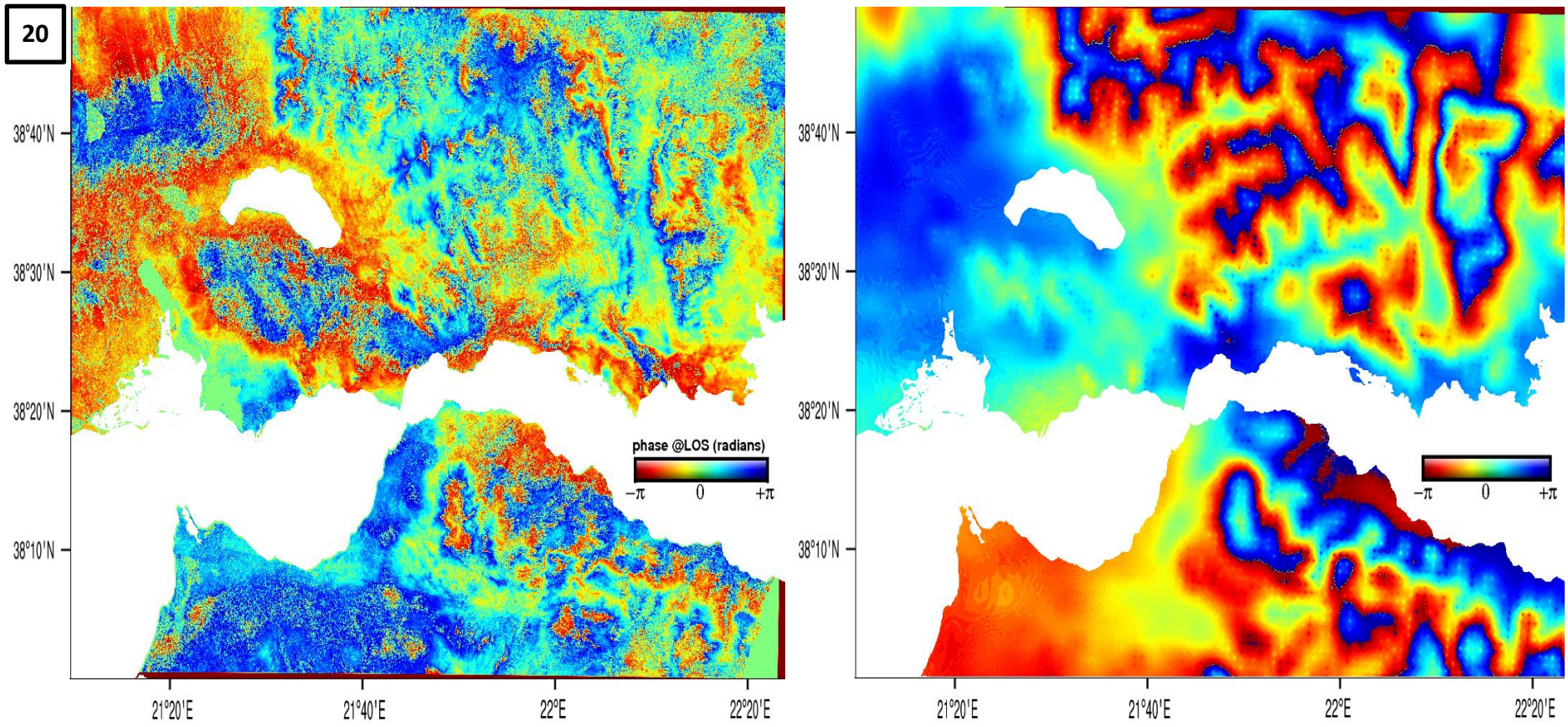

Figure 7-42. Wrapped interferogram from SAR acquisitions on 05/12/2016 and 11/12/2016, track 80 in radar geometry (left). Corresponding WRF-derived wrapped differential LOS delay map (right). Good agreement between interferogram and delay map is observed, particularly on the eastern part.

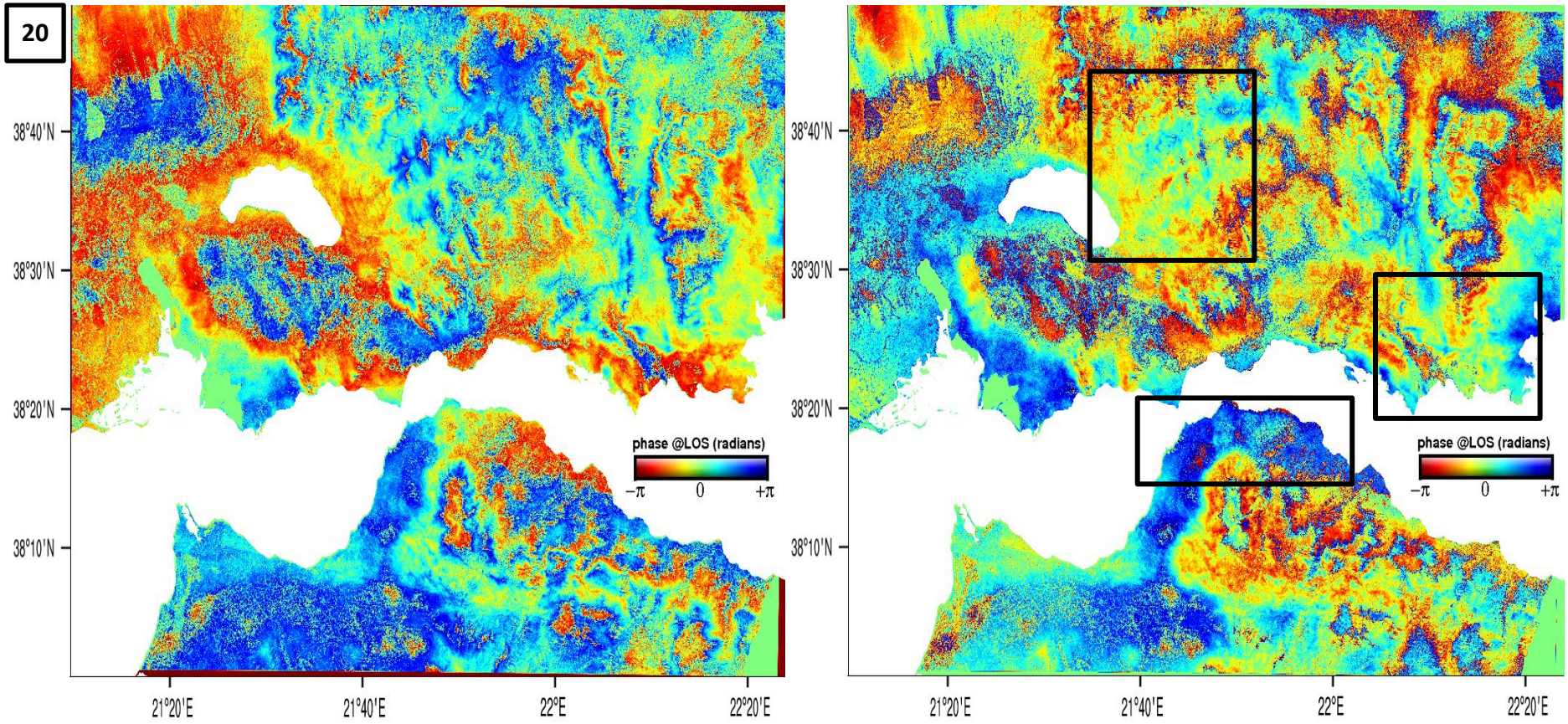

Figure 7-43. Wrapped interferogram from SAR acquisitions on 05/12/2016 and 11/12/2016, track 80 in radar geometry (left). Corresponding residual map after subtraction of WRF-derived wrapped differential LOS delay map from the interferogram (right). Some tropospheric corrections are observed across certain areas of the interferogram, but to a lesser degree compared with similar cases.

Table 7.1: Dates of Sentinel-1 interferograms examined, corresponding WRF vs. GNSS ZTD average bias differences (Δbias), and RMS and SD differences between original and corrected interferograms

Example	Track	Dates	Δbias	RMS % reduction	SD % reduction	Coherence
1	175	30/09 – 06/10	20.4	7.5	23.7	HC
2	175	30/09 – 24/10	7.1	2.9	13.4	MC
3	175	30/09 – 05/11	20.7	2.9	17.4	MC
4	175	06/10 – 24/10	16.1	2.9	17.1	MC
5	175	06/10 – 11/12	18.4	2.9	27.2	LC
6	175	24/10 – 05/11	19	7.7	18.9	HC
7	175	24/10 – 17/11	9.8	9.4	23.2	MC
8	175	24/10 – 23/11	8	2.8	13.7	MC
9	175	24/10 – 05/12	8.7	5.1	16.0	MC
10	80	25/08 – 18/09	31	0.0	14.2	MC
11	80	25/08 – 30/09	34.1	0.0	10.8	LC
12	80	25/08 – 18/10	13.6	-4.1	8.3	LC
13	80	18/09 – 30/09	7.2	3.8	19.0	HC
14	80	18/09 – 06/10	23.8	4.4	13.7	HC
15	80	18/09 – 18/10	18.9	12.3	23.5	MC
16	80	06/10 – 24/10	7.6	2.3	15.5	MC
17	80	18/10 – 24/10	4.9	7.3	15.5	HC
18	80	17/11 – 23/11	6.3	10.8	30.6	HC
19	80	29/11 – 11/12	21	-1.1	11.9	MC
20	80	05/12 – 11/12	3.9	14.1	32.7	HC

Apart from the quantitative assessment, corrections are also assessed qualitatively case by case, by identifying visible improvements in fringe continuity. In wrapped interferograms, the use of numerical indicators is not always adequate for assessing the degree of tropospheric phase gradient improvement, due to potential problems with pixel de-correlation (low coherence) in parts of the interferogram, or the existence of other components which contribute to the phase gradient. Case by case comments can be found in the legend of each figure. Summarising, we see that in examples where interferogram coherence is high and the forecasting skill of the WRF simulation is good, as predicted by GNSS measurements, the differential troposphere is significantly removed and the residual phase map exhibits smoother fringe continuity. However, corrections are not always visible across the whole interferogram, first of all because of the low coherence in the western part of the image (and other parts as well), secondly because of other errors (geometrical etc.), thirdly because the model does not recreate the differential atmosphere properly. More specifically:

- In cases where coherence is good (temporal baselines usually < 30 days) and Δ_{bias} is small (between 0 and 10 mm), the degree of tropospheric correction is high, resulting in a significant reduction of the density of tropospheric fringes in large sections of the interferogram, as indicated by the black boxes. This is illustrated in examples 2, 7, 8, 9 (track 175), and 13, 17, 18, 20 (track 80).
- In cases where coherence is low (temporal baselines usually > 30 days) and Δ_{bias} is small (between 0 and 10 mm), the degree of tropospheric correction is high only in areas with high coherence, as illustrated in examples 5 (track 175), and 12, 16, 19 (track 80).
- In cases where WRF-GNSS average bias differences are high (Δ_{bias} > 20 mm), the density of tropospheric fringes is reduced at a lesser degree, and the correction is localised in smaller areas of the interferogram, as illustrated in examples 1, 3 (track 175), and 10, 11, 14 (track 80).
- In interferograms where no differential troposphere is present, such as example 18, the application of tropospheric correction has a minimal impact on the resulting residual map. However, as atmospheric conditions are "dry" in both acquisition dates and Δbias is low, the meteogram is recreated accurately and improvements are visible in the residual map.
- Results suggest a reduction of both long-wavelength (5-50 km) and short-wavelength (< 5 km) phase delays. Residual maps exhibit a reduction of the stratified topography-correlated atmospheric signal, but most importantly, a reduction of the difficult to detect turbulent atmospheric signal (i.e. "wet" delay) in complex topographical structures of the scale of a few km, such as river incisions, valleys etc. (e.g. Figures 2, 9, 10, 13, 14, 15, 17).

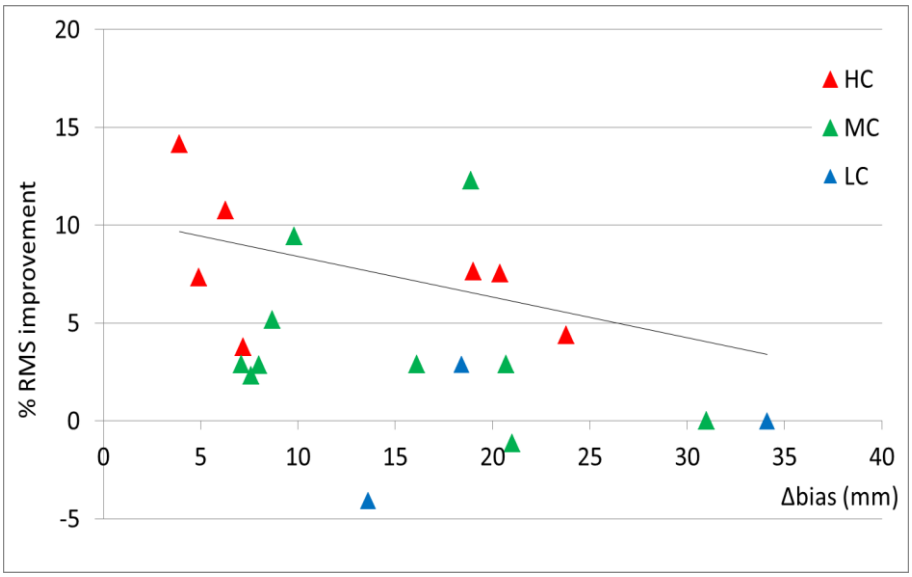

Figure 7-44: Correlation of RMS reduction between original and corrected interferograms and Δ_{bias}. Colours correspond to coherence (red=high, green=medium, blue=low).

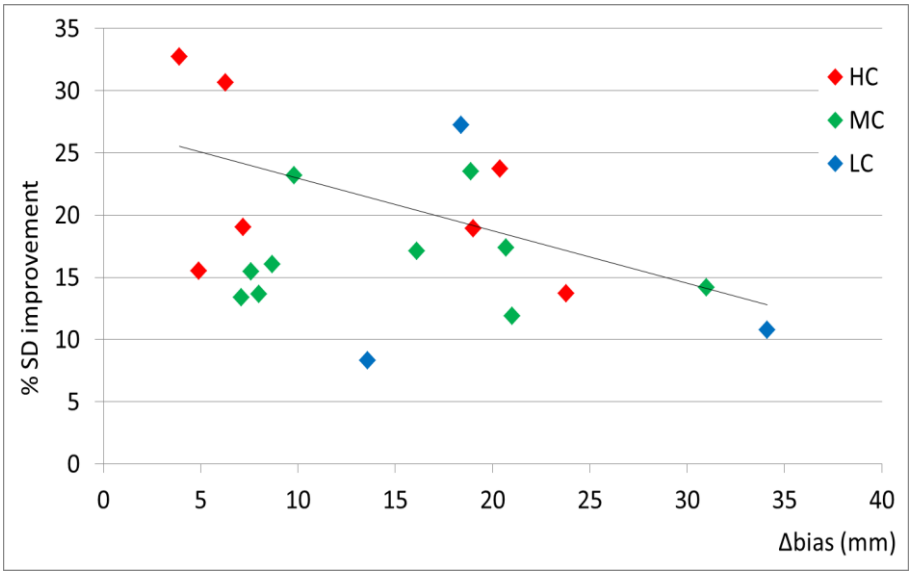

Figure 7-45: Correlation of SD reduction between original and corrected interferograms and Δ_{bias}. Colours correspond to coherence (red=high, green=medium, blue=low).

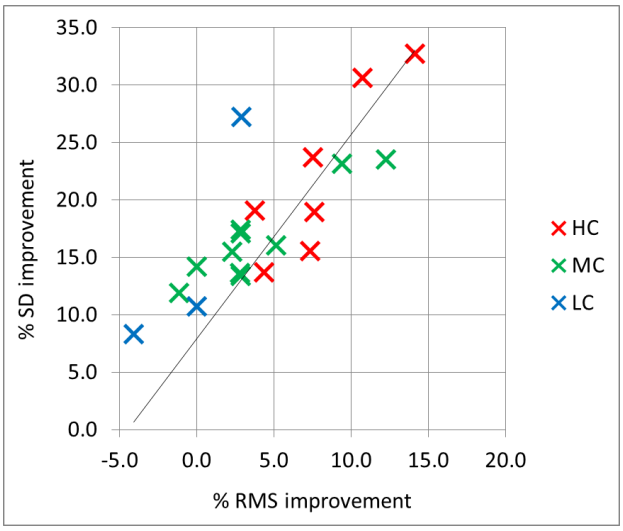

Figure 7-46: Correlation of % SD reduction vs. % RMS reduction for the 20 cases studied. Colours correspond to coherence (red=high, green=medium, blue=low).

7.4 Concluding Remarks

Overall, the current study demonstrates the high potential and effectiveness of using high-resolution atmospheric modelling (WRF in this instance), for correcting the effects of tropospheric delay on InSAR observations and correcting atmospheric phase gradients in interferograms. The proposed methodology augments the model's ability to predict zenithal delays in the western Gulf of Corinth, by fine-tuning its physical parameterization with the use of ZTD measurements from GNSS permanent stations. Furthermore, by introducing a high-resolution topography (ASTER 1s DEM), the calculation of ZTD delay fields has become more accurate and bias has been minimised.

The use of high-resolution LAMs, validated by GNSS measurements has a number of advantages over other methods which are currently used for removing the atmospheric phase screen in InSAR observations. First of all, it can be used over day and night and under any weather conditions. The method can be applied in any geographical location, as long as the LAM is locally configured and parameterized. Model output data can be retrieved at the exact times of InSAR acquisitions and the high spatial resolution (1-km) and dense vertical layering is capable of capturing near-surface atmospheric processes where complex topography is present (such as sea breezes, orographic flows, turbulent boundary layer interactions etc.). This is particularly useful when it comes to estimating the highly variable water vapour signals which are exhibited in the differential atmosphere as densely distributed short-wavelength phase gradients.

Tropospheric corrections performed over a set of 20 wrapped Sentinel-1 interferograms with the use of high-resolution WRF-derived delay fields have led to significant reductions of atmospherically-related phase gradients. The actual degree of correction is related to the WRF-GNSS ZTD average bias difference between the two acquisition epochs, and this can be a useful indicator for determining the effectiveness of the approach based on the model's forecasting skill. Results suggest that both the stratified and the turbulent atmospheric signal can be reduced from wrapped interferograms. This is a fair improvement compared with predictive methods based on coarser GAMs, which are effective in reducing only lateral variations in stratification.

The removal of the differential tropospheric signal before the unwrapping process is beneficial for the correct estimation of the remaining noise in the interferogram. The phase ambiguity due to aliasing of atmospheric gradients in regions of rough topography is reduced and this minimises unwrapping errors. This will eventually lead to more reliable final products, thus enabling the detection of ground deformation signals in single interferograms (i.e. in the case of an earthquake), and improving velocity field estimates by resolving lateral variations in stratification in InSAR time series analysis.

8. Conclusions – Recommendations for Future Work

The primary objective of the PhD Thesis was to investigate the extent to which a high-resolution weather model, such as WRF, tied with GNSS zenithal tropospheric delays, can produce tropospheric delay maps of the required accuracy, for performing corrections of the atmospheric phase screen on SAR interferograms. Results suggest a potential of the proposed methodology in regions with similar characteristics as the Western Gulf of Corinth, where InSAR detection of ground deformations due to active tectonic processes is inhibited by complex topography and variable tropospheric conditions. The principal findings of this Thesis are the following:

1. In the first phase, the WRF model was operated with varying parameterization in order to assess the best possible configuration for our case study, with GNSS measurements providing a benchmark of accurate ZTDs at 19 locations. Five different WRF schemes were tested (all with a 1-km resolution in the inner domain), ranging from schemes with relatively simple physical and dynamical parameterization to more complex schemes which require longer computational times. Results from the sensitivity analysis that followed were tested for their statistical significance and demonstrated that a more complex physical parameterization scheme suited for high-resolution scenarios, coupled with a high-resolution ASTER 1s DEM underlying topography, had the best performance with respect to ZTD output.

2. Following the selection of the optimal WRF scheme, model output was validated for the year 2016 with the use of observational tropospheric data from the CRL GNSS network in the western Gulf of Corinth. Correlation between predicted and observed ZTDs at the 19 PaTrop stations was high throughout the year (correlation co-efficient ranges from 0.91-0.93), with mean bias (MB) ranging from -29.5 mm (PAT0 station) to 6.4 mm (KRIN station), indicating that the model tends to slightly underestimate the tropospheric ZTD as compared to the GNSS derived values. A further analysis of statistical indices revealed that this systematic negative offset (of the order of 15 mm) is caused by uncertainties in the model output, as well as uncertainties during processing of the tropospheric GNSS data. This systematic offset is however removed when a differential delay map is generated for the tropospheric correction of InSAR data. With respect to the seasonal component, model performance is better during the autumn period (October-December), followed by the spring period (April-June). On the contrary, model forecasting skill seems to deteriorate during summer (July-September), where correlation is weaker and MAB and RMSE values are higher.

3. Examining possible model failure mechanisms, WRF output was validated with independent meteorological data from a network of ground stations in the PaTrop area. A case where model output shows significant bias with respect to the observational GNSS dataset is investigated. Data analysis demonstrates that for the selected time period, large ZTD biases are mainly caused by “poor” surface pressure prediction due to errors in boundary

conditions ingested by the model, whereas smaller (and more frequent) ZTD biases are caused by a misrepresentation of the vertical water vapour profile by the model.

4. Tropospheric corrections performed over a set of 20 wrapped Sentinel-1 interferograms with the use of high-resolution WRF-derived delay fields have led to reductions of atmospherically-related phase gradients. The actual degree of correction is related to the WRF-GNSS ZTD average bias difference between the two acquisition epochs, and this can be a useful indicator for determining the effectiveness of the approach based on the model's forecasting skill.

5. Results suggest that both the long-wavelength stratified atmospheric signal and the short-wave turbulent atmospheric component might be reduced from interferograms. This could be an improvement compared to predictive methods based on coarser GAMs, which are effective in reducing only long-wavelength lateral variations in stratification.

6. The removal of the differential tropospheric signal before the unwrapping process is beneficial for the correct estimation of the remaining noise in the interferogram. The phase ambiguity due to aliasing of atmospheric gradients in regions of rough topography is reduced and this minimises unwrapping errors. This will eventually lead to more reliable final products, thus enabling the detection of ground deformation signals in single interferograms (i.e. in the case of an earthquake), and improving velocity field estimates by resolving lateral variations in stratification in InSAR time series analysis.

As far as future work and possible improvements to the proposed methodology, the following points can be made:

1. Efforts to improve the WRF high-resolution re-analysis forecasting skill over the western Gulf of Corinth, are expected to increase the accuracy of tropospheric correction on InSAR measurements. Such improvements could include: a) Use of newly available datasets of input conditions (such as the ERA5 re-analysis dataset available in 2018, with an improved 30-km resolution and an advanced data assimilation system), which can minimise errors due to unrepresentative boundary conditions ingested by WRF. b) A greater number of high-resolution physical parameterization schemes can be tested, as they become available, for possible improvements in the model's forecasting scheme, as well as an ensemble approach of different WRF parameterizations. c) Data assimilation of independent meteorological measurements, particularly related to water vapour forecasting (i.e. GNSS derived ZTDs), may also have a positive impact on model output.

2. The model evaluation analysis would further benefit from using integrated water vapour measurements in the vertical tropospheric column (IWV values) from remote sensing spectrometers (i.e. MERIS and MODIS), for studying 3-D water vapour fluctuations as estimated by the model.

3. Improvements in the calculation of the WRF-derived delay fields can also be tested as a method for increasing the degree of atmospheric correction across the entire interferogram. For example, using slant ranges of varying angles instead of zenithal delay values, may lead to better constraints on the tropospheric models at the 1-km scale.

4. Future research efforts should also focus on extending the applicability of the proposed method to cover more geographical areas of interest (e.g. the Ionian Islands, Etna Volcano in Sicily, Santorini Volcano), where similar geophysical characteristics are present and a large amount of data also exists, with respect to GNSS measurements and InSAR acquisitions. The tropospheric correction of interferograms and subsequent improvements in the detection of co-seismic, post-seismic and other types of ground deformation, following the same methodology, will prove the applicability of the model that was developed on a global scale, reflecting the strong impact that the current research will have for the study of geophysical processes with the use of remote sensing techniques.

Appendix A – Timeseries and bias plots of WRF MOD1-MOD5 vs. GNSS ZTDs for the test period (17-29 June 2016).

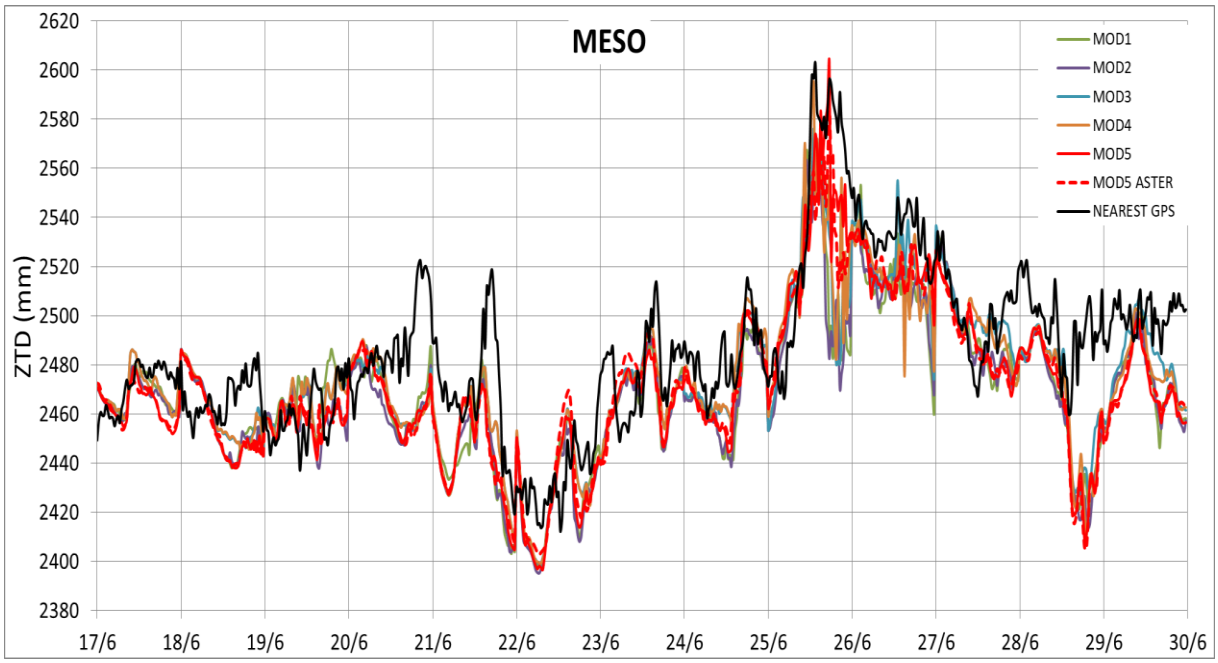

Figure A-1. MOD1-MOD5 WRF ZTDs vs. GNSS ZTDs, station MESO

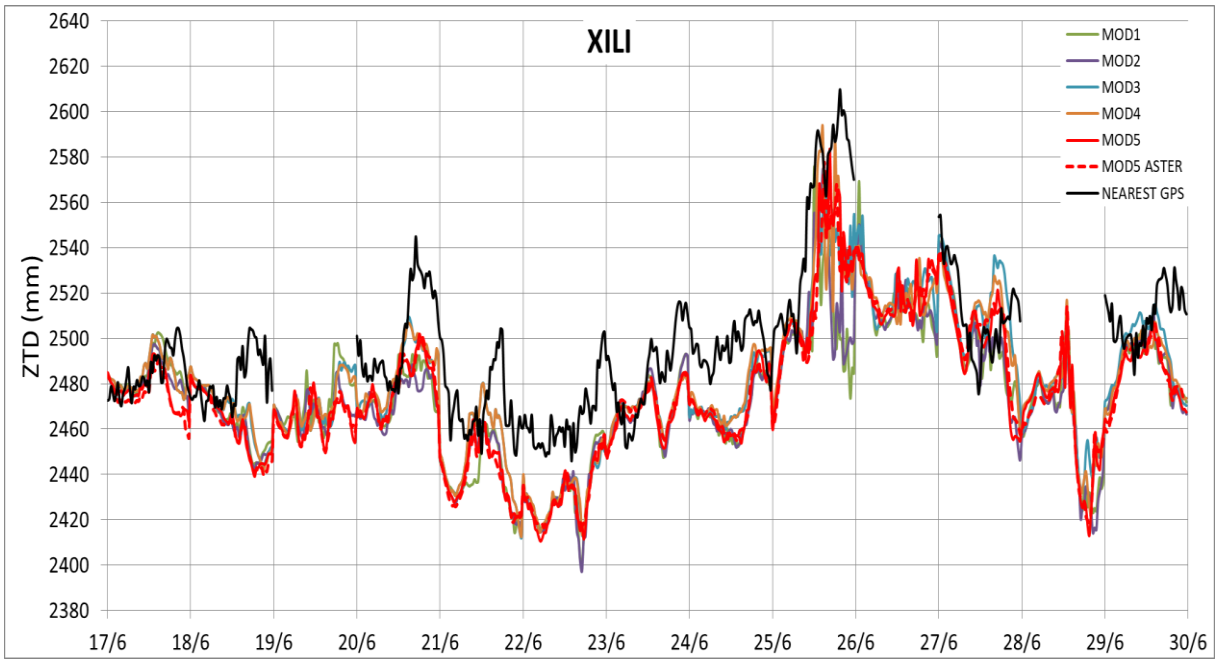

Figure A-2. MOD1-MOD5 WRF ZTDs vs. GNSS ZTDs, station XILI

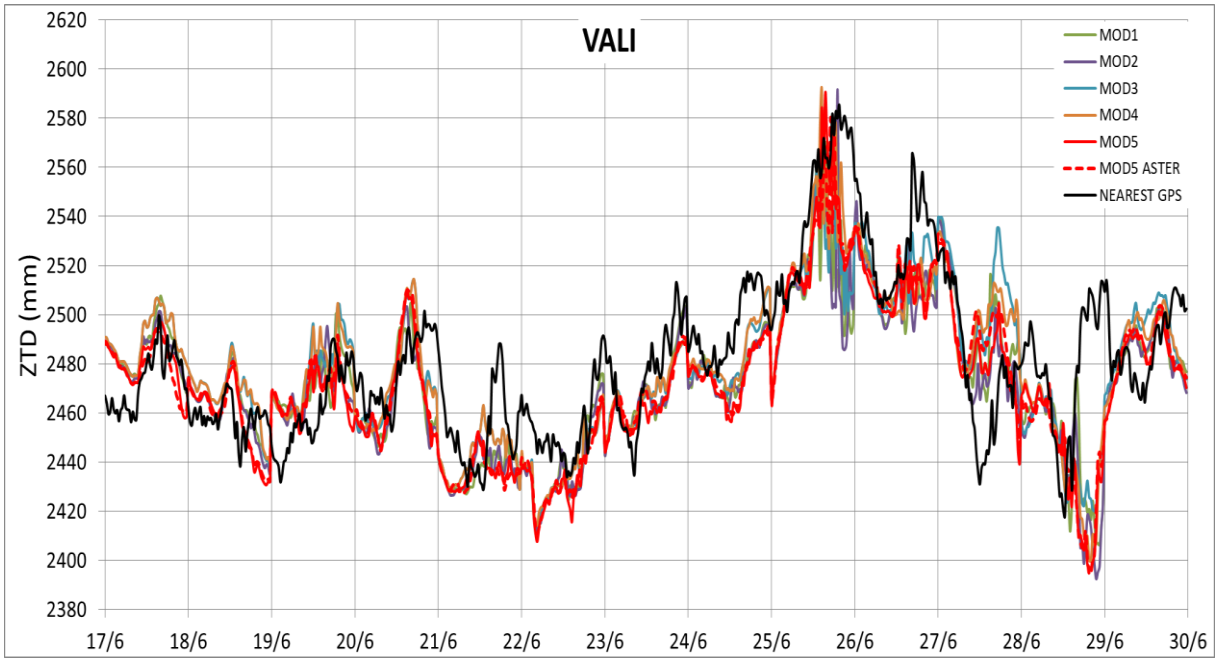

Figure A-3. MOD1-MOD5 WRF ZTDs vs. GNSS ZTDs, station VALI

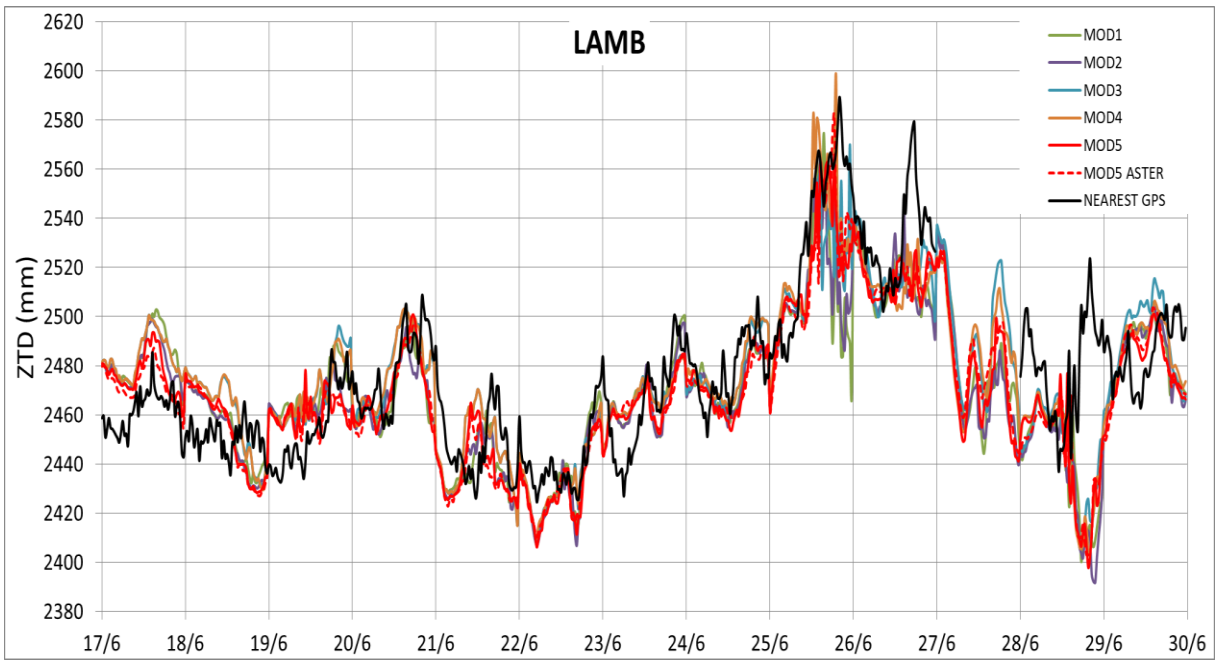

Figure A-4. MOD1-MOD5 WRF ZTDs vs. GNSS ZTDs, station LAMB

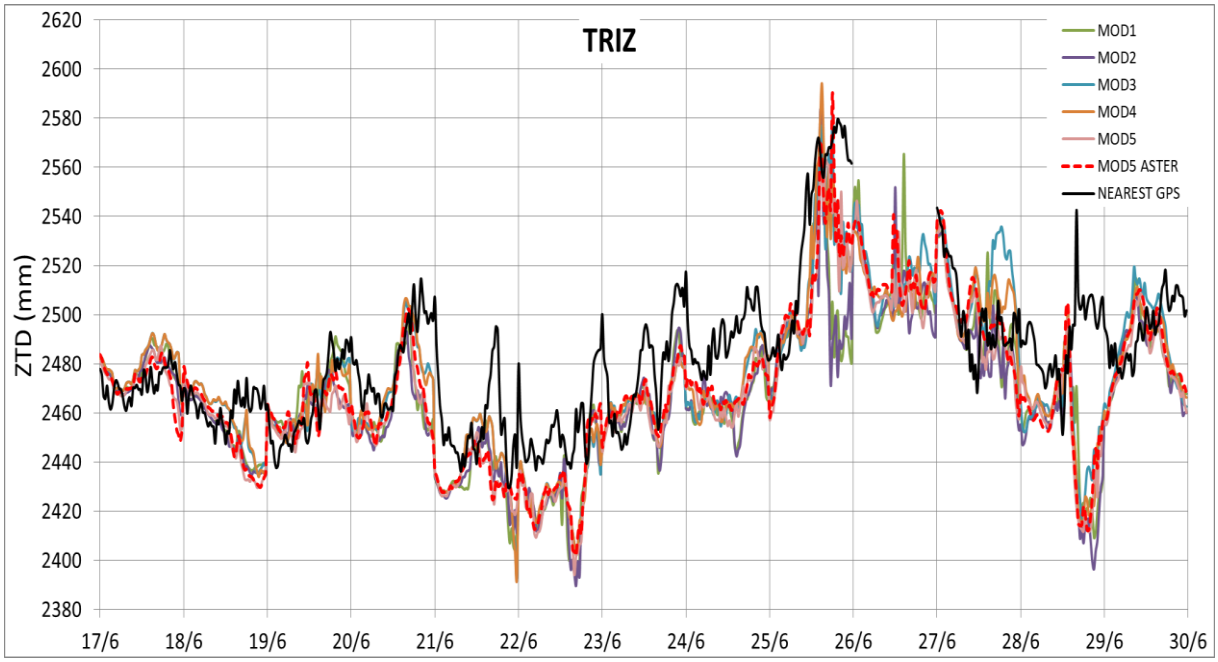

Figure A-5. MOD1-MOD5 WRF ZTDs vs. GNSS ZTDs, station TRIZ

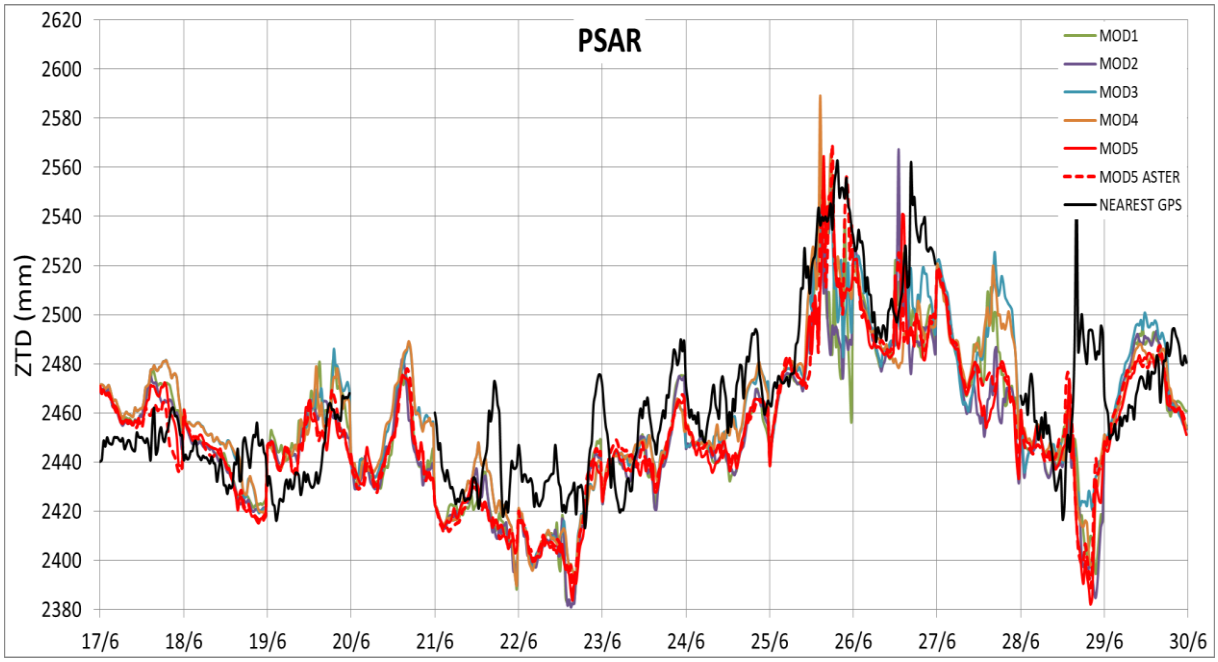

Figure A-6. MOD1-MOD5 WRF ZTDs vs. GNSS ZTDs, station PSAR

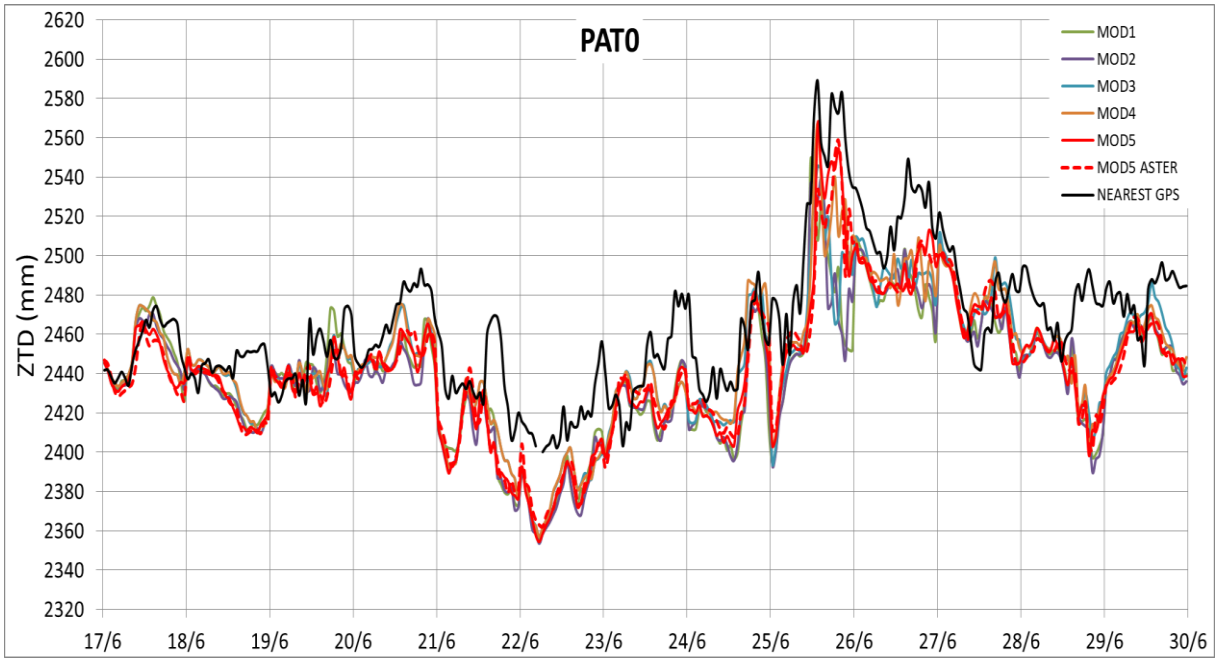

Figure A-7. MOD1-MOD5 WRF ZTDs vs. GNSS ZTDs, station PAT0

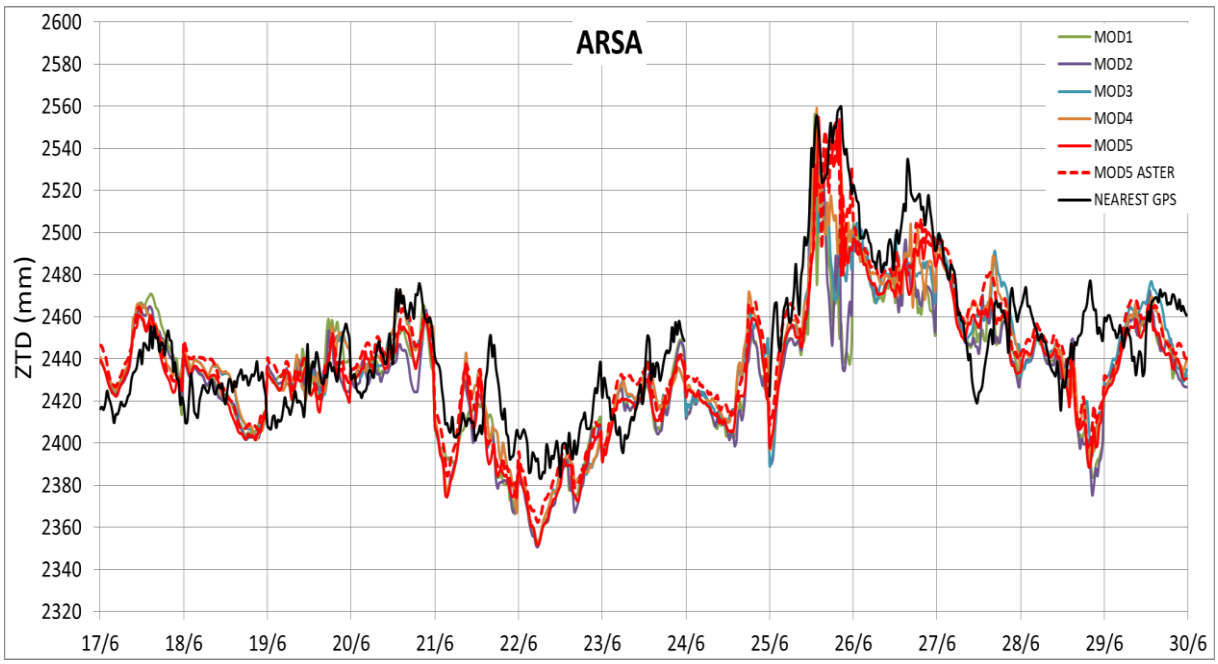

Figure A-8. MOD1-MOD5 WRF ZTDs vs. GNSS ZTDs, station ARSA

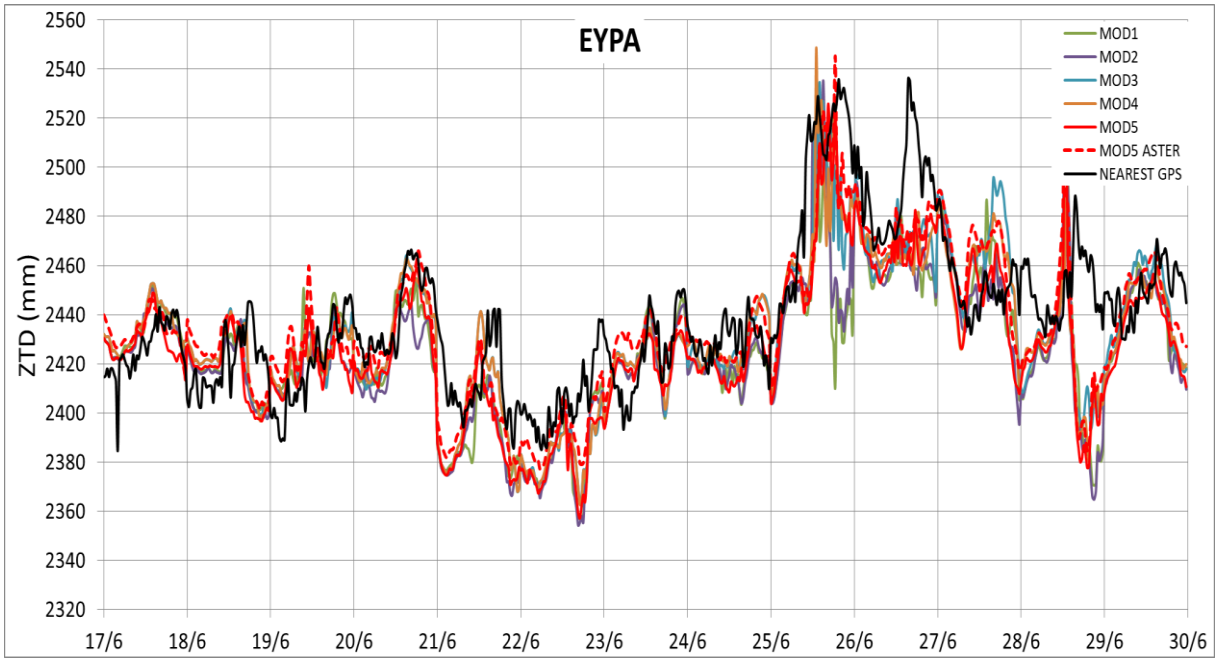

Figure A-9. MOD1-MOD5 WRF ZTDs vs. GNSS ZTDs, station EYPA

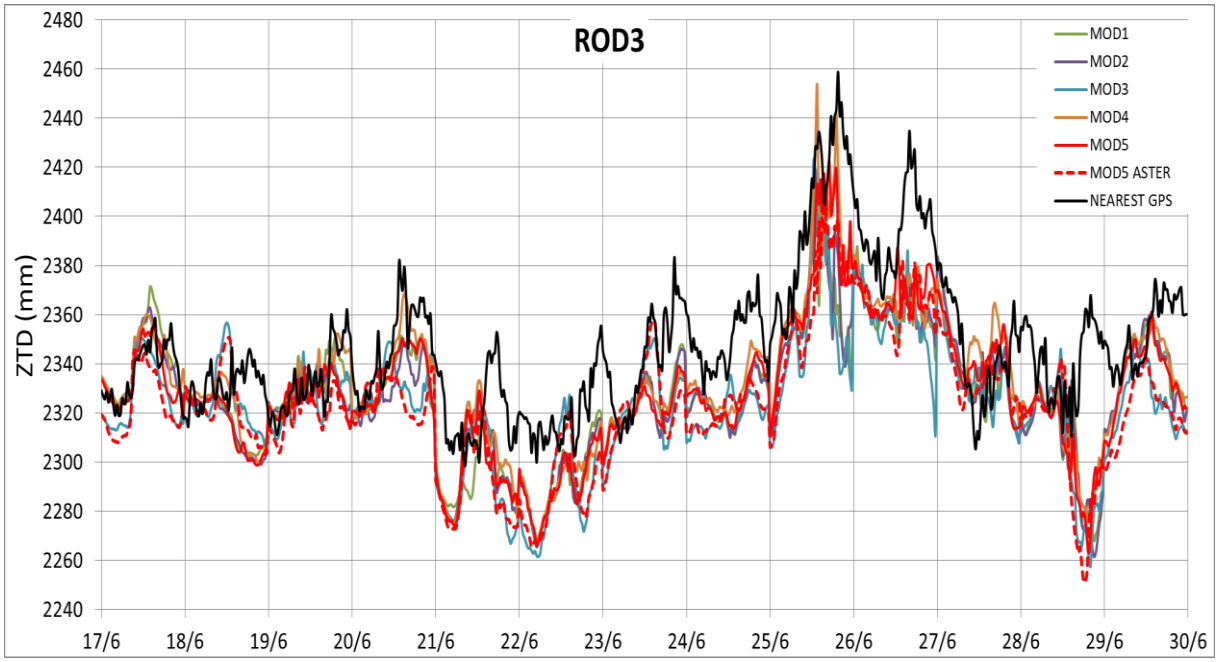

Figure A-10. MOD1-MOD5 WRF ZTDs vs. GNSS ZTDs, station ROD3

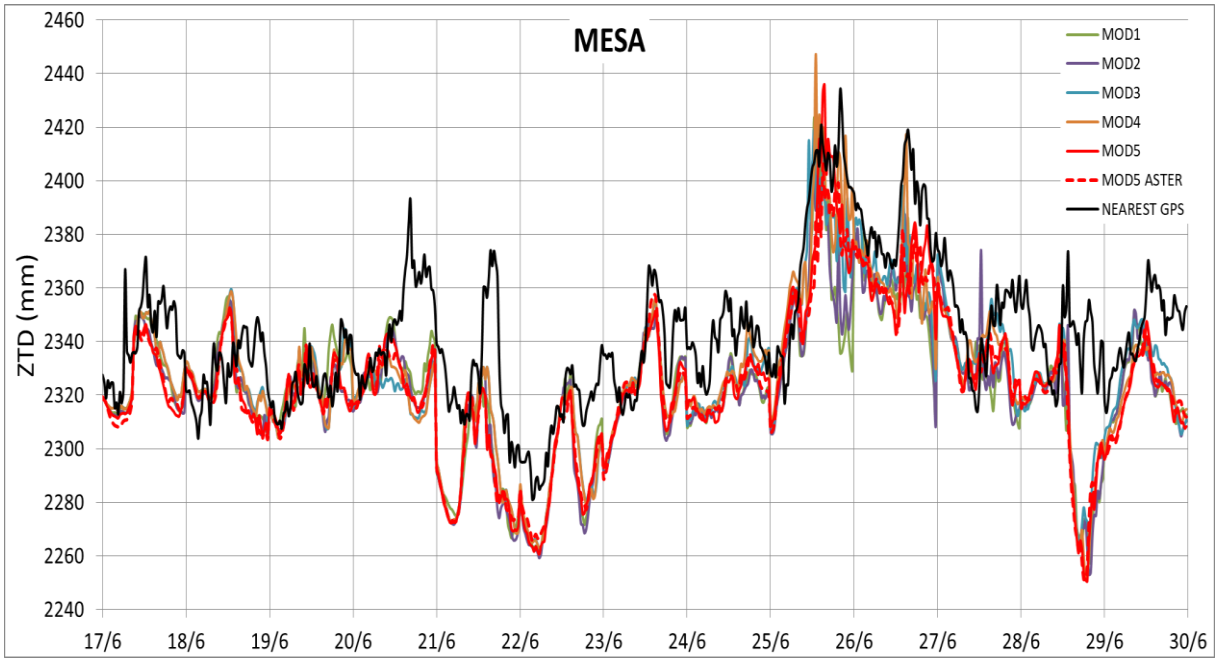

Figure A-11. MOD1-MOD5 WRF ZTDs vs. GNSS ZTDs, station MESA

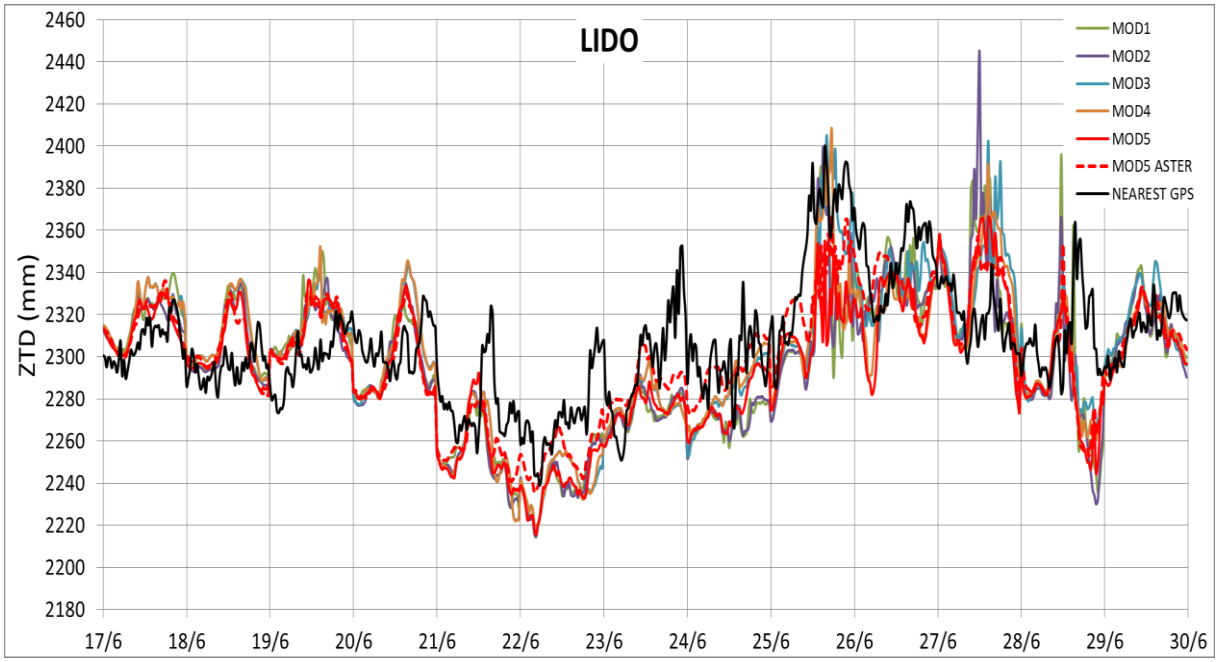

Figure A-12. MOD1-MOD5 WRF ZTDs vs. GNSS ZTDs, station LIDO

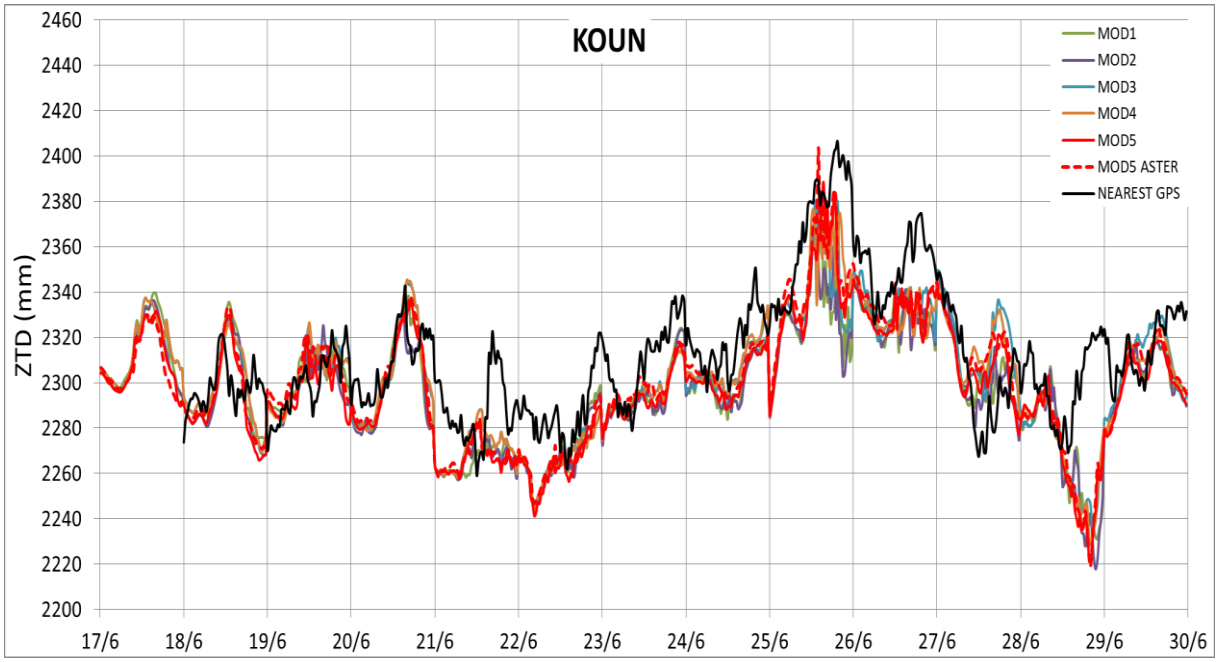

Figure A-13. MOD1-MOD5 WRF ZTDs vs. GNSS ZTDs, station KOUN

Figure A-14. MOD1-MOD5 WRF ZTDs vs. GNSS ZTDs, station KALA

Figure A-15. MOD1-MOD5 WRF ZTDs vs. GNSS ZTDs, station KRIN

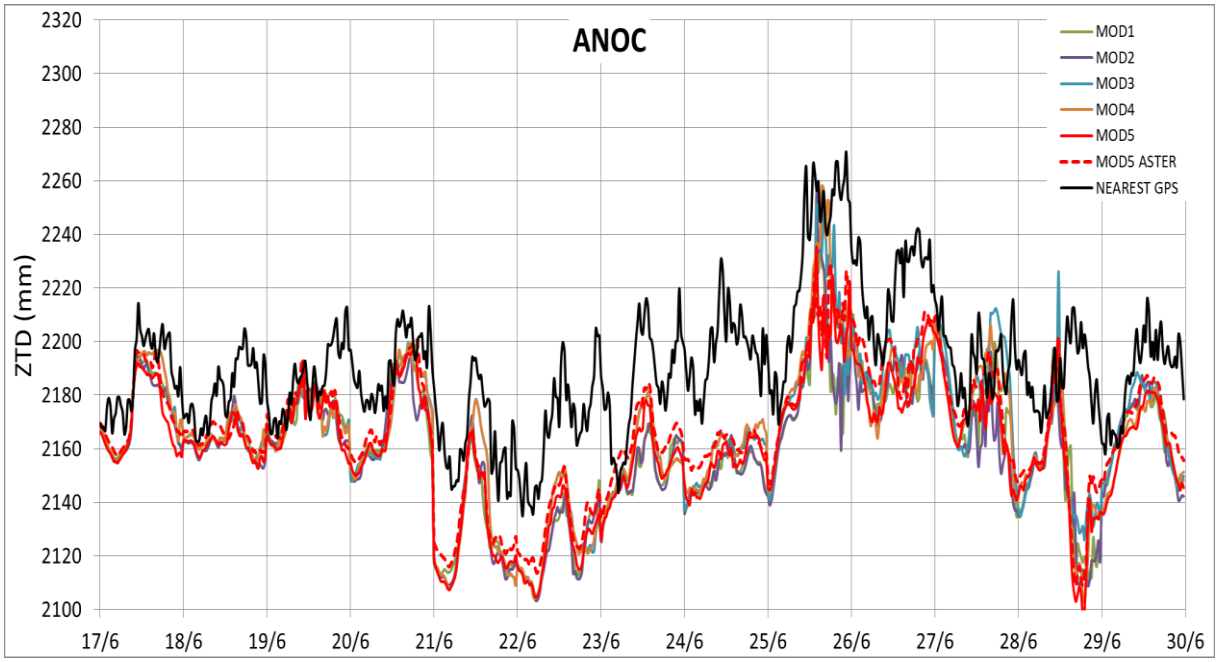

Figure A-16. MOD1-MOD5 WRF ZTDs vs. GNSS ZTDs, station ANOC

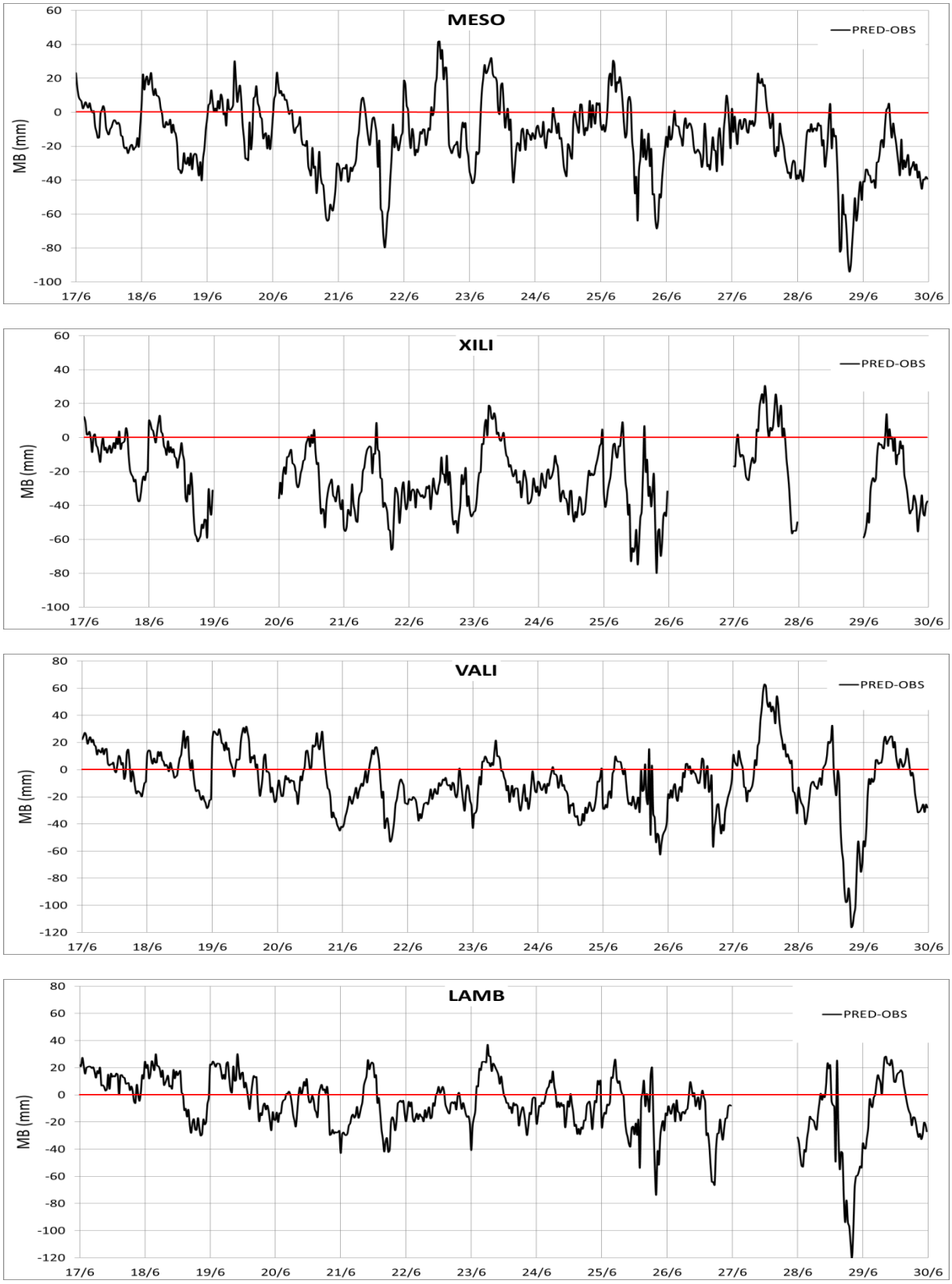

Figure A-17. Bias plots of predicted (WRF MOD5 ASTER) minus observed (GNSS) ZTD at stations MESO, XILI, VALI and LAMB.

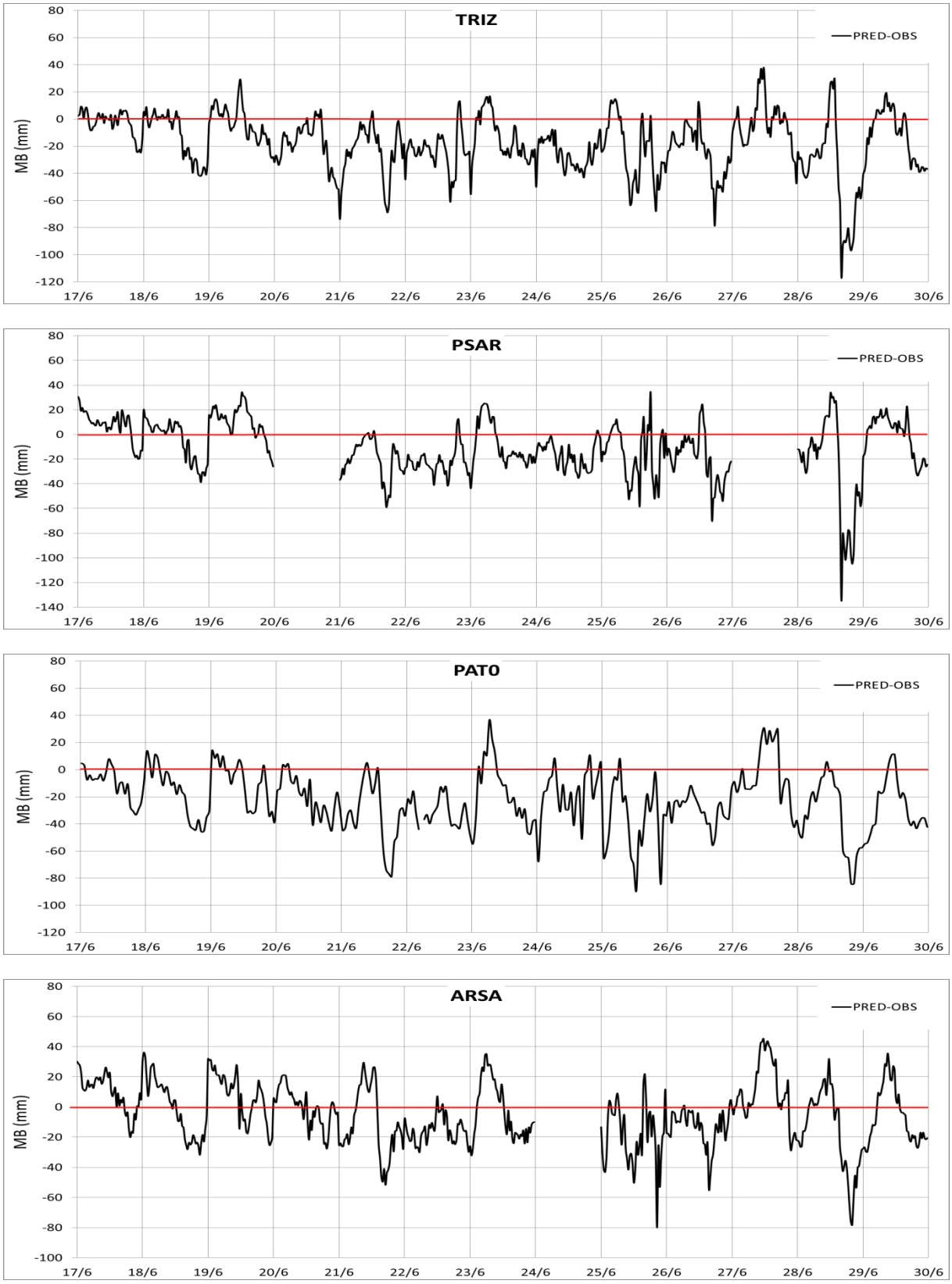

Figure A-18. Bias plots of predicted (WRF MOD5 ASTER) minus observed (GNSS) ZTD at stations TRIZ, PSAR, PAT0 and ARSA.

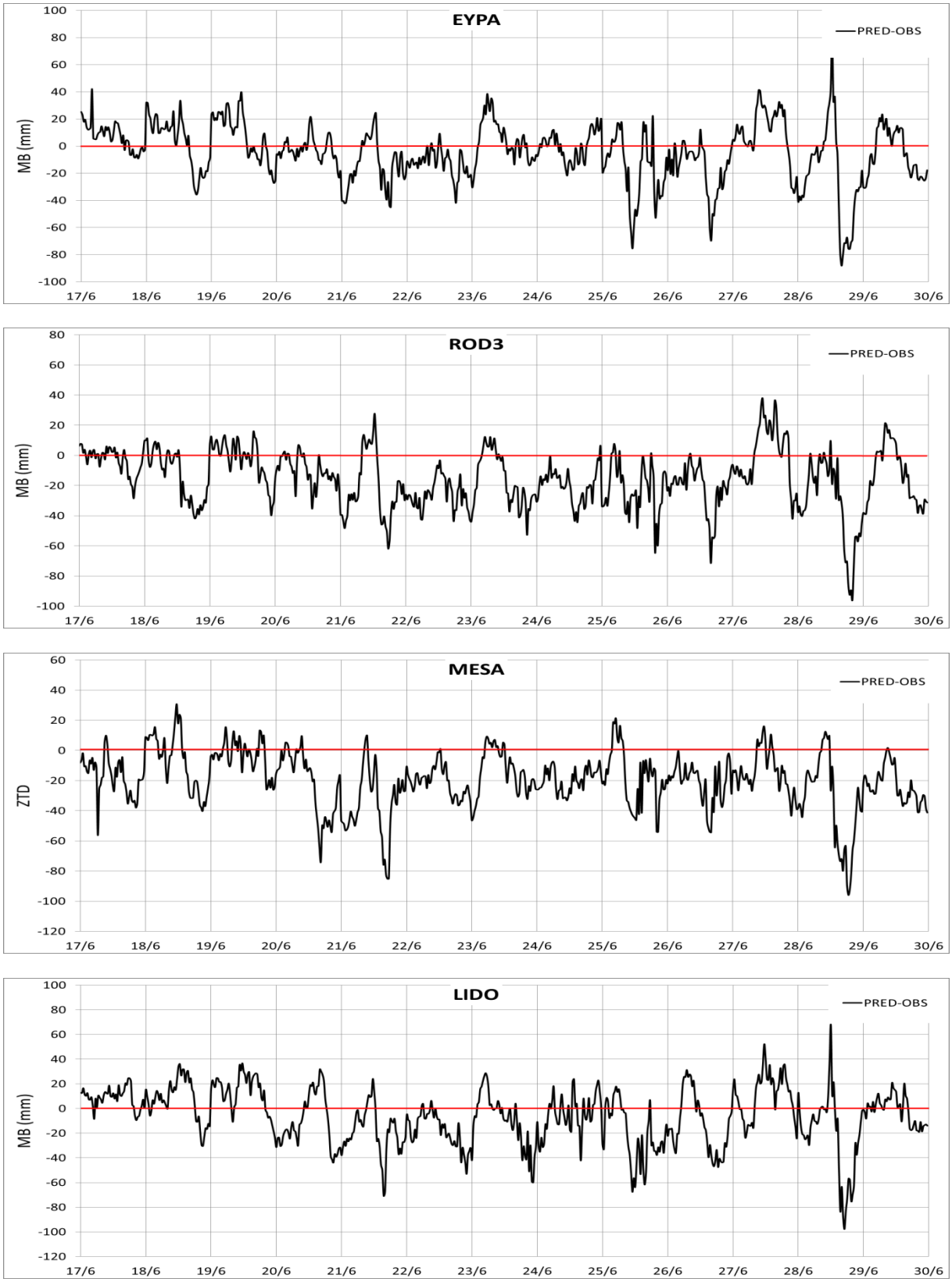

Figure A-19. Bias plots of predicted (WRF MOD5 ASTER) minus observed (GNSS) ZTD at stations EYPA, ROD3, MESA and LIDO.

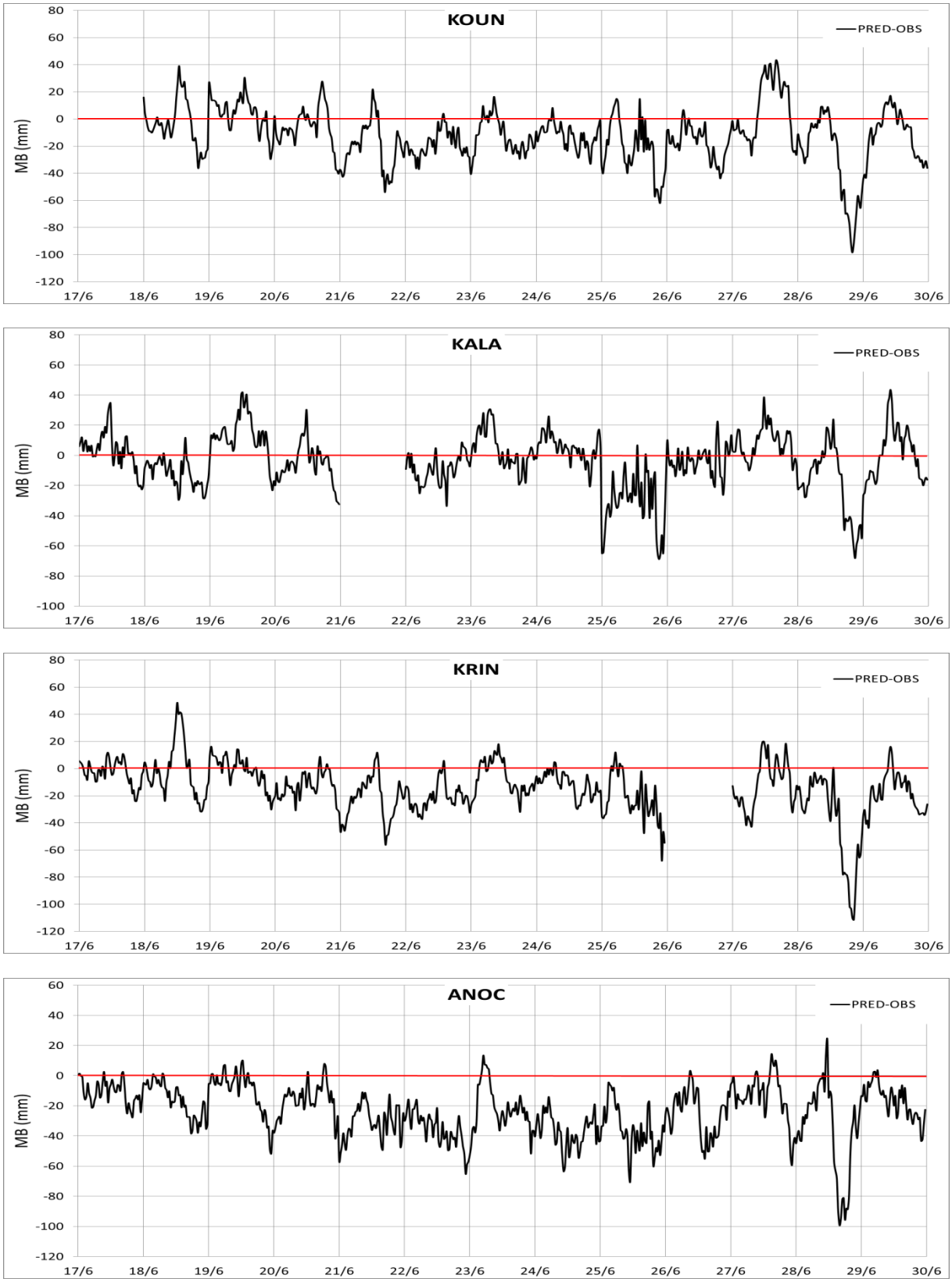

Figure A-20. Bias plots of predicted (WRF MOD5 ASTER) minus observed (GNSS) ZTD at stations KOUN, KALA, KRIN and ANOC.

Appendix B – Timeseries, bias plots and correlation plots of WRF MOD5 vs. GNSS ZTDs for the whole PaTrop period (Jan-Dec 2016).

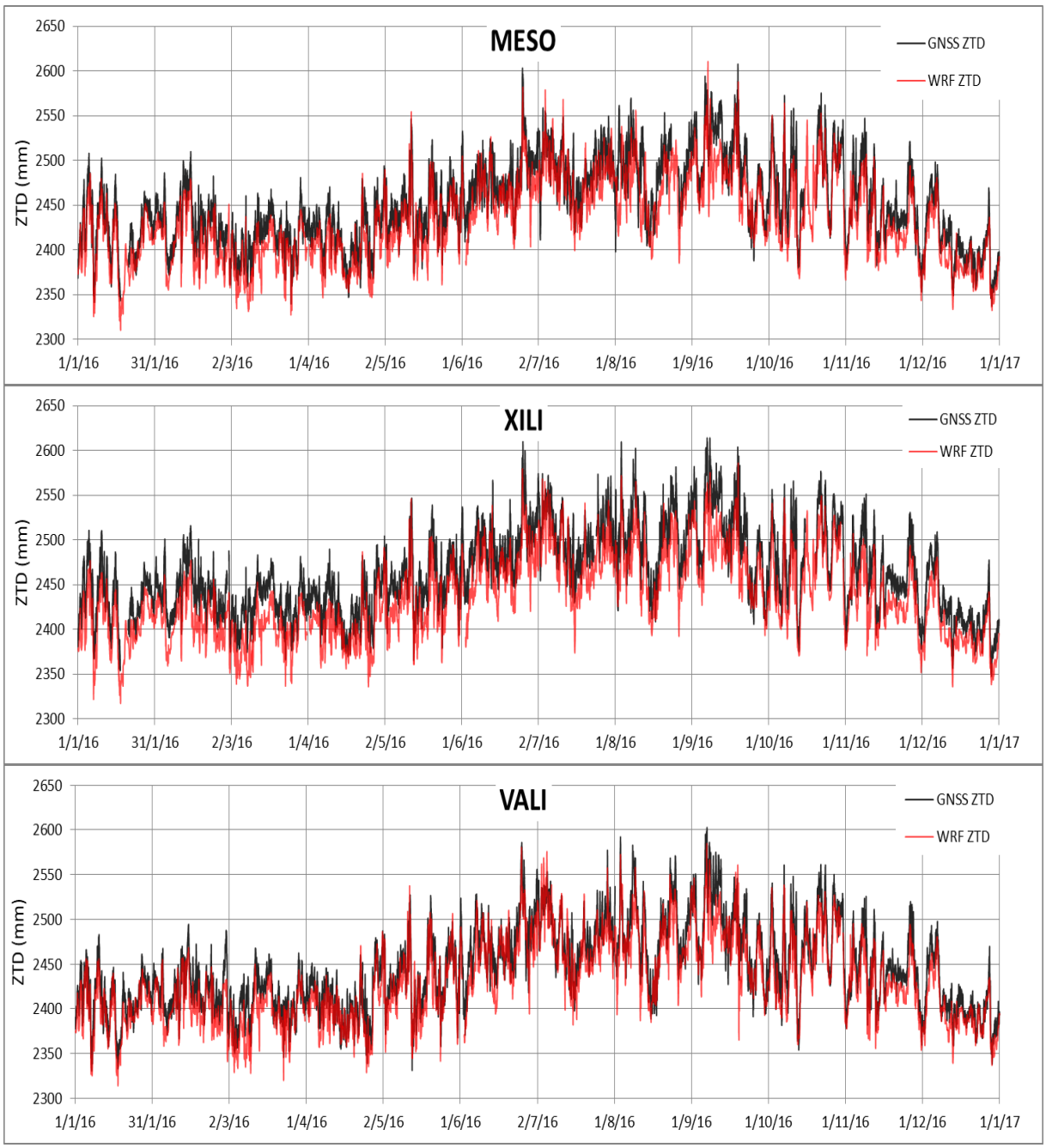

Figure B-1. Annual time series of WRF ZTDs vs. GNSS ZTDs, stations MESO, XILI, VALI.

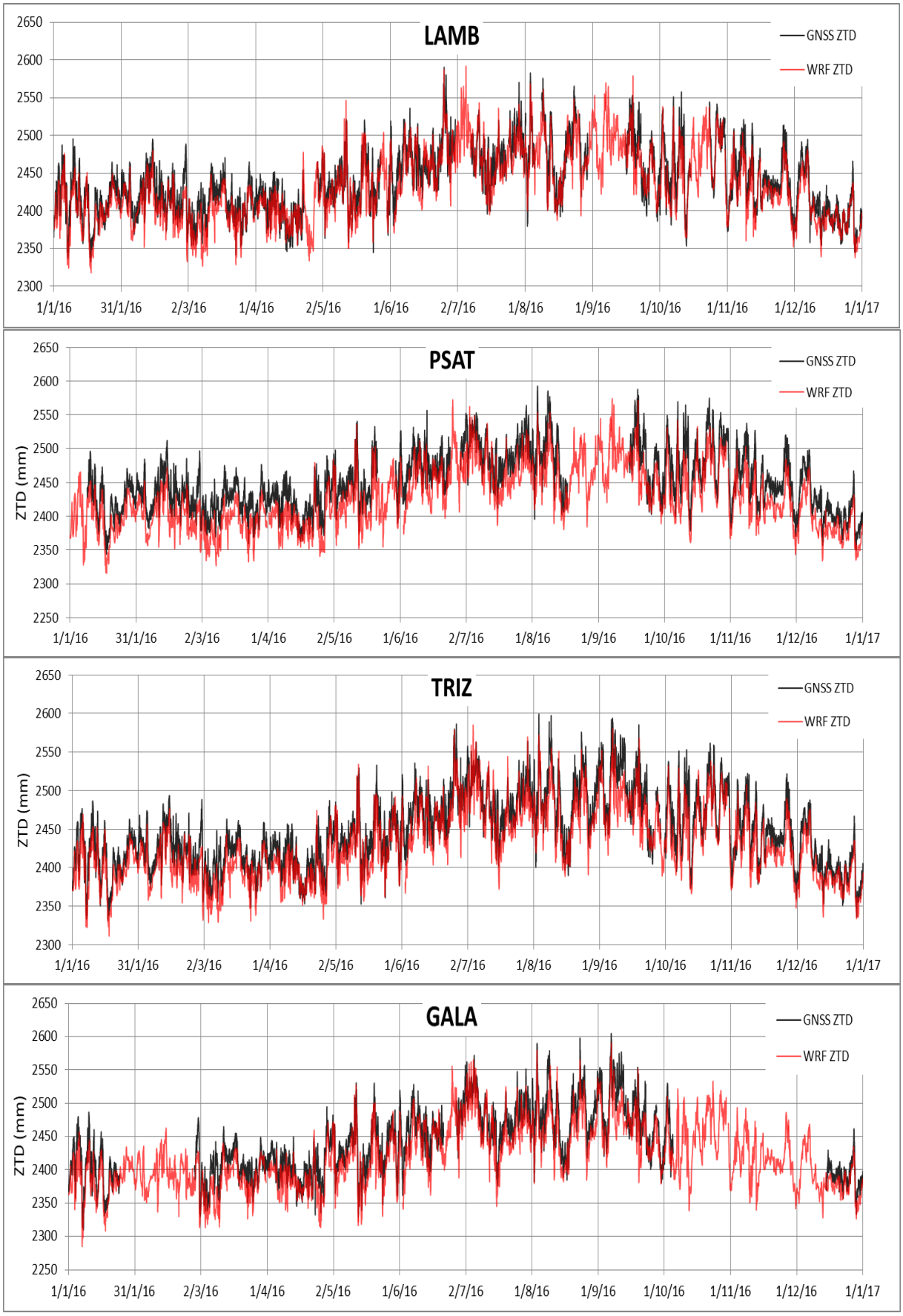

Figure B-2. Annual time series of WRF ZTDs vs. GNSS ZTDs, stations LAMB, PSAT, TRIZ, GALA.

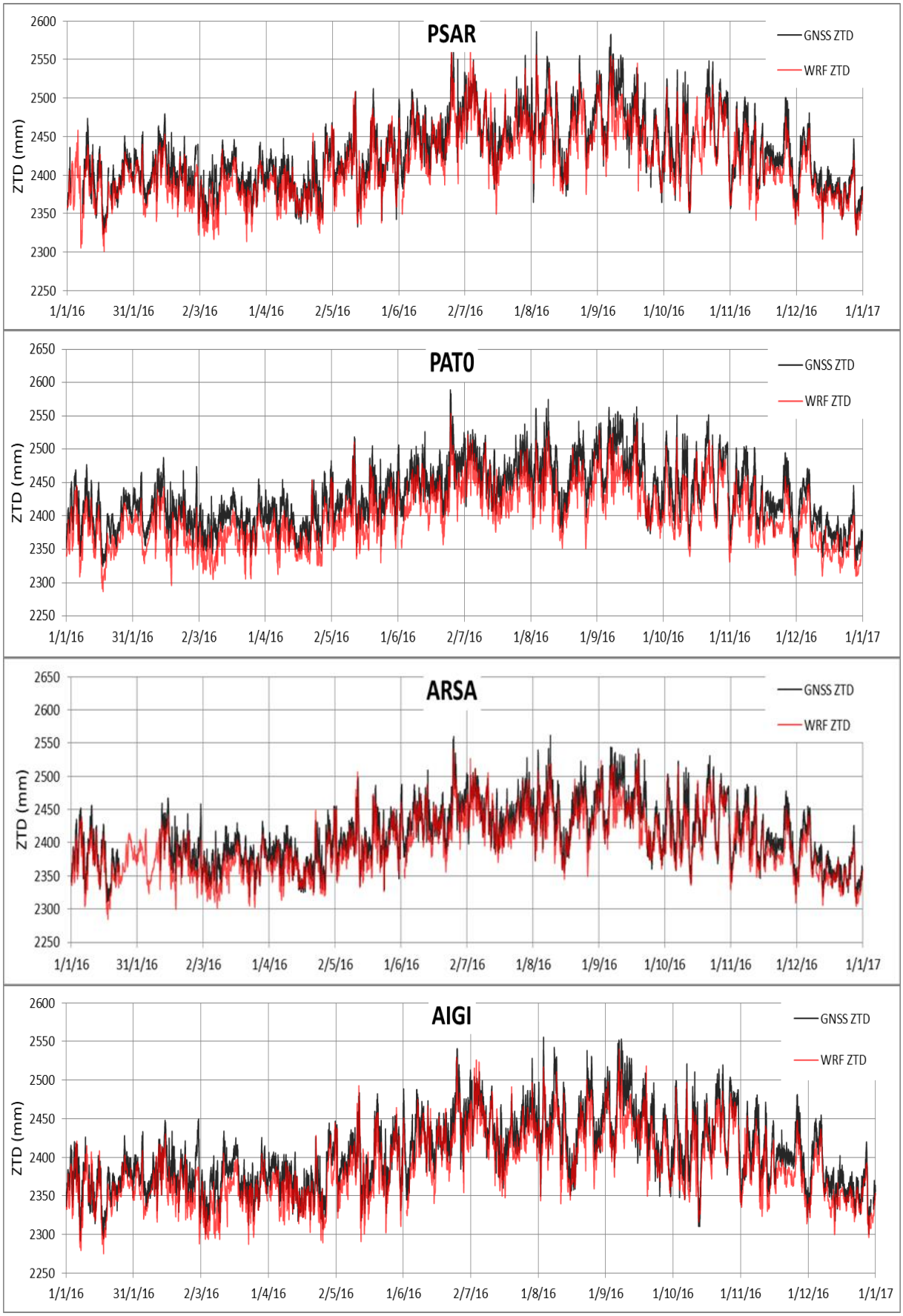

Figure B-3. Annual time series of WRF ZTDs vs. GNSS ZTDs at stations PSAR, PAT0, ARSA, AIGI.

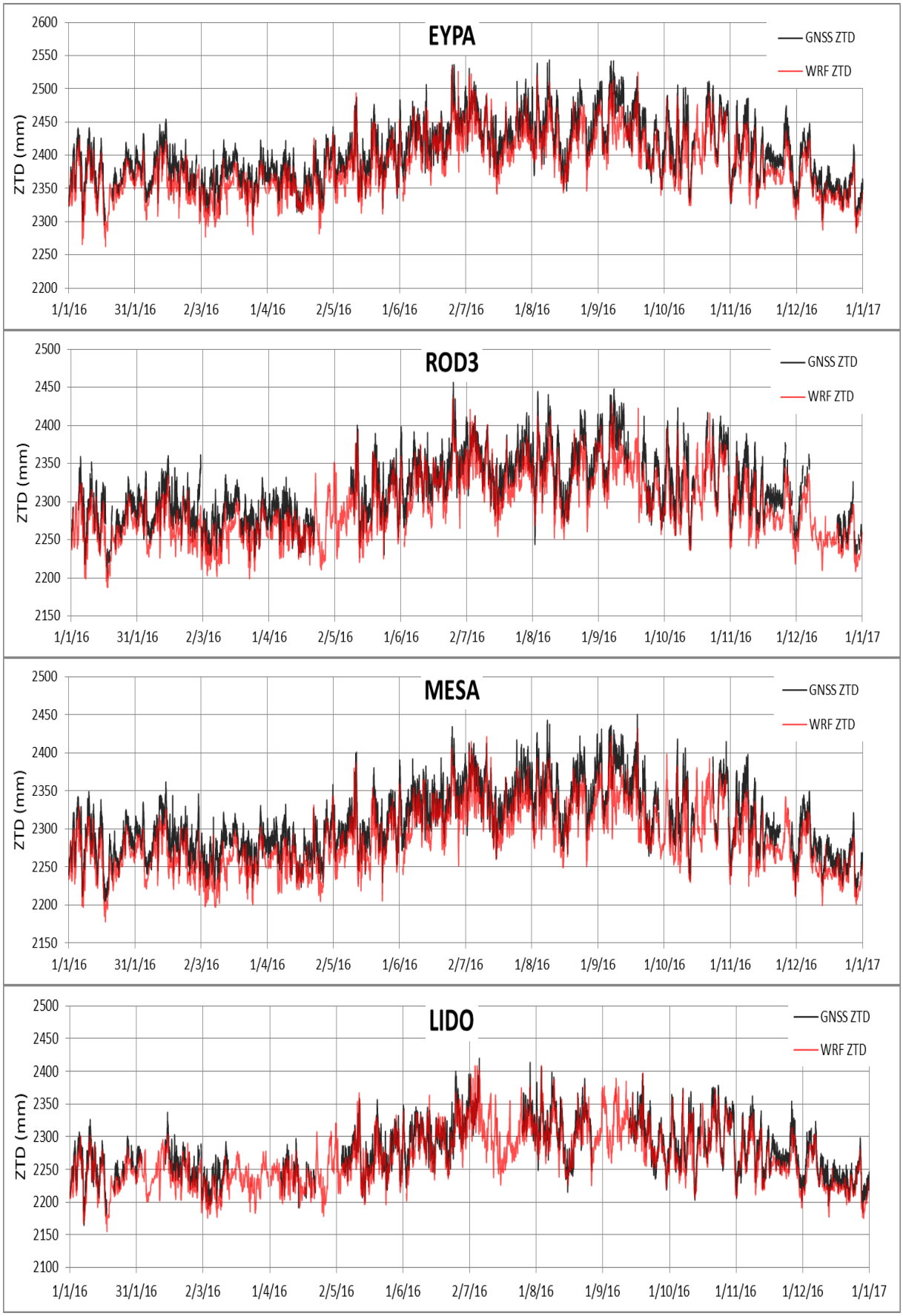

Figure B-4: Annual time series of WRF ZTDs vs. GNSS ZTDs at stations EYPA, ROD3, MESA, LIDO.

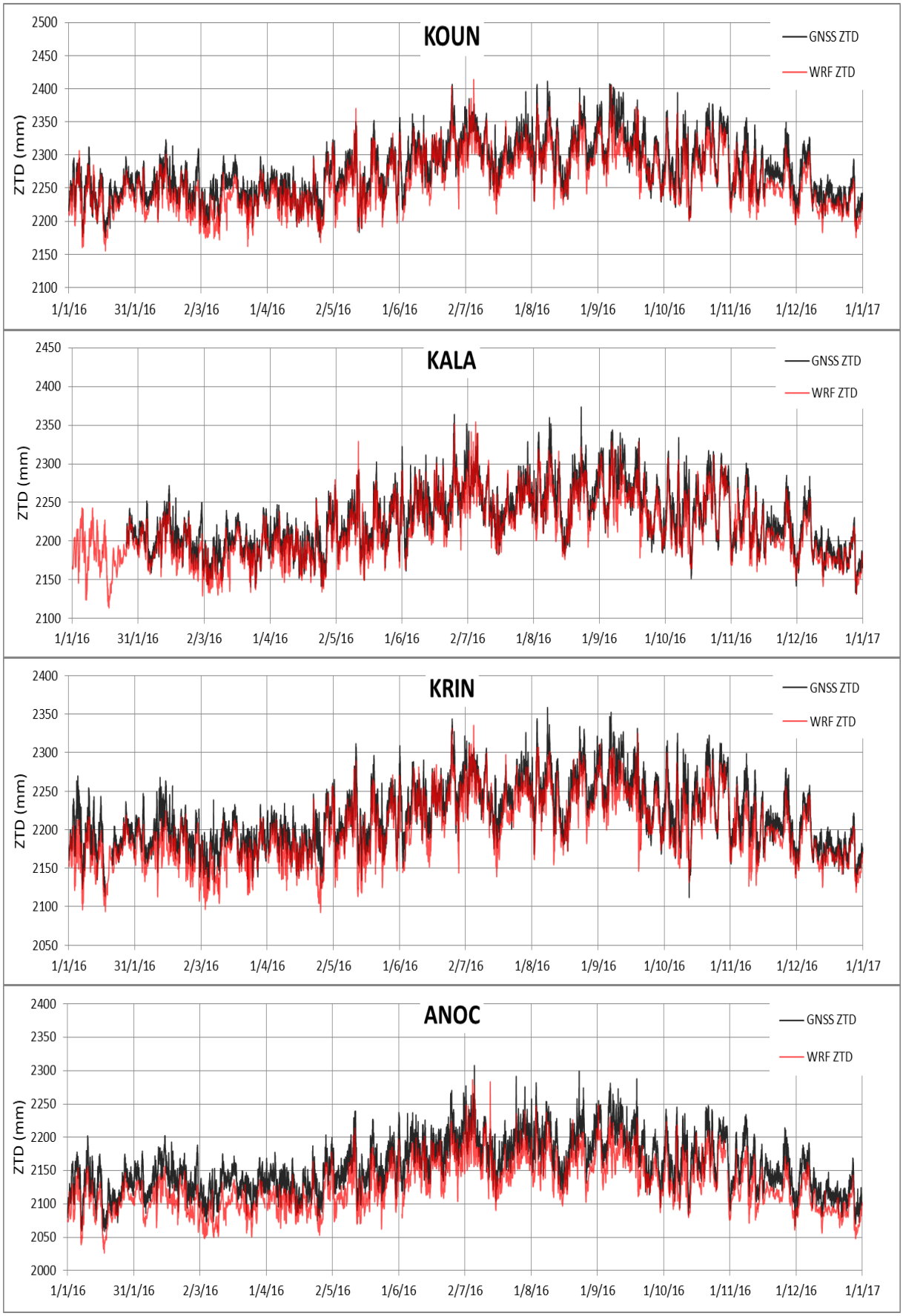

Figure B-5: Annual time series of WRF ZTDs vs. GNSS ZTDs at stations KOUN, KALA, KRIN, ANOC.

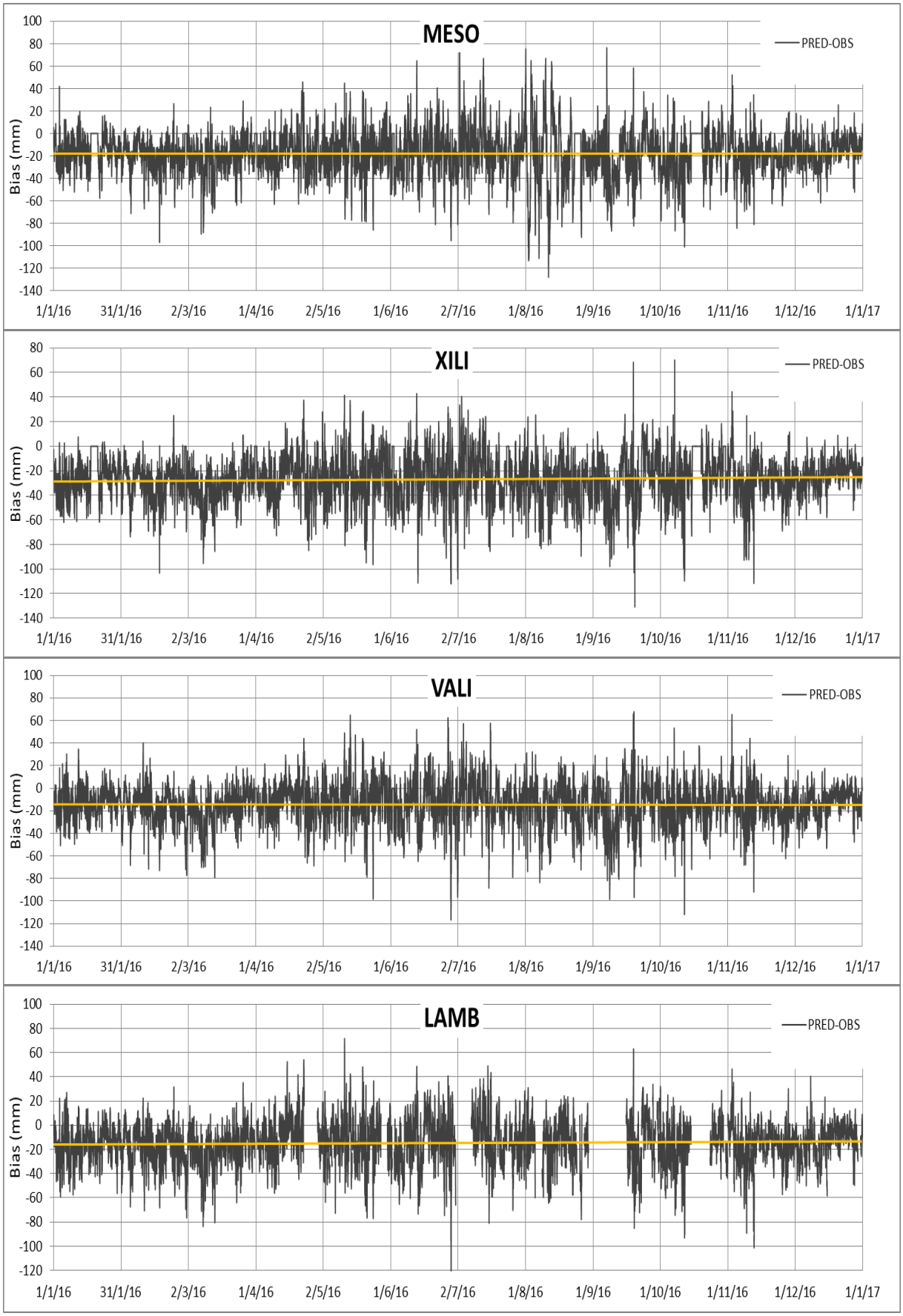

Figure B-6: Bias plots of predicted (WRF) minus observed (GNSS) ZTD at stations MESO, XILI, VALI, LAMB.

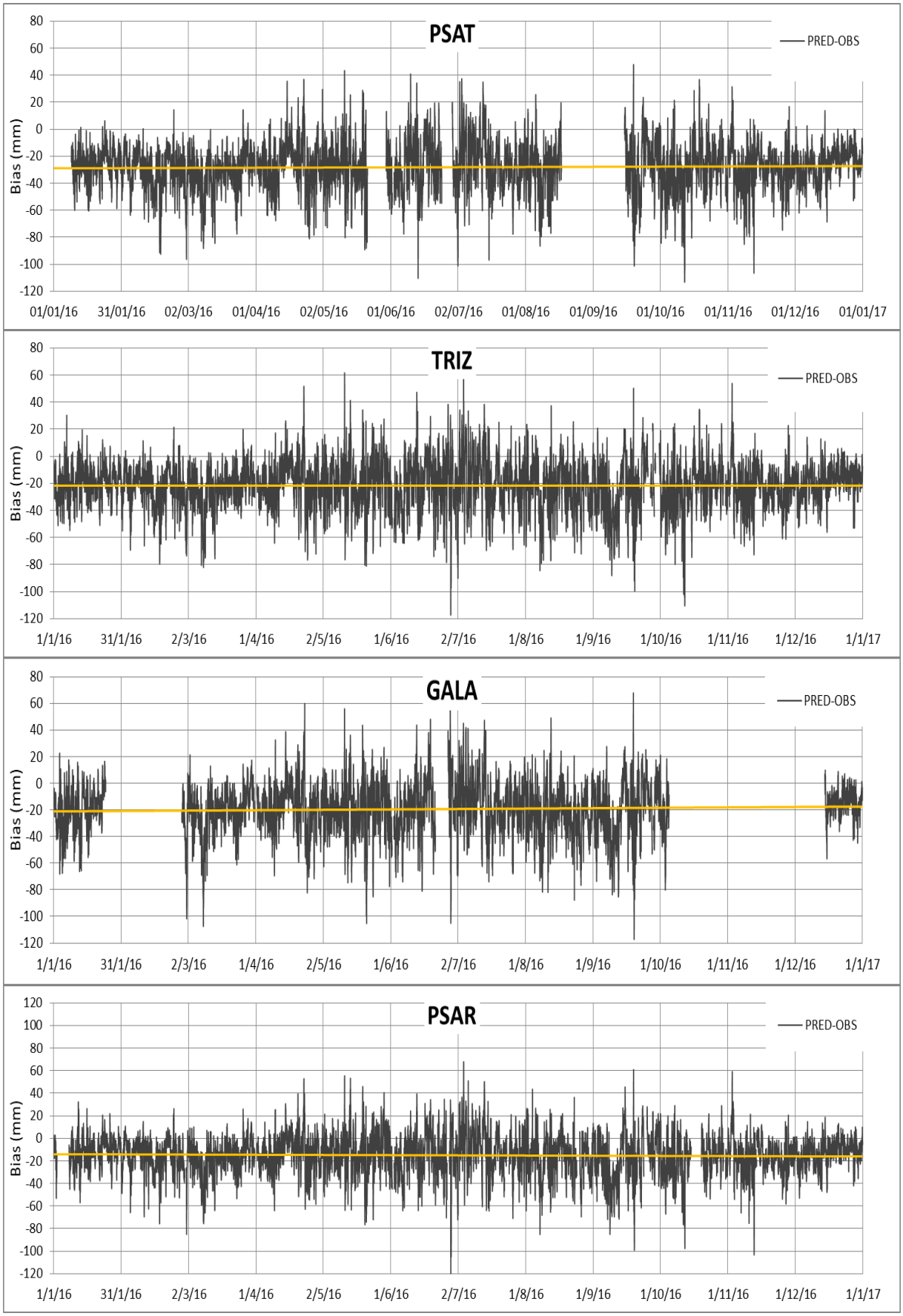

Figure B-7: Bias plots of predicted (WRF) minus observed (GNSS) ZTD at stations PSAT, TRIZ, GALA, PSAR.

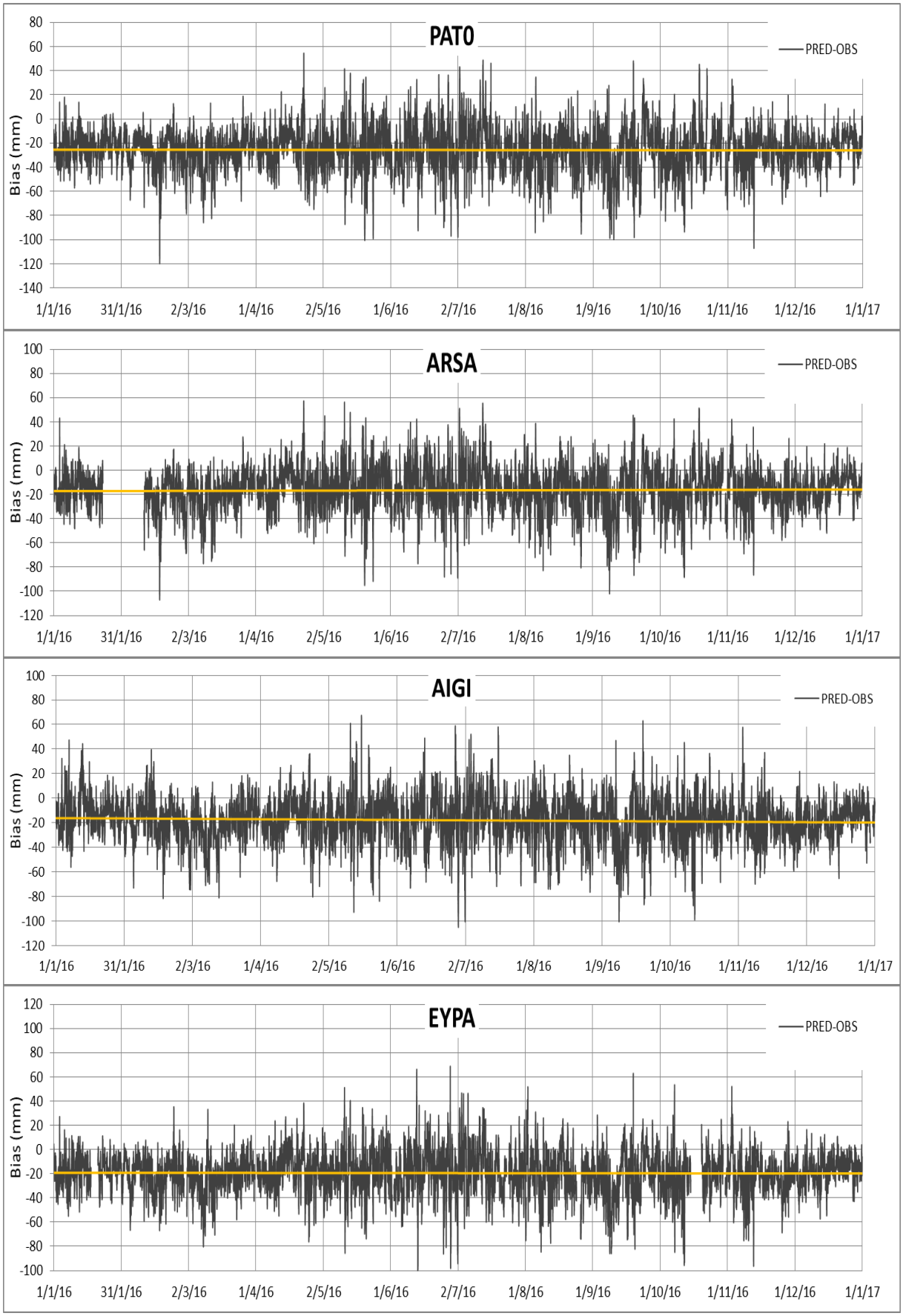

Figure B-8: Bias plots of predicted (WRF) minus observed (GNSS) ZTD at stations PAT0, ARSA, AIGI, EYPA.

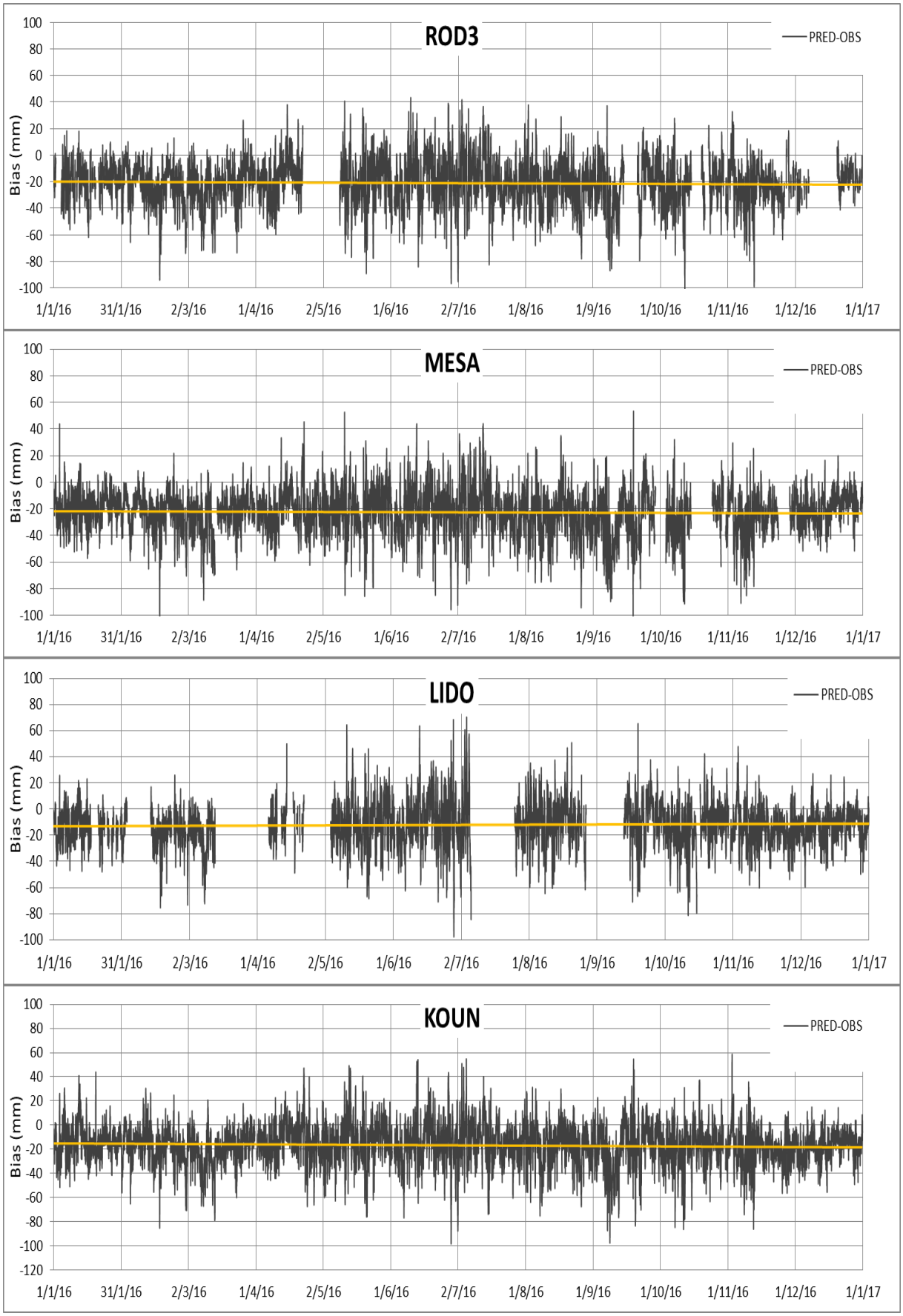

Figure B-9: Bias plots of predicted (WRF) minus observed (GNSS) ZTD at stations ROD3, MESA, LIDO, KOUN.

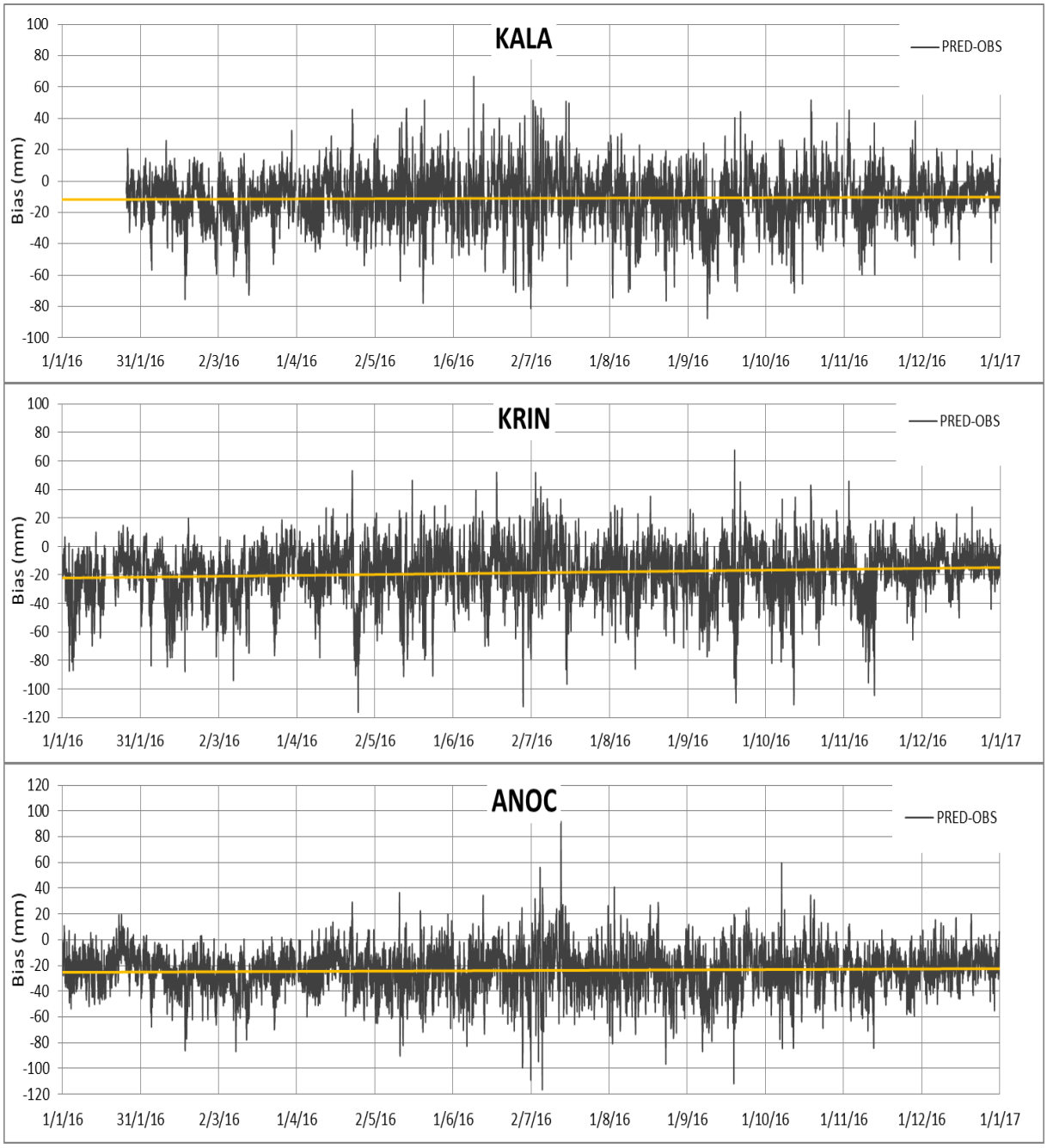

Figure B-10: Bias plots of predicted (WRF) minus observed (GNSS) ZTD at stations KALA, KRIN, ANOC.

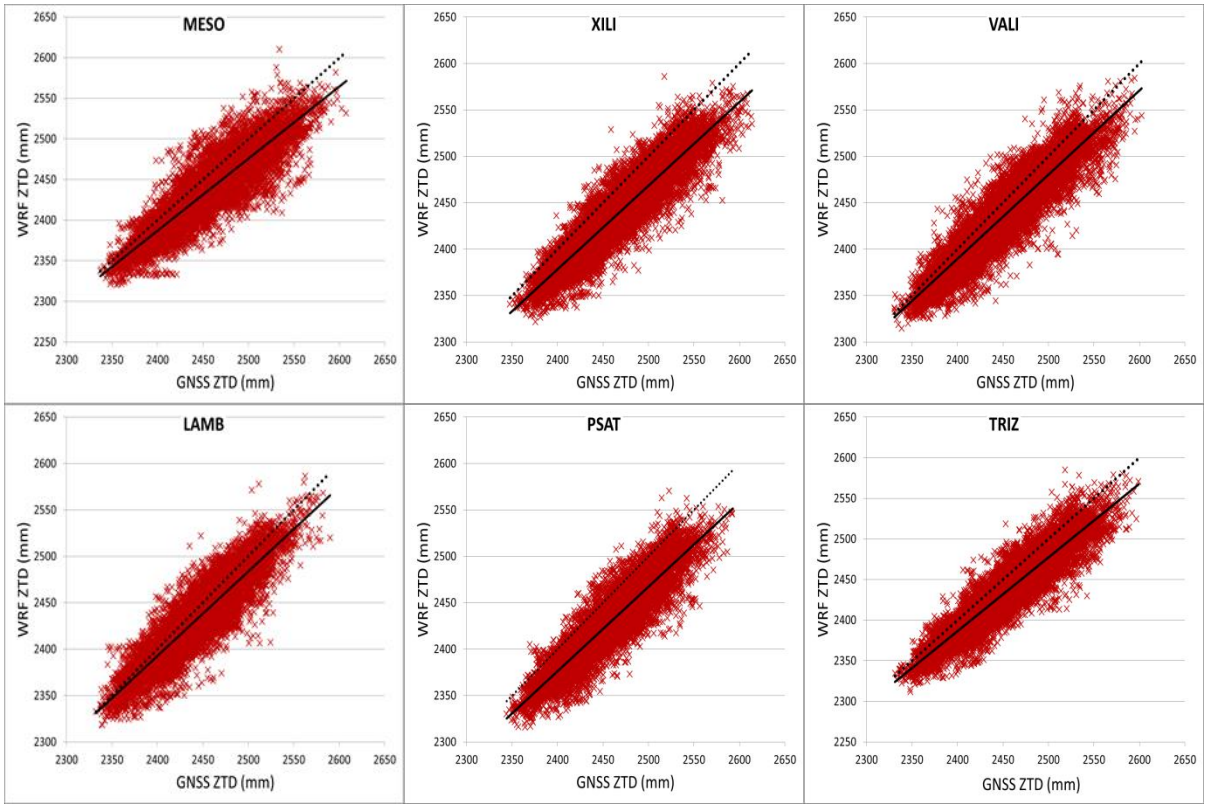

Figure B-11: Correlation plots of WRF ZTDs vs. GNSS ZTDs at stations MESO, XILI, VALI, LAMB, PSAT, TRIZ.

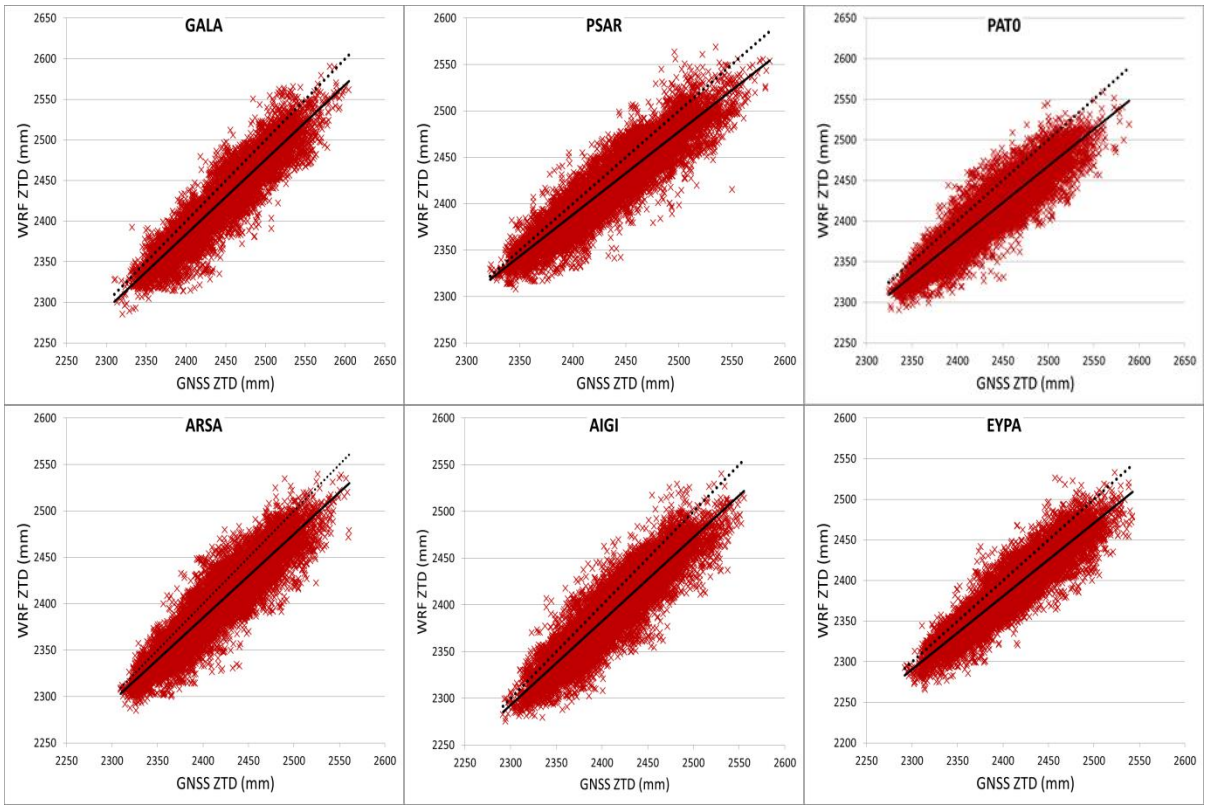

Figure B-12: Correlation plots of WRF ZTDs vs. GNSS ZTDs at stations GALA, PSAR, PAT0, ARSA, AIGI, EYPA.

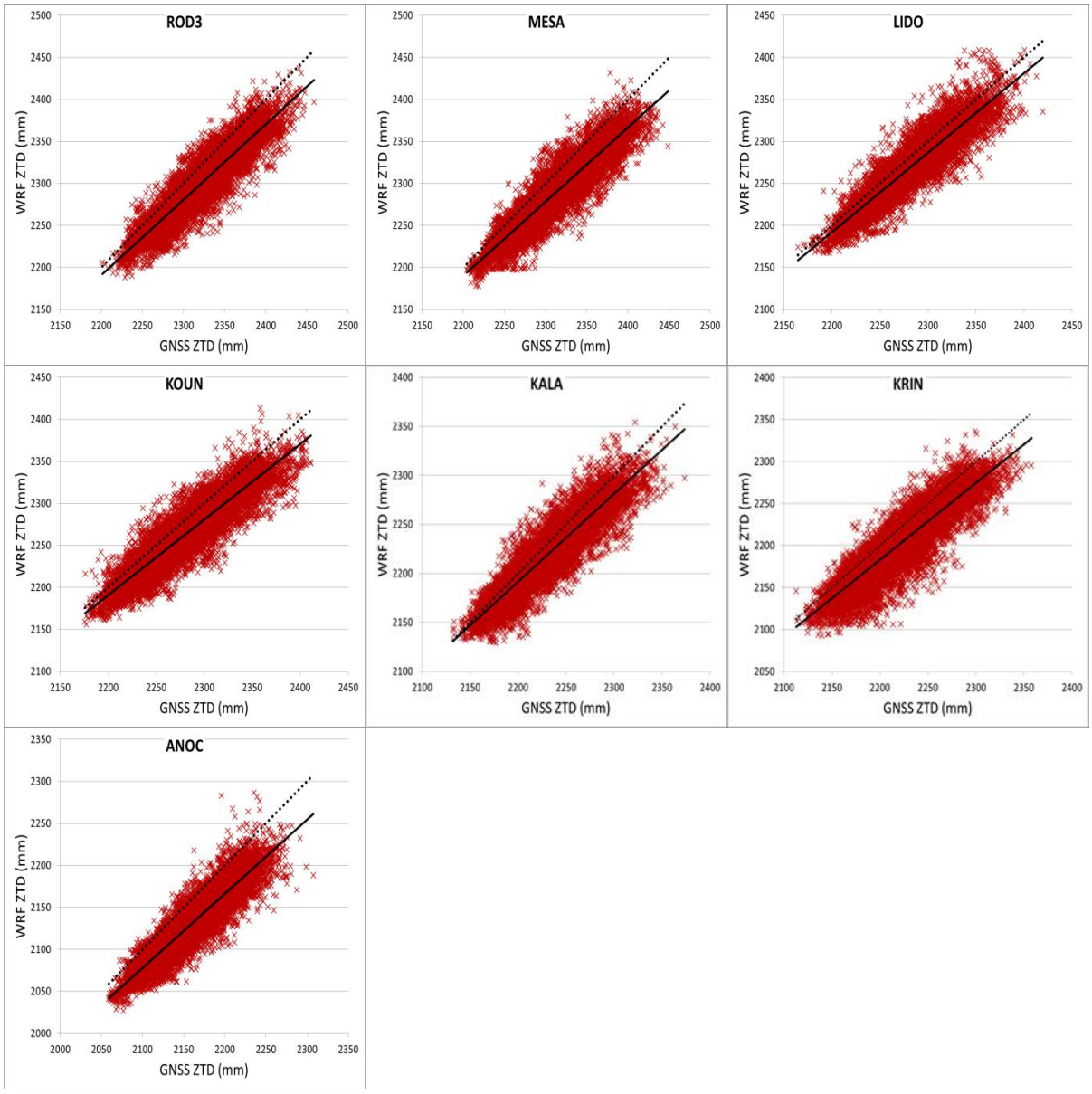

Figure B-13: Correlation plots of WRF ZTDs vs. GNSS ZTDs at stations ROD3, MESA, LIDO, KOUN, KALA, KRIN, ANOC.

Bibliography

Alshawaf F., Fersch B., Hinz S., Kunstmann H., Mayer M., Meyer F. J. (2015). Water vapor mapping by fusing InSAR and GNSS remote sensing data and atmospheric simulations, Hydrol. Earth Syst. Sci., 19, 4747–4764.

Ancell B., Mass C., Hakim G. (2011). Evaluation of surface analyses and forecasts with a multiscale ensemble Kalman filter in regions of complex terrain, Monthly Weather Review, 139(6), 2008-2024.

Arnold J., Moriasi D., Gassman P., Abbaspour K., White M., Srinivasan R., Santhi C., Van Harmel R., Van Griensven A., Van Liew M., Kannan N., Jha M. (2012). SWAT: model use, calibration, and validation, Trans. ASABE, 55(4), 1491-1508.

Arriola J. S., Lindskog M., Thorsteinsson S., Bojarova J. (2016). Variational Bias Correction of GNSS ZTD in the HARMONIE Modeling System, J. App. Meteorol. Clim., 55, 1259–1276.

Askne J. and Nordius H. (1987). Estimation of tropospheric delay for microwaves from surface weather data, Radio Sci., 22, 379–386.

Avallone, A. (2003). Analyse de dix ans de déformation du rift de Corinthe (Grèce) par géodésie spatiale. PhD Thesis. IPGP: France.

Avallone A., Briole P., Agatza-Balodimou A.M., Billiris H., Charade O. , Mitsakaki C., Nercessian A., Papazissi K., Paradissis D., Veis G. (2004). Analysis of eleven years of deformation measured by GPS in the Corinth Rift Laboratory area, C.R. Geoscience, 336, 301-312.

Awan N., Truhetz H., Gobiet A. (2011). Parameterization-induced error characteristics of MM5 and WRF operated in climate mode over the Alpine Region: an ensemble-based analysis, Journal of Climate, 24(12), 3107-3123.

Balzarini A., Angelini F., Ferrero L., Moscatelli M., Perrone M.G., Pirovano G., Riva G.M., Sangiorgi G., Toppetti A.M., Gobbi G.P., Bolzacchini E. (2014). Sensitivity analysis of PBL schemes by comparing WRF model and experimental data, Geosci. Model Dev.Discuss., 7, 6133–6171.

Barlage M., Miao S., Chen F. (2016). Impact of physics parameterizations on high-resolution weather prediction over two Chinese megacities, J. Geophys. Res. Atmos., 121, 4487–4498.

Barnhart, W. D., and Lohman R. B. (2013). Characterizing and estimating noise in InSAR and InSAR time series with MODIS, Geochem. Geophys. Geosyst., 14, 4121–4132.

Bassiri S. and Hajj G. (1993). High-Order ionospheric effects of the global positioning system observables and means of modeling them. Manuscripta Geodetica, 18, 280-289.

Beauducel F., Briole P., Froger J. (2000). Volcano-wide fringes in ERS synthetic aperture radar interferograms of Etna (1992-1998): Deformation or tropospheric effect? J. Geophys. Res., 105, 16391-16402.

Béjar-Pizarro M., Socquet A., Armijo R., Carrizo D., Genrich J., Simon M. (2013). Andean structural control on interseismic coupling in the North Chile subduction zone, Nature Geoscience, 6(6), 462-467.

Bekaert, D. P. S., Hooper A., Wright T. J. (2015). A spatially variable power law tropospheric correction technique for InSAR data, J. Geophys. Res. Solid Earth, 120, 1345–1356.

Bekaert, D. P. S., Walters R. J., Wright T. J., Hooper A., Parker D. J. (2015). Statistical comparison of InSAR tropospheric correction techniques, Remote Sensing of Environment, 170, 40–47.

Bell R., McNeill L., Bull J., Henstock T., Collier R. Leeder R. (2009). Fault Architecture, basin structure and evolution of the Gulf of Corinth Rift, central Greece, Basin Research, 21(6), 824-855.

Bender M., Dick G., Wickert J., Ramatschi M., Ge M., Gendt G., Rothacher M., Raabe A., Tetzlaff G. (2009). Estimates of the information provided by GPS slant data observed in Germany regarding tomographic applications, J. Geophys. Res., 114.

Benestad R., Hanssen-Bauer I., Forland E. (2007). An evaluation of statistical models for downscaling precipitation and their ability to capture long-term trends, Int. J. Climatol., 27, 649–665.

Bernard P., Lyon-Caen H., Briole P., Deschamps A., Boudin F., Makropoulos K., Papadimitriou P., Lemeille F., Patau G., Billiris H., Paradissis D., Papazissi K., Castarède H., Charade O., Nercessian A., Avallone A., Pacchiani F., Zahradnik J., Sacks S., Linde A. (2006), Seismicity, Deformation and seismic hazard in the western rift of Corinth: New insights from the Corinth Rift Laboratory (CRL), Tectonophysics, 426, 7–30.

Bevis M., Businger S., Herring T. A., Rocken C., Anthes R. A., Ware R. H. (1992). GPS meteorology: remote sensing of atmospheric water vapour using global positioning system, J. Geophys. Res., 97, 15787–15801.

Bevis M., Businger S., Chiswell S.R., Herring T.A., Anthes R.A., Rocken C., Ware R.H. (1994). GPS meteorology: mapping zenith wet delay onto precipitable water, J. Appl. Meteorol., 33, 379–386.

Bevis M., Chiswell S., Businger S. (1996). Estimating wet delays using numerical weather analyses and predictions, Radio Science, 31-3, 477-487.

Blewitt G. (2007). GPS and Space-Based Geodetic Methods. In T. Herring (ed.), Geodesy: Treatise on Geophysics, vol. 3.11, Elsevier B.V.

Boccolari M., Fazlagic S., Lombroso L., Frontero P., Pugnaghi S., Santangelo R., Corradini S., Teggi S. (2001). Precipitable water estimation in comparison between Zenith Total Delays (ZTD) by radiosounding data and by GPS Data, MAP Newsletter, 15, 218-221.

Bock O., Willis P., Wang J., Mears C. (2014). A high-quality, homogenized, global, long-term (1993–2008) DORIS precipitable water data set for climate monitoring and model verification, J. Geophys. Res. Atmos., 119, 7209–7230.

Boehm J., Werl B., Schuh H. (2006b). Troposphere mapping functions for GPS and very long baseline interferometry from European Centre for Medium-Range Weather Forecasts operational analysis data, J. Geophys. Res., 111, B02406.

Boehm J., Heinkelmann R., Weber R. (2007). A global model of pressure and temperature for geodetic applications, J. Geod., 81(10), 679–683.

Boehm J., Möller G., Schindelegger M., Pain G., Weber R. (2015). Development of an improved blind model for slant delays in the troposphere (GPT2w), GPS Solut., 19, 433.

Bonafoni S., Mazzoni A., Cimini D., Montopoli M., Pierdicca N., Basili P., Ciotti P., Carlesimo G. (2013). Assessment of water vapor retrievals from a GPS receiver network, GPS Solut., 17, 475–484.

Brenot H., Nemeghaire J., Delobbe L., Clerbaux N., De Meutter P., Deckmyn A., Delcloo A., Frappez L., Van Roozendael M. (2013). Preliminary signs of the initiation of deep convection by GNSS, Atmos. Chem. Phys., 13, 5425-5449.

Briole P., Rigo A., Lyon-Caen H., Ruegg J.C., Papazissi K., Mitsakaki C., Balodimou A., Veis G., Hatzfeld D., Deschamps A. (2001). Results from repeated Global Positioning System surveys between 1990 and 1995, J. Geophys. Res.,105, 25605—25625.

Brousseau P., Berre L., Bouttier F., Desroziers G. (2011). Background-error covariances for a convective-scale data-assimilation system: AROME–France 3D-Var, Quarterly Journal of the Royal Meteorological Society, 137(655), 409-422.

Byun S. and Bar-Sever Y. (2009). A new type of troposphere zenith path delay product of the international GNSS service, Journal of Geodesy, 83(3), 1–7.

Cardoso R., Soares P., Miranda P., Belo-Pereira M. (2013). WRF high resolution simulation of Iberian mean and extreme precipitation climate, Int. J. Climatol., 33, 2591–2608.

Carvalho J., Anfossi D., Castelli S., Degrazia G. (2002). Application of a model system for the study of transport and diffusion in complex terrain to the TRACT experiment, Atmos. Environ. 36(7), 1147–1161.

Cavalié, O., Doin M. P., Lasserre C., Briole P. (2007). Ground motion measurement in the Lake Mead area, Nevada, by differential synthetic aperture radar interferometry time series analysis: Probing the lithosphere rheological structure, J. Geophys. Res., 112, B03403.

Cavalié O., Lasserre C., Doin M., Peltzer G., Sun J., Xu X., Shen Z. (2008). Measurement of interseismic strain across the Haiyuan fault (Gansu, China) by InSAR, Earth and Plan. Sci. Lett., 275, 246–257.

Champollion C., Masson F., Bouin M. N., Walpersdorf A., Doerflinger E., Bock O., Van Baelen J. (2005). GPS Water vapour tomography: Preliminary results from the ESCOMPTE field experiment, Atmos. Res., 74, 253–274.

Chang L. and He X. (2011). InSAR atmospheric distortions mitigation: GPS observations and NCEP FNL data, J. Atmos. Sol. Terr. Phys., 73(4), 464-471.

Chen Q., Song S., Heise S., Liou Y., Zhu W., Zhao J. (2011). Assessment of ZTD derived from ECMWF/NCEP data with GPS ZTD over China, GPS Solutions, 15(4), 415–425.

Chen Y., Li Z., Penna N. T. (2018). Interferometric synthetic aperture radar atmospheric correction using a GPS-based iterative tropospheric decomposition model, Remote Sensing of Environment, 204, 109-121.

Cimini D., Pierdicca N., Pichelli E., Ferretti R., Mattioli V., Bonafoni S., Montopoli M., Perissin D. (2012). On the accuracy of integrated water vapor observations and the potential for mitigating electromagnetic path delay error in InSAR, Atmos. Meas. Tech., 5, 1015–1030.

Davis J., Herring T., Shapiro I., Rogers A., Elgered G. (1985). Geodesy by radio interferometry: Effects of atmospheric modeling errors on estimates of baseline length, Radio Sci., 20(6), 1593-1607.

Deblonde G., Macpherson S., Mireault Y., Heroux P. (2005). Evaluation of GPS precipitable water over Canada and the IGS network, J. Appl. Meteorol., 44, 153– 166.

Delacourt C., Briole P., Achache J.A. (1998). Tropospheric corrections of SAR interferograms with strong topography. Application to Etna, Geophys. Res. Lett., 25, 2849-2852.

Desportes C., Obligis E., Eymard L. (2007). On the wet tropospheric correction for altimetry in coastal regions, IEEE Transactions on Geoscience and Remote Sensing, 45(7), 2139 – 2149.

Deng Z., Bender M., Zus F., Ge M., Dick G., Ramatschi M., Wickert J., Lohnert U., Schon S. (2011). Validation of tropospheric slant path delays derived from single and dual frequency GPS receivers, Radio Science, 46.

Ding X.L., Li Z, Zhu J., Feng G. C., Long J. (2008). Atmospheric effects on InSAR measurements and their mitigation, Sensors, 8(9), 5426-5448.

Doin M. P., Lasserre C., Peltzer G., Cavali O., Doubre C. (2009). Corrections of stratified tropospheric delays in SAR interferometry: Validation with global atmospheric models, J. Appl. Geophys., 69(1), 35–50.

Dousa J., and Bennitt G. V. (2013). Estimation and evaluation of hourly updated global GPS Zenith Total Delays over ten months, GPS Solut., 17(4), 453–464.

Duan J., Bevis M., Fang P., Bock Y., Chiswell S., Businger S., Rocken C., Solheim S., Van Hove T., Ware R., McClusky S., Herring T., King R. W. (1995). GPS meteorology: direct estimation of the absolute value of precipitable water, Journal of Applied Meteorology, 35, 830-838.

Eff-Darwich A., Perez J., Fernandez J., Garcia-Lorenzo B. (2011). Using a mesoscale meteorological model to reduce the effect of tropospheric water vapour from DInSAR data: A case study for the island of Tenerife, Pure and Applied Geophysics, 169(8), 1-17.

Elgered G., Ning T., Johansson J., Willén U., Kjellström E., Jarlemark P., Emardson R., Nilsson T. (2010). Validation of climate models using ground-based GNSS observations, Proc. General Assembly of the Nordic Geodetic Commission, 26–30 Sep., Hønefoss, Norway.

Elgered G., and Jarlemark P. O. J. (1998). Ground-based microwave radiometry and long-term observations of atmospheric water vapor, Radio Sci., 33, 707–717.

Elgered G., Davis J.L., Herring T.A., Shapiro I.I. (1991). Geodesy by radio interferometry: water vapor radiometry for estimation of the wet delay, J.Geophys. Res., 96, 6541–6555.

Elias P., Sykioti O., Kontoes C., Avallone A., Van Gorp S., Briole P., Paradissis D. (2006). A method for rapid elimination of high frequency signal noise and unwrapping artefacts from interferometric calculation, International Journal of Remote Sensing, 27(14), 3079-3086.

Elias P. (2013). Ground deformation observed in the western Corinth rift (Greece) by means of SAR interferometry. PhD Thesis. ENS-UPAT: France.

Elliott J. R., Biggs J., Parsons B., Wright T. J. (2008). InSAR slip rate determination on the Altyn Tagh Fault, northern Tibet, in the presence of topographically correlated atmospheric delays, Geophys. Res. Lett., 35, L12309.

Emardson T. R., Elgered G., Johansson J. M. (1998). Three months of continuous monitoring of atmospheric water vapor with a network of Global Positioning System receivers, J. Geophys. Res., 103, 1807–1820.

Emardson T. R., Simons M., Webb F. H. (2003). Neutral atmospheric delay in interferometric synthetic aperture radar applications: Statistical description and mitigation, J. Geophys. Res., 108, 2231.

Fattahi H. and Amelung F. (2013). DEM error correction in InSAR time series, IEEE Trans. Geosci. Remote Sens., 51(7), 4249–4259.

Fattahi H. and Amelung F. (2015). InSAR bias and uncertainty due to the systematic and stochastic tropospheric delay, J. Geophys. Res. Solid Earth, 120, 8758–8773.

Ferretti A., Savio G., Barzaghi R., Borghi A., Musazzi S., Novali F., Prati C., Rocca F. (2007). Submillimeter accuracy of InSAR time series: Experimental validation, IEEE Trans. Geosci. Remote Sens., 45(5), 1142–1153.

Fersch B., Kunstmann H., Devaraju B., Sneeuw N. (2012). Large scale water storage variations from regional atmospheric water budgets and comparison to the GRACE spaceborne gravimetry, J. Hydrometeorol., 13, 1589–1603.

Fersch B. and Kunstmann H. (2014). Atmospheric and terrestrial water budgets: sensitivity and performance of configurations and global driving data for long term continental scale WRF simulations, Clim. Dynam., 42, 2367–2396.

Foster J., Brooks B., Cherubini T., Shacat C., Businger S., Werner C. L. (2006). Mitigating atmospheric noise for InSAR using a high resolution weather model, Geophys. Res. Lett., 33, L16304.

Foster J., Kealy J., Cherubini T., Businger S., Lu Z., Murphy M. (2013). The utility of atmospheric analyses for the mitigation of artifacts in InSAR, J. Geophys. Res. Solid Earth, 118, 748–758.

Ford M., Rohais S., Williams E., Bourlange S., Jousselin D., Backert N., Malartre F. (2013). Tectono-sedimentary evolution of the western Corinth rift (Central Greece), Basin Research, 25, 3-25.

Fournier T., Pritchard M. E., Finnegan N. (2011a). Accounting for atmospheric delays in InSAR data in a search for long wavelength deformation in South America, IEEE Trans. Geosci. Remote Sens., 49(10), 3856–3867.

Garcia-Diez M., Fernandez J., Fita L., Yague C. (2013). Seasonal dependence of WRF model biases and sensitivity to PBL schemes over Europe, Q. J. R. Meteorol. Soc., 139, 501–514.

Gegout P., Biancale R., Soudarin L. (2011). Adaptive mapping functions to the azimuthal anisotropy of the neutral atmosphere, J. Geod., 85, 661–677.

Gendt G., Dick G., Reigber C., Tomassini M., Liu Y., Ramatschi M. (2004). Near real time GPS water vapor monitoring for numerical weather prediction in Germany, J. Meteorol. Soc. Jpn., 82, 361– 370.

Gradinarsky L. P. and Jarlemark P. (2004). Ground-based GPS tomography of water vapour: Analysis of simulated and real data, J. Meteor. Soc. Japan., 82, 551–560.

Guerova G., Jones J., Dousa J., Dick G., De Haan S., Pottiaux E., Bock O., Pacione R., Elgered G., Vedel H., Bender M. (2016). Review of the state of the art and future prospects of the ground-based GNSS meteorology in Europe, Atmos. Meas. Tech., 9, 5385–5406.

Gutman S. I., Sahm S. R., Benjamin S. G., Schwartz B. E., Holub K. L., Stewart J. Q., Smith T. L. (2004a). Rapid retrieval and assimilation of ground based GPS precipitable water observations at the NOAA forecast systems laboratory: Impact on weather forecasts, J. Meteorol. Soc. Jpn., 82, 351–360.

Haase J., Ge M., Vedel H., Calais E. (2003). Accuracy and variability of GPS tropospheric delay measurements of water vapor in the western Mediterranean, J. Appl. Meteorol., 42, 1547– 1568.

Hanssen R. (2001). Radar interferometry data interpretation and error analysis, Ed. Kluwer Academic Publishers, Dordrecht (The Netherlands).

Herring, T., Davis J. L., Shapiro I. I. (1990). Geodesy by radio interferometry: The application of Kalman filtering to the analysis of very long baseline interferometry data, J. Geophys. Res., 95, 12,561-12,581.

Herring T. (2007). Overview. In T. Herring (ed.), Geodesy: Treatise on Geophysics, vol. 3.11, Elsevier B.V.

Hesselbarth A. and Wanninger L. (2008). Short-term stability of GNSS satellite clocks and its effects on Precise Point Positioning, Proceedings of the 21st International Technical Meeting ION GNSS 2008, Savannah, U.S.A., 1855-1863.

Hogg D. C., Guiraud F. O., Decker M. T. (1981). Measurement of excess radio transmission length on earth-space paths, Astronomy and Astrophysics, 95, 304-307.

Hong S., Kim J., Lim J., Dudhia J. (2006). The WRF single moment microphysics scheme (WSM), J. Korean Met. Soc. 42, 129-151.

Hooper A., Bekaert D., Spaans K., Arıkan M. (2012). Recent advances in SAR interferometry time series analysis for measuring crustal deformation, Tectonophysics, 514, 1-13.

Houlié N., Funning G.J., Bürgmann R. (2016). Use of a GPS-derived troposphere model to improve InSAR deformation estimates in the San Gabriel Valley, California, IEEE Trans. Geosci. Remote Sens., 54(9), 5365-5374.

Jade S., and Vijayan M. S. M. (2008). GPS-based atmospheric precipitable water vapor using meteorological parameters from NCEP global reanalysis, J. Geophys. Res., 113.

Janssen V., Ge L., Rizos C. (2004). Tropospheric corrections to SAR interferometry from GPS observations, GPS Solutions, 8(3), 140-151.

Jimenez P. A., Gonzalez-Rouco J. F., Montavez J. P., Garcia-Bustamante E., Navarro J., Dudhia J. (2013). Analysis of the long-term surface wind variability over complex terrain using a high spatial resolution WRF simulation, Clim. Dyn., 40,1643–1656.

Jin S. and Luo O. (2009). Variability and climatology of PWV from global 13-year GPS observations, IEEE Trans. Geosc. Rem. Sens., 47(7), 1918-1924.

Jolivet R., Grandin R., Lasserre C., Doin M.P., Peltzer G. (2011). Systematic InSAR tropospheric phase delay corrections from global meteorological reanalysis data, Geophys. Res. Lett., 38, L17311.

Jolivet R., Agram P. S., Lin N.Y., Simons M., Doin M. P., Peltzer G., Li Z. (2014). Improving InSAR geodesy using Global Atmospheric Models, J. Geophys. Res. Solid Earth, 119, 2324-2341.

Katsanos D., Garcia-Ortega E., De Castro M., Arias E., Tapiador F. J. (2014). High-resolution, near real-time simulation of microwave radiance using a simple land-cover based emissivity prior, Advances in Meteorology, 2014(7).

Kedar S., Hajj G., Wilson B., Heflin M. (2003). The effect of the second order GPS ionospheric correction on receiver positions, Geophys. Res. Lett., 30(16), 1829.

Kinoshita Y., Furuya M., Hobiger T., Ichikawa R. (2013). Are numerical weather model outputs helpful to reduce tropospheric delay signals in InSAR data? J. Geod., 87, 267–277.

Kioutsioukis I., De Meij A., Jakobs H., Katragkou E., Vinuesa J. F., Kazantzidis A. (2016). High resolution WRF ensemble forecasting for irrigation: Multi-variable evaluation, Atmos. Res., 167, 156–174.

Koletsis I., Giannaros T. M., Lagouvardos K., Kotroni V. (2016). Observational and numerical study of the Vardaris wind regime in northern Greece, Atmos. Res., 171, 107–120.

Kotlarski S., Block A., Bohm U., Jacob D., Keuler K., Knoche R., Rechid D., Walter A. (2005). Regional climate model simulations as input for hydrological applications: evaluation of uncertainties, Adv. Geosci., 5, 119–125.

Lagler K., Schindelegger M., Boehm J., Krasna H., Nilsson T. (2013). GPT2: Empirical slant delay model for radio space geodetic techniques, Geophys. Res. Letters, 40, 1069–1073.

Landskron D., and Boehm J. (2018). VMF3/GPT3: refined discrete and empirical troposphere mapping functions, J. Geod., 9, 349–360.

Li Z., Muller J. P., Cross P. (2003). Comparison of precipitable water vapor derived from radiosonde, GPS, and Moderate-Resolution Imaging Spectroradiometer measurements, J. Geophys. Res., 108.

Li Z., Muller J. P., Cross P., Fielding E. J. (2005). Interferometric synthetic aperture radar (InSAR) atmospheric correction: GPS, Moderate Resolution Imaging Spectroradiometer (MODIS), and InSAR integration, J. Geophys. Res., 110, B03410.

Li Z., Fielding E. J., Cross P., Preusker R. (2009). Advanced InSAR atmospheric correction: MERIS/MODIS combination and stacked water vapour models, Int. J. Remote Sens., 30(13), 3343–3363.

Li Z., Pasquali P., Cantone A., Singleton A., Funning G., Forrest D. (2012). MERIS atmospheric water vapor correction model for wide swath interferometric synthetic aperture radar, IEEE Geoscience and Remote Sensing Letters, 9(2).

Lin Y. N., Simons M., Hetland E. A., Muse P., DiCaprio C. (2010). A multiscale approach to estimating topographically correlated propagation delays in radar interferograms, Geochem. Geophys. Geosyst., 11, Q09002.

Liu J., Chen S., Yeh W., Tsai H., Rajesh P. (2016). Worst-case GPS scintillations on the ground estimated from radio occultation observations of FORMOSAT-3/COSMIC during 2007–2014, Surv. Geophys., 37, 791–809.

Löfgren J. S., Björndahl F., Moore A. W., Webb F. H., Fielding E. J., Fishbein E. F. (2010). Tropospheric correction for InSAR using interpolated ECMWF data and GPS Zenith Total Delay from the Southern California integrated GPS network, IEEE International Geoscience and Remote Sensing Symposium, 4503–4506.

Lopez-Quiroz P., Doin M., Tupin F., Briole P., Nicolas J. (2009). Time series analysis of Mexico City subsidence constrained by radar interferometry, J. Appl. Geophys., 69(1), 1–15.

Lorenz T. and Barstad I. (2016). A dynamical downscaling of ERA-Interim in the North Sea using WRF with a 3km grid for wind resource applications, Wind Energ., 19, 1945–1959.

Massonnet D., Rossi M., Carmona C., Adragna F., Peltzer G., Feigl K., Rabaute T. (1993). The displacement field of the Landers earthquake mapped by radar interferometry, Nature, 364(6433), 138–142.

Massonnet D. and Feigl K. (1998). Radar interferometry and its application to changes in the Earth's surface, Rev. Geophys., 36, 441-500.

Mooney P.A., Mulligan F.J., Fealy R. (2013). Evaluation of the sensitivity of the weather research and forecasting model to parameterization schemes for regional climates of Europe over the period 1990–95, J. Clim., 26, 1002–1017.

Madala S., Satyanarayana A., Srinivas C., Bhishma T. (2016). Performance evaluation of PBL schemes of ARW model in simulating thermo-dynamical structure of pre-monsoon convective episodes over Kharagpur using STORM data sets, Pure Appl. Geophys., 173, 1803–1827.

Marini J. (1972). Correction of satellite tracking data for an arbitrary tropospheric profile, Radio Science, 7(2).

Michas G., Vallianatos F., Sammonds P. (2015). Statistical mechanics and scaling of fault populations with increasing strain in the Corinth Rift, Earth and Planetary Science Letters, 431, 150–163.

Niell A. E. (1996). Global mapping functions for the atmosphere delay at radio wavelengths, J. Geophys. Res., 101, 3227–3246.

Ning T. and Elgered G. (2012). Trends in the atmospheric water vapor content from ground-based GPS: The impact of the elevation cutoff angle, IEEE Journal of Selected Topics in Applied Earth Observations and Remote Sensing, 5(3), 744-751.

Nunalee C. G., Horvath A., Basu S. (2015). High-resolution numerical modeling of mesoscale island wakes and sensitivity to static topographic relief data, Geosci. Model Dev., 8, 2645–2653.

Onn F., and Zebker H. A. (2006). Correction for interferometric synthetic aperture radar atmospheric phase artifacts using time series of zenith wet delay observations from a GPS network, J. Geophys. Res., 111, B09102.

Ozawa T., Fujita E., Ueda H. (2016). Crustal deformation associated with the 2016 Kumamoto earthquake and its effect on the magma system of Aso volcano, Earth Planets Space, 68, 186.

Papanastasiou D., Melas D., Bartzanas T., Kittas C. (2010). Temperature, comfort and pollution levels during heat waves and the role of sea breeze, Int. J. Biometeorol., 54, 307-317.

Parcharidis I., Foumelis M., Kourkouli P., Wegmuller U. (2009). Persistent Scatterers InSAR to detect ground deformation over Rio-Antirio area (Western Greece) for the period 1992-2000, J. of App. Geophys., 68, 348-355.

Pinel V., Hooper A., De la Cruz-Reyna S., Reyes-Davila G., Doin M., Bascou P. (2011). The challenging retrieval of the displacement field from InSAR data for andesitic stratovolcanoes: Case study of Popocatepetl and Colima volcano, Mexico, J. Volcanol. Geotherm. Res., 200, 49–61.

Poli, P., Moll P., Rabier F., Desrozier G., Chapnik B., Berre L., Healy S. B., Andersson E., El Guelai F. Z. (2007). Forecast impact studies of zenith total delay data from European near real-time GPS stations in Météo France 4DVAR, J. Geophys. Res., 112, D06114.

Prein A., Langhans W., Fosser G., Ferrone A., Ban N., Goergen K., Keller M., Tölle M., Gutjahr O., Feser F., Brisson E., Kollet S., Schmidli J., Van Lipzig N., Leung R. (2015). A review on regional

convection-permitting climate modeling: Demonstrations, prospects, and challenges, Rev. Geophys., 53(2), 323-361.

Pu Z., Zhang H., Anderson J. (2013). Ensemble Kalman filter assimilation of near-surface observations over complex terrain: comparison with 3DVAR for short-range forecasts, Tellus A: Dynamic Meteorology and Oceanography, 65(1).

Puliafito S. E., Allende D. G., Mulena C. G., Cremades P., Lakkis S. G. (2015). Evaluation of the WRF model configuration for Zonda wind events in a complex terrain, Atmos. Res., 166, 24–32.

Puysségur B., Michel R., Avouac J.P. (2007). Tropospheric phase delay in interferometric synthetic aperture radar estimated from meteorological model and multispectral imagery, J. Geophys. Res., 112.

Pytharoulis J., Kotsopoulos S., Tegoulias I., Kartsios S., Bampzelis D., Karacostas T. (2016). Numerical modeling of an intense precipitation event and its associated lightning activity over northern Greece, Atmos. Res., 169, 523-538.

Resch G. M. (1984). Water vapor radiometry in geodetic applications, in Geodetic Refraction, F. K. Brunner (ed.), 53-84, Springer-Verlag, New York.

Rocken C., Van Hove T., Ware R. (1997). Near real-time GPS sensing of atmospheric water vapor, Geophys. Res. Lett., 24, 3221– 3224.

Rosen P.A., Hensley S., Joughin I., Li F., Madsen S., Rodriguez E., Goldstein R. (2000) Synthetic aperture radar interferometry, Proc. IEEE 88, 333–382.

Saastamoinen, J. (1973). Contributions to the theory of atmospheric refraction - Part II. Refraction corrections in satellite geodesy, Bull. Géod., 47(1), 13–34.

Schwitalla T., Zangl G., Bauer H. S., Wulfmeyer V. (2008). Systematic errors of QPF in low-mountain regions. Special issue on quantitative precipitation forecasting. Meteorol. Z., 17, 903–919.

Schwitalla T., Bauer H. S., Wulfmeyer V., Aoshima F. (2011). High-resolution simulation over central Europe: assimilation experiments during COPS IOP 9c, Q. J. R. Meteorol. Soc., 137, 156 – 175.

Seity Y., Brousseau P., Malardel S., Hello G., Benard P., Bouttier F., Lac C., Masson V. (2011). The AROME-France Convective-Scale Operational Model, M. W. R., 139, 976-991.

Shangguan M., Bender M., Ramatschi M., Dick G., Wickert J., Raabe A., Galas R. (2013). GPS tomography: validation of reconstructed 3-D humidity fields with radiosonde profiles, Ann. Geophys., 31, 1491–1505.

Shirzaei M., and Burgmann R. (2012). Topography correlated atmospheric delay correction in radar interferometry using wavelet transforms, Geophys. Res. Lett., 39, L01305.

Simonetto E., Durand F., Morel L., El Hamri Y., Froger J., Nicolas J., Durand S., Polidori L. (2015). Influence of GNSS configuration and map interpolation method on InSAR atmospheric phase assessment, Proceedings of the FRINGE workshop, vol. 731.

Simons M. and Rosen P. A. (2007). Interferometric synthetic aperture radar geodesy. In G. Schubert (ed.), Treatise on Geophysics (2007), pp. 391-446, Elsevier B.V.

Simpson J. J., Berg J. S., Koblinsky C. J., Hufford G. L., Beckley B. (2001). The NVAP global water vapor dataset: Independent cross comparison and multiyear variability, Remote Sens. Environ., 76, 112–129.

Skamarock W., Klemp J.B., Dudhia J., Gill D.O., Barker D., Duda M.G., Huang X. Y., Wang W. (2008). A description of the advanced research WRF version 3. NCAR Technical Note NCAR/TN-475.

Smith E. and Weintraub S. (1953). The constants in the equation for atmospheric refractive index at radio frequencies, Proceedings of the IRE 50(8), 1035 – 1037.

Sokos, E., Zahradnik, J., Kiratzi, A., Jansky, J., Gallovic, F., Novotny, O., Kostelecky, J., Serpetsidaki, A., Tselentis, G. A. (2012). The January 2010 Efpalio earthquake sequence in the western Corinth Gulf (Greece), Tectonophysics, 530-531, 299–309.

Solheim F., Vivekanandan J., Ware R., Rocken C. (1999). Propagation delays induced in GPS signals by dry air, water vapor, hydrometeors, and other particulates, Journal of Geophys. Res. Atm., 104, 9663-9670.

Soltanzadeh I., Bonnardot V., Sturman A., Quénol H., Zawar-Reza P. (2016). Assessment of the ARW-WRF model over complex terrain: the case of the Stellenbosch Wine of Origin district of South Africa, Theor. Appl. Climatol., 129(3–4), 1407–1427.

Spilker J. (1978). GPS signal structure and performance characteristics, Navigation, 25(2), 121-146.

Tang Y., Lean H., Bornemann J. (2013). The benefits of the Met Office variable resolution NWP model for forecasting convection, Meteorological Applications, 20(4), 417-426.

Tarayre H. and Massonnet D. (1996). Atmospheric propagation heterogeneities revealed by ERS-1 interferometry, Geophys. Res. Letters, 23(9), 989-992.

Taylor B., Weiss J. R., Goodliffe A. M., Sachpazi M., Laigle M., Hirn A. (2011). The structures, stratigraphy and evolution of the Gulf of Corinth rift, Greece, Geophys. J. Int., 185, 1189–1219.

Teke, K., Böhm J., Nilsson T., Schuh H., Steigenberger P., Dach R., Heinkelmann R., Willis P., Haas R., García-Espada S., Hobiger T., Ichikawa R., Shimizu S. (2011). Multi-technique comparison of troposphere zenith delays and gradients during CONT08, J. Geod., 85(7), 395–413.

Teke K., Nilsson T., Boehm J., Hobiger T., Steigenberger P., Garcia-Espada S., Haas R., Willis P. (2013). Troposphere delays from space geodetic techniques, water vapor radiometers, and numerical weather models over a series of continuous VLBI campaigns, J. Geod., 87, 981-1001.

Thompson G., Tewari M., Ikeda K., Tessendorf S., Weeks C., Otkin J., Kong F. (2016). Explicitly-coupled cloud physics and radiation parameterizations and subsequent evaluation in WRF high-resolution convective forecasts, Atmos. Res., 168, 92–104.

Tomassini M., Gendt G., Dick G., Ramatschi M., Schraff C. (2002). Monitoring of Integrated Water Vapour from ground-based GPS observations and their assimilation in a limited-area NWP model, Physics and Chemistry of the Earth Parts A/B/C, 27(4-5), 341-346.

Tralli D. M. and Lichten S. M. (1990). Stochastic estimation of tropospheric path delays in global positioning system geodetic measurements, Bull. Géod., 64(2), 127–159.

Tregoning, P., Boers R., O'Brien D., Hendy M. (1998). Accuracy of absolute precipitable water vapor estimates from GPS observations, J. Geophys. Res., 103, 28,701–710.

Trenberth, K., Fasullo J., Smith L. (2005). Trends and variability in column integrated atmospheric water vapour, Climate Dyn., 24, 741–758.

Treuhaft R. and Lanyi G. (1987). The effect of the dynamic wet troposphere on radio interferometric measurements, Radio Science, 22(2), 251-265.

Troller M., Geiger A., Brockmann E., Bettems J. M., Burki B., Kahle H.G. (2006). Tomographic determination of the spatial distribution of water vapour using GPS observations, Adv. Space Res., 37, 2211–2217.

Van Baelen J., Reverdy M., Tridon F., Labbouz L., Dick G., Bender M., Hagen M. (2011). On the relationship between water vapour field evolution and the life cycle of precipitation systems, Q J R Meteorol. Soc., 137, 204-223.

Wadge G., Webley P., James I., Bingley R., Dodson A., Waugh S., Veneboer S., Puglisi G., Mattia M., Baker D., Edwards S., Clarke P. (2002). Atmospheric models, GPS and InSAR measurements of the tropospheric water vapour field over Mount Etna, Geophys. Res. Lett., 29(19), 11–1–11-4.

Walpersdorf A., Calais E., Haase J., Eymard L., Desbois M., Vedel H. (2001). Atmospheric gradients estimated by GPS compared to a high resolution Numerical Weather Prediction (NWP) model, Physics and Chemistry of the Earth Part A Solid Earth and Geodesy, 26(3), 147-152.

Walters R., Elliott J., Li Z., Parsons B. (2013). Rapid strain accumulation on the Ashkabad fault (Turkmenistan) from atmosphere-corrected InSAR, J. Geophys. Res., 118, 1-17.

Wang J., Zhang L., Dai A., Van Hove T., Van Baelen J. (2007). Near-global 2h dataset of atmospheric precipitable water from GPS measurements , J. Geoph. Res., 112, D11107.

Wang H. and Wright T. (2012). Satellite geodetic imaging reveals internal deformation of western Tibet, Geophys. Res. Letters, 39(7), L07303.

Warrach-Sagi K., Schwitalla T., Wulfmeyer V., Bauer H. (2013). Evaluation of a climate simulation in Europe based on the WRF–NOAH model system: precipitation in Germany, Climate Dynamics, 41(3–4), 755–774.

Ware R., Exner M., Feng D., Gorbunov M., Hardy K., Herman B., Kuo Y., Meehan T., Melbourne W., Rocken C., Schreiner W., Sokolovskiy S., Solheim F., Zou X., Anthes R., Businger S., Trenberth K. (1996). GPS sounding of the atmosphere from Low Earth Orbit: preliminary results, Bull. Amer. Meteor. Soc., 77, 19-40.

Wicks C., Thatcher W., Dzurisin D. (2002). Satellite InSAR reveals a new style of deformation at Yellowstone caldera, EOS Trans. AGU Fall Meet. Suppl. 83, 1291.

Wilby R. and Dawson C. (2013). The Statistical Downscaling Model: insights from one decade of application, Int. J. Climatol., 33(7), 1707-1719.

Williams S., Bock Y., Fang P. (1998). Integrated satellite interferometry: tropospheric noise, GPS estimates and implications for interferometric synthetic aperture radar products, J. Geophys. Res., 103, 27051-27067.

Wright T., Fielding E., Parsons B. (2001). Triggered slip: observations of the 17 August 1999 Izmit (Turkey) earthquake using radar interferometry, Geophys. Res. Letters, 28(6), 1079-1082.

Yague-Martinez N., Prats-Iraola P., Rodríguez González F., Brcic R., Shau R., Geudtner D., Eineder M., Bamler R. (2016). Interferometric Processing of Sentinel-1 TOPS Data. IEEE Trans. Geosci. Remote Sens., 54, 2220-2234.

Yun Y., Zeng Q., Green B. W., Zhang F. (2015). Mitigating atmospheric effects in InSAR measurements through high-resolution data assimilation and numerical simulations with a weather prediction model, International Journal of Remote Sensing, 36(8), 2129-2147.

Zebker H. and Villasenor J. (1992). Decorrelation in interferometric radar echoes, IEEE Transactions on Geoscience and Remote Sensing, 30(5), 950 – 959.

Zhang C., Lin H., Chen M., Yang L. (2014). Scale matching of multiscale digital elevation model (DEM) data and the Weather Research and Forecasting (WRF) model: a case study of meteorological simulation in Hong Kong, Arab J. Geosci., 7, 2215–2223.

Zhang X., Xiong Z., Jingyun Z., Ge Q. (2017). High-resolution precipitation data derived from dynamical downscaling using the WRF model for the Heihe River Basin, northwest China, Theor. Appl. Climatol., 131, 1249-1259.

Zhou X., Chang N. Li S. (2009). Applications of SAR Interferometry in Earth and Environmental Science Research, Sensors, 9, 1876-1912.

Zumberge J.F., Heflin M.B., Jefferson D.C., Watkins M.M., Webb F.H. (1997). Precise point positioning for the efficient and robust analysis of GPS data from large networks. Journal of Geophys. Res., 102, 5005-5017.

Zus F., Dick G., Dousa J., Wickert J. (2014b). Systematic errors of mapping functions which are based on the VMF1 concept, GPS Solut., 19, 277– 286.

RÉSUMÉ

La Géodésie spatiale, par interférométrie radar à synthèse d'ouverture (InSAR) et Global Navigation Satellite System (GNSS), permet de cartographier les déformations tectoniques de la Terre. Les vitesses inter-sismiques, sont petites, de l'ordre de quelques mm an^{-1}. Pour atteindre une précision de positionnement relatif millimétrique, surtout dans la composante verticale, les délais troposphériques affectant les signaux GNSS et InSAR doivent être parfaitement corrigés.

Pour le GNSS, les délais troposphériques peuvent être évalués précisément grâce à la géométrie d'observation et à la redondance des données. La précision est telle que ces délais sont désormais assimilés en routine dans les modèles météorologiques.

La correction des interférogrammes est plus complexe parce que les données InSAR ne contiennent pas d'information permettant de remonter explicitement aux délais troposphériques. Au premier ordre, il est possible de calculer la part de l'interférogramme corrélée avec la topographie et de la corriger. Mais cette correction n'éliminer pas les hétérogénéités de courte longueurs d'onde ni les gradients régionaux. Pour cela il faut utiliser d'autres méthodes qui peuvent être basées sur l'utilisation des délais zénithaux GNSS disponibles dans la région ou sur des modèles météorologiques à haute résolution, ou sur une combinaison des deux.

Les délais zénithaux GNSS présentent l'intérêt de leur exactitude et de leur précision maîtrisée, mais dans la plupart des régions, ils ne sont disponibles, au mieux, qu'à quelques dizaines de points dans une image typique de 100 x 100 km. A l'opposé les modèles troposphériques à haute résolution apportent une vision matricielle globale, cependant leur précision est difficile à évaluer, surtout en zone de montagne.

Dans ma thèse, je calcule, sur la partie ouest du golfe de Corinthe, et pour l'année 2016, des modèles météorologiques à la résolution de 1 km, à l'aide du modèle américain WRF (Weather Research and Forecasting). Je compare les délais zénithaux prédits par le modèle avec ceux observés à dix-neuf stations GNSS permanentes. Ces données GNSS me permettent de choisir, parmi cinque jeux différents de paramètres de calcul WRF, celui qui aboutit au meilleur accord entre les délais GNSS et ceux issus de mes modèles. Je compare ensuite les séries temporelles GNSS de l'année 2016 aux sorties de modèles aux dix-neuf pixels correspondants. J'utilise enfin les sorties de mes modèles pour corriger les interférogrammes Sentinel-1 produits dans la zone d'étude avec des intervalles d'acquisition de 6, 12, 18 et 24 jours pour lesquels la cohérence des interférogramme demeure généralement élevée. Je montre qu'un modèle météorologique à haute résolution, ajusté à l'échelle locale à l'aide de données GNSS disponibles, permet une correction troposphérique des interférogrammes qui élimine une partie significative des effets de courte longueur d'onde, jusqu'à 5 km environ, donc plus courte que la longueur d'onde typique du relief.

MOTS CLÉS

Modèles météorologiques à haute résolution, WRF, météorologie GNSS, correction troposphérique des interférogrammes InSAR.

ABSTRACT

Space geodesy techniques (SAR interferometry and GNSS) have recently emerged as an important tool for mapping regional surface deformations due to tectonic movements. A limiting factor to this technique is the effect of the troposphere, as horizontal and vertical surface velocities are of the order of a few mm yr-1, and high accuracy (to mm level) is essential. The troposphere introduces a path delay in the microwave signal, which, in the case of GNSS Precise Point Positioning (PPP), can nowadays be successfully removed with the use of specialized mapping functions. Moreover, tropospheric stratification and short wavelength spatial turbulences produce an additive noise to the low amplitude ground deformations calculated by the (multitemporal) InSAR methodology. InSAR atmospheric phase delay corrections are much more challenging, as opposed to GNSS PPP, due to the single pass geometry and the gridded nature of the acquired data. Several methods have been proposed, including Global Navigation Satellite System (GNSS) zenithal delay estimations, satellite multispectral imagery analysis, and empirical phase/topography estimations. These methods have their limitations, as they rely either on local data assimilation, which is rarely available, or on empirical estimations which are difficult in situations where deformation and topography are correlated. Thus, the precise knowledge of the tropospheric parameters along the propagation medium is extremely useful for the estimation and minimization of atmospheric phase delay, so that the remaining signal represents the deformation mostly due to tectonic or other geophysical processes.

In this context, the current PhD Thesis aims to investigate the extent to which a high-resolution weather model, such as WRF, can produce detailed tropospheric delay maps of the required accuracy, by coupling its output (in terms of Zenith Total Delay or ZTD) with the vertical delay component in GNSS measurements. The model initially is operated with varying parameterization in order to demonstrate the best possible configuration for our study, with GNSS measurements providing a benchmark of real atmospheric conditions. In the next phase, the two datasets (predicted and observed) are compared and statistically evaluated for a period of one year, in order to investigate the extent to which meteorological parameters that affect ZTD, can be simulated accurately by the model under different weather conditions. Finally, a novel methodology is tested, in which ZTD maps produced from WRF and validated with GNSS measurements in the first phase of the experiment are used as a correction method to eliminate the tropospheric effect from selected InSAR interferograms. Results show that a high-resolution weather model which is fine-tuned at the local scale can provide a valuable tool for the tropospheric correction of InSAR remote sensing data.

KEYWORDS

High-resolution numerical weather modeling, WRF, GNSS meteorology, InSAR tropospheric correction.